

Understanding the impact of molecular reorganization on morphology formation and charge transfer in organic solar cells

Dissertation

Von der Universität Bayreuth
zur Erlangung des Grades eines
Doktors der Naturwissenschaften (Dr. rer. nat.)
genehmigte Abhandlung

von
Stefan Sebastian Wedler

geboren in Dachau, Deutschland

Erste Gutachterin:	Prof. Dr. Anna Köhler
Zweiter Gutachter:	Prof. Dr. Axel Enders

Tag der Einreichung:	18.12.2020
Tag des Kolloquiums:	04.03.2021

*Experiments never deceive.
It is our judgement that deceives itself because
it expects results which experiments do not give.*

LEONARDO DA VINCI
15th century

Deutsche Kurzzusammenfassung

Organische Halbleiter sind eine interessante Materialklasse, die bereits im Alltag verbreitet ist. Organische Leuchtdioden werden kommerziell beispielsweise in Smartphonedisplays oder Flachbildfernseher benutzt. Hingegen steckt die organische Photovoltaik noch in den Kinderschuhen, obwohl es schon einige Pilotprojekte und Produkte gibt. Diese Bauteile können auf flexiblen Substraten in verschiedenen Farben und Formen produziert werden, und im Labor werden schon beeindruckende Effizienzen jenseits von 18 % erreicht. Eine Schlüsselerkenntnis für diesen Fortschritt ist die maßgebliche Rolle der Morphologie der aktiven Schicht. Dies liegt an der amorphen Beschaffenheit von organischen Halbleitern sowie der exzitonisch geprägten elektronischen Struktur. Außerdem sind intermolekulare Wechselwirkungen gewöhnlich stark abhängig von inter- und intramolekularen Konformationen. Es scheint also plausibel, dass molekulare Flexibilität und die damit verbundene Möglichkeit zur molekularen Reorganisation die elektronische Struktur konjugierter Materialien im kondensierten Zustand beeinflusst. Die vorliegende Arbeit untersucht das Zusammenspiel zwischen molekularer Reorganisation und dessen Folgen für die elektronische Struktur in molekularen Verbänden. Dabei konzentriere ich mich auf zwei verschiedene Aspekte.

Die molekulare Geometrie kann sich während Transferprozessen ändern, welche für die Funktionsfähigkeit organischer Bauteile essentiell sind. Beispielsweise ist in Solarzellen der erste Ladungstransfer von einem photoangeregten Donormolekül zu einem neutralen Akzeptormoleküle wichtig, wodurch ein sogenannter Charge-Transfer-Zustand erzeugt wird. Dieser Ladungstransfer wird in der Forschungsgemeinde gerne mit der klassischen Marcustheorie beschrieben, welche bei der theoretischen Modellierung von Transferprozessen die Hochtemperaturnäherung darstellt. Hierdurch wird jedoch der Beitrag des quantenmechanischen Tunneleffekts unterschätzt. Ich habe mich daher kritisch mit den Vorhersagen des Marcus-Modells für Elektronentransfer in Donor-Akzeptor Blend-Systemen auseinandergesetzt. Die Transferrate sollte theoretisch stark temperaturabhängig sein. Es stellt sich jedoch heraus, dass die Anwendung der Marcustheorie hier eher fragwürdig ist, weil im Experiment bei allen untersuchten Temperaturen ultraschnelle Transferzeiten beobachtet wurden, innerhalb derer kein thermodynamisches Gleichgewicht möglich ist.

Existenz und Eigenschaften dieser Charge-Transfer-Zustände hängen von den lokalen intermolekularen Anordnungen sowie dem Ordnungsgrad ab. Daher untersuche ich als zweiten Aspekt, wie geordnete Strukturen und Aggregate entstehen, und wie die Möglichkeit von

konformationeller Reorganisation sich auf Wege in Aggregatstrukturen auswirken. Aggregate zeichnen sich hierbei durch elektronische intermolekulare Wechselwirkungen aus. Dafür habe ich die Modelloligomere TT und CT verwendet, die sich nur in ihrem zentralen Baustein unterscheiden, und deren Aggregatbildung verglichen. Das flexible TT besteht aus zwei Thiophenen, die in einer head-to-head Anordnung verbunden sind. Dadurch erzeugen die Hexylseitenketten eine Verdrillung im Zentrum, die übrige Struktur ist planar. Das Gegenstück CT hat als zentrale Einheit ein Cyclopentadithiophen, wodurch das gesamte Molekül planar und steif ist. Zunächst habe ich die intrinsischen Aggregationseigenschaften in Lösung mit temperaturabhängiger Absorptions- und Emissionsspektroskopie untersucht. TT aggregiert relativ stark, wobei CT im Gegensatz dazu unerwartet schwach aggregiert und eher strahlungslose Exzimer-ähnliche Wechselwirkungen ausbildet. Ausführliche Analysen der Spektren haben zusammen mit Molekulardynamiksimulationen und quantenchemischen Rechnungen gezeigt, dass die Flexibilität von TT dabei hilft, genügend intermolekulare anziehende Kontaktpunkte auszubilden. Zudem planarisiert TT auf dem Weg ins Aggregat sogar trotz der sterischen Abstoßung durch die Seitenketten.

Obleich die Aggregationseigenschaften in Lösung einen Anhaltspunkt für die Eigenschaften im Festkörper darstellen, ist ein detailliertes Verständnis der Filmbildung unerlässlich, um die Mikrostruktur in dünnen Filmen zu kontrollieren. Deshalb müssen die optischen Eigenschaften beim Prozessieren untersucht werden. Hierfür habe ich einen einfach nutzbaren Aufbau entwickelt, der gleichzeitig Absorption und Emission bei der Filmbildung messen kann. Hiermit kann ich das Aggregationsverhalten von CT und TT in Lösung mit den jeweiligen Eigenschaften bei der Filmbildung korrelieren. Bei beiden Molekülen sieht man, dass dies in gleichen Phasen mit verschiedenen Timings stattfindet. Die Flexibilität und die damit verbundene Fähigkeit zur molekularen Reorganisation von TT führt zu molekularen Umorientierungen hin zu geordneten Strukturen, was sogar nach der Filmtrocknung stattfindet. Hingegen werden bei CT Molekülanordnungen kinetisch eingefroren und die Steifheit verhindert, dass sich intermolekulare Anordnungen zu mehr Ordnung hin ausbilden. Eine gewisse Flexibilität hilft somit, geordnete Strukturen zu erzeugen.

CT und TT sind wohl-definierte Oligomere, deren Filmbildungseigenschaften nicht repräsentativ für Polymere sein müssen. Bei Polymeren ist bekannt, dass Prozessierung bei Temperaturen unter oder über der Temperatur des Unordnungs-Ordnungs-Übergangs in Lösung zu mehr oder weniger geordneter Mikrostruktur führt. In der letzten Studie habe ich diesen Ansatz verallgemeinert und die Relevanz von sowohl Löslichkeit als auch Verdampfungsrates des Lösungsmittels am Beispiel von P3HT untersucht. Dabei hat sich gezeigt, dass beim Prozessieren Mikrotimings das Zünglein an der Waage sein können und Phasen der Aggregation im noch nassen Film gezielt verstärken oder unterdrücken können, was sich letztendlich direkt auf den Ordnungsgrad in aggregierten Domänen im fertigen Film niederschlägt.

English abstract

Organic semiconductors are an interesting material class, which is present in everyday life. Organic light emitting diodes are commercially exploited in smartphone displays or flat screen televisions. Organic photovoltaics are still in the early commercial stages despite several pilot projects and products. Fabrication of these devices can be performed onto flexible substrates in different colours and shapes, with laboratory scale solar cell efficiency exceeding already 18%. On the way toward this impressive value, one key insight was that the morphology of the active layer massively impacts on the performance. This is due to the amorphous nature of organic semiconductors as well as the excitonic character of the electronic structure. Furthermore, intermolecular interactions can be highly sensitive to changes of inter- and intramolecular conformations. Thus, it seems plausible that the degree of molecular flexibility and the associated capability for molecular reorganization impacts on the electronic structure of conjugated materials in the condensed state. This thesis investigates the interplay between molecular reorganization and its implications on the electronic structure in molecular assemblies. Hereby, I examine two different aspects.

Molecular geometries can change during transfer processes, which are relevant for the functioning of organic devices. In solar cells, for example, special relevance comes to the initial charge transfer from a photoexcited donor material to a neutral acceptor material, which generates an interfacial charge transfer state and comprises a first step for charge separation. In literature, this electron transfer is often described in the framework of classical Marcus theory. However, the relevance of quantum mechanical tunneling effects is underestimated here, as the Marcus mechanism resembles the high-temperature limit of charge transfer theories. I critically tested its applicability for electron transfer in donor-acceptor blend systems, utilizing the strong temperature dependence of the predicted transfer rate within the Marcus framework. It turns out that Marcus theory is at least questionable in this context, as the required thermodynamic equilibrium is not established within the ultrafast transfer times observed in experiment for all investigated temperatures.

The existence and properties of these charge transfer states are determined by local intermolecular arrangements and the degree of order. Thus, the second aspect deals with the formation of ordered structures and aggregates, which are characterized by electronic interaction, and how aggregation pathways are influenced by the extend of possible conformational reorganization. I used two oligomer model compounds, which differ only in their central

molecular unit, and compare their propensity to establish aggregates. The flexible TT consists of two twistable thiophene units. Their head-to-head linkage for the hexyl side chains induce a twisted dihedral angle in the otherwise planar structure, retaining sufficient rotational freedom. Its counterpart CT comprises a carbon-bridged cyclopentadithiophene. The central connected thiophenes make the molecule stiff and entirely planar. First, I examined their intrinsic aggregation properties in solution using temperature dependent absorption and emission spectroscopy. Unexpectedly, the flexible TT shows a strong propensity to aggregate formation in contrast to CT, where non-emissive excimer-like interactions prevail. Detailed spectral analysis supported by molecular dynamics and quantum-chemical simulations revealed that the flexibility of TT helps to establish a sufficient number of attractive intermolecular contact points. Even more, the twisted central dihedral angle planarizes against the steric obstructions of the side chains during the pathway into aggregated structures.

While it seems intuitive that solution aggregation is indicative for solid state properties, a detailed understanding of film formation is essential to control the microstructure in thin films. Hence, it is necessary to investigate the optical properties during processing. For this, I developed an easy-to-use experimental setup, which allows to monitor absorption and emission simultaneously while a film forms. This setup enabled me to correlate the aggregation behaviour of CT and TT in solution to their respective film formation properties. For both molecules I showed that film formation takes place in similar stages, yet timings are remarkably different. The flexibility of TT and the ascribed ability for molecular reorganization leads to molecular reorientation into well-ordered structures even after complete solvent evaporation. In contrast, CT molecules are kinetically trapped and their stiffness prevents further optimization of local intermolecular arrangements. Thus, a certain amount of flexibility is beneficial for the establishment of ordered structures.

As CT and TT are well-defined oligomers, their film formation properties may not be representative for the case of polymers. Here, it is known that processing at temperatures above or below the disorder-order transition in solution results in less or more ordered microstructures. In the final study of this thesis I generalized this framework to the importance of both solubility and solvent evaporation rate for the final morphology, investigating prototypical P3HT. It turns out that microtimings during processing can turn the scale and specifically enhance or suppress the formation of aggregates in the still wet film, which directly impacts on the amount of order within aggregated domains in the final film.

Contents

Deutsche Kurzzusammenfassung	v
English abstract	vii
I Introduction	1
1 Motivation	3
2 Mechanisms of charge transfer and charge generation	7
3 Photophysics from isolated molecules to the condensed state	11
3.1 The Franck-Condon principle	11
3.2 Optical signatures of aggregates	13
4 Establishment of ordered structures	19
4.1 General relations between molecular properties and order	19
4.2 Influence of processing parameters on the formation of ordered structures . .	21
5 Overview of the thesis	25
5.1 Summary and overall context	25
5.2 Contents of the individual publications	31
5.2.1 The Impact of Driving Force and Temperature on the Electron Transfer in Donor-Acceptor Blend Systems	31
5.2.2 What is the role of planarity and torsional freedom for aggregation in a π -conjugated donor-acceptor model oligomer?	34
5.2.3 Setup to Study the in Situ Evolution of Both Photoluminescence and Absorption during the Processing of Organic or Hybrid Semiconductors	38
5.2.4 Role of Torsional Flexibility in the Film Formation Process in Two π -Conjugated Model Oligomers	41
5.2.5 Processing condition dependent aggregation pathways in conjugated polymers	45
5.3 Individual contributions to the publications	50
References	53

II Publications	71
6 The Impact of Driving Force and Temperature on the Electron Transfer in Donor–Acceptor Blend Systems	73
7 What is the role of planarity and torsional freedom for aggregation in a π-conjugated donor–acceptor model oligomer?	99
8 Setup to Study the in Situ Evolution of Both Photoluminescence and Absorption during the Processing of Organic or Hybrid Semiconductors	141
9 Role of Torsional Flexibility in the Film Formation Process in Two π-Conjugated Model Oligomers	151
10 Processing condition dependent aggregation pathways in conjugated polymers	167
Appendix	209
A Graphical user interface for Franck-Condon analysis	209
B Analysis of time-resolved data using reconvolution fitting	217
C Improvements of the ultrafast transient absorption setup	223
D Analysis of in situ data	229
Acknowledgements	247
Erklärung und eidesstattliche Versicherung	249

Part I

Introduction

1 Motivation

Organic semiconductors have arrived in everyday life. Commercially relevant applications are organic light emitting diode (OLED) displays, which are used for example by Samsung in their Galaxy smartphones since 10 years.¹ Televisions with OLED displays can be found in many different screen sizes nowadays. Organic photovoltaics (OPV) is still in its early commercial stages, yet several products and projects from companies like Heliatek, ARMOR (former OPVIUS) or BELECTRIC already show its promising potential. OPVs can be fabricated on flexible substrates in different colours and shapes,²⁻⁶ which renders them interesting for applications as power generating design elements, as exemplary shown in Figure 1.1. The power conversion efficiency of research devices utilizing fullerenes as acceptors stagnated around 12 %, until the field received a new boost through the discovery and optimization of nonfullerene acceptors.^{7,8} The current record device has an impressive efficiency of 18.22 % (certified: 17.6 %)⁹ and brings the psychologically important value of 20 % in closer proximity.

The material class of organic semiconductors consists of organic small molecules or polymers, whose core units are dominated by conjugated bonds.¹⁰ This results in extrinsic semiconducting properties, which are dominated by $\pi\pi^*$ -transitions for the photophysical properties as well as excitonic interactions due to the low dielectric constant.^{10,11} In contrast, their inorganic counterparts are characterized by electronic band structures and intrinsic conductivity. The reason for this remarkable difference is the strength of the interactions between individual building blocks. Inorganic materials are usually crystalline and strong electronic interactions prevail between adjacent atoms, leading to high dielectric constants and vanishing exciton binding energies in the electronic band structure. In contrast, the building blocks in organic

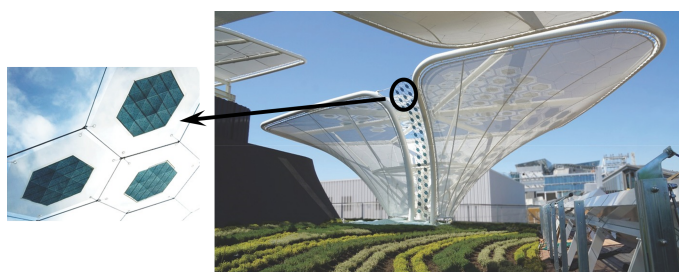


Figure 1.1: Example of commercial OPV modules from BELECTRIC OPV and their application as design elements at the Universal Exhibition Milan 2015. Images from Berny et al. [2].

systems are segments of polymers or entire molecules with comparably weak interaction. They organize mainly in amorphous or semicrystalline structures, which is manifested in the strong influence of disorder on nearly all physical properties.¹² Nonetheless, there is almost no design limit for synthesizing new materials. Polymers are widely used, which usually show broad distributions of their chain length.¹³ Furthermore, organic semiconductor materials can be processed from solution. Consequently, the properties of organic optoelectronic devices are the result of a complex interplay between the molecular electronic structure, intermolecular interactions as well as the morphology on a microscopic, mesoscopic and macroscopic length scale.

To improve the efficiency of an organic solar cell device, it is necessary to first understand the basic working principle. The active layer of a simple organic solar cell consists of two components. One material serves as donor (D) for electrons, which are transferred to an acceptor (A) component. This active layer is sandwiched between two electrodes, further functional layers can be included for better extraction efficiency. Figure 1.2 shows the energy levels of the highest occupied molecular orbital (HOMO) and lowest unoccupied molecular orbital (LUMO) for D and A molecules, and indicates the workfunctions of the electrodes. Several processes take place until charges are extracted^{7,14} and are indicated as well. First, a photon is absorbed and creates an exciton, which is sketched for the case of absorption in the D material (1). This excitation is a tightly bound electron-hole pair and can be created anywhere in the material. Thus, the excitation needs to diffuse to the D-A interface (2), where the electron is transferred from the LUMO of the D to the LUMO of the A (3), generating an interfacial charge transfer (CT) state. In case of light absorption in the A material in step (1), the CT state is generated by hole transfer from the HOMO of the A to the HOMO of the D. Step (4) is the dissociation of the electron-hole pair against their mutual Coulomb attraction into free charges, which is usually assisted by an applied electric field. Finally, the charges move to the electrodes (5) and are extracted from the device.

This simple outline already shows that each process contributes individually to the overall efficiency and needs to be optimized separately. This is not always possible, as these processes are related to each other to some extent. Over the last years, it turned out that a key factor is the morphology of the active layer.¹⁵⁻²¹ Intermixing of D and A molecules increases the interface, which is advantageous for charge separation. Though, too much intermixing destroys the percolation paths needed for charge extraction. Ordered domains enhance transport processes for charges and excitations,^{20,22} yet decrease the D-A interfacial area.²³ The energy of the CT state is a measure for the achievable open-circuit voltage V_{oc} . In a simple picture it is the energy difference between the LUMO of the A and the HOMO of the D. A large energy offset between the LUMOs should be beneficial for CT state formation, which, however, obstructs V_{oc} .¹⁴ Furthermore, local order and intermolecular conformations directly affect molecular energy levels and in particular energy and character of the CT

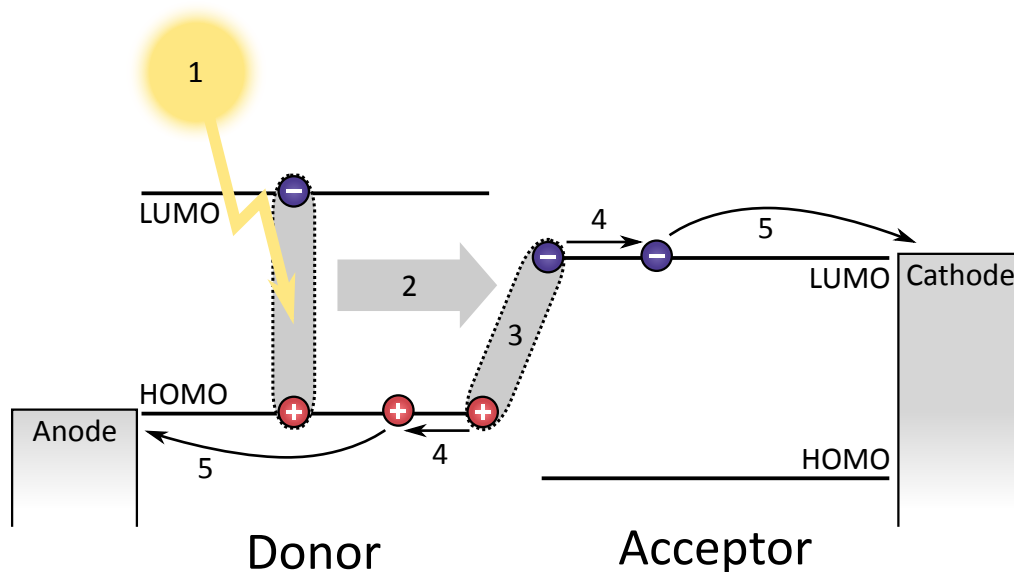


Figure 1.2: Working principle of an organic solar cell. The relevant molecular frontier orbitals are indicated as well as the workfunctions of the electrodes. The alignment of the energy levels corresponds to open-circuit conditions. See text for explanation of the contributing processes during charge generation.

states.^{19,21} Hence, optimizing one process will also impact on all other processes.

Optimising device efficiencies was mainly performed through heuristic approaches.^{7,24,25} For instance, small amounts of high boiling point additives in the processing solution can improve solar cell performance drastically, yet the exact amount needs to be determined empirically for every system. Furthermore, molecular planarity was exploited as a design rule, as it correlates with the propensity to form ordered structures, despite unclear direction of causality. In contrast, the explicit link between molecular flexibility, the related ability for molecular reorganization and the ability to establish order is less known. Herewith associated is the question of how the molecular electronic structure during intermolecular interactions is affected by molecular stiffness. In addition, the connection between molecular parameters and the efficiency of the different processes during charge generation is not completely understood.

This thesis investigates the influence of molecular reorganization on fundamental mechanisms in solar cell materials. I focussed on several aspects, using dominantly spectroscopic methods. On one hand I consider electronic transfer processes in solar cell blend systems, in particular which effects are relevant for the efficiency of CT state formation and how reorganization contributes. For this purpose, I studied CT state formation in different material systems for different temperatures, as thermal energy can drive reorganization processes. On the other hand I address how ordered structures can evolve, as they are relevant for the existence of CT states and the efficiency of all processes prior and after CT state formation. I focus on the interplay between molecular flexibility and tendency to establish local order

as well as implications on the electronic structure. For this, I used two model compounds differing mainly in their stiffness and compared their pathways into aggregated structures. I subsequently transferred the insights from static solution aggregation to the dynamic situation during film formation. Finally, I investigated the film formation process for a polymer under different boundary conditions to derive guidelines, which conditions lead to more or less ordered structures in the solid state.

This thesis is structured in two parts. Part I gives an overview about the current state of research, relevant concepts and my own contributions. Chapter 2 contains basic mechanisms of charge transfer and generation as well as how they are discussed in literature. Chapter 3 explains fundamental concepts, which can be used to draw conclusions on local order by means of spectroscopy. Chapter 4 summarizes the current state of research regarding the establishment of ordered structures and how they can be manipulated. Chapter 5 presents my publications and their interconnection, before the content of each publication is summarized in more detail in individual subchapters. Finally, the publications are reprinted in Part II.

2 Mechanisms of charge transfer and charge generation

Charged molecules are often called *polarons* in the organic semiconductor community, albeit one of the notations *charged molecule*, *cation* or *anion* would be more appropriate. This goes back to Holstein’s discussion of charges and their motion in molecular crystals, where he used the description (*small*) *polaron*.^{26,27} Even though organic semiconductors are mostly amorphous, it is still instructive to consider Holstein’s ideas. The basic concept of the small polaron is that a charge distorts the molecular geometry of the residing and the surrounding molecular sites. These molecular reorganizations result in a localization of the charge on individual molecules, which is the origin of the associated polaron binding energy E_{pol} . Several things need to happen if the charge is transferred from one lattice site to an adjacent site. The geometry of the charged site needs to reorganize to a neutral site geometry and vice versa for the target site. Further, the distortion of the surrounding lattice needs to adapt to the new situation. This process is activated by thermal fluctuations, which results in an activation energy E_A of the hopping process. Austin and Mott [28] performed simple geometric considerations using configurational coordinates and showed that this activation energy is half of the polaron binding energy $E_A = \frac{1}{2}E_{\text{pol}}$ for weak electronic exchange interactions. The corresponding polaron hopping rate k_{pol} was calculated by Holstein²⁷ as

$$k_{\text{pol}} = \frac{J^2}{\hbar} \sqrt{\frac{\pi}{2E_{\text{pol}}k_{\text{B}}T}} \exp\left(-\frac{E_{\text{pol}}}{2k_{\text{B}}T}\right) \quad (2.1)$$

where J is the overlap integral and T the temperature.

A very similar result was found by Marcus for charge transfer in redox reactions in solution.^{29,30} Marcus recognized that the solvent surrounding the reactants needs to reorient due to electrostatic interactions, as well as the reactants themselves. This is considered with an associated reorganization energy λ . The transfer reaction can be described along a generalized reaction coordinate Q , which is sketched in Figure 2.1 a for the case of two isoenergetic reactants. Initial and final state of the reaction are characterized with individual energy surfaces, which are approximated to be harmonic. In the initial state, the electron resides on the donor and is transferred to the acceptor at the intersection between initial and final state. The intersection is again reached through thermal fluctuations, which requires an

activation energy of $E_A = \lambda/4$. The resulting transfer rate thus reads

$$k_{\text{Marcus}} = \frac{J^2}{\hbar} \sqrt{\frac{\pi}{\lambda k_{\text{B}}T}} \exp\left(-\frac{\lambda}{4k_{\text{B}}T}\right) \quad (2.2)$$

Differences of the electronic energies of donor and acceptor can be included with the driving force ΔG_0 . Increasing the driving force shifts the minimum of the final state parabola to lower energies (in this case $\Delta G_0 < 0$ by convention) as sketched in Figure 2.1 b. Hence, the intersection point of both parabolas changes and the activation energy is altered, resulting in the modified expression

$$k_{\text{ET}} = \frac{J^2}{\hbar} \sqrt{\frac{\pi}{\lambda k_{\text{B}}T}} \exp\left[-\frac{(\lambda + \Delta G_0)^2}{4\lambda k_{\text{B}}T}\right] \quad (2.3)$$

Increasing the driving force will move the intersection point towards the energetic minimum of the initial state, lowering the activation energy. Thus, the transfer rate increases until the driving force reaches the value of the reorganization energy, $-\Delta G_0 = \lambda$. This behaviour is called *normal regime*. When increasing the driving force further to $-\Delta G > \lambda$, the activation energy again increases. The transfer rate decreases, which is called the *inverted regime* and illustrated in Figure 2.1 c.

Strictly speaking, Marcus theory is only valid in the high temperature limit, meaning that the thermal energy is larger than the energies of all relevant phonon modes $k_{\text{B}}T \gg \hbar\omega$. Typical molecular vibrations in conjugated molecules range from few meV for low frequency bending modes to around 150 meV for C–C and C=C stretching modes in cyclic rings up to 400 meV for C–H stretching modes.¹⁰ In comparison, the thermal energy at room temperature is around $k_{\text{B}}T \approx 25$ meV. Therefore, transfer processes in organic semiconductors can be beyond the limits of the classical assumptions of Marcus theory.

The semiclassical Marcus-Levich-Jortner formalism extends the validity of the Marcus mechanism to an intermediate temperature regime.^{31,32} It accounts for high energy vibrations $\hbar\omega_{\text{high}} \gg k_{\text{B}}T$ in a quantum mechanical fashion, while low energy vibrations $\hbar\omega_{\text{low}} \ll k_{\text{B}}T$ are still treated classically. The high energy vibrations are intramolecular modes with an associated Huang-Rhys factor S , and the low energy phonons are again related to the relaxation of solvent or the surrounding media, described by an outer reorganization energy λ_o . The modified expression reads

$$k_{\text{MLJ}} = \frac{J^2}{\hbar} \sqrt{\frac{\pi}{\lambda_o k_{\text{B}}T}} \sum_{n=0}^{\infty} \frac{e^{-S} S^n}{n!} \exp\left[-\frac{(\lambda_o + \Delta G_0 + n\hbar\omega_{\text{high}})^2}{4\lambda_o k_{\text{B}}T}\right] \quad (2.4)$$

In this framework, the reorganization energy for charge transfer splits up into two individual contributions, which sum up to the total reorganization energy $\lambda = \lambda_o + \lambda_i = \lambda_o + S\hbar\omega_{\text{high}}$.

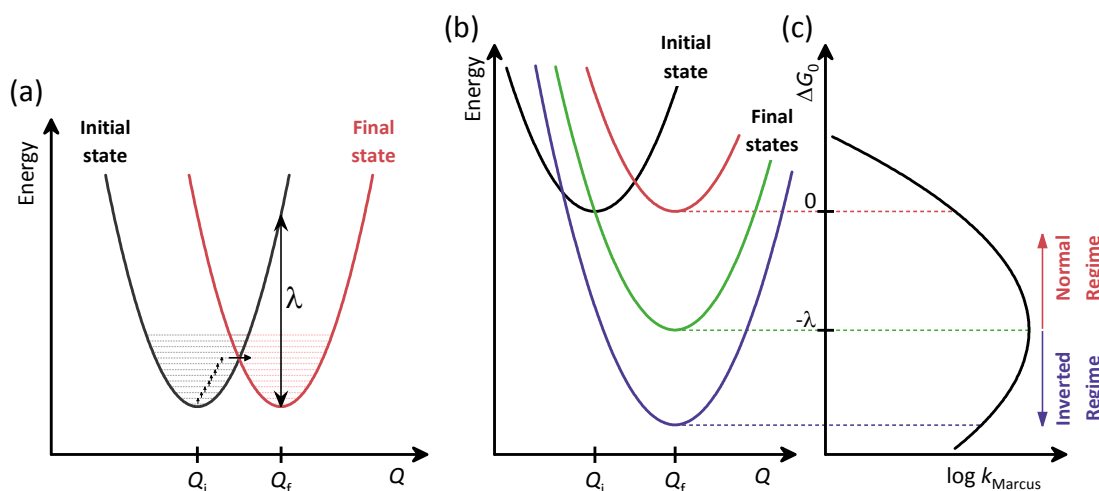


Figure 2.1: Transfer reactions in the Marcus framework. (a) Energy surface for reactions between two isoenergetic reactants and the reorganization energy λ . Arrows indicate thermal fluctuations distorting the system to the crossing point between initial and final state, where the transfer reaction takes place. (b) Energy surfaces for reactions with nonzero driving force ΔG_0 and (c) the resulting variation of the transfer rate as function of ΔG_0 .

Marcus theory was experimentally confirmed in many systems in solution, both in the normal and in the inverted regime.^{30,33–35} This success motivated researchers to apply it to charge generation and charge transport in organic semiconductor solids. For theoretical considerations of charge transport, Marcus-type rates are an established concept.^{36,37} In contrast, applications to charge generation and CT state formation are more disputed. The Marcus mechanism was utilized to explain charge generation in several systems. Cook et al. [38] used it to rationalize hole transfer in P3HT:PCBM blends measured by ultrafast transient spectroscopy, Ward et al. [39] described photoluminescence quenching for the donor polymer PTB7 blended with several acceptors in the Marcus framework, and Coffey et al. [40] strongly advocated the Marcus mechanism to be able to account for charge generation in microwave conductivity measurements. Further, full device characteristics were simplistically explained in the Marcus framework. Vandewal et al. [41] used it to describe external quantum efficiency (EQE) and electroluminescence (EL) spectra in solar cell devices, based on the adaption from Gould et al. [42]. This motivated several researchers to exploit this model for solar cell characterization.^{43–46} However, they did not consider the effect of Gaussian disorder,¹² which is more likely to account for the broad line shape of EQE and EL spectra.⁴⁷ Furthermore, predicting ΔG_0 and λ from quantum chemical calculations renders cumbersome and computationally expensive⁴⁸ and was for example performed for the systems P3HT:PCBM,⁴⁹ PCPDTBT:fullerenes,⁵⁰ oligothiophene:C60 and oligothiophene:PBI,⁵¹ or p-DTS(FBTTh₂)₂:NIDCS-MO.⁵² Inherently for all of these considerations is the idea that

there is an optimum value for ΔG_0 , and that the CT generation yield is a main objective for device improvement. However, Barbara et al. [53] pointed out already in 1996 that fast electron transfer typically observed in solar cell systems results from nonequilibrium dynamics. This renders the applicability of Marcus-type equilibrium descriptions at least questionable in this context.

Indeed, it was found by several groups that CT state formation is an ultrafast⁵⁴⁻⁵⁹ and coherent⁵⁹⁻⁶¹ phenomenon with strong electron-phonon couplings to high energy vibrations. Charge separation was also observed from vibronically relaxed CT states.⁶²⁻⁶⁴ A priori, this is not speaking for or against a Marcus-type description, but highlights the importance of all subsequent processes, indicating that a Marcus framework may not be appropriate as the unifying explanation. Hence, the applicability of the Marcus mechanism, including the role of energetic offsets and molecular reorganization, remains unclear and needs clarification.

3

Photophysics from isolated molecules to the condensed state

The electronic structure of molecules is coupled to the photophysics, as transitions between different electronic states can be assessed by means of optical spectroscopy. Intra- and inter-molecular interactions thus directly reflect on the shapes and energetic positions of absorption and emission spectra. This chapter recapitulates the relevant concepts for describing and interpreting optical spectra used in this thesis.

3.1 The Franck-Condon principle

Optical transitions in molecules are usually coupled to molecular vibrations. A successful framework for describing optical spectra is the Franck-Condon principle. It results from the Born-Oppenheimer approximation when applying it to radiative transitions starting from Fermi's golden rule.¹¹ The Born-Oppenheimer approximation exploits the fact that the motion of electrons takes place on faster time scales than the motion of the nuclei. Thus, their dynamics separate and the total wavefunction of a molecule can be written as a product of independent wavefunctions for the electronic contribution, nuclear vibrations, and the electron spin.^{11,65} The rate for an optical transition from state $|\Psi_i\rangle$ to $|\Psi_f\rangle$ is proportional to the squared modulus of the transition dipole moment $|\boldsymbol{\mu}|^2 = |\langle\Psi_f|e\tilde{\mathbf{r}}|\Psi_i\rangle|^2$, as the dipole operator $e\tilde{\mathbf{r}}$ provides the coupling between the electromagnetic radiation field and the electronic states.¹¹ Putting everything together results in the expression

$$|\boldsymbol{\mu}|^2 = |\langle\Psi_{\text{el},f}|e\tilde{\mathbf{r}}|\Psi_{\text{el},i}\rangle|^2 \cdot |\langle\Psi_{\text{vib},f}|\Psi_{\text{vib},i}\rangle|^2 \cdot |\langle\Psi_{\text{spin},f}|\Psi_{\text{spin},i}\rangle|^2 \quad (3.1)$$

The consequence is that the probability for a transition is also composed of three factors. The electronic factor $|\langle\Psi_{\text{el},f}|e\tilde{\mathbf{r}}|\Psi_{\text{el},i}\rangle|^2$ determines selection rules and states whether the transition is in principle allowed. The spin factor $|\langle\Psi_{\text{spin},f}|\Psi_{\text{spin},i}\rangle|^2$ allows transitions only within one spin manifold. The vibronic factor $|\langle\Psi_{\text{vib},f}|\Psi_{\text{vib},i}\rangle|^2$ is the so-called Franck-Condon factor and is responsible for the relative intensities I_{0-m} of the vibronic structure. It arises from vibrations of the nuclei, which are described using generalized coordinates Q for each vibrational mode. For organic molecules, a harmonic approximation is usually sufficient⁶⁶

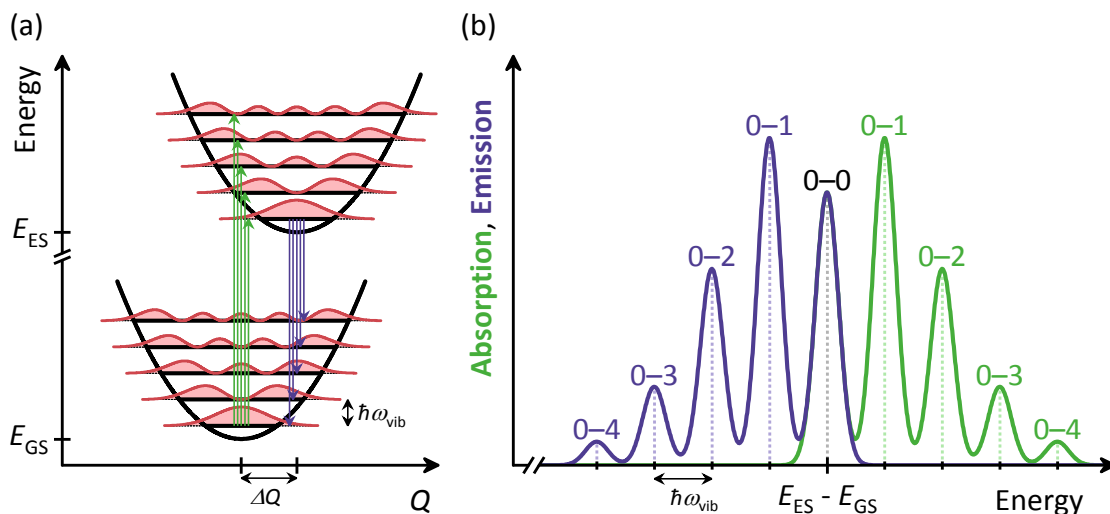


Figure 3.1: Illustration of the Franck-Condon principle. (a) Electronic energies of the ground state (GS) and the lowest excited state (ES) along a generalized coordinate Q in the harmonic approximation. GS and ES are displaced by $\Delta Q = 1.55 \cdot \sqrt{\frac{\hbar}{M\omega_{\text{vib}}}}$, resulting in $S = 1.2$. The first five vibrational levels with a spacing of $\hbar\omega_{\text{vib}}$ are indicated along with the respective probability density drawn in red for both GS and ES. Arrows illustrate vertical electronic transitions. (b) Exemplary absorption and emission spectra, resulting from the vertical transitions as sketched in (a).

and shown in Figure 3.1 for a two-level system consisting of ground state (GS) and excited state (ES) in the presence of a single vibrational mode. The displaced oscillators differ by ΔQ in their equilibrium positions and the associated vibrational energy is $\hbar\omega_{\text{vib}}$ for both.

According to the Franck-Condon principle, electronic transitions are vertical in this energy diagram, starting from the lowest vibrational level due to Kasha's rule.^{10,67} Hence, the transition probability and therefore the intensity I_{0-m} of each vibrational $0-m$ transition is given by the overlap of the respective vibronic wavefunctions. For a displaced harmonic oscillator with effective mass M and force constant $k = M\omega_{\text{vib}}^2$, calculations result in a Poisson distribution⁶⁶

$$I_{0-m} = \frac{S^m e^{-S}}{m!} \quad (3.2)$$

with Huang-Rhys parameter $S = \frac{1}{2}k \frac{\Delta Q^2}{\hbar\omega_{\text{vib}}} = \frac{1}{2}M\omega_{\text{vib}} \frac{\Delta Q^2}{\hbar}$. Expressions for distorted oscillators or both displaced and distorted oscillators are more complex.⁶⁶ The Huang-Rhys parameter is a dimensionless number and can be interpreted as the average number of excited vibrational quanta per optical transition. The molecule relaxes into the new equilibrium conformation after the vertical transition. The associated reorganization energy can be calculated as $\lambda = S\hbar\omega_{\text{vib}}$.

The Franck-Condon principle can be used to model absorption and emission spectra

according to⁶⁸

$$\frac{I_{\text{Abs}}(E)}{n(E) \cdot E} \propto \sum_{m \geq 0} \frac{S^m e^{-S}}{m!} \cdot \Gamma(E - (E_0 + m\hbar\omega_{\text{vib}})) \quad (3.3a)$$

$$\frac{I_{\text{PL}}(E)}{(n(E) \cdot E)^3} \propto \sum_{m \geq 0} \frac{S^m e^{-S}}{m!} \cdot \Gamma(E - (E_0 - m\hbar\omega_{\text{vib}})) \quad (3.3b)$$

where E_0 denotes the energy of the 0–0 transition, $n(E)$ is the refractive index, and $\Gamma(E)$ is the line shape of the transition, which is usually taken as Gaussian. The factors $n(E) \cdot E$ and $(n(E) \cdot E)^3$ result from the Einstein coefficients and take the density of states of the photons within the surrounding medium into account.^{69,70} $n(E)$ can be approximated to be independent of the photon energy, which is a good approximation for dilute solutions or emission sufficiently separated from absorption bands. In cases where N vibrational modes with energy $\hbar\omega_{i,\text{vib}}$ and Huang-Rhys parameter S_i need to be considered, the expressions become slightly more complex:⁶⁸

$$\frac{I_{\text{Abs}}(E)}{n(E) \cdot E} \propto \sum_{(m_1, \dots, m_N)} \left\{ \left(\prod_{i=1}^N \frac{S_i^{m_i} e^{-S_i}}{m_i!} \right) \cdot \Gamma \left[E - \left(E_0 + \sum_{i=1}^N m_i \hbar\omega_{i,\text{vib}} \right) \right] \right\} \quad (3.4a)$$

$$\frac{I_{\text{PL}}(E)}{(n(E) \cdot E)^3} \propto \sum_{(m_1, \dots, m_N)} \left\{ \left(\prod_{i=1}^N \frac{S_i^{m_i} e^{-S_i}}{m_i!} \right) \cdot \Gamma \left[E - \left(E_0 - \sum_{i=1}^N m_i \hbar\omega_{i,\text{vib}} \right) \right] \right\} \quad (3.4b)$$

The summation needs to be carried out over all possible combinations of vibrational quanta, which is indicated by the tuple notation (m_1, \dots, m_N) . In the past, these equations have been successfully applied to describe optical spectra of conjugated polymers and small molecules.^{68,71–78} For fitting actual spectra, numerical evaluation can become cumbersome. Therefore, I wrote a graphical user interface to simplify the fitting workflow, which is described in Appendix A.

3.2 Optical signatures of aggregates

The Franck-Condon model can be used to extract important molecular parameters from absorption and emission spectra. However, the electronic states and thus also the photophysical properties can change substantially once intermolecular interactions become significant. This constellation is termed an *electronically interacting aggregate*, or *aggregate* in short. Aggregates are characterized by shifting and splitting of molecular energy levels, which complicates the picture and modifies the expressions in equations 3.3 and 3.4. Pioneering work was performed by Kasha,^{79,80} who considered intermolecular interactions using the point-dipole approximation. A description in the Kasha framework can already account for

basic properties of interacting chromophores. Therefore, the basic features of this theory are first explained using the illustrative example of an interacting dimer, before more complex arrangements and interactions will be addressed.

A system consisting of two identical molecules can be described with the Hamiltonian $\tilde{H} = \tilde{H}_1 + \tilde{H}_2 + \tilde{V}_{12}$, where \tilde{H}_1 and \tilde{H}_2 are the Hamiltonians for the isolated molecules and \tilde{V}_{12} contains the intermolecular interaction. Solving the Schrödinger equation using the combined wavefunction $\Psi_{\text{GS}} = \Psi_1\Psi_2$ yields the energy of the common ground state $E_{\text{GS}} = E_1 + E_2 + D$, with E_1 and E_2 being the (identical) ground state energy for both molecules, and $D = \langle \Psi_1\Psi_2 | \tilde{V}_{12} | \Psi_1\Psi_2 \rangle$ is the van der Waals interaction. When considering the excited state, it is impossible to tell which molecule bears the excitation. Hence, the wavefunction is a superposition in the form of $\Psi_{\text{ES}\pm} = \frac{1}{\sqrt{2}} (\Psi_1^*\Psi_2 \pm \Psi_1\Psi_2^*)$, where the star denotes the excited molecule. This results in a splitting of the excited state into two levels with energies $E_{\text{ES}\pm} = E_1^* + E_2 + D' \pm \beta$. Here, D' is analogous to the van der Waals interaction in the ground state and $\beta = \langle \Psi_1^*\Psi_2 | V_{12} | \Psi_1\Psi_2^* \rangle$ is the resonance interaction. Thus, the transition energy between ground state and excited state changes from $\Delta E_1 = E_1^* - E_1$ to $\Delta E_{\text{dimer}} = \Delta E_1 + \Delta D \pm \beta$.

The distance and the relative orientation of both molecules critically determines how the energy levels change with the intermolecular interaction as sketched in Figure 3.2. It is instructive to consider the interaction in the point dipole approximation, which is a good approximation if the spacial extensions of the wavefunctions are small compared to the intermolecular distance. Depending on the sign of β , the intermolecular interaction can result in two borderline cases for the excited state and the optical transitions. The first case comprises the dipoles in a collinear arrangement, which corresponds to the $\theta = 0^\circ$ geometry in Figure 3.2. Here, $\beta < 0$ and the state $\Psi_{\text{ES}+}$ is the low-energy state. Its total transition dipole is twice the value for the isolated molecule, whereas the high-energy state $\Psi_{\text{ES}-}$ has a vanishing transition dipole. Absorption and emission are both possible to and from the low energy state, making the Stokes' shift small. Further, the transition is shifted to lower energies and the radiative rates are increased compared to the isolated molecule. This constellation is termed *J-aggregate* or *Scheibe-aggregate* after Jelley and Scheibe, who independently discovered this type of aggregation mechanism more than 80 years ago.⁸¹⁻⁸³

In the second case, the dipoles arrange parallel to each other, which is called *H-aggregate*. β is positive, thus the high-energy state is $\Psi_{\text{ES}+}$. The energetic ordering is exactly opposite compared to the J-aggregate. Therefore, $\Psi_{\text{ES}+}$ bears a non-zero transition dipole and the absorption shifts hypsochromic. After absorption, the excitation quickly relaxes to the low-energy state $\Psi_{\text{ES}-}$. Emission is forbidden due to the vanishing transition dipole. Hence, the radiative rate is strongly diminished and the Stokes' shift is increased compared to the monomolecular case. Perturbations such as static disorder or finite temperatures soften this selection rule and allow for some emission. For intermolecular arrangements between these

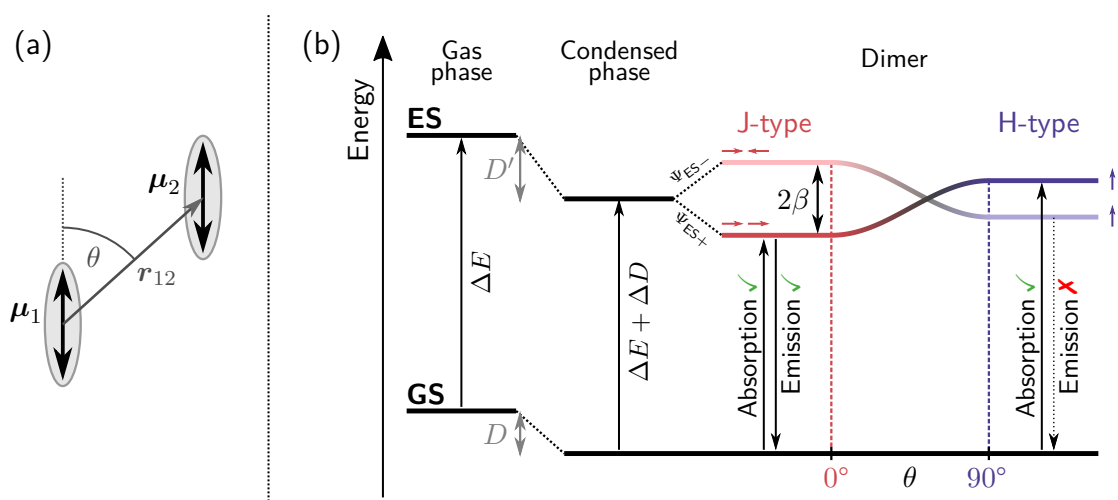


Figure 3.2: (a) Geometric orientation of two coplanar dipole moments. θ is the angle between the distance vector r_{12} and the polarization axes. (b) Influence of intermolecular interactions on energy levels and level splitting upon dimer formation. Small arrows indicate the relative orientation of the dipoles for each dimer level. The crossover between J-type and H-type interaction is indicated for constant $|r_{12}|$ and varying θ using the point dipole approximation.⁸⁰

two extreme cases, similar effects can be observed. Depending on the orientation of the transition dipoles and the sign of the resonance interaction, the energy levels for the excited state split and the oscillator strength is redistributed among them.⁷⁹

Energetic shifts of aggregate signatures are ambiguous for the assignment of an aggregate, as the dispersion shift ΔD can be more pronounced compared to the resonance interaction β . Among vibronic signatures as detailed below, a further important criterion for the identification of the aggregate character is the exciton lifetime. It is strongly reduced for J-aggregates due to the increased radiative decay rate. In contrast, the lifetime for H-aggregates is only limited by non-radiative decay pathways, which increases the lifetime compared to isolated molecules. When performing time-resolved measurements, it can be necessary to evaluate experimental data using deconvolution algorithms. This is especially crucial in cases where the exciton lifetime is close to the temporal resolution of the setup as given by the instrument response function. For this, I programmed a script in Python, which can be found in Appendix B.

These considerations apply for situations, where the intermolecular interaction does not change the intermolecular conformation significantly. If β is larger, the intermolecular interaction can lead to a change in the dimer geometry in the excited state.¹⁰ As a result, the intermolecular distance decreases due to the attractive intermolecular potential in the excited state to a point, where the dimer ground state potential is repulsive and non-bonding. This behaviour is called an excimer, as it is only stable in the excited state. The dynamic change of the intermolecular distance upon excitation causes a broad and unstructured

emission, which is strongly shifted to lower energies. Excimer formation is common in flat or elongated conjugated molecules. A prominent example is pyrene and its derivatives, which has extensively been studied by Birks.^{84–86} Recent work showed that the pathway into excimer formation can also include non-emissive precursor species.⁸⁷ The example of distyrylbenzene and its derivatives further demonstrates that intermolecular interactions can strongly depend on substituents.⁸⁸ Choosing appropriate substituents as well as substitution positions allows to tune the character of the intermolecular interaction from J-type to H-type or excimer-like by controlling the local intermolecular structure.

The concept of two interacting molecules in the dimer can be generalized to larger aggregates, which is then called *Frenkel exciton*. For a linear chain consisting of N chromophores spaced by a distance of a with nearest-neighbour-coupling, the excited state splits into N states with transition energy $\Delta E_{\text{Frenkel}} = \Delta E + \Delta D + 2\beta \cos(ka)$. The resonance interaction β is defined analogous to the dimer case, while the factor of 2 arises from the fact that each molecule has two interaction partners. $k = 0, \pm \frac{2\pi}{Na}, \dots, \pm \frac{\pi}{a}$ can be interpreted as a wavenumber of the delocalized exciton. This allows optical transitions only into states with $k = 0$. For large N , an exciton band evolves with exciton bandwidth $W = 4\beta$. Again, geometric arrangements and the extent of intermolecular interactions determine the photophysical properties similar to the dimer case.

Kasha’s model can account for basic properties of aggregated chromophores, yet it lacks the description of the vibronic structure of absorption and emission spectra. Spano and co-workers extended Kasha’s work by including coupling to molecular vibrations along with static and dynamic disorder.^{89–92} The relevant advancement is that they used an expansion of the wavefunctions in a multi-particle picture, where one-particle and two-particle states needed to be incorporated. One-particle states resemble ensembles of molecules in the ground state, except one molecule being in the excited state including a vibronic excitation. For two-particle states, one additional molecule bears a vibrational excitation but remains in the electronic ground state. Including these two-particle states can be visualised as the vibrational distortion induced by the exciton in the aggregate ensemble.⁹³ Hence, calculations become complicated, as more and more wavefunctions need to be included into the electronic states. Similar to the Frenkel exciton, every vibronic sublevel forms a band structure. However, as the higher vibronic bands are incoherent, the optical properties of the Kasha aggregate transfer mainly to the 0–0 transition, while the higher vibronic transitions are less affected. The peak ratio between the 0–0 and 0–1 transitions can therefore be indicative for the type of interaction rather than energetic shifts. In absorption, the 0–0 peak is increasingly suppressed (enhanced) for increasing exciton bandwidth in H-aggregates (J-aggregates). The emission of perfect H-aggregates has no intensity in the 0–0 transition, which becomes again visible when static disorder or the influence of temperature is considered. The emission spectrum of J-aggregates shows a strongly enhanced 0–0 peak intensity, which decreases due

to static disorder or temperature. To incorporate these effects into the Franck-Condon model in equations 3.3 and 3.4, they can be modified according to^{94,95}

$$\frac{I_{\text{Abs}}(E)}{n(E) \cdot E} \propto \sum_{m \geq 0} \left(\frac{S^m e^{-S}}{m!} \right) \left(1 - \frac{W e^{-S}}{2\hbar\omega_{\text{vib}}} G_m \right)^2 \Gamma(E - (E_0 + m\hbar\omega_{\text{vib}})) \quad (3.5a)$$

$$\frac{I_{\text{PL}}(E)}{(n(E) \cdot E)^3} \propto e^{-S} \alpha \Gamma(E - E_0) + \sum_{m > 0} \frac{S^m e^{-S}}{m!} \cdot \Gamma(E - (E_0 - m\hbar\omega_{\text{vib}})) \quad (3.5b)$$

The additional factors in absorption are the exciton bandwidth W and $G_m = \sum_{n \neq m} \frac{S^n}{n!(n-m)}$. For emission, the first term in the sum is examined separately and multiplied with an empirical factor α , which modifies the intensity of the 0–0 transition.

Up to now intermolecular interactions are solely discussed for Coulomb interactions. Strictly speaking, this is only valid for negligible overlap of molecular orbitals between different molecules. In cases where wavefunction overlap is significant, this could lead to short-range charge transfer interactions, which alter the character of the excited state and impact on the photophysical properties.¹⁹ The character of this interaction is highly sensitive to intermolecular displacements, as the phase of a wavefunction can invert within one molecular ring unit. Spano and co-workers also included this mechanism into their calculations.^{96–99} They found that alike to the case of Coulomb mediated interactions, the sign of the short-range interaction determines whether the character of the aggregate is H-like or J-like. Moreover, the principal character of the aggregate is determined by the superposition of both, Coulomb and short-range interactions. In particular, destructive interference can occur if both interactions have similar magnitude yet opposite sign, which results in photophysical properties similar to isolated molecules. For further details and an elaborate presentation of the theoretical calculations, the reader is referred to the comprehensive and thorough review from Hestand and Spano [92].

4 Establishment of ordered structures

Chapter 3 summarizes how different intermolecular interactions and conformations influence the shapes and energetic positions of absorption and emission spectra. This toolbox allows to draw conclusions about intermolecular arrangements and couplings from simple optical measurements. However, they only provide information about the final structure. The pathway into these structures is less established as well as the interplay between molecular design parameters and aggregate properties. It is desirable to have simple design rules that connect specific molecular parameters to distinct intermolecular conformations and solid state morphologies, as this directly impacts on the efficiency of organic semiconductor devices. Many theoretical efforts try to predict how a certain molecular structure will perform in the final device.^{100–103} Unfortunately, this goal remains elusive to date, as different processes and mechanisms work together on different length scales and influence each other. Thus the search for firm design principles keeps going.

4.1 General relations between molecular properties and order

The phenomenon that conjugated materials can form ordered structures is not new. Examples include but are not limited to oligomers and polymers consisting of thiophenes,^{104–108} phenylene vinylenes,^{75,76,88,109–111} rylenes,^{84,85,87,112–118} or donor-acceptor compounds^{77,119–121} among others.^{83,92,121} In solution, one driving factor originates in the thermodynamic interactions between the molecules and the solvent. Ordered structures can be achieved if the quality of the solvent is systematically decreased. As a result, the material will start to precipitate at some point and form agglomerates or physical aggregates. These physical aggregates do not necessarily lead to intermolecular interactions that alter the electronic structure of the molecules. Physical aggregates should not be confused with electronic aggregates, despite both phenomena can appear at the same time. In this thesis, the notation *aggregate* is used for electronically interacting aggregates as introduced in Chapter 3. For polymers, the interactions between solvent and polymer chain segments alter the conformation of the overall chain.¹³ An ideal polymer chain has a certain size, which depends on the number of repeat units n . The size of a polymer can be quantified by the root-mean-square value of the end-to-end distance $\langle r^2 \rangle^{1/2}$, which is proportional to $n^{1/2}$ for ideal polymer chains. In good solvents, the chain swells and $\langle r^2 \rangle^{1/2}$ is larger than for the ideal chain. The solvent-polymer interaction

increases the excluded volume of individual chain segments, which try to avoid each other. For bad solvents, the situation is opposite. The interaction between chain segments is more favourable than with the solvent. Individual chain segments try to increase mutual contact points and $\langle r^2 \rangle^{1/2}$ is smaller than for the ideal polymer chain. However, different chain segments still avoid each other due to steric repulsion. If repulsive intrachain and attractive solvent-chain interactions balance perfectly, the solvent is a so-called *theta* solvent and the chain conformation is identical to the ideal chain. When starting in a good solvent and decreasing solvent quality below the theta point by decreasing the temperature, the swollen polymer chains collapse and undergo a coil-globule transition. In globules, local order is better established for stiffer polymers.¹²² Due to finite chain lengths, the critical temperature is below the theta temperature and the transition is a pseudo-second-order transition.¹²³ It is further smeared out by statistical variations of the overall chain length,¹⁰⁷ which are always present due to the random nature of a polymerization reaction.¹³ The amount of electronic aggregates also increases for higher chain lengths as observed in several systematic studies.^{107,124–126} An additional possibility to induce the coil-globule transition is mixing good and bad solvents in different ratios, which also varies solvent quality in a systematic way.^{106,127} Furthermore, entanglement will occur for long polymer chains in solutions with higher concentrations up to the point where gel formation may be possible.^{128–130}

Up to now the propensity of molecules or segments of molecules to come closer was discussed mainly on their solubility. The solubility of a conjugated molecule is usually enabled by side chains.^{131–133} They provide access points for solvent molecules to interact with the conjugated backbone. In addition, they can be used to indirectly control how two molecules can arrange with respect to each other. For example, sterically demanding side chains inhibit sufficient approximation of two molecules¹³⁴ and can be utilized to specifically prevent excessive aggregation.^{112–118} Suitable side chains can also introduce bends^{135–137} or provide planarity^{138,139} in the molecular backbone. Tiny changes in the size or structure of the side chains can already have a large impact on the amount and propensity to form ordered structures,^{128,140–143} as the example of the non-fullerene acceptor Y6 and its derivatives convincingly shows.^{134,137,144,145} A further influencing factor is the overall shape of a molecule, which can be easily designed during synthesis. To stay with the example of Y6, its largely flat backbone resembles a strong banana shape. The extent of this banana shape was already related to improved crystallinity for small conjugated molecules.^{146,147} Deviations from a purely linear shape were in general found to result in better device performance as well as a stronger propensity to form aggregated structures.^{77,148–152} For the molecule pair p-DTS(FBTTh₂)₂ and p-SIDT(FBTTh₂)₂, Bourdick et al. [152] were able to further relate this difference to the need for repelling the solvation shell from the conjugated core, which is more difficult for the linear p-SIDT(FBTTh₂)₂ and inhibits solution aggregation for this molecule.

All of these phenomena show a distinct correlation between molecular planarity and their tendency to form ordered structures. However, a clear direction of argumentation is difficult to establish. On one hand, there is clear evidence that backbone planarity is present for oligomers as well as polymers once the molecules are in aggregated conformations,^{111,153–155} which could be a side effect of intermolecular proximity.^{111,155} On the other hand, disorder-order transitions in solution upon decreasing the temperature usually exhibit an increased average planarity of the chromophores prior to the actual transition,^{77,108,120,121,156} which is also observed during film formation.^{157,158} Therefore, it renders a reasonable design approach for highly ordered materials to specifically use structures that make the backbone more planar. This can be achieved by introducing rotational barriers or conformational locks through halogenation, incorporating heteroatoms, or using suitable substituents.^{159–165} Their effect on molecular conformations can easily be calculated in density functional theory calculations, and it was possible to link high rotational barriers to planar structures in the solid state.^{163,166} An additional degree of freedom can arise from available rotational conformations for asymmetric building blocks, which further correlates with the degree of solid state order.^{166,167}

In principle, backbone planarity is accompanied with a corresponding degree of molecular stiffness. This stiffness ultimately complicates reproducible film processing, as can exemplarily be seen for the polymer PffBT4T-2OD.^{157,168,169} In contrast, molecular flexibility could be used as a design principle to overcome this problem. However, recent research focussed mainly on stiff materials. Therefore, it is not well understood to what extent molecular flexibility and the associated ability for molecular reorganization is beneficial for establishing ordered structures. It is important to address this research gap, as molecular reorganization can support charge separation in organic solar cells and result in higher efficiencies.¹⁷⁰

4.2 Influence of processing parameters on the formation of ordered structures

There are different methods for solution processing with individual processing kinetics and dynamics, which impact on the final morphology.^{171,172} Spin coating is the most established processing method for fundamental research, as it is simple and quick.¹⁷¹ Other methods include blade coating, slot die coating, inkjet printing and roll-to-roll processes. These methods require more time and effort, but are highly relevant for upscaling and industrial applications.^{3,4,171,173}

One factor that controls the amount of order in the final film is the duration of film formation. Processing from solvents with different boiling points can lead to films with different ratios of aggregated and amorphous phases, as was for example shown for PFO⁷³ or P3HT.^{95,174} Solvents with higher boiling points evaporate slower, which leaves more time for

the molecules to form ordered structures.²² The evaporation rate can further be tuned by the processing temperature,¹⁷⁵ by stopping the spin coater rotation early,^{176,177} by processing in a solvent saturated atmosphere,^{178,179} or adding further electronically and optical inert compounds like polystyrene to retain solvent in the film.¹⁸⁰ The elongated evaporation period did in all reported cases result in higher crystallinities in the final film, emphasising the delicate interplay between the intrinsic propensity of a material to crystallize and the actual time it is allowed to form ordered domains during processing.¹⁷⁷

A further common approach is using high boiling point additives in the processing solution. They usually boost device efficiencies by increasing the crystallinity^{149,181–183} and fine-tune intermixing of different phases.¹⁸⁴ There is a vast number of studies investigating the effect of additives, both on final films^{22,115,149,182–185} as well as in situ during film formation.^{25,180,186–190} Additives remain in the film after evaporation of the main solvent and can provide molecular mobility to some degree, which facilitates subsequent crystallization and prevents the establishment of kinetically locked arrangements or intermediate liquid crystalline phases.^{188,190} Further, depending on whether the interaction is mainly via the side chains or on the conjugated backbone,¹⁹⁰ aggregation can be specifically induced during processing.¹⁸⁹ However, the application of processing additives remains largely heuristic and lacks general systematic rules, as the optimum amount of additive needs to be found empirically for every system.¹⁸⁷

While solvent interactions and possible influences of additives impact on the morphology during processing, it is also possible to tune the morphology by post-processing. Thermal annealing^{140,149,185,191,192} and solvent vapor annealing^{120,185} are two common approaches. For thermal annealing, the films are put on a hot plate for a fixed amount of time, which promotes phase separation and ordering. During solvent vapor annealing, the film is exposed to a solvent saturated atmosphere. Solvent molecules diffuse inside the film and allow for increased molecular mobility due to swelling of the material. Both annealing methods result in altered and mostly more crystalline morphologies.¹⁸⁵ The reason is that the morphology is usually kinetically quenched after processing. Annealing provides the possibility to relax the morphology towards the thermodynamic equilibrium.¹⁶⁴

It is desirable to overcome the need for additional processing steps as well as using additional components like additives. They introduce further complexity and require time consuming heuristic screening of processing parameters for best device performance. This could be circumvented by establishing firm structure-property relationships. They could be used to specifically design materials that form the desired morphology already during processing. In the last years it became more and more evident that the presence of aggregated conformations already in solution can provide a simple toolbox to control the degree of order in the condensed state.^{157,168,193,194} However, it was considered more as an intrinsic material parameter instead of a distinct design principle. Molecular flexibility and the associated

ability for reorganization is a factor that could be exploited to systematically control the desired behaviour. In contrast, little is known about the interplay of flexibility and the establishment of order during processing. Different degrees of flexibility could also impact on possibly relevant microtimings during film formation. This thesis aims to contribute in closing this research gap.

5 Overview of the thesis

5.1 Summary and overall context

This thesis aims to understand the influence of molecular reorganization on the electronic structure in conjugated organic molecules, which I address from two different points of view. First, molecular reorganization impacts on intermolecular transfer processes, as both intra- and intermolecular geometries can change during this process. While this holds true for all types of transfer processes, I focus my investigation on the formation of the interfacial charge transfer state between a polymeric donor and fullerene acceptor in the solid state. Here, intermolecular arrangements are defined a priori by the conditions during film processing as well as molecular properties, which do in principle not change afterwards. These molecular properties include the capability of molecular reorganization, which can further influence how and to what extent intermolecular order is established. Therefore, the second aspect of reorganization investigated in this thesis is devoted to the question of how molecular stiffness and flexibility impacts on the propensity to form ordered structures. As initial study I consider the formation of aggregates in solution and apply the findings in subsequent investigations to the actual film formation process. I used different material systems to specifically target different aspects in this thesis. Figure 5.1 gives an overview about the different molecules and shows their chemical structures.

P3HT, MeLPPP, PCPDTBT and PTB7 are conjugated polymers, which can be utilized as donor components in organic solar cells. I used them in combination with the fullerene derivative PCBM as the acceptor component in the first study, which is reprinted in Chapter 6. In this publication I investigated the mechanism of CT state formation, where an electron is transferred from a photoexcited donor to the neutral acceptor. The mechanism of CT state formation is not fully understood, and several partly contradicting concepts are used in literature. A widely used but in this context doubtful framework is the Marcus mechanism. It was derived for chemical redox reactions in solution and requires thermal equilibrium, as it represents the high temperature limit for charge transfer theories. The relevant factors are the driving force ΔG_0 and the reorganization energy λ . A description in the Marcus framework implies that ΔG_0 needs to be sufficiently large for efficient electron transfer. However, this would obstruct the performance of organic solar cell devices, as the open circuit voltage decreases with increasing ΔG_0 , having a direct consequence for device optimization.

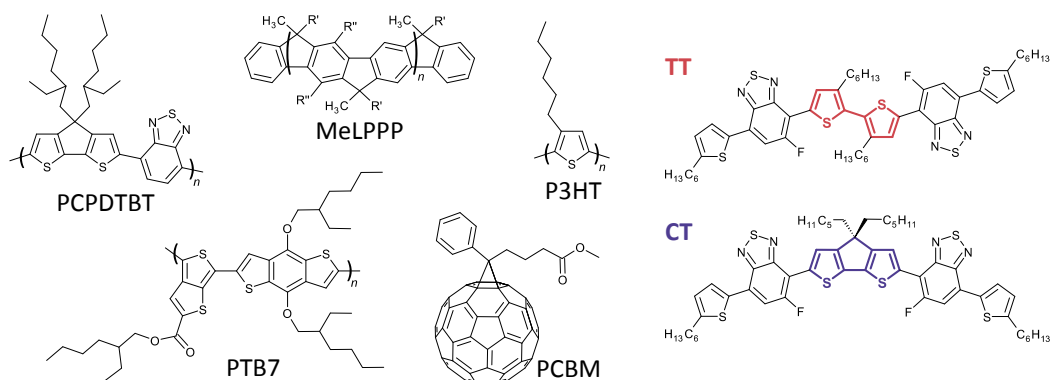


Figure 5.1: Molecules used in this thesis.

The Marcus formula predicts a pronounced change of the transfer rate with varying temperature, as charge transfer is mediated in this framework by thermal fluctuations. I tested these predictions using temperature dependent ultrafast transient absorption spectroscopy. The systems PCPDTBT:PCBM and PTB7:PCBM are representative for combinations of moderate ΔG_0 and λ values, whereas the MeLPPP:PCBM system is exemplary for high values of ΔG_0 and low λ , the latter being due to the high molecular stiffness. To complete the picture, P3HT:PCBM was included into the discussion with electron transfer rates from literature. I showed that electron transfer from donor to acceptor cannot be described adequately by models which require thermal activation, including extensions that consider tunneling in a semi-classical way. Even if, the driving force would not be the limiting factor, which I was able to directly relate to the influence of molecular reorganization in combination with static disorder. In this case, the predicted ultrafast transfer rate as function of ΔG_0 would be the dominant process for many efficient material systems, relaxing the requirements for optimizing molecular energy levels.

In the course of this work I recognized some shortcomings of the transient absorption setup. Most of them concern monochromatic detection using the lock-in technique. This makes measurements rather slow, as detection is only possible for fixed time delay and wavelength, allowing to scan only one parameter. To overcome this issue, I implemented a fast line scan camera with a suitable fast mechanical chopper, which allows measuring full spectra on a shot-to-shot basis for fixed time delays. Appendix C contains the technical details and further minor improvements.

The properties of the CT states and further intermolecular interactions heavily depend on local intermolecular arrangements. In addition, transport processes for excitations as well as charges within one domain are influenced by couplings between chromophores and hence the morphology. There are several parameters that determine the evolution of electronic aggregates and thus the formation of morphology. Among different side chains, molecular size

and shape, interactions with solvents, and processing methods and protocols, it is possible to specifically tune molecular flexibility or stiffness during material design. It is known that planar and stiff molecules tend to aggregate more easily. However, there was no systematic study, which directly addresses the influence of molecular flexibility on the ability to form aggregates.

I used the model oligomers TT and CT to investigate this issue. These two molecules consist of typical building blocks for solar cell materials and differ only in their central unit as indicated by the red and blue colours in Figure 5.1. TT comprises two *twistable thiophene* units with hexyl side chains linked in a head-to-head fashion. The side chains induce a twisted dihedral angle of around 70° in the otherwise planar structure. CT contains a carbon-bridged cyclopentadithiophene. These *connected thiophenes* make the molecule entirely planar. In Chapter 7, I utilized temperature dependent absorption and emission spectroscopy to investigate how this difference in molecular stiffness influences the formation of aggregates and the character of intermolecular interactions in solution. For spectral analysis I employed Franck-Condon modelling and programmed a graphical user interface, which is explained in Appendix A. The solution environment is different to the solid state, but allows to study the intrinsic nature of intermolecular interactions. Supported by molecular dynamics simulations, I showed that the rigid structure of CT can prevent two molecules from establishing a sufficient number of contact points. Intermolecular coupling is not well-defined and results in non-emissive excimer-like interactions. In contrast, TT can achieve sufficient stabilizing intermolecular contact points due to its flexibility. Even more, the twisted central dihedral angle planarizes against the steric obstructions of the side chains during the pathway into aggregated structures.

While it seems intuitive that the behaviour in solution is related to the morphological properties in thin films, a profound understanding of film formation itself is necessary to finally tailor the desired microstructure. As a further goal I wanted to apply the insights from different aggregation properties in solution to differences during film formation. Steady state characterization techniques on thin films can provide first insights. However, they cannot account for different processes and temporal evolutions during film formation, which is desirable to ultimately control the morphology during processing. Therefore, an experimental method is needed, which can directly monitor the film formation process using absorption and emission spectroscopy in situ. Chapter 8 describes the development of a corresponding setup, which allows for the first time to detect both absorption and emission from the same spot on the sample simultaneously. This setup consists of two individual parts. The first part is a spin coater device, which allows different substrate temperatures during processing. The second part is a complementary detection system, which requires only one CCD spectrograph for quasi-simultaneous measurements of absorption and emission in an alternating fashion. This results in a compact and easy-to-use system, in contrast to in situ scattering approaches,

which require beam times at synchrotron radiation sources. The measurement equipment capability was shown using P3HT. Films were processed at different temperatures and the results are in line with previous work. Furthermore, preliminary analysis of the emission anticipates deeper insights compared to in situ studies utilizing absorption only.

Simultaneous absorption and emission measurements result in loads of data, where overview easily gets lost. I implemented a graphical user interface in Python to ease analysis of measurement data. The program takes over routine calculations and allows for interactive inspection. More details can be found in Appendix D as well as some algorithms used for evaluation.

This setup enabled me to continue the investigation about the impact of molecular stiffness on aggregate formation during film formation. I correlated the results from the solution study in Chapter 7 to the film formation process, which is published in the fourth work and reprinted in Chapter 9. For both molecules, stiff CT and flexible TT, I could show that film formation takes place in similar stages, but with different timings. These timings give rise to kinetic constraints. The flexibility of TT opens up time windows for the molecules to reorient into intermolecular geometries with pronounced intermolecular coupling, even after solvent evaporation in the dry film. This is specifically ascribed to its ability for molecular reorganization. In contrast, the rigid CT only establishes weak intermolecular interaction during film formation. The molecules are forced into close proximity during solvent evaporation, and their stiffness prevents further optimization of the local intermolecular arrangement.

TT and CT comprises a pair of model oligomers specifically designed to investigate the implications of flexibility and stiffness on the ability to achieve ordered structures. Direct comparison revealed that flexibility can help to ensure pathways into electronic aggregates. In addition, TT showed a strong urge to planarize in the solid state, which is expected to be less pronounced for polymeric compounds. Hence, in a follow-up study I investigated the interplay between molecular reorganization and the dynamics of film formation for the polymer P3HT, which is the fruit fly of the organic semiconductor community. Albeit P3HT was extensively studied in the past, this study revealed further important insights. The solvents chloroform (CF) and tetrahydrofuran (THF) with a similar boiling point yet different solubility for P3HT were used for processing. Thus, the critical temperature of the disorder-order transition in solution $T_{c,sol}$ is markedly different at 10 °C for CF and 40 °C for THF. Blade coating films at different substrate temperatures and analysing the spectra of the aggregated species reveals the existence of a critical temperature $T_{c, film}$ also for processing. Aggregates in films processed below $T_{c, film}$ show an enhanced degree of order. Interestingly, the relation between $T_{c,sol}$ and $T_{c, film}$ is ambiguous. For CF, $T_{c, film}$ is above $T_{c,sol}$, for THF opposite behaviour was observed. Concomitant absorption and emission spectroscopy in situ during blade coating shows that the origin of this observation is the existence of two aggregation pathways. The interplay

between solution aggregation, leading to aggregate precursors, and aggregation through concentration quenching is responsible for the properties in the final film. During solution aggregation, structures with increased order are stabilized, while concentration quenching due to the final evaporation of remaining solvent results in more disordered morphologies. Of particular importance is timing during processing. It can control the selection of the aggregation pathway, as even a small amount of solution aggregate precursors dominates the aggregate properties of the final film. The low $T_{c,sol}$ for CF results in slower solvent evaporation and enables solution aggregation also slightly above $T_{c,sol}$. For THF, $T_{c,sol}$ is closer to the boiling point of the solvent, which suppresses the solution aggregation pathway and shifts $T_{c,filn}$ to lower temperatures. I was able to confirm this mechanism by blade coating from THF solution at a substrate temperature between $T_{c,sol}$ and $T_{c,filn}$ in a solvent rich atmosphere. Here, solvent evaporation is decelerated, which allows again for solution aggregation due to the elongated drying period, and the spectra of the aggregated phase resemble the properties characteristic for processing below $T_{c,filn}$.

To conclude, in this thesis I investigated the relationship between molecular flexibility and electronic structure under different aspects. Figure 5.2 shows a summary of the five individual works and their interconnection. In Chapter 6 I could show that populating interfacial CT states is not the bottleneck for higher device efficiencies due to reorganization effects. The existence and nature of the CT states depends on the molecular ability to establish ordered structures. Therefore, I examined the influence of molecular reorganization on the ability to form ordered arrangements. I demonstrated in Chapter 7 for the model compounds TT and CT that molecular flexibility is beneficial for aggregation in solution, as the number of attractive intermolecular contact points can be maximised. Chapter 8 lays the foundation for the subsequent studies and describes the development of an experimental setup to measure simultaneously absorption and emission during processing of thin films. In Chapter 9 I use this setup to link the aggregation properties of TT and CT in solution to their film formation behaviour. Finally, in Chapter 10 I showed that during film formation microtimings can play a major role for the decision on the aggregation pathway.

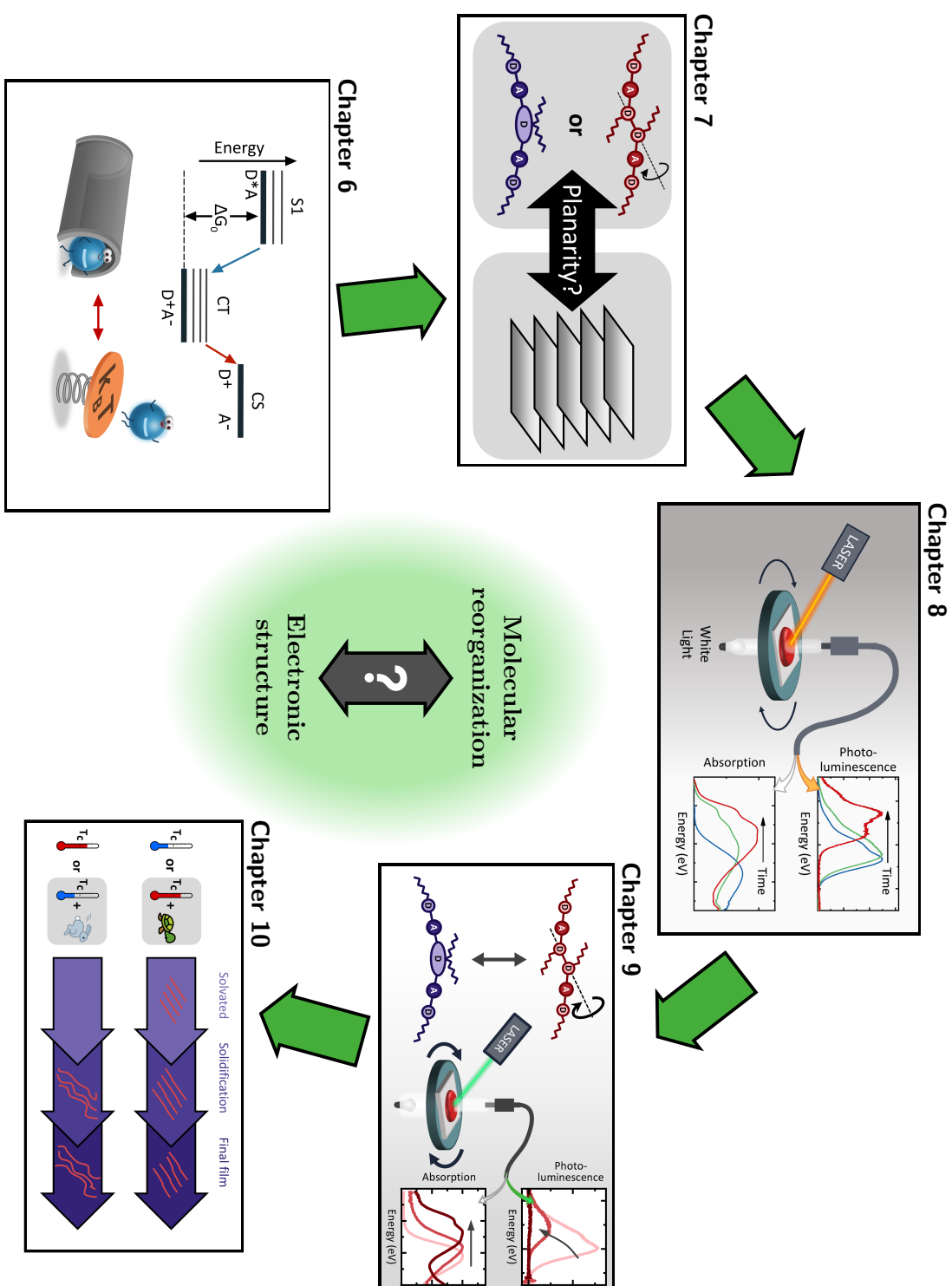


Figure 5.2: Context of the individual publications in this thesis.

5.2 Contents of the individual publications

5.2.1 The Impact of Driving Force and Temperature on the Electron Transfer in Donor-Acceptor Blend Systems

Classical Marcus theory was in its original formulation derived for chemical redox reactions in solution, and its successful predictions rewarded Marcus with the Nobel prize in 1992.³⁰ This achievement motivated many researchers to apply it to electron transfer processes from a donor to an acceptor in organic semiconductor devices. However, the Marcus mechanism underestimates the relevance of quantum mechanical tunneling effects, which is due to the amorphous nature of organic solids, strong coupling to high-energy molecular vibrations and low reorganization effects of the surrounding media. Hence, it remains to be clarified whether classical Marcus theory or its semiclassical Marcus-Levich-Jortner (MLJ) extension are actually suitable to describe charge transfer in organic donor-acceptor systems.^{39,40,49,59,195–199} In this publication we critically tested the applicability of the Marcus framework for electron transfer in donor-acceptor blend systems in general, and the implications of the input parameters driving force ΔG_0 and reorganization energy λ in particular. As this formalism requires thermal activation, it predicts a strong temperature dependence of the electron transfer rate, which renders it suitable for experimental verification. Consequently, we measured the electron transfer rate from a photoexcited donor to an acceptor for a wide range of temperatures between room temperature and 12 K.

Comparing the results with predictions from the Marcus and MLJ models show that their applicability is at least questionable in this instance. The transfer rates for material systems in the normal regime or not far in the inverted regime are mathematically consistent, but very large. In contrast, material systems far in the inverted regime cannot be adequately described in this framework. Including the influence of disorder, tunneling and coupling to vibrations can eliminate the dependence on temperature and push absolute numbers closer to experimental values. But as predicted transfer rates are high, the required thermal equilibrium is unlikely to be established during these ultrafast time scales.

We used three donor-acceptor systems covering different regimes in the Marcus picture. As donor material we used the stiff ladder polymer MeLPPP and the low-bandgap polymers PCPDTBT and PTB7. The acceptor was PCBM for all donors. We first determined the spectral signatures of the charged polymers by chemically oxidizing pristine thin films. These signatures were subsequently monitored in blend films using temperature dependent ultrafast transient absorption spectroscopy, yielding the time scale for electron transfer from donor to acceptor. If the Marcus framework is appropriate to describe this process, the rise of the cation signal should slow down upon cooling. However, we observed unchanged transfer dynamics for all systems and all temperatures, which is limited by the duration of the

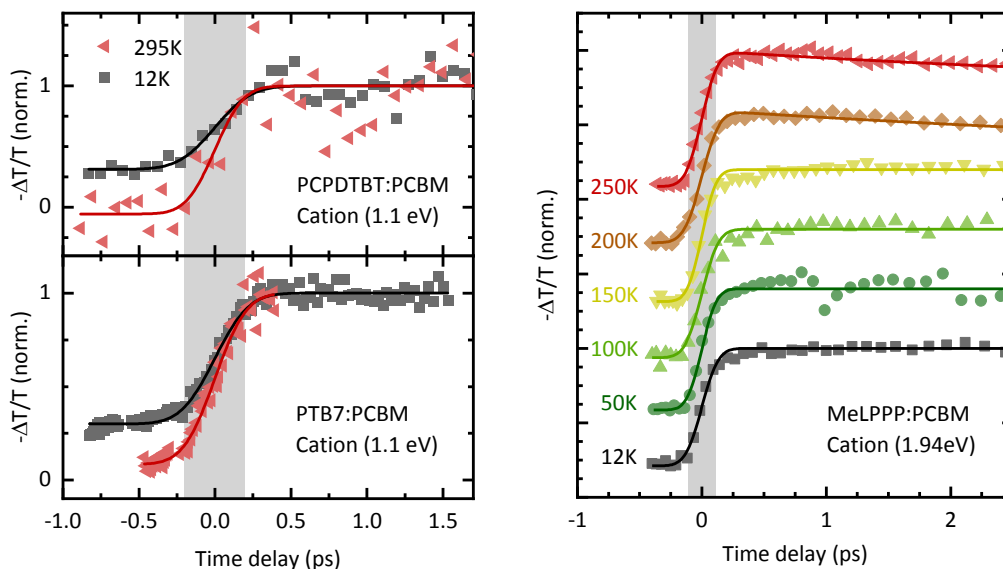


Figure 5.3: Normalized pump-probe transients of the cation absorption for blend films of PCPDTBT:PCBM, PTB7:PCBM and MeLPPP:PCBM taken at different temperatures. The solid lines represent fits to extract the rise time, the gray box indicates the temporal resolution.

laser pulses and shown in Figure 5.3. To compare experiment against Marcus and MLJ theory, we thoroughly searched literature for molecular energy levels as input parameters. Own measurements were performed for MeLPPP:PCBM, and special care was taken to get reasonable uncertainty ranges.

For PCPDTBT:PCBM and PTB7:PCBM it turned out that $\lambda + \Delta G_0 \gtrsim 0$. They are in the Marcus normal regime and the activation energy for charge transfer almost vanishes. As a result, the temperature dependence is negligible, and the parameter input range would in principle also allow for increased rates at low temperatures. MeLPPP:PCBM is far in the inverted regime, as the driving force is large and the reorganization energy is small due to the stiffness of MeLPPP. Figure 5.4 a shows how Marcus theory and the MLJ extension perform for this system. The Marcus formalism is largely off, and for the MLJ mechanism there are strong variations of the transfer rate with varying ΔG_0 at lower temperatures due to coupling to vibrations. This would imply that the molecular parameters for the MeLPPP:PCBM system just combine right to be in resonance with the correct molecular vibration. Given the fact that organic semiconductor materials are strongly disordered,¹² this is rather implausible. Therefore, we included Gaussian disorder into the calculation, which indeed does eliminate the strong temperature dependence as shown in Figure 5.4 a for $\sigma = 50$ meV. However, the observed ultrafast transfer rate still can only be reproduced if the errors for all input parameters combine most fortunately and strong vibrational coupling is assumed. The same holds true for reported values of P3HT:PCBM system,⁵⁹ which are included in Figure 5.4 b.

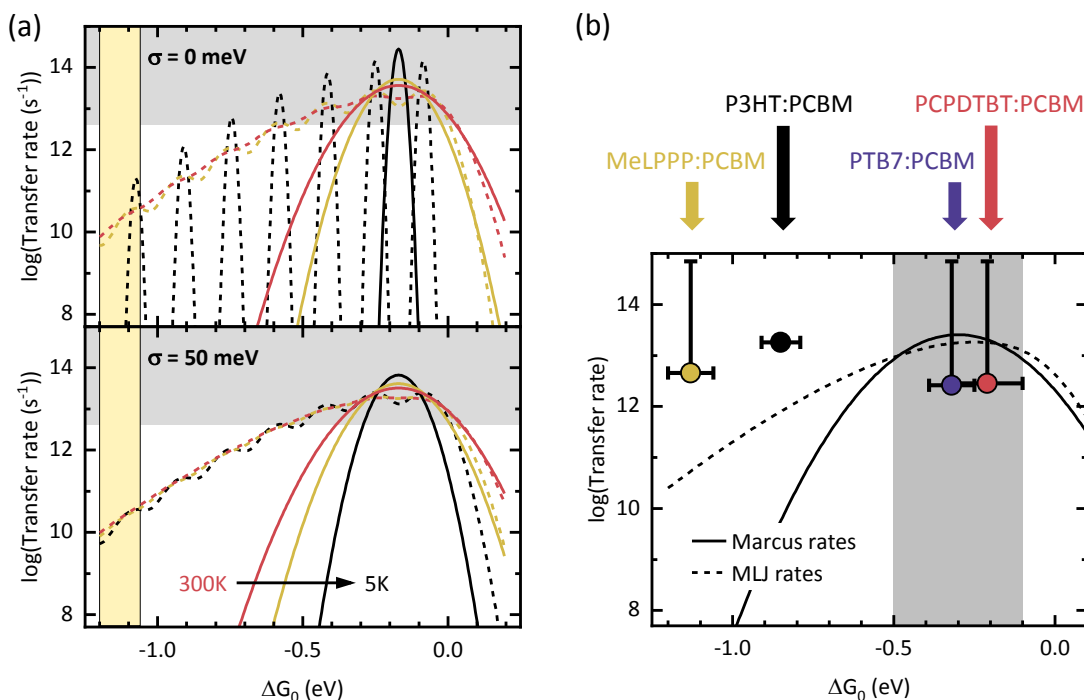


Figure 5.4: Calculated electron transfer rates in the Marcus framework (solid lines) and the MLJ framework (dashed lines). (a) Transfer rates for the MeLPPP:PCBM system at temperatures of 300 K, 150 K and 5 K without (top) and including (bottom) disorder effects. The gray area indicates values beyond the instrumental resolution, the yellow area indicates the parameter range for the driving force. (b) Calculated transfer rates for typical input parameters at 300 K. The gray area indicates typical driving force values. Experimental values from this work are complemented by values from literature for P3HT:PCBM.

If the MLJ framework would be a suitable description, what would follow for the influence of ΔG_0 ? Considering other typical efficient solar cell systems, ΔG_0 usually ranges between -0.1 eV and -0.5 eV as indicated in Figure 5.4 b by the gray area,^{195,200} resulting in transfer rates in excess of $1 \times 10^{13} \text{ s}^{-1}$. This is faster by four orders of magnitude in comparison to characteristic excitation lifetimes. As a result, the efficiency for electron transfer is close to 100% and basically independent of ΔG_0 . Apparent dependencies on ΔG_0 for charge generation^{39,40,195} can be rationalized as trade-offs among different subsequent processes.

The observed transfer rates are still fast in comparison to the frequency of a thermally activated molecular vibration. Further, as consideration of our measured values as well as P3HT:PCBM from literature⁵⁹ shows, rates for larger driving forces cannot be reconciled with Marcus-type descriptions, even when including quantum couplings to vibrations and tunneling effects. This can be rationalized when considering the fact that these theories are derived for nonadiabatic charge transfer in thermodynamic equilibrium. This cannot be established within the short transfer times observed in experiment, and it is thus necessary to apply models that include adiabatic and coherent mechanisms.

5.2.2 What is the role of planarity and torsional freedom for aggregation in a π -conjugated donor–acceptor model oligomer?

In this publication I addressed the influence of backbone planarity and flexibility on the aggregation properties in solution using the two model oligomers CT and TT. These compounds differ only in the stiffness and planarity of their respective central building block. I showed that TT is more prone to form aggregates with electronic interaction, while CT rather forms non-emissive excimers. This different behaviour can be rationalized with the different number of attractive intermolecular contact points. More specifically, I was able to correlate the flexibility of TT with its ability to establish these contact points. This allows for a sufficient stabilization of the intermolecular coupling instead of creating undesirable non-radiative decay channels for electronic excitations. A suitable method for investigating ordering phenomena in solution is to measure absorption and emission upon cooling, as solvent quality decreases in a controlled way. This approach was used for a variety of conjugated oligomers and polymers before and lead to important insights.^{75,77,108,119–121,141} Here, I applied this method to solutions of TT and CT in hexane for different concentrations ranging from 5.0×10^{-6} M to 2.5×10^{-4} M. Furthermore, most of the spectra were analysed by means of a Franck-Condon analysis. To simplify the work flow, I wrote a graphical user interface in Python, which is described in Appendix A.

Figure 5.5 shows the absorption and emission of TT and CT exemplary for an intermediate concentration of 5.0×10^{-5} M between 300 K and 180 K. The emission spectra are normalized to coincide at around 2.1 eV for TT and 1.7 eV for CT to highlight the evolution of the spectral shapes. TT in Figure 5.5 a undergoes a typical disorder-order transition at the critical temperature of $T_c \approx 230$ K. Above T_c , the absorption is broad and unstructured, increases in intensity and shifts to lower energies upon cooling. This is typically interpreted as an increased average planarization among adjacent subunits, as torsional movements are frozen out. Below T_c , a well-structured feature emerges at lower energies, while the broad component disappears and an isosbestic point is visible. A concomitant evolution can be observed in emission. These observations are a clear sign that the molecules form aggregates in solution. For the high concentration (2.5×10^{-4} M), corresponding measurements show an increased critical temperature of $T_c \approx 260$ K and more pronounced aggregate features, while there is no evidence of a disorder-order transition for the low concentration (5.0×10^{-6} M). All emission spectra of TT show an unusual shoulder at the high-energy side, which becomes more prominent at lower temperatures. Thorough investigations at even lower concentrations, time-resolved measurements and analysis using Franck-Condon fits showed that there are two independent contributions with no energy transfer among them. Quantum-chemical calculations suggest that the origin lies in the flexibility of the central molecular unit, as there are two stable conformations in the excited state.

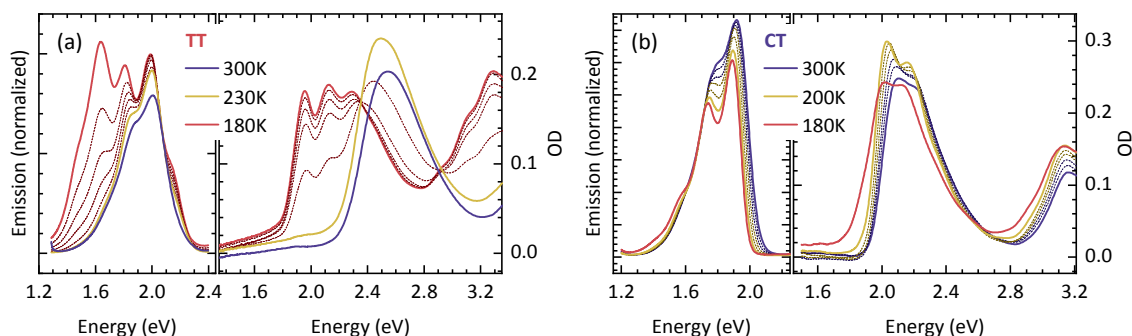


Figure 5.5: Absorption and emission of (a) TT and (b) CT in hexane at a concentration of 5.0×10^{-5} M. The emission spectra are normalized to 2.1 eV for TT and 1.7 eV for CT. Spectra taken at characteristic temperatures given in the legend are drawn as solid lines. The spectra in between are shown for TT in steps of 10 K between 180 K and 230 K, and for CT in steps of 20 K.

The evolution of the spectral signatures for CT in Figure 5.5 b is more subtle. The absorption shows little vibronic structure, which becomes more pronounced upon cooling. Further, it shifts to lower energies and increases in intensity. However, for temperatures below 200 K the absorption intensity and the 0–0/0–1 peak ratio both decrease. The low energy tail broadens at the same time and a scattering offset appears. The structured emission changes little between 300 K and 200 K. Nonetheless, an additional weak feature appears at energies below 1.6 eV at the lowest temperature of 180 K. These observations are indicative for some intermolecular interaction. Yet, clear signatures of distinct electronic aggregates are missing. Alike to the case of TT, spectral signatures of intermolecular interaction are missing for the low concentration (5.0×10^{-6} M) and are more pronounced for the high concentration (2.5×10^{-4} M).

The emission spectra contain more information about the nature of the intermolecular interactions. These spectra are normalized in Figure 5.5 to ease comparison of the spectral shapes. Figure 5.6 contains the relative emission intensities as a function of temperature. It was further possible to separate the emission spectra of the aggregated phase, which is also shown in Figure 5.6 c for the high concentration. For TT, the emission intensity remains constant above T_c and decreases steeply below T_c . This is reminiscent for an H-type interaction, which is confirmed by the concomitant decrease of the 0–0 peak intensity as well as an increase of the non-radiative decay rate. In contrast, for CT the emission intensity decreases continuously already from 250 K onwards for the intermediate and high concentration. This decrease does not correlate with the changes of the spectral shapes. Thus, aggregate precursors do also exist for CT. However, they resemble non-emissive excimer-like precursors, similar to the case of pyrene derivatives.⁸⁷

These differences are at variance with the expectation that more planar structures should

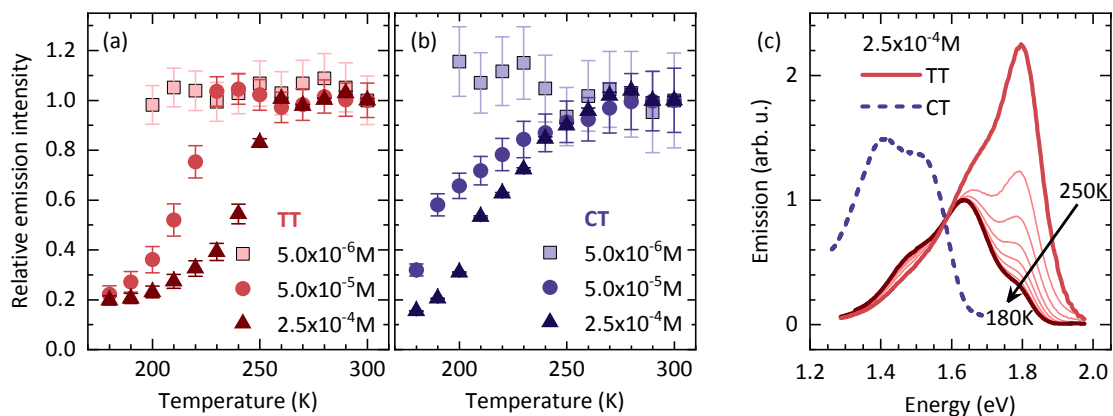


Figure 5.6: Relative emission intensities for (a) TT and (b) CT as function of temperature for different concentrations, normalized to the respective values at 300 K. (c) Separated emission spectra of the aggregated species at the concentration of 2.5×10^{-4} M. The spectra for TT are shown in steps of 10 K and normalized to 1.6 eV. For CT only the spectrum at 180 K is shown.

form aggregates more easily. Therefore, we conducted molecular dynamics (MD) simulations to get a picture of the underlying processes on a molecular scale. For these calculations, two copies of either a TT molecule or a CT molecule are placed in a simulation box together with many solvent molecules. Evaluating the temporal evolution of the system statistically results in the free energy of the dimer as a function of the distance between the central units. The simulations further allow to inspect the relevant mean dimer conformations.

Figure 5.7 shows the results of the MD calculations. For both molecules the dimer geometries are energetically preferred and sketched in Figure 5.7 c. The pathway into the stable dimer geometry is established by sliding along the long axis of the molecules while crossing several local minima along the free energy curves. These local minima correspond for both TT and CT to conformations where subunits are stacked on top of each other. The two molecules in the dimer conformation of TT wrap around each other due to the twisted nature of the central dihedral angle. For CT there are two possible orientations. The side chains on the central unit are either oriented to opposite sides (type A) or to the same side (type B). Both conformations for CT are equally likely, and in particular they are stabilized stronger compared to the dimer conformation of TT. These simulation results suggest that CT has a stronger propensity for aggregation, at variance with experimental observations. However, the models for the TT molecules incorporate the torsional potential derived from quantum-chemical calculations on isolated molecules, which is responsible for the strong twist. Molecular dynamics cannot account for possible changes of this torsional potential, which may result from a change of the electronic structure due to the intermolecular interaction. In fact, reports show that TT adopts a planar conformation in the solid state,^{201,202} and planarization has also been observed for other conjugated compounds.^{111,153,203}

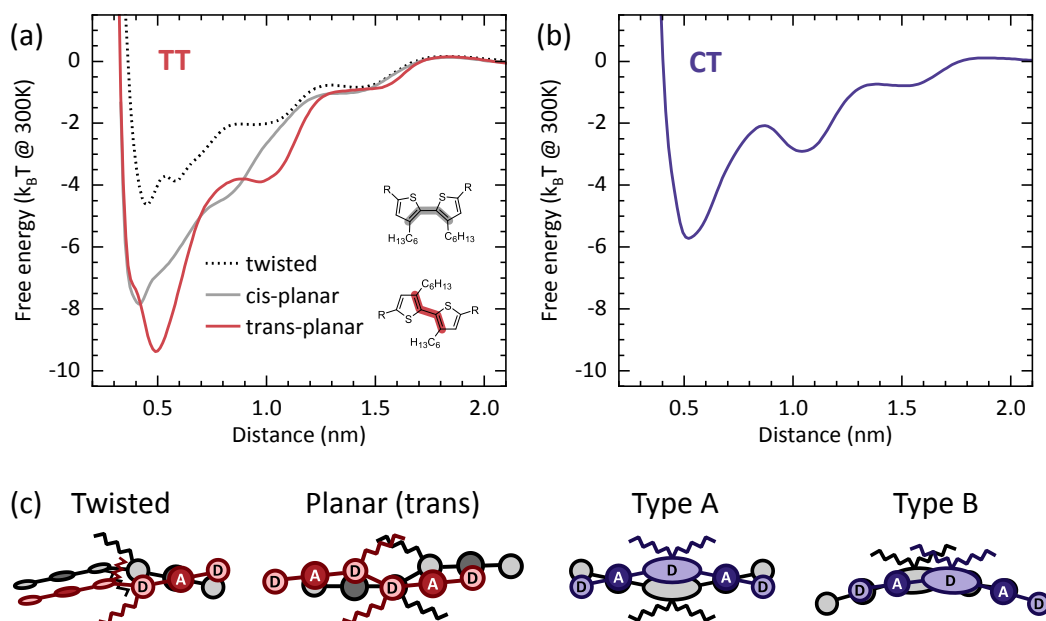


Figure 5.7: Free energy curves for (a) TT and (b) CT. Structural insets in (a) indicate the orientation of cis and trans conformations for planarized TT. (c) Sketches of the dimer geometries at the global minimum of their respective free energy curve.

Essentially, it was necessary to explicitly allow TT to planarize in the MD simulations. The free energy curves for both cis- and trans-planar conformations in Figure 5.7 a show considerably larger stabilization of the TT dimer compared to the CT dimer in Figure 5.7 b. Inspecting these conformations closer revealed that the mechanism is the possibility to establish a sufficient number of stabilizing intermolecular contact points. For TT, there are five stabilizing contacts in the most stable trans-planar conformation, whereas for CT these contacts are less in both number and strength. The flexibility of TT ensures that there is a pathway into the relevant conformation.

Finally, quantum-chemical calculations on the averaged dimer structures confirm the emission properties we observed in experiment. For CT, the electronic transition of the type A conformation has no oscillator strength. The type B conformation is subject to significant changes in the dimer geometry, which is a textbook example for an excimer. The electronic transition of the TT dimer has a weak but finite oscillator strength without significant molecular reorientation upon excitation. Hence, this conformation is a stable electronic aggregate and can account for the decreasing emission intensity.

5.2.3 Setup to Study the *in Situ* Evolution of Both Photoluminescence and Absorption during the Processing of Organic or Hybrid Semiconductors

In the previous chapter I investigated how backbone flexibility affects both the nature of intermolecular interactions as well as the propensity to form ordered structures in solution. As a next step it seemed plausible to examine how these molecular parameters influence the film formation process. There was already a setup available, which was capable to measure the absorption of a film during processing.^{152,157,189} However, as these measurements were restricted to absorption data without concurrent detection of emission, they could provide only incomplete pictures of the underlying processes. This work overcomes this limitation by developing a suitable detection system, which can monitor both absorption and emission simultaneously at the same detection spot on the sample, probing the same ensemble of chromophores during processing.

It is inherently difficult to measure absorption and emission both at the same time and the same position on the sample. Absorption measurements require a broadband light source as a reference, which is transmitted by the sample. For emission measurements, the sample material needs to get excited by a source for excitation, preferably a laser. This excitation light can result in unwanted stray signal, or in destruction of the detector as a worst case scenario. It must be suppressed during detection with suitable optical filters, which obstructs absorption measurements in the respective blocking region. Hence, both measurement modes will interfere with each other, which ultimately hinders data evaluation. One possibility is measuring at different spots on the sample.^{204,205} However, direct comparability of absorption and emission could be hampered through inhomogeneous film formation dynamics.

We tackled this challenge by changing the measurement mode to an alternating detection scheme. Absorption and emission spectra are collected one after each other. The different requirements for each measurement mode are ensured by a new detection system. Figure 5.8 shows a sketch for this detection system and its different operational states for absorption measurements in Figure 5.8 a and emission measurements in Figure 5.8 b. A mechanical chopper with mirrored blades (1) comprises the heart of this system. Light collected from the spin coater enters the detection system through an optical fiber (2), where it is collimated by a focussing lens (3). For absorption measurements, the blade of the chopper wheel (1) completely reflects the collimated light. A second focussing lens (4) couples this light into a second optical fiber (5), which is connected to a spectrograph bearing a CCD camera for detection. During emission measurements, the incident light from the spin coater passes through a hole of the chopper wheel. An adequately chosen optical filter (6) removes laser stray light, before two mirrors (7,8) reflect the emission back through the same hole of the chopper wheel. Behind the chopper, both beam paths for absorption and emission again coincide, which allows using the same spectrograph for detection. A white light LED is used

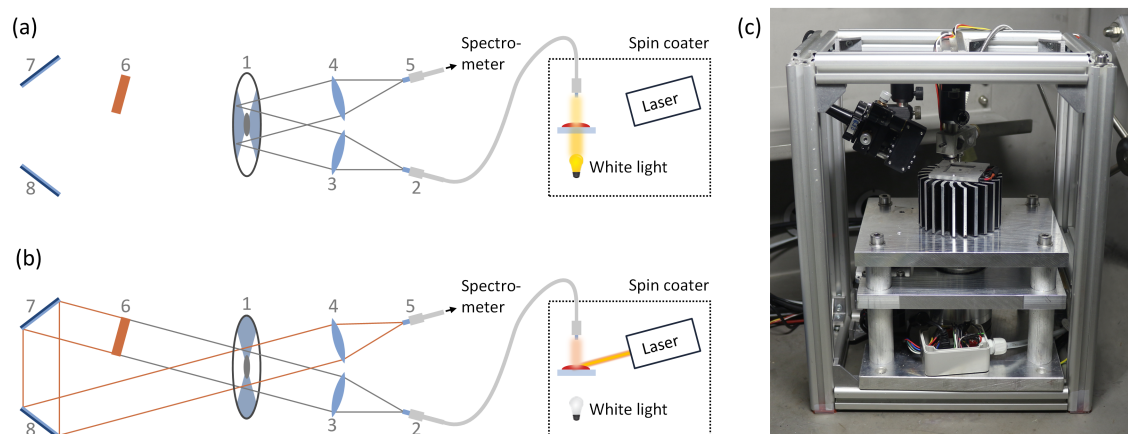


Figure 5.8: (a,b) Schematic illustration of the main components of the detection system and the operational states of white light and the laser for (a) absorption and (b) emission measurements. The optical components are labeled by numbers and explained in the text. (c) Photograph of the assembled spin coater.

as reference for absorption measurements, while a laser diode is used as the excitation source during emission measurements. All electrical components are controlled by a microcontroller to ensure their correct interplay. For data evaluation I wrote a graphical user interface in Python, which simplifies inspection and performs routine calculations on the data. Details of this program are explained in appendix Appendix D.

We further developed a spin coater device, which complements the detection system. Figure 5.8 c shows a photograph of this device fully assembled, including the laser diode and the optical fiber. The spin coater features a bore through the shaft of the rotating chuck, which guides light from the LED for absorption measurements to the sample. A further technical detail is the Peltier plate on top of the chuck. It allows to vary the temperature of the substrate between 0 °C and 150 °C and draws electrical power from a rotary transformer in the lower part of the chuck. The heat diffuser with cooling fins ensures dissipation of excess heat for thermal equilibration at the substrate.

The measuring equipment capability was then demonstrated using the polymer P3HT. 2D heat maps of absorption and emission during spin coating from chlorobenzene solution are shown in Figure 5.9 a and b at room temperature, spectra at distinct times are shown on top. At initial times, both absorption and emission resemble spectra in solution above the critical temperature of aggregation. Around 8 s there is a distinct transition and optical signatures appear, which are associated with the well-known disorder-order transition and usually occur during film formation.^{106–108,121}

We performed further test measurements at additional substrate temperatures of 3 °C, 43 °C and 65 °C. For easier comparison among all processing temperatures we extracted the

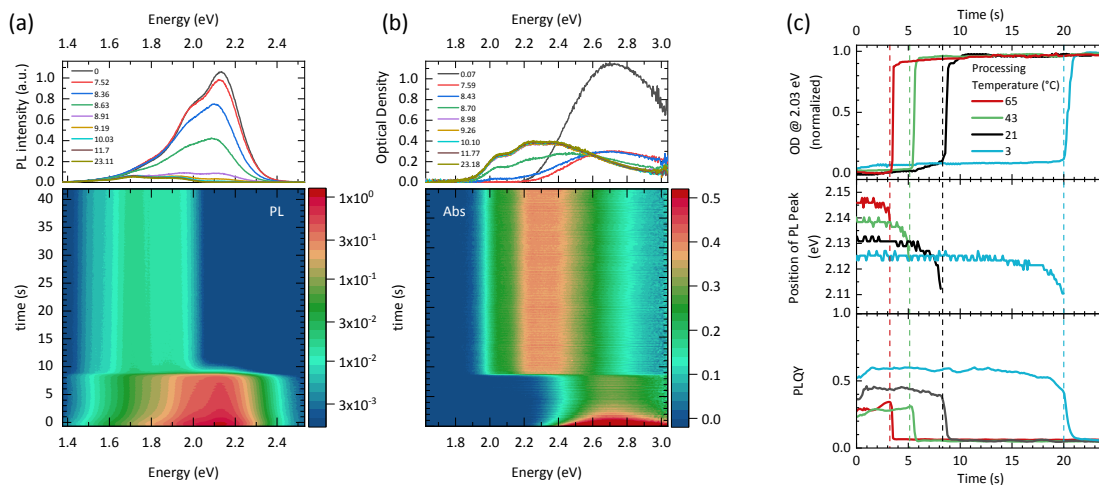


Figure 5.9: (a) Photoluminescence and (b) absorption spectra of P3HT during spin coating from chlorobenzene solution at room temperature. The panels on top show spectra at distinct time steps, the heat maps on the bottom show the evolution during the first 40 s after starting the rotation. (c) Temporal evolution of (top) the optical density at 2.03 eV normalized to the final value, (middle) the energy position of the emission peak, and (bottom) the PLQY for processing at different substrate temperatures.

temporal evolution of different simple spectral features, which is shown in Figure 5.9 c. The normalized optical density at 2.03 eV monitors the amount of aggregated phase during film formation.^{157,189} We find that the onset time for the transition decreases from 21.1 s, 8.6 s, 5.3 s to 3.6 s for increasing the temperature from 3 °C, 21 °C, 43 °C to 65 °C, respectively, in accordance with earlier findings.¹⁵⁷

The spectral changes for the emission spectra largely correspond to the absorption spectra. With increasing processing temperature we observe a higher energy position of the initial emission peak and a decreased starting level of the photoluminescence quantum yield (PLQY). Further, the absolute PLQY decreases drastically upon aggregate formation, which is all in accordance with literature.^{121,206} Upon closer inspection we observe a redshift of the emission peak position prior to the transition, and for processing temperatures of 43 °C and 65 °C there is an additional increase in PLQY shortly before the transition. These findings indicate that more complex processes happen during processing even for the simple P3HT. However, a profound analysis is beyond the scope of this work and part of a follow-up study.

This newly developed detection system lays the foundation for in-depth investigations on film formation in different material systems. In particular, the quasi-simultaneous detection of both absorption and emission proves beneficial and already provided deep insights into the role of torsional flexibility during film formation in Chapter 9, the follow-up study on P3HT in Chapter 10 and the two-step method for processing the hybrid material methylammonium lead iodide.²⁰⁷

5.2.4 Role of Torsional Flexibility in the Film Formation Process in Two π -Conjugated Model Oligomers

Having understood the different aggregation properties of CT and TT in solution, the next step was to transfer this knowledge to the film formation process. The experimental setup developed in Chapter 8 allowed to investigate this in more detail. I measured absorption and emission during processing of thin films using the same solvent hexane for the spin coating solution to ensure comparability with previous results from Chapter 7. As the existence of preaggregates in the spin coating solution can influence the final film morphology,^{157,194} processing was performed at substrate temperatures well above the critical temperature T_c for aggregation. We find that the flexible TT forms amorphous films right after solvent evaporation, which seems to be at variance to the case in solution. Structures with local order and electronic interaction are established only subsequently in the dry film on a time scale of minutes. The rigid CT immediately evolves into structures, which are characterized by some degree of electronic interaction and local order. These apparent differences to the aggregation properties in solution can be rationalized by the kinetic constraints of the spin coating process, as the morphology emerges in similar stages for both compounds.

We first consider the results for CT. Processing was performed at room temperature, as T_c is around -18°C . Figure 5.10 a and b shows the emission and absorption spectra during processing, either at distinct times on top or as 2D heat maps on the bottom. The temporal evolution of different spectral features is shown in Figure 5.10 c. From these, we identify four distinct stages during film formation. The first two stages mark the drying of the film, where excess solution is thrown off and solvent evaporates. Already in stage II there are signs of excimer-like intermolecular interaction in emission, while the absorption remains largely unchanged. The PLQY decreases and the monomeric emission disappears, being replaced by a feature at lower energies, which results in a net shift of the PL peak position. Stage III is characterized by a fast change in absorption from a broad and unstructured shape towards a slightly more structured contribution at lower energies in combination with an isosbestic point. Film formation is completed in stage IV, where no further changes occur.

The emergence of the structured absorption in stage III along with the reduction in PLQY and a concomitant redshift in emission strongly points to the formation of aggregates. The existence of intermolecular interaction is unambiguously confirmed by heating a film above the melting point of CT. Figure 5.10 d shows the absorption spectra at different temperatures during heating. If the structured feature was of monomeric origin, we would expect that the structure mainly broadens due to the increased conformational freedom. The structured absorption with the dominant peak at 1.95 eV disappears instead, while a broad spectral shape remains at higher energies in the melt. Thus, for CT film formation is fast and intermolecular interaction is established. The optical signatures upon condensation mimic the properties in

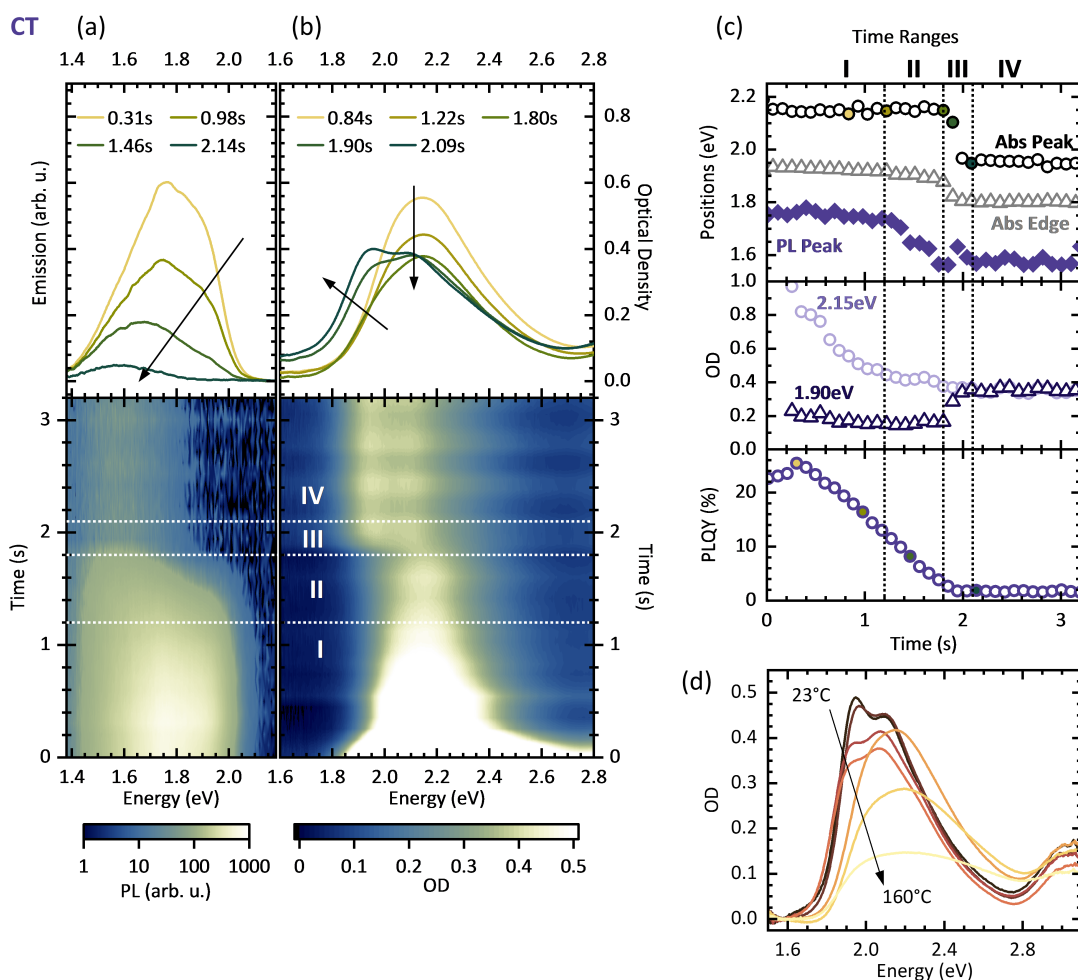


Figure 5.10: (a) Emission and (b) absorption spectra of a CT film during spin coating from hexane at room temperature. The spectra on top are taken at fixed times after starting the spin coater rotation. The heat maps on the bottom show the evolution in the first three seconds. The white dotted lines indicate four different time ranges during film formation. (c) Temporal evolution of (top) the peak positions for absorption and emission as well as the low energy edge of absorption, (middle) the optical density at 2.15 eV and 1.90 eV, and (bottom) the PLQY. The filled circles correspond to the spectra shown in the top panels of (a) and (b). (d) Absorption spectra of a CT film upon heating.

solution upon aggregation. However, ground state interaction is more pronounced in the thin film due to the different environment. The molecules are forced into close proximity during solvent evaporation, which increases intermolecular interaction to an extent that aggregates are clearly observed in absorption.

We next turn to the film formation process of TT, which is summarized in Figure 5.11. Processing was performed using a substrate temperature of 51 °C, as T_c for aggregation is around 42 °C. The most obvious difference compared to film formation of CT is the duration of the whole process. It is finished within 3 s for CT, while it is drawn out over approximately 80 s for TT. Overall, we can divide the evolution of absorption and emission spectra in two parts. Figure 5.11 a shows the first part, which spans the first 3 s. Solvent quickly evaporates here and the transition from solution to the solid film takes place. It is followed by a subsequent slow crystallization process in the dry film as noted earlier²⁰¹ and shown in Figure 5.11 b. Figure 5.11 c further shows the complete evolution of both absorption and emission as 2D heat maps using a logarithmic time axis, and Figure 5.11 d contains the temporal evolution of distinct spectral features. Again we can identify four unique stages, which differ in their time scales.

During the initial stage I excess solution is again thrown off and spectral features remain largely unchanged. In stage II the remaining solvent evaporates and some intermolecular interaction is established. However, the torsional potential of the central bithiophene obstructs the formation of well-ordered structures and leads to a quenched amorphous morphology, which results in a broad and unstructured absorption. These conformations are further characterized by excimer-like interactions, as the PLQY and the emission peak position both decrease. Stage III is drawn out over about 80 s, which is the most prominent difference compared to CT. For TT, a structured absorption feature emerges continuously at lower energies. This can directly be ascribed to the establishment of ground state interaction, as the fraction of aggregates increases, while emission is quenched concomitantly. Stage IV again marks the end of the overall process.

Direct comparison between both compounds shows that the flexibility of the central core significantly affects stage III of film formation. This is the relevant stage for aggregate formation and takes place on largely different time scales. For CT this stage is fast and lasts less than half a second. TT needs around 80 s, which is longer by two orders of magnitude. This finding seems to suggest that aggregate formation is hindered for TT, at variance with the aggregation properties in solution. Closer inspection and comparing with the dimer structures from the solution study resolves this apparent contradiction. CT can adopt two different conformations. Type A is non-emissive without any contribution to absorption, while type B bears a finite oscillator strength for absorption and emission. Apparently, some of these conformations are formed during stage III, as the molecules are forced into proximity by evaporating solvent. As a result, they are fixed in these positions due to the rigidity of

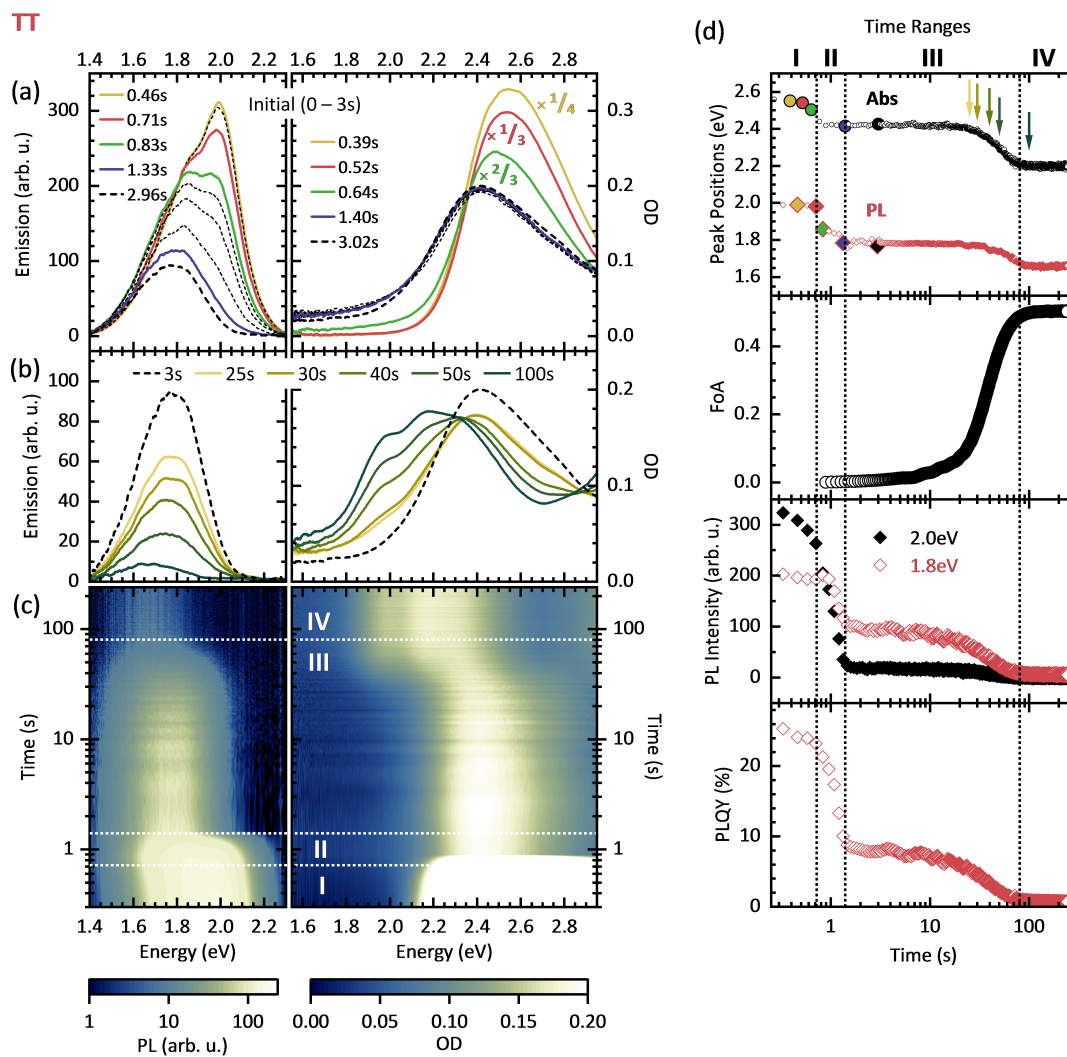


Figure 5.11: (a,b,c) Emission (left) and absorption (right) spectra of a TT film during spin coating from hexane at a substrate temperature of 51 °C during (a) the first 3 s and (b) subsequently. The spectra in (a) are shown in steps of 0.125 s between 0.39 s and 1.40 s. The complete evolution is shown in (c) as 2D heat map. The white dotted lines indicate four different time ranges during film formation. (d) Temporal evolution of the energy peak positions, the fraction of aggregates (FoA) in absorption, the emission intensity at 2.0 eV and 1.8 eV, and the PLQY. The coloured symbols and arrows indicate the temporal positions of the spectra shown in (a) and (b).

the backbone. Correlating previous grazing incidence wide-angle X-ray scattering (GIWAXS) measurements²⁰¹ confirms that order is established only on a short-range length scale.

In contrast, the pathway into conformations with strong intermolecular interactions is more complex for TT. In solution, the molecules have sufficient time to approach each other and planarize during aggregate formation. Upon film formation, the twisted nature only allows for a kinetically quenched amorphous morphology due to the high torsional barrier, which cannot be overcome spontaneously. It is the molecular flexibility and the strong urge to adopt a planar conformation in the solid state,^{201,202} which subsequently results in slow crystallisation. Corresponding GIWAXS measurements²⁰¹ prove that order pertains on long-range length scales in thin films.

Thus, the apparent discrepancy between aggregate formation in solution and during film formation can be rationalized by the kinetic constraints during highly dynamic processing situations. Furthermore, the torsional flexibility of the TT molecule is not necessarily a disadvantage to establish well-ordered structures. It can rather open up time windows during processing, which could in principle be exploited to fine-tune the morphology. In contrast, the stiffness of the CT backbone prevents subsequent intermolecular reorganization. Therefore, moderately flexible structures with sufficient driving force toward planarization should be used as a design rule for next-generation materials, which would allow to specifically tailor the desired morphology in thin films.

5.2.5 Processing condition dependent aggregation pathways in conjugated polymers

The comparison of the film formation process for CT and TT showed that the establishment of ordered structures is dominated by the dynamic constraints imposed during processing. CT molecules are fixed in the positions they end up after solvent evaporation, showing short-ranged order at most. For TT, the flexibility and the strong urge to planarize in the solid state results in significant molecular reorientation and the formation of well-ordered structures. However, this aggregation mechanism renders difficult for polymers. Their increased chain length affects the mechanical properties of processing solutions and can lead to entanglement,²⁴ making time consuming optimizations of the film morphology necessary.^{191,208–210} Therefore, we investigated the interplay of molecular reorganization and the dynamics during film formation for the polymer P3HT. To date, several extensive in situ studies exist, often utilizing X-ray scattering and partly in combination with optical methods.^{15,25,205,211,212} However, optical properties were often only examined superficially. Here, we apply the established models of Spano^{89,90,92,94,95} for the first time to optical signatures during processing. This allows to identify the importance of timing, which can be decisive for selecting the aggregation pathway and hence the final morphological and optical properties.

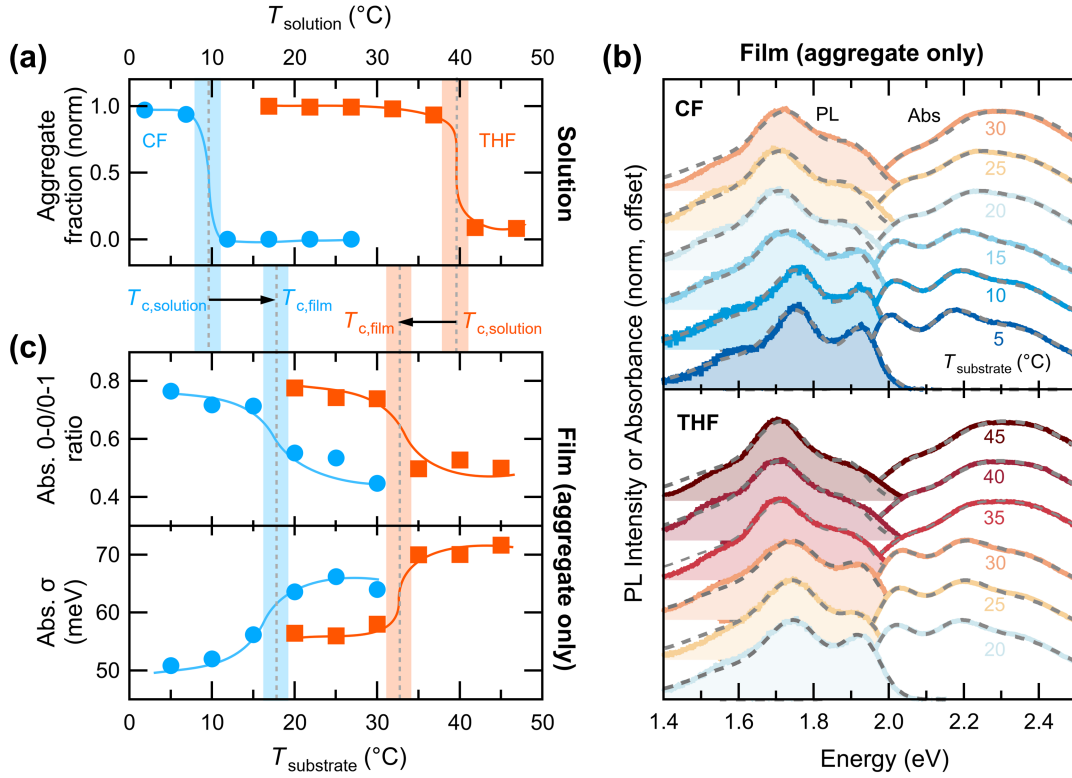


Figure 5.12: (a) Critical temperature $T_{c,\text{solution}}$ for aggregation in solution of P3HT in CF and THF. (b) Isolated aggregate spectra in thin films blade coated from CF (top) and THF (bottom) at different substrate temperatures. Dashed lines represent fits. (c) 0–0/0–1 peak ratios and line widths extracted from fits to absorption aggregate spectra in (b), indicating the existence of a critical processing temperature $T_{c,\text{film}}$. The inflection points of sigmoidal fits in (a) and (c) define the respective critical temperatures.

We processed P3HT films using blade coating from the solvents chloroform (CF) and tetrahydrofuran (THF). They have a similar boiling point, yet different solubilities for P3HT,²¹³ which directly transfers to the critical temperature $T_{c,\text{solution}}$ of the disorder-order transition in solution as shown in Figure 5.12a. Processing thin films at different substrate temperatures $T_{\text{substrate}}$ results in aggregates with different amounts of order and interactions, which are expected to be of stronger interchain character with reduced 0–0 peak intensities above $T_{c,\text{solution}}$.¹⁵⁷ The spectral signatures of the aggregates can be obtained by the scaling approach¹²¹ and are displayed in Figure 5.12b for the final films. Qualitatively, the spectral shapes are as expected and show a more pronounced vibronic structure for lower $T_{\text{substrate}}$. Using a Franck-Condon approach allows to further quantify the optical parameters. Figure 5.12c contains the extracted 0–0/0–1 peak ratios and Gaussian line widths of the absorption. Obviously, there is a critical processing temperature $T_{c,\text{film}}$, above which the 0–0/0–1 ratio is decreased and the line width is increased. Below $T_{c,\text{film}}$, order is more pronounced and results in stronger relative weighting of intra-chain interactions.²¹⁴

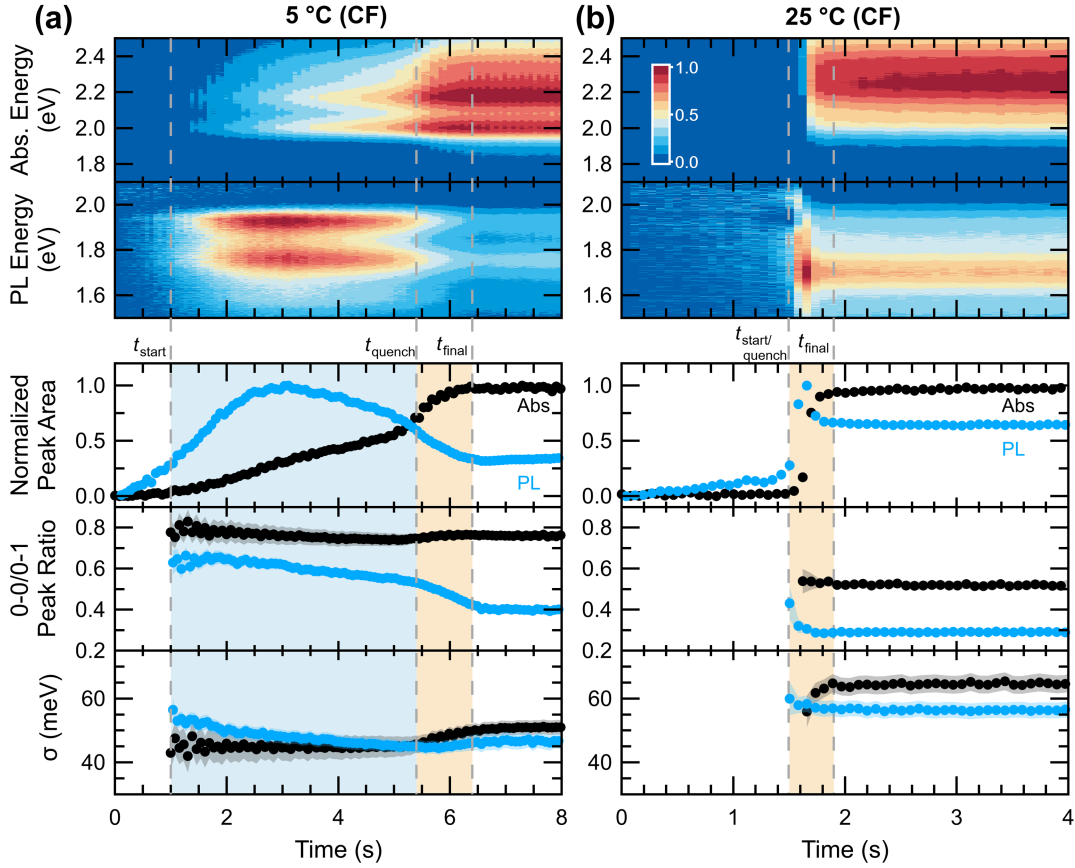


Figure 5.13: Evolution of the separated aggregate spectra and spectral parameters during processing from CF solution at (a) 5 °C and (b) 25 °C substrate temperature. Top panels show 2D heat maps of absorption and PL normalized to the respective maximum value. Bottom panels show normalized aggregate fraction or normalized PL intensity, 0–0/0–1 peak ratio and line width for absorption (black) and PL (blue). Different stages of aggregation are indicated by the coloured areas.

Interestingly, $T_{c,solution}$ and $T_{c,fil m}$ do not match. Processing from CF at $T_{substrate} = 15\text{ °C}$ results in better ordered films compared to expectation, shifting $T_{c,fil m}$ to higher temperatures. For THF, the situation is opposite, as less order is observed for $T_{substrate} = 35\text{ °C}$ than expected, shifting $T_{c,fil m}$ to lower temperatures.

We utilized in situ spectroscopy to examine this discrepancy. To get a basic understanding, we started the investigation at $T_{substrate}$ well below and above $T_{c,solution}$. For evaluation, we separated the spectra of the aggregated contributions and fitted them alike in Figure 5.12 b for each detection frame. For processing from CF solution at $T_{substrate} = 5\text{ °C}$ and $T_{substrate} = 25\text{ °C}$, Figure 5.13 shows 2D heat maps of the separated aggregate spectra along with the extracted normalized evolution of the aggregate intensities, the 0–0/0–1 peak ratios and the line width. At $T_{substrate} = 5\text{ °C}$, aggregate signatures are visible early on, and a two-step process is evident from the optical parameters. In particular, the 0–0/0–1 peak ratios in

emission and σ in absorption vary slowly up to 5.4 s, where a kink is visible and speeds up the overall evolution. We determine the corresponding time t_{quench} of the kink by the intersection of linear fits. Furthermore, t_{start} denotes the time where aggregate absorption reaches 3% of its final value for the first time, generally allowing for reliable fitting. At t_{final} no further changes occur. In contrast, no aggregates are discernible for $T_{\text{substrate}} = 25^\circ\text{C}$ in the beginning, until aggregate signatures quickly appear between 1.5 s and 2.0 s. This suggests that two distinct aggregation pathways exist.

For $T_{\text{substrate}} = 5^\circ\text{C}$, the blue area between t_{start} and t_{quench} indicates the formation of stabilized aggregates in the still wet film, noticeable by the larger 0–0/0–1 ratios and fairly low σ values. The subsequent orange area between t_{quench} and t_{final} indicates a highly dynamic stage where the morphology is quenched by a rapid increase of concentration due to ongoing evaporation of the solvent. The solution aggregates form in a situation with low steric hindrance that allows more ordered conformations, which is retained in the final film even through the quenching stage. At $T_{\text{substrate}} = 25^\circ\text{C}$, we observe no signs of a solution aggregation process and aggregate formation directly starts with a concentration quench, possibly already influenced by intermolecular steric hindrance, resulting in a shift from intra- to intermolecular interaction and larger conformational disorder. Measurements for other substrate temperatures in CF and THF confirm this picture except the anomalous data points from Figure 5.12 c.

These results can be used to analyse the film formation process for the odd ones. Figure 5.14 a contains the analysis of the separated aggregate spectra for blade coating P3HT from CF at $T_{\text{substrate}} = 15^\circ\text{C}$. Despite aggregate formation being completed within 2 s, a short stabilization period can still be observed between 1.0 s and 1.2 s. Here, formation of solution aggregates can be identified in emission by the initially high and constant 0–0/0–1 ratio and the pronounced kink for σ . In sharp contrast to the situation well below $T_{\text{c,solution}}$, the total amount of solution aggregates and their duration of formation is small. This suggests that it is rather the absence of steric restrictions for the initially formed aggregates, which determines the final film properties. In contrast, for blade coating from THF at $T_{\text{substrate}} = 35^\circ\text{C}$ we observe only a concentration induced aggregation pathway as shown in Figure 5.14 b. Here, it can be rationalized with the increased evaporation rate compared to CF at $T_{\text{substrate}} = 15^\circ\text{C}$, which dominates film formation and suppresses the solution aggregation pathway. If the evaporation rate would be decreased here, we would therefore expect to achieve films with aggregate properties for processing well below $T_{\text{c,solution}}$. Therefore, we repeated this experiment in a solvent rich atmosphere. The evolution of the optical parameters in Figure 5.14 c confirms that the delayed film formation exhibits a short stage of solution aggregation, similar to blade coating from CF at $T_{\text{substrate}} = 15^\circ\text{C}$ in Figure 5.14 a. The results from Figure 5.14 thus underline the crucial importance of timing on the formation of solution aggregates, and thus on the overall film formation dynamics as well as final film properties. Despite our

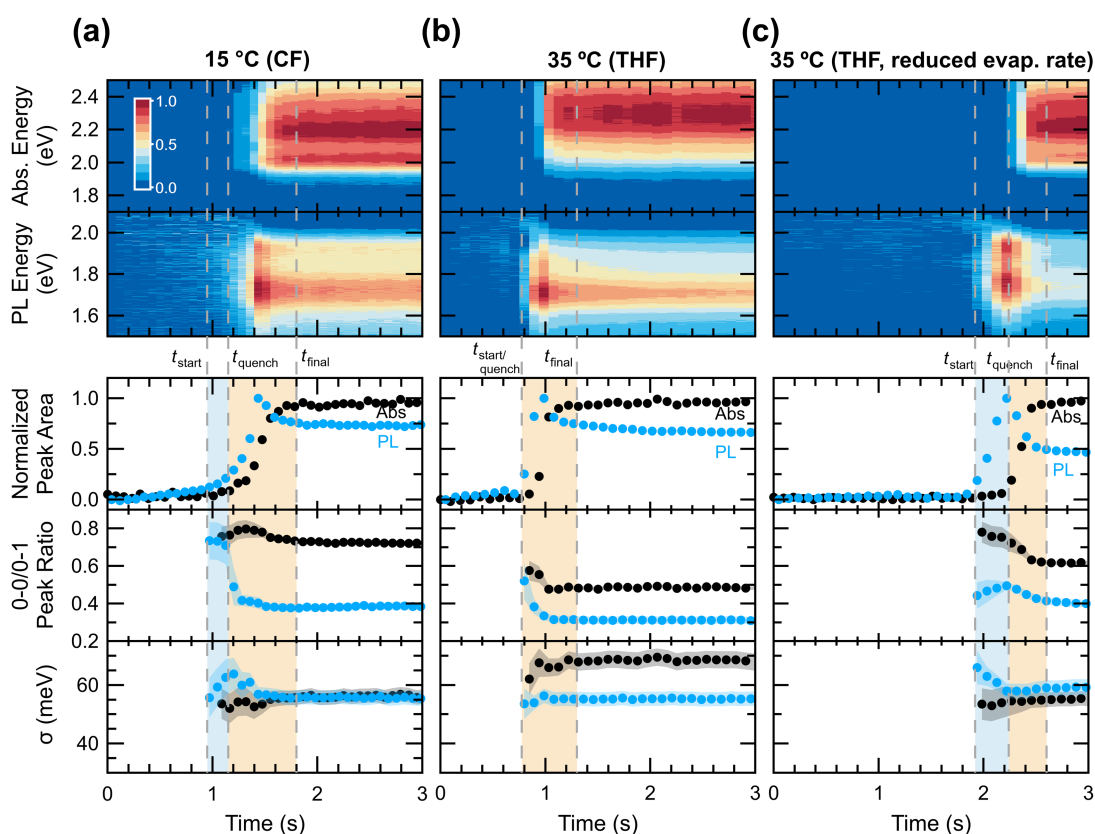


Figure 5.14: Evolution of the separated aggregate spectra and spectral parameters during processing (a) from CF solution at 15 °C substrate temperature and from THF solutions at 35 °C substrate temperature in (b) dry and (c) solvent atmosphere. Top panels show 2D heat maps of absorption and PL normalized to the respective maximum value. Bottom panels show normalized aggregate fraction or normalized PL intensity, 0–0/0–1 peak ratio and line width for absorption (black) and PL (blue). Different stages of aggregation are indicated by the coloured areas.

focus on the single polymer P3HT, we suggest that our approach is generalisable and could thus simplify processing parameter selection for a wide range of conjugated polymers across multiple applications.

5.3 Individual contributions to the publications

The Impact of Driving Force and Temperature on the Electron Transfer in Donor-Acceptor Blend Systems

This work is published in *The Journal of Physical Chemistry C*, **2017**, 121, 22739–22752 and reprinted in Chapter 6. The authors are:

Thomas Unger[#], Stefan Wedler[#], Frank-Julian Kahle, Ullrich Scherf, Heinz Bässler, and Anna Köhler. [#]Authors contributed equally.

Heinz Bässler had the idea for the project. I performed the transient absorption measurements for PCPDTBT:PCBM and PTB7:PCBM blend films. Furthermore, I performed the corresponding measurements for MeLPPP:PCBM in close collaboration with Thomas Unger. Corresponding measurements for the neat films were carried out by Thomas Unger. I extracted all electron transfer rates from the ultrafast transient absorption measurements. In addition, I conducted all doping experiments. The polymer MeLPPP was provided by Ullrich Scherf. Thomas Unger and me discussed the results and thoroughly searched the relevant molecular energies in literature. Frank-Julian Kahle measured the reorganization energy and the energy of the CT state for MeLPPP:PCBM. I calculated all electron transfer rates in the framework of Marcus theory and the Marcus-Levich-Jortner extension. I further raised the idea of the influence of energetic disorder for these calculations. Thomas Unger and me both wrote parts of the manuscript and contributed equally to this work. Anna Köhler and Heinz Bässler critically read and edited the manuscript.

What is the role of planarity and torsional freedom for aggregation in a π -conjugated donor–acceptor model oligomer?

This work is published in *Journal of Materials Chemistry C*, **2020**, 8, 4944–4955 and reprinted in Chapter 7. The authors are:

Stefan Wedler, Axel Bourdick, Stavros Athanasopoulos, Stephan Gekle, Fabian Panzer, Caitlin McDowell, Thuc-Quyen Nguyen, Guillermo C. Bazan, and Anna Köhler.

I designed and organised the study, performed and analysed all experiments, interpreted the data, and wrote and revised major parts of the manuscript. The materials were synthesized by Caitlin McDowell under the supervision of Thuc-Quyen Nguyen and Guillermo C. Bazan. The molecular dynamics calculations were performed by Axel Bourdick and visualised by me. Axel Bourdick and I intensely discussed the simulation results. I coordinated the quantum-chemical calculations between Stavros Athanasopoulos and Axel Bourdick, who both contributed theoretical sections to the manuscript. Stephan Gekle supervised Axel Bourdick and critically read the manuscript. Anna Köhler helped with the interpretation of the datasets and critically edited the manuscript.

Setup to Study the in Situ Evolution of Both Photoluminescence and Absorption during the Processing of Organic or Hybrid Semiconductors

This work is published in *The Journal of Physical Chemistry A*, **2018**, 122, 9115–9122 and reprinted in Chapter 8. The authors are:

Michael Buchhorn, Stefan Wedler, and Fabian Panzer.

Michael Buchhorn designed and built the spin coating system and the detection system in the framework of his bachelor thesis, which was supervised by Fabian Panzer. The test measurements were performed by Fabian Panzer. I measured the photoluminescence quantum yield of the final thin films. I further performed stability measurements of the setup and wrote a Python program with a graphical user interface for data evaluation. All authors contributed in writing of the manuscript.

Role of Torsional Flexibility in the Film Formation Process in Two π -Conjugated Model Oligomers

This work is published in *The Journal of Physical Chemistry Letters*, **2020**, 11, 9379–9386 and reprinted in Chapter 9. The authors are:

Stefan Wedler, *Cheng Zhou, Guillermo C. Bazan, Fabian Panzer, and Anna Köhler.*

I designed the study, performed and analysed all experiments, interpreted the data, and wrote the manuscript. The material was provided by Cheng Zhou and Guillermo C. Bazan. I discussed the data with Fabian Panzer and Anna Köhler. Anna Köhler helped writing and editing the manuscript.

Processing condition dependent aggregation pathways in conjugated polymers

This work is in preparation. The draft is reprinted in Chapter 10. The authors are:

Matthew J Dyson, Hazem Bakr, Stefan Wedler, Konstantin Schötz, Mihirsinh Chauhan, Paul N Stavrinou, Natalie Stingelin, Anna Köhler, Fabian Panzer.

Matthew J Dyson and Hazem Bakr designed the study. Konstantin Schötz determined $T_{c,solution}$ for all processing solutions. In situ experiments were carried out by Matthew J Dyson, Hazem Bakr, Mihir Chauhan and me. In particular, I carried out the experiments for THF at 35 °C. Based on preparatory work from Matthew J Dyson, I developed and performed fitting of all in situ data. Matthew J Dyson, Fabian Panzer and me wrote the manuscript. Paul N Stavrinou, Natalie Stingelin and Anna Köhler supervised work in their respective groups.

References

- [1] Wikipedia. *Samsung Galaxy S Series*. https://en.wikipedia.org/wiki/Samsung_Galaxy_S_series (accessed 08.12.2020).
- [2] S. Berny, N. Blouin, A. Distler, H.-J. Egelhaaf, M. Krompiec, A. Lohr, O. R. Lozman, G. E. Morse, L. Nanson, A. Pron, T. Sauermann, N. Seidler, S. Tierney, P. Tiwana, M. Wagner, and H. Wilson (2016). Solar Trees: First Large-Scale Demonstration of Fully Solution Coated, Semitransparent, Flexible Organic Photovoltaic Modules. *Advanced Science* **3** (5), 1500342.
- [3] F. C. Krebs, S. A. Gevorgyan, and J. Alstrup (2009). A Roll-to-Roll Process to Flexible Polymer Solar Cells: Model Studies, Manufacture and Operational Stability Studies. *Journal of Materials Chemistry* **19** (30), 5442–5451.
- [4] R. Søndergaard, M. Hösel, D. Angmo, T. T. Larsen-Olsen, and F. C. Krebs (2012). Roll-to-Roll Fabrication of Polymer Solar Cells. *Materials Today* **15** (1), 36–49.
- [5] B. Qu and S. R. Forrest (2018). Continuous Roll-to-Roll Fabrication of Organic Photovoltaic Cells via Interconnected High-Vacuum and Low-Pressure Organic Vapor Phase Deposition Systems. *Applied Physics Letters* **113** (5), 053302.
- [6] J. Yang, Y. Lin, W. Zheng, A. Liu, W. Cai, X. Yu, F. Zhang, Q. Liang, H. Wu, D. Qin, and L. Hou (2018). Roll-to-Roll Slot-Die-Printed Polymer Solar Cells by Self-Assembly. *ACS Applied Materials & Interfaces* **10** (26), 22485–22494.
- [7] K. A. Mazzi and C. K. Luscombe (2015). The Future of Organic Photovoltaics. *Chemical Society Reviews* **44** (1), 78–90.
- [8] P. Meredith, W. Li, and A. Armin (2020). Nonfullerene Acceptors: A Renaissance in Organic Photovoltaics? *Advanced Energy Materials* **10** (33), 2001788.
- [9] Q. Liu, Y. Jiang, K. Jin, J. Qin, J. Xu, W. Li, J. Xiong, J. Liu, Z. Xiao, K. Sun, S. Yang, X. Zhang, and L. Ding (2020). 18% Efficiency Organic Solar Cells. *Science Bulletin* **65** (4), 272–275.
- [10] A. Köhler and H. Bässler (2015). *Electronic Processes in Organic Semiconductors: An Introduction*. Weinheim, Germany: Wiley-VCH Verlag GmbH & Co. KGaA.
- [11] M. Pope and C. E. Swenberg (1982). *Electronic Processes in Organic Crystals*. Oxford: Clarendon Press.
- [12] H. Bässler (1993). Charge Transport in Disordered Organic Photoconductors a Monte Carlo Simulation Study. *physica status solidi (b)* **175** (1), 15–56.
- [13] I. W. Hamley (2007). *Introduction to Soft Matter: Synthetic and Biological Self-Assembly Materials*. Revised Edition. West Sussex, England: John Wiley & Sons, Ltd.

- [14] C. Deibel, T. Strobel, and V. Dyakonov (2010). Role of the Charge Transfer State in Organic Donor-Acceptor Solar Cells. *Advanced Materials* **22** (37), 4097–4111.
- [15] D. Moseguí González, C. J. Schaffer, S. Pröller, J. Schlipf, L. Song, S. Bernstorff, E. M. Herzig, and P. Müller-Buschbaum (2017). Codependence between Crystalline and Photovoltage Evolutions in P3HT:PCBM Solar Cells Probed with in-Operando GIWAXS. *ACS Applied Materials & Interfaces* **9** (4), 3282–3287.
- [16] F.-J. Kahle, C. Saller, S. Olthof, C. Li, J. Lebert, S. Weiß, E. M. Herzig, S. Hüttner, K. Meerholz, P. Stroehriegl, and A. Köhler (2018). Does Electron Delocalization Influence Charge Separation at Donor–Acceptor Interfaces in Organic Photovoltaic Cells? *The Journal of Physical Chemistry C* **122** (38), 21792–21802.
- [17] G. Feng, J. Li, Y. He, W. Zheng, J. Wang, C. Li, Z. Tang, A. Osvet, N. Li, C. J. Brabec, Y. Yi, H. Yan, and W. Li (2019). Thermal-Driven Phase Separation of Double-Cable Polymers Enables Efficient Single-Component Organic Solar Cells. *Joule* **3** (7), 1765–1781.
- [18] N. Gasparini, S. Kahmann, M. Salvador, J. D. Perea, A. Sperlich, A. Baumann, N. Li, S. Rechberger, E. Spiecker, V. Dyakonov, G. Portale, M. A. Loi, C. J. Brabec, and T. Ameri (2019). Favorable Mixing Thermodynamics in Ternary Polymer Blends for Realizing High Efficiency Plastic Solar Cells. *Advanced Energy Materials* **9** (19), 1803394.
- [19] Y. Huang, S. Westenhoff, I. Avilov, P. Sreearunothai, J. M. Hodgkiss, C. Deleener, R. H. Friend, and D. Beljonne (2008). Electronic Structures of Interfacial States Formed at Polymeric Semiconductor Heterojunctions. *Nature Materials* **7** (6), 483–489.
- [20] T. A. Papadopoulos, L. Muccioli, S. Athanasopoulos, A. B. Walker, C. Zannoni, and D. Beljonne (2011). Does Supramolecular Ordering Influence Exciton Transport in Conjugated Systems? Insight from Atomistic Simulations. *Chemical Science* **2** (6), 1025–1032.
- [21] X. Liu, B. P. Rand, and S. R. Forrest (2019). Engineering Charge-Transfer States for Efficient, Low-Energy-Loss Organic Photovoltaics. *Trends in Chemistry* **1** (9), 815–829.
- [22] M. T. Dang, L. Hirsch, G. Wantz, and J. D. Wuest (2013). Controlling the Morphology and Performance of Bulk Heterojunctions in Solar Cells. Lessons Learned from the Benchmark Poly(3-Hexylthiophene):[6,6]-Phenyl-C61-Butyric Acid Methyl Ester System. *Chemical Reviews* **113** (5), 3734–3765.
- [23] M. Schubert, D. Dolfen, J. Frisch, S. Roland, R. Steyrlleuthner, B. Stiller, Z. Chen, U. Scherf, N. Koch, A. Facchetti, and D. Neher (2012). Influence of Aggregation on the Performance of All-Polymer Solar Cells Containing Low-Bandgap Naphthalenediimide Copolymers. *Advanced Energy Materials* **2** (3), 369–380.
- [24] N. D. Treat, P. Westacott, and N. Stingelin (2015). The Power of Materials Science Tools for Gaining Insights into Organic Semiconductors. *Annual Review of Materials Research* **45** (1), 459–490.
- [25] L. J. Richter, D. M. DeLongchamp, and A. Amassian (2017). Morphology Development in Solution-Processed Functional Organic Blend Films: An In Situ Viewpoint. *Chemical Reviews* **117** (9), 6332–6366.

-
- [26] T. Holstein (1959). Studies of Polaron Motion: Part I. The Molecular-Crystal Model. *Annals of Physics* **8** (3), 325–342.
- [27] T. Holstein (1959). Studies of Polaron Motion: Part II. The "Small" Polaron. *Annals of Physics* **8** (3), 343–389.
- [28] I. Austin and N. Mott (1969). Polarons in Crystalline and Non-Crystalline Materials. *Advances in Physics* **18** (71), 41–102.
- [29] R. A. Marcus (1960). Exchange Reactions and Electron Transfer Reactions Including Isotopic Exchange. Theory of Oxidation-Reduction Reactions Involving Electron Transfer. Part 4.—A Statistical-Mechanical Basis for Treating Contributions from Solvent, Ligands, and Inert Salt. *Discussions of the Faraday Society* **29**, 21–31.
- [30] R. A. Marcus (1993). Electron Transfer Reactions in Chemistry. Theory and Experiment. *Reviews of Modern Physics* **65** (3), 599–610.
- [31] J. Jortner (1976). Temperature Dependent Activation Energy for Electron Transfer between Biological Molecules. *The Journal of Chemical Physics* **64** (12), 4860–4867.
- [32] N. R. Kestner, J. Logan, and J. Jortner (1974). Thermal Electron Transfer Reactions in Polar Solvents. *The Journal of Physical Chemistry* **78** (21), 2148–2166.
- [33] R. Marcus and N. Sutin (1985). Electron Transfers in Chemistry and Biology. *Biochimica et Biophysica Acta (BBA) - Reviews on Bioenergetics* **811** (3), 265–322.
- [34] G. L. Closs and J. R. Miller (1988). Intramolecular Long-Distance Electron Transfer in Organic Molecules. *Science* **240** (4851), 440–447.
- [35] S. Fukuzumi, K. Ohkubo, H. Imahori, and D. M. Guldi (2003). Driving Force Dependence of Intermolecular Electron-Transfer Reactions of Fullerenes. *Chemistry - A European Journal* **9** (7), 1585–1593.
- [36] V. Coropceanu, J. Cornil, D. A. da Silva Filho, Y. Olivier, R. Silbey, and J.-L. Brédas (2007). Charge Transport in Organic Semiconductors. *Chemical Reviews* **107** (4), 926–952.
- [37] I. I. Fishchuk, A. Kadashchuk, S. T. Hoffmann, S. Athanasopoulos, J. Genoe, H. Bässler, and A. Köhler (2013). Unified Description for Hopping Transport in Organic Semiconductors Including Both Energetic Disorder and Polaronic Contributions. *Physical Review B* **88** (12), 125202.
- [38] S. Cook, R. Katoh, and A. Furube (2009). Ultrafast Studies of Charge Generation in PCBM:P3HT Blend Films Following Excitation of the Fullerene PCBM. *The Journal of Physical Chemistry C* **113** (6), 2547–2552.
- [39] A. J. Ward, A. Ruseckas, M. M. Kareem, B. Ebenhoch, L. A. Serrano, M. Al-Eid, B. Fitzpatrick, V. M. Rotello, G. Cooke, and I. D. W. Samuel (2015). The Impact of Driving Force on Electron Transfer Rates in Photovoltaic Donor-Acceptor Blends. *Advanced Materials* **27** (15), 2496–2500.
- [40] D. C. Coffey, B. W. Larson, A. W. Hains, J. B. Whitaker, N. Kopidakis, O. V. Boltalina, S. H. Strauss, and G. Rumbles (2012). An Optimal Driving Force for Converting Excitons into Free Carriers in Excitonic Solar Cells. *The Journal of Physical Chemistry C* **116** (16), 8916–8923.

- [41] K. Vandewal, K. Tvingstedt, A. Gadisa, O. Inganäs, and J. V. Manca (2010). Relating the Open-Circuit Voltage to Interface Molecular Properties of Donor:Acceptor Bulk Heterojunction Solar Cells. *Physical Review B* **81** (12), 125204.
- [42] I. R. Gould, D. Noukakis, L. Gomez-Jahn, R. H. Young, J. L. Goodman, and S. Farid (1993). Radiative and Nonradiative Electron Transfer in Contact Radical-Ion Pairs. *Chemical Physics* **176** (2), 439–456.
- [43] R. A. J. Janssen and J. Nelson (2013). Factors Limiting Device Efficiency in Organic Photovoltaics. *Advanced Materials* **25** (13), 1847–1858.
- [44] K. Vandewal (2016). Interfacial Charge Transfer States in Condensed Phase Systems. *Annual Review of Physical Chemistry* **67** (1), 113–133.
- [45] W. Zhao, D. Qian, S. Zhang, S. Li, O. Inganäs, F. Gao, and J. Hou (2016). Fullerene-Free Polymer Solar Cells with over 11% Efficiency and Excellent Thermal Stability. *Advanced Materials* **28** (23), 4734–4739.
- [46] K. Vandewal, J. Benduhn, K. S. Schellhammer, T. Vangerven, J. E. Rückert, F. Piersimoni, R. Scholz, O. Zeika, Y. Fan, S. Barlow, D. Neher, S. R. Marder, J. Manca, D. Spoltore, G. Cuniberti, and F. Ortman (2017). Absorption Tails of Donor:C60 Blends Provide Insight into Thermally Activated Charge-Transfer Processes and Polaron Relaxation. *Journal of the American Chemical Society* **139** (4), 1699–1704.
- [47] F.-J. Kahle, A. Rudnick, H. Bässler, and A. Köhler (2018). How to Interpret Absorption and Fluorescence Spectra of Charge Transfer States in an Organic Solar Cell. *Materials Horizons* **5** (5), 837–848.
- [48] B. Kaduk, T. Kowalczyk, and T. Van Voorhis (2012). Constrained Density Functional Theory. *Chemical Reviews* **112** (1), 321–370.
- [49] T. Liu and A. Troisi (2011). Absolute Rate of Charge Separation and Recombination in a Molecular Model of the P3HT/PCBM Interface. *The Journal of Physical Chemistry C* **115** (5), 2406–2415.
- [50] C. Leng, H. Qin, Y. Si, and Y. Zhao (2014). Theoretical Prediction of the Rate Constants for Exciton Dissociation and Charge Recombination to a Triplet State in PCPDTBT with Different Fullerene Derivatives. *The Journal of Physical Chemistry C* **118** (4), 1843–1855.
- [51] Y. Yi, V. Coropceanu, and J.-L. Brédas (2011). A Comparative Theoretical Study of Exciton-Dissociation and Charge-Recombination Processes in Oligothiophene/Fullerene and Oligothiophene/Perylenediimide Complexes for Organic Solar Cells. *Journal of Materials Chemistry* **21** (5), 1479–1486.
- [52] J. Shi, A. Isakova, A. Abudulimu, M. VAN DEN Berg, O. K. Kwon, A. J. Meixner, S. Y. Park, D. Zhang, J. Gierschner, and L. Lüer (2018). Designing High Performance All-Small-Molecule Solar Cells with Non-Fullerene Acceptors: Comprehensive Studies on Photoexcitation Dynamics and Charge Separation Kinetics. *Energy & Environmental Science* **11** (1), 211–220.
- [53] P. F. Barbara, T. J. Meyer, and M. A. Ratner (1996). Contemporary Issues in Electron Transfer Research. *The Journal of Physical Chemistry* **100** (31), 13148–13168.

-
- [54] J. Liu, S. Chen, D. Qian, B. Gautam, G. Yang, J. Zhao, J. Bergqvist, F. Zhang, W. Ma, H. Ade, O. Inganäs, K. Gundogdu, F. Gao, and H. Yan (2016). Fast Charge Separation in a Non-Fullerene Organic Solar Cell with a Small Driving Force. *Nature Energy* **1** (7), 16089.
- [55] G. Grancini, M. Maiuri, D. Fazzi, A. Petrozza, H.-J. Egelhaaf, D. Brida, G. Cerullo, and G. Lanzani (2013). Hot Exciton Dissociation in Polymer Solar Cells. *Nature Materials* **12** (1), 29–33.
- [56] K. Chen, A. J. Barker, M. E. Reish, K. C. Gordon, and J. M. Hodgkiss (2013). Broadband Ultrafast Photoluminescence Spectroscopy Resolves Charge Photogeneration via Delocalized Hot Excitons in Polymer:Fullerene Photovoltaic Blends. *Journal of the American Chemical Society* **135** (49), 18502–18512.
- [57] A. C. Jakowetz, M. L. Böhm, J. Zhang, A. Sadhanala, S. Huettner, A. A. Bakulin, A. Rao, and R. H. Friend (2016). What Controls the Rate of Ultrafast Charge Transfer and Charge Separation Efficiency in Organic Photovoltaic Blends. *Journal of the American Chemical Society* **138** (36), 11672–11679.
- [58] O. V. Kozlov, V. G. Pavelyev, H. D. de Gier, R. W. A. Havenith, P. H. M. van Loosdrecht, J. C. Hummelen, and M. S. Pshenichnikov (2016). Ultrafast Electron and Hole Transfer in Bulk Heterojunctions of Low-Bandgap Polymers. *Organic Photonics and Photovoltaics* **4** (1), 24–34.
- [59] S. M. Falke, C. A. Rozzi, D. Brida, M. Maiuri, M. Amato, E. Sommer, A. De Sio, A. Rubio, G. Cerullo, E. Molinari, and C. Lienau (2014). Coherent Ultrafast Charge Transfer in an Organic Photovoltaic Blend. *Science* **344** (6187), 1001–1005.
- [60] V. Abramavicius, V. Pranculis, A. Melianas, O. Inganäs, V. Gulbinas, and D. Abramavicius (2016). Role of Coherence and Delocalization in Photo-Induced Electron Transfer at Organic Interfaces. *Scientific Reports* **6** (1), 32914.
- [61] J.-L. Brédas, E. H. Sargent, and G. D. Scholes (2017). Photovoltaic Concepts Inspired by Coherence Effects in Photosynthetic Systems. *Nature Materials* **16** (1), 35–44.
- [62] S. Albrecht, K. Vandewal, J. R. Tumbleston, F. S. U. Fischer, J. D. Douglas, J. M. J. Fréchet, S. Ludwigs, H. Ade, A. Salleo, and D. Neher (2014). On the Efficiency of Charge Transfer State Splitting in Polymer:Fullerene Solar Cells. *Advanced Materials* **26** (16), 2533–2539.
- [63] K. Vandewal, S. Albrecht, E. T. Hoke, K. R. Graham, J. Widmer, J. D. Douglas, M. Schubert, W. R. Mateker, J. T. Bloking, G. F. Burkhard, A. Sellinger, J. M. J. Fréchet, A. Amassian, M. K. Riede, M. D. McGehee, D. Neher, and A. Salleo (2014). Efficient Charge Generation by Relaxed Charge-Transfer States at Organic Interfaces. *Nature Materials* **13** (1), 63–68.
- [64] J. Kurpiers, T. Ferron, S. Roland, M. Jakoby, T. Thiede, F. Jaiser, S. Albrecht, S. Janietz, B. A. Collins, I. A. Howard, and D. Neher (2018). Probing the Pathways of Free Charge Generation in Organic Bulk Heterojunction Solar Cells. *Nature Communications* **9** (1).
- [65] H. Haken and H. C. Wolf (2006). *Molekulphysik und Quantenchemie*. 5. Auflage. Berlin: Springer.

- [66] W. Siebrand (1967). Radiationless Transitions in Polyatomic Molecules. I. Calculation of Franck-Condon Factors. *The Journal of Chemical Physics* **46** (2), 440–447.
- [67] M. Kasha (1950). Characterization of Electronic Transitions in Complex Molecules. *Discussions of the Faraday Society* **9**, 14–19.
- [68] P. K. H. Ho, J.-S. Kim, N. Tessler, and R. H. Friend (2001). Photoluminescence of Poly(p-Phenylenevinylene)–Silica Nanocomposites: Evidence for Dual Emission by Franck–Condon Analysis. *The Journal of Chemical Physics* **115** (6), 2709–2720.
- [69] J. B. Birks and D. J. Dyson (1963). The Relations between the Fluorescence and Absorption Properties of Organic Molecules. *Proceedings of the Royal Society of London. Series A. Mathematical and Physical Sciences* **275** (1360), 135–148.
- [70] S. J. Strickler and R. A. Berg (1962). Relationship between Absorption Intensity and Fluorescence Lifetime of Molecules. *The Journal of Chemical Physics* **37** (4), 814–822.
- [71] J. Gierschner, H.-G. Mack, L. Lüer, and D. Oelkrug (2002). Fluorescence and Absorption Spectra of Oligophenylenevinylenes: Vibronic Coupling, Band Shapes, and Solvatochromism. *The Journal of Chemical Physics* **116** (19), 8596.
- [72] J. Gierschner, H.-G. Mack, D. Oelkrug, I. Waldner, and H. Rau (2004). Modeling of the Optical Properties of Cofacial Chromophore Pairs: Stilbenophane. *The Journal of Physical Chemistry A* **108** (2), 257–263.
- [73] A. L. T. Khan, P. Sreearunothai, L. M. Herz, M. J. Banach, and A. Köhler (2004). Morphology-Dependent Energy Transfer within Polyfluorene Thin Films. *Physical Review B* **69** (8), 085201.
- [74] S. T. Hoffmann, H. Bässler, and A. Köhler (2010). What Determines Inhomogeneous Broadening of Electronic Transitions in Conjugated Polymers? *The Journal of Physical Chemistry B* **114** (51), 17037–17048.
- [75] A. Köhler, S. T. Hoffmann, and H. Bässler (2012). An Order–Disorder Transition in the Conjugated Polymer MEH-PPV. *Journal of the American Chemical Society* **134** (28), 11594–11601.
- [76] H. Yamagata, N. J. Hestand, F. C. Spano, A. Köhler, C. Scharsich, S. T. Hoffmann, and H. Bässler (2013). The Red-Phase of Poly[2-Methoxy-5-(2-Ethylhexyloxy)-1,4-Phenylenevinylene] (MEH-PPV): A Disordered HJ-Aggregate. *The Journal of Chemical Physics* **139** (11), 114903.
- [77] M. Reichenberger, J. A. Love, A. Rudnick, S. Bagnich, F. Panzer, A. Stradomska, G. C. Bazan, T.-Q. Nguyen, and A. Köhler (2016). The Effect of Intermolecular Interaction on Excited States in p-DTS(FBTTh₂)₂. *The Journal of Chemical Physics* **144** (7), 074904.
- [78] A. Rudnick, C. Wetzels, S. Tscheuschner, H. Schmalz, A. Vogt, A. Greiner, H. Bässler, E. Mena-Osteritz, P. Bäuerle, and A. Köhler (2017). Spectroscopic Study of Thiophene-Pyrrole-Containing S,N-Heteroheptacenes Compared to Acenes and Phenacenes. *The Journal of Physical Chemistry B* **121** (31), 7492–7501.
- [79] M. Kasha (1963). Energy Transfer Mechanisms and the Molecular Exciton Model for Molecular Aggregates. *Radiation Research* **20** (1), 55–70.

-
- [80] M. Kasha, H. R. Rawls, and M. Ashraf El-Bayoumi (1965). The Exciton Model in Molecular Spectroscopy. *Pure and Applied Chemistry* **11** (3-4), 371–392.
- [81] E. E. Jelley (1936). Spectral Absorption and Fluorescence of Dyes in the Molecular State. *Nature* **138** (3502), 1009–1010.
- [82] G. Scheibe (1937). Über die Veränderlichkeit der Absorptionsspektren in Lösungen und die Nebenvalenzen als ihre Ursache. *Angewandte Chemie* **50** (11), 212–219.
- [83] F. Würthner, T. E. Kaiser, and C. R. Saha-Möller (2011). J-Aggregates: From Serendipitous Discovery to Supramolecular Engineering of Functional Dye Materials. *Angewandte Chemie International Edition* **50** (15), 3376–3410.
- [84] J. B. Birks, D. J. Dyson, and I. H. Munro (1963). 'Excimer' Fluorescence II. Lifetime Studies of Pyrene Solutions. *Proceedings of the Royal Society of London. Series A. Mathematical and Physical Sciences* **275** (1363), 575–588.
- [85] J. Birks and L. Christophorou (1963). Excimer Fluorescence Spectra of Pyrene Derivatives. *Spectrochimica Acta* **19** (2), 401–410.
- [86] J. B. Birks, M. D. Lumb, and I. H. Munro (1964). 'Excimer' Fluorescence V. Influence of Solvent Viscosity and Temperature. *Proceedings of the Royal Society of London. Series A. Mathematical and Physical Sciences* **280** (1381), 289–297.
- [87] A. T. Haedler, H. Misslitz, C. Buehlmeier, R. Q. Albuquerque, A. Köhler, and H.-W. Schmidt (2013). Controlling the π -Stacking Behavior of Pyrene Derivatives: Influence of H-Bonding and Steric Effects in Different States of Aggregation. *ChemPhysChem* **14** (9), 1818–1829.
- [88] J. Gierschner and S. Y. Park (2013). Luminescent Distyrylbenzenes: Tailoring Molecular Structure and Crystalline Morphology. *Journal of Materials Chemistry C* **1** (37), 5818.
- [89] F. C. Spano (2005). Modeling Disorder in Polymer Aggregates: The Optical Spectroscopy of Regioregular Poly(3-Hexylthiophene) Thin Films. *The Journal of Chemical Physics* **122** (23), 234701.
- [90] F. C. Spano (2010). The Spectral Signatures of Frenkel Polarons in H- and J-Aggregates. *Accounts of Chemical Research* **43** (3), 429–439.
- [91] H. Yamagata and F. C. Spano (2012). Interplay between Intrachain and Interchain Interactions in Semiconducting Polymer Assemblies: The HJ-Aggregate Model. *The Journal of Chemical Physics* **136** (18), 184901.
- [92] N. J. Hestand and F. C. Spano (2018). Expanded Theory of H- and J-Molecular Aggregates: The Effects of Vibronic Coupling and Intermolecular Charge Transfer. *Chemical Reviews* **118** (15), 7069–7163.
- [93] R. Tempelaar, A. Stradomska, J. Knoester, and F. C. Spano (2013). Anatomy of an Exciton: Vibrational Distortion and Exciton Coherence in H- and J-Aggregates. *The Journal of Physical Chemistry B* **117** (1), 457–466.
- [94] J. Clark, C. Silva, R. H. Friend, and F. C. Spano (2007). Role of Intermolecular Coupling in the Photophysics of Disordered Organic Semiconductors: Aggregate Emission in Regioregular Polythiophene. *Physical Review Letters* **98** (20), 206406.

- [95] J. Clark, J.-F. Chang, F. C. Spano, R. H. Friend, and C. Silva (2009). Determining Exciton Bandwidth and Film Microstructure in Polythiophene Films Using Linear Absorption Spectroscopy. *Applied Physics Letters* **94** (16), 163306.
- [96] H. Yamagata, C. M. Pochas, and F. C. Spano (2012). Designing J- and H-Aggregates through Wave Function Overlap Engineering: Applications to Poly(3-Hexylthiophene). *The Journal of Physical Chemistry B* **116** (49), 14494–14503.
- [97] H. Yamagata, D. S. Maxwell, J. Fan, K. R. Kittilstved, A. L. Briseno, M. D. Barnes, and F. C. Spano (2014). HJ-Aggregate Behavior of Crystalline 7,8,15,16-Tetraazaterrylene: Introducing a New Design Paradigm for Organic Materials. *The Journal of Physical Chemistry C* **118** (49), 28842–28854.
- [98] N. J. Hestand and F. C. Spano (2015). Interference between Coulombic and CT-Mediated Couplings in Molecular Aggregates: H- to J-Aggregate Transformation in Perylene-Based π -Stacks. *The Journal of Chemical Physics* **143** (24), 244707.
- [99] N. J. Hestand and F. C. Spano (2017). Molecular Aggregate Photophysics beyond the Kasha Model: Novel Design Principles for Organic Materials. *Accounts of Chemical Research* **50** (2), 341–350.
- [100] V. Rühle, A. Lukyanov, F. May, M. Schrader, T. Vehoff, J. Kirkpatrick, B. Baumeier, and D. Andrienko (2011). Microscopic Simulations of Charge Transport in Disordered Organic Semiconductors. *Journal of Chemical Theory and Computation* **7** (10), 3335–3345.
- [101] K. M. Pelzer and S. B. Darling (2016). Charge Generation in Organic Photovoltaics: A Review of Theory and Computation. *Molecular Systems Design & Engineering* **1** (1), 10–24.
- [102] G. Gryn'ova, K.-H. Lin, and C. Corminboeuf (2018). Read between the Molecules: Computational Insights into Organic Semiconductors. *Journal of the American Chemical Society* **140** (48), 16370–16386.
- [103] G. Han, Y. Yi, and Z. Shuai (2018). From Molecular Packing Structures to Electronic Processes: Theoretical Simulations for Organic Solar Cells. *Advanced Energy Materials* **8** (28), 1702743.
- [104] J. K. Politis, F. B. Somoza, J. W. Kampf, M. D. Curtis, L. G. Ronda, and D. C. Martin (1999). A Comparison of Structures and Optoelectronic Properties of Oxygen- and Sulfur-Containing Heterocycles: Conjugated Nonylbisoxazole and Nonylbithiazole Oligomers. *Chemistry of Materials* **11** (8), 2274–2284.
- [105] J. J. Apperloo, R. A. J. Janssen, P. R. L. Malenfant, and J. M. J. Fréchet (2000). Concentration-Dependent Thermochromism and Supramolecular Aggregation in Solution of Triblock Copolymers Based on Lengthy Oligothiophene Cores and Poly(Benzyl Ether) Dendrons. *Macromolecules* **33** (19), 7038–7043.
- [106] C. Scharsich, R. H. Lohwasser, M. Sommer, U. Asawapirom, U. Scherf, M. Thelakkat, D. Neher, and A. Köhler (2012). Control of Aggregate Formation in Poly(3-Hexylthiophene) by Solvent, Molecular Weight, and Synthetic Method. *Journal of Polymer Science Part B: Polymer Physics* **50** (6), 442–453.

- [107] F. Panzer, H. Bässler, R. Lohwasser, M. Thelakkat, and A. Köhler (2014). The Impact of Polydispersity and Molecular Weight on the Order–Disorder Transition in Poly(3-Hexylthiophene). *The Journal of Physical Chemistry Letters* **5** (15), 2742–2747.
- [108] F. Panzer, M. Sommer, H. Bässler, M. Thelakkat, and A. Köhler (2015). Spectroscopic Signature of Two Distinct H-Aggregate Species in Poly(3-Hexylthiophene). *Macromolecules* **48** (5), 1543–1553.
- [109] M. Yan, L. J. Rothberg, E. W. Kwock, and T. M. Miller (1995). Interchain Excitations in Conjugated Polymers. *Physical Review Letters* **75** (10), 1992–1995.
- [110] C. J. Collison, L. J. Rothberg, V. Treemanekarn, and Y. Li (2001). Conformational Effects on the Photophysics of Conjugated Polymers: A Two Species Model for MEH-PPV Spectroscopy and Dynamics. *Macromolecules* **34** (7), 2346–2352.
- [111] C. De Leener, E. Hennebicq, J.-C. Sancho-Garcia, and D. Beljonne (2009). Modeling the Dynamics of Chromophores in Conjugated Polymers: The Case of Poly(2-Methoxy-5-(2'-Ethylhexyl)Oxy 1,4-Phenylene Vinylene) (MEH-PPV). *The Journal of Physical Chemistry B* **113** (5), 1311–1322.
- [112] T. E. Kaiser, V. Stepanenko, and F. Würthner (2009). Fluorescent J-Aggregates of Core-Substituted Perylene Bisimides: Studies on Structure-Property Relationship, Nucleation-Elongation Mechanism, and Sergeants-and-Soldiers Principle. *Journal of the American Chemical Society* **131** (19), 6719–6732.
- [113] Q. Yan, Y. Zhou, Y.-Q. Zheng, J. Pei, and D. Zhao (2013). Towards Rational Design of Organic Electron Acceptors for Photovoltaics: A Study Based on Perylenediimide Derivatives. *Chemical Science* **4** (12), 4389–4394.
- [114] Y. Liu, J. Zhao, Z. Li, C. Mu, W. Ma, H. Hu, K. Jiang, H. Lin, H. Ade, and H. Yan (2014). Aggregation and Morphology Control Enables Multiple Cases of High-Efficiency Polymer Solar Cells. *Nature Communications* **5** (1), 5293.
- [115] W. Chen and Q. Zhang (2017). Recent Progress in Non-Fullerene Small Molecule Acceptors in Organic Solar Cells (OSCs). *Journal of Materials Chemistry C* **5** (6), 1275–1302.
- [116] B. McDearmon, E. Lim, I.-H. Lee, L. M. Kozycz, K. O'Hara, P. I. Robledo, N. R. Venkatesan, M. L. Chabynyc, and C. J. Hawker (2018). Effects of Side-Chain Topology on Aggregation of Conjugated Polymers. *Macromolecules* **51** (7), 2580–2590.
- [117] B. McDearmon, Z. A. Page, M. L. Chabynyc, and C. J. Hawker (2018). Organic Electronics by Design: The Power of Minor Atomic and Structural Changes. *Journal of Materials Chemistry C* **6** (14), 3564–3572.
- [118] Y. Yang, Z. Liu, G. Zhang, X. Zhang, and D. Zhang (2019). The Effects of Side Chains on the Charge Mobilities and Functionalities of Semiconducting Conjugated Polymers beyond Solubilities. *Advanced Materials* **31** (46), 1903104.
- [119] D. Qian, L. Ye, M. Zhang, Y. Liang, L. Li, Y. Huang, X. Guo, S. Zhang, Z. Tan, and J. Hou (2012). Design, Application, and Morphology Study of a New Photovoltaic Polymer with Strong Aggregation in Solution State. *Macromolecules* **45** (24), 9611–9617.

- [120] C. Scharsich, F. S. U. Fischer, K. Wilma, R. Hildner, S. Ludwigs, and A. Köhler (2015). Revealing Structure Formation in PCPDTBT by Optical Spectroscopy. *Journal of Polymer Science Part B: Polymer Physics* **53** (20), 1416–1430.
- [121] F. Panzer, H. Bässler, and A. Köhler (2017). Temperature Induced Order–Disorder Transition in Solutions of Conjugated Polymers Probed by Optical Spectroscopy. *The Journal of Physical Chemistry Letters* **8** (1), 114–125.
- [122] A. Kolinski, J. Skolnick, and R. Yaris (1986). The Collapse Transition of Semiflexible Polymers. A Monte Carlo Simulation of a Model System. *The Journal of Chemical Physics* **85** (6), 3585–3597.
- [123] I. C. Sanchez (1979). Phase Transition Behavior of the Isolated Polymer Chain. *Macromolecules* **12** (5), 980–988.
- [124] C. W. Cone, R. R. Cheng, D. E. Makarov, and D. A. Vanden Bout (2011). Molecular Weight Effect on the Formation of β Phase Poly(9,9'-Diocetylfluorene) in Dilute Solutions. *The Journal of Physical Chemistry B* **115** (43), 12380–12385.
- [125] T. J. Fauvell, T. Zheng, N. E. Jackson, M. A. Ratner, L. Yu, and L. X. Chen (2016). Photophysical and Morphological Implications of Single-Strand Conjugated Polymer Folding in Solution. *Chemistry of Materials* **28** (8), 2814–2822.
- [126] J. Wollmann, F.-J. Kahle, I. Bauer, A. Köhler, and P. Strohhriegl (2020). Versatile Approach to Well-Defined Oligofluorenes and Polyfluorenes with Low Dispersity. *Macromolecules* **53** (22), 10137–10146.
- [127] Y. D. Park, H. S. Lee, Y. J. Choi, D. Kwak, J. H. Cho, S. Lee, and K. Cho (2009). Solubility-Induced Ordered Polythiophene Precursors for High-Performance Organic Thin-Film Transistors. *Advanced Functional Materials* **19** (8), 1200–1206.
- [128] M. Knaapila, D. W. Bright, R. Stepanyan, M. Torkkeli, L. Almásy, R. Schweins, U. Vainio, E. Preis, F. Galbrecht, U. Scherf, and A. P. Monkman (2011). Network Structure of Polyfluorene Sheets as a Function of Alkyl Side Chain Length. *Physical Review E* **83** (5), 051803.
- [129] F. P. V. Koch, J. Rivnay, S. Foster, C. Müller, J. M. Downing, E. Buchaca-Domingo, P. Westacott, L. Yu, M. Yuan, M. Baklar, Z. Fei, C. Luscombe, M. A. McLachlan, M. Heeney, G. Rumbles, C. Silva, A. Salleo, J. Nelson, P. Smith, and N. Stingelin (2013). The Impact of Molecular Weight on Microstructure and Charge Transport in Semicrystalline Polymer Semiconductors–Poly(3-Hexylthiophene), a Model Study. *Topical Issue on Conductive Polymers* **38** (12), 1978–1989.
- [130] S. Samson, J. Rech, L. Perdígón-Toro, Z. Peng, S. Shoaee, H. Ade, D. Neher, M. Stolterfoht, and W. You (2020). Organic Solar Cells with Large Insensitivity to Donor Polymer Molar Mass across All Acceptor Classes. *ACS Applied Polymer Materials* **2** (11), 5300–5308.
- [131] Y. Chen, X. Wan, and G. Long (2013). High Performance Photovoltaic Applications Using Solution-Processed Small Molecules. *Accounts of Chemical Research* **46** (11), 2645–2655.
- [132] Y. Lin, Y. Li, and X. Zhan (2012). Small Molecule Semiconductors for High-Efficiency Organic Photovoltaics. *Chemical Society Reviews* **41** (11), 4245–4272.

- [133] A. F. Eftaiha, J.-P. Sun, I. G. Hill, and G. C. Welch (2013). Recent Advances of Non-Fullerene, Small Molecular Acceptors for Solution Processed Bulk Heterojunction Solar Cells. *Journal of Materials Chemistry A* **2** (5), 1201–1213.
- [134] Z. Luo, R. Sun, C. Zhong, T. Liu, G. Zhang, Y. Zou, X. Jiao, J. Min, and C. Yang (2020). Altering Alkyl-Chains Branching Positions for Boosting the Performance of Small-Molecule Acceptors for Highly Efficient Nonfullerene Organic Solar Cells. *Science China Chemistry* **63** (3), 361–369.
- [135] Z. Chen, U. Baumeister, C. Tschierske, and F. Würthner (2007). Effect of Core Twisting on Self-Assembly and Optical Properties of Perylene Bisimide Dyes in Solution and Columnar Liquid Crystalline Phases. *Chemistry – A European Journal* **13** (2), 450–465.
- [136] J. Yuan, Y. Zhang, L. Zhou, G. Zhang, H.-L. Yip, T.-K. Lau, X. Lu, C. Zhu, H. Peng, P. A. Johnson, M. Leclerc, Y. Cao, J. Ulanski, Y. Li, and Y. Zou (2019). Single-Junction Organic Solar Cell with over 15% Efficiency Using Fused-Ring Acceptor with Electron-Deficient Core. *Joule* **3** (4), 1140–1151.
- [137] B. Zhao, W. Wang, Y. Xie, H. Zhao, L. Wang, S. Liu, J. Xin, Z. Cong, H. Wu, Q. Liang, W. Ma, C. Gao, H. Wu, and Y. Cao (2020). Efficient Polymer Solar Cells Enabled by Alkoxy-Phenyl Side-Chain-Modified Main-Chain-Twisted Small Molecular Acceptors. *Journal of Materials Chemistry A* **8** (42), 22335–22345.
- [138] F. M. Keheze, D. Raithel, T. Wu, D. Schiefer, M. Sommer, R. Hildner, and G. Reiter (2017). Signatures of Melting and Recrystallization of a Bulky Substituted Poly(Thiophene) Identified by Optical Spectroscopy. *Macromolecules* **50** (17), 6829–6839.
- [139] D. Raithel, L. Simine, S. Pickel, K. Schötz, F. Panzer, S. Baderschneider, D. Schiefer, R. Lohwasser, J. Köhler, M. Thelakkat, M. Sommer, A. Köhler, P. J. Rossky, and R. Hildner (2018). Direct Observation of Backbone Planarization via Side-Chain Alignment in Single Bulky-Substituted Polythiophenes. *Proceedings of the National Academy of Sciences* **115** (11), 2699–2704.
- [140] L. Lu, T. Zheng, Q. Wu, A. M. Schneider, D. Zhao, and L. Yu (2015). Recent Advances in Bulk Heterojunction Polymer Solar Cells. *Chemical Reviews* **115** (23), 12666–12731.
- [141] H. Hu, P. C. Y. Chow, G. Zhang, T. Ma, J. Liu, G. Yang, and H. Yan (2017). Design of Donor Polymers with Strong Temperature-Dependent Aggregation Property for Efficient Organic Photovoltaics. *Accounts of Chemical Research* **50** (10), 2519–2528.
- [142] K. P. Goetz, K. Sekine, F. Paulus, Y. Zhong, D. Roth, D. Becker-Koch, Y. J. Hofstetter, E. Michel, L. Reichert, F. Rominger, M. Rudolph, S. Huettner, Y. Vaynzof, E. M. Herzig, A. S. K. Hashmi, and J. Zaumseil (2019). The Effect of Side-Chain Length on the Microstructure and Processing Window of Zone-Cast Naphthalene-Based Bispentalenes. *Journal of Materials Chemistry C* **7** (43), 13493–13501.
- [143] T. Wang, V. Coropceanu, and J.-L. Brédas (2019). All-Polymer Solar Cells: Impact of the Length of the Branched Alkyl Side Chains on the Polymer Acceptors on the Interchain Packing and Electronic Properties in Amorphous Blends. *Chemistry of Materials* **31** (16), 6239–6248.

- [144] K. Jiang, Q. Wei, J. Y. L. Lai, Z. Peng, H. K. Kim, J. Yuan, L. Ye, H. Ade, Y. Zou, and H. Yan (2019). Alkyl Chain Tuning of Small Molecule Acceptors for Efficient Organic Solar Cells. *Joule* **3** (12), 3020–3033.
- [145] Y. Han, W. Song, J. Zhang, L. Xie, J. Xiao, Y. Li, L. Cao, S. Song, E. Zhou, and Z. Ge (2020). Annealing-Free Efficient Organic Solar Cells via an Alkylbenzene Side-Chain Strategy of Small-Molecule Electron Acceptors. *Journal of Materials Chemistry A*.
- [146] G. C. Welch, R. C. Bakus II, S. J. Teat, and G. C. Bazan (2013). Impact of Regiochemistry and Isoelectronic Bridgehead Substitution on the Molecular Shape and Bulk Organization of Narrow Bandgap Chromophores. *Journal of the American Chemical Society* **135** (6), 2298–2305.
- [147] L. F. Lai, J. A. Love, A. Sharenko, J. E. Coughlin, V. Gupta, S. Tretiak, T.-Q. Nguyen, W.-Y. Wong, and G. C. Bazan (2014). Topological Considerations for the Design of Molecular Donors with Multiple Absorbing Units. *Journal of the American Chemical Society* **136** (15), 5591–5594.
- [148] S. Loser, H. Miyauchi, J. W. Hennek, J. Smith, C. Huang, A. Facchetti, and T. J. Marks (2012). A “Zig-Zag” Naphthodithiophene Core for Increased Efficiency in Solution-Processed Small Molecule Solar Cells. *Chemical Communications* **48** (68), 8511–8513.
- [149] J. A. Love, C. M. Proctor, J. Liu, C. J. Takacs, A. Sharenko, T. S. VAN DER Poll, A. J. Heeger, G. C. Bazan, and T.-Q. Nguyen (2013). Film Morphology of High Efficiency Solution-Processed Small-Molecule Solar Cells. *Advanced Functional Materials* **23** (40), 5019–5026.
- [150] J. A. Love, I. Nagao, Y. Huang, M. Kuik, V. Gupta, C. J. Takacs, J. E. Coughlin, L. Qi, T. S. van der Poll, E. J. Kramer, A. J. Heeger, T.-Q. Nguyen, and G. C. Bazan (2014). Silaindacenodithiophene-Based Molecular Donor: Morphological Features and Use in the Fabrication of Compositionally Tolerant, High-Efficiency Bulk Heterojunction Solar Cells. *Journal of the American Chemical Society* **136** (9), 3597–3606.
- [151] T. S. van der Poll, J. A. Love, T.-Q. Nguyen, and G. C. Bazan (2012). Non-Basic High-Performance Molecules for Solution-Processed Organic Solar Cells. *Advanced Materials* **24** (27), 3646–3649.
- [152] A. Bourdick, M. Reichenberger, A. Stradomska, G. C. Bazan, T.-Q. Nguyen, A. Köhler, and S. Gekle (2018). Elucidating Aggregation Pathways in the Donor–Acceptor Type Molecules p-DTS(FBTTh₂)₂ and p-SIDT(FBTTh₂)₂. *The Journal of Physical Chemistry B* **122** (39), 9191–9201.
- [153] G. Barbarella, M. Zambianchi, A. Bongini, and L. Antolini (1992). Crystal Structure of 4,4',3'',4'''-Tetramethyl-2,2':5',2'':5'',2'''-Tetrathiophene: A Comparison with the Conformation in Solution. *Advanced Materials* **4** (4), 282–285.
- [154] S. Garreau, M. Leclerc, N. Errien, and G. Louarn (2003). Planar-to-Nonplanar Conformational Transition in Thermochromic Polythiophenes: A Spectroscopic Study. *Macromolecules* **36** (3), 692–697.
- [155] J. Kärnbratt, M. Gilbert, J. K. Sprafke, H. L. Anderson, and B. Albinsson (2012). Self-Assembly of Linear Porphyrin Oligomers into Well-Defined Aggregates. *The Journal of Physical Chemistry C* **116** (37), 19630–19635.

-
- [156] T. Unger, F. Panzer, C. Consani, F. Koch, T. Brixner, H. Bässler, and A. Köhler (2015). Ultrafast Energy Transfer between Disordered and Highly Planarized Chains of Poly[2-Methoxy-5-(2-Ethylhexyloxy)-1,4-Phenylenevinylene] (MEH-PPV). *ACS Macro Letters* **4**(4), 412–416.
- [157] M. Reichenberger, D. Kroh, G. M. M. Matrone, K. Schötz, S. Pröller, O. Filonik, M. E. Thordardottir, E. M. Herzig, H. Bässler, N. Stingelin, and A. Köhler (2018). Controlling Aggregate Formation in Conjugated Polymers by Spin-Coating below the Critical Temperature of the Disorder-Order Transition. *Journal of Polymer Science Part B: Polymer Physics* **56**(6), 532–542.
- [158] M. Buchhorn, S. Wedler, and F. Panzer (2018). Setup to Study the in Situ Evolution of Both Photoluminescence and Absorption during the Processing of Organic or Hybrid Semiconductors. *The Journal of Physical Chemistry A* **122**(46), 9115–9122.
- [159] N. E. Jackson, B. M. Savoie, K. L. Kohlstedt, M. Olvera de la Cruz, G. C. Schatz, L. X. Chen, and M. A. Ratner (2013). Controlling Conformations of Conjugated Polymers and Small Molecules: The Role of Nonbonding Interactions. *Journal of the American Chemical Society* **135**(28), 10475–10483.
- [160] T. S. van der Poll, A. Zhugayevych, E. Chertkov, R. C. Bakus, J. E. Coughlin, S. J. Teat, G. C. Bazan, and S. Tretiak (2014). Polymorphism of Crystalline Molecular Donors for Solution-Processed Organic Photovoltaics. *The Journal of Physical Chemistry Letters* **5**(15), 2700–2704.
- [161] W. Zhang, Z. Mao, N. Zheng, J. Zou, L. Wang, C. Wei, J. Huang, D. Gao, and G. Yu (2016). Highly Planar Cross-Conjugated Alternating Polymers with Multiple Conformational Locks: Synthesis, Characterization and Their Field-Effect Properties. *Journal of Materials Chemistry C* **4**(39), 9266–9275.
- [162] H. Huang, L. Yang, A. Facchetti, and T. J. Marks (2017). Organic and Polymeric Semiconductors Enhanced by Noncovalent Conformational Locks. *Chemical Reviews* **117**(15), 10291–10318.
- [163] J. B. Lin, Y. Jin, S. A. Lopez, N. Druckerman, S. E. Wheeler, and K. N. Houk (2017). Torsional Barriers to Rotation and Planarization in Heterocyclic Oligomers of Value in Organic Electronics. *Journal of Chemical Theory and Computation* **13**(11), 5624–5638.
- [164] M. T. Seifrid, S. D. Oosterhout, M. F. Toney, and G. C. Bazan (2018). Kinetic Versus Thermodynamic Orientational Preferences for a Series of Isomorphous Molecular Semiconductors. *ACS Omega* **3**(8), 10198–10204.
- [165] K. J. Thorley and I. McCulloch (2018). Why Are S–F and S–O Non-Covalent Interactions Stabilising? *Journal of Materials Chemistry C* **6**(45), 12413–12421.
- [166] J. E. Coughlin, A. Zhugayevych, R. C. Bakus II, T. S. van der Poll, G. C. Welch, S. J. Teat, G. C. Bazan, and S. Tretiak (2014). A Combined Experimental and Theoretical Study of Conformational Preferences of Molecular Semiconductors. *The Journal of Physical Chemistry C* **118**(29), 15610–15623.

- [167] C. McDowell, K. Narayanaswamy, B. Yadagiri, T. Gayathri, M. Seifrid, R. Datt, S. M. Ryno, M. C. Heifner, V. Gupta, C. Risko, S. P. Singh, and G. C. Bazan (2018). Impact of Rotamer Diversity on the Self-Assembly of Nearly Isostructural Molecular Semiconductors. *Journal of Materials Chemistry A* **6** (2), 383–394.
- [168] W. Ma, G. Yang, K. Jiang, J. H. Carpenter, Y. Wu, X. Meng, T. McAfee, J. Zhao, C. Zhu, C. Wang, H. Ade, and H. Yan (2015). Influence of Processing Parameters and Molecular Weight on the Morphology and Properties of High-Performance PffBT4T-2OD:PC71BM Organic Solar Cells. *Advanced Energy Materials* **5** (23), 1501400.
- [169] Z. Bi, H. B. Naveed, Y. Mao, H. Yan, and W. Ma (2018). Importance of Nucleation during Morphology Evolution of the Blade-Cast PffBT4T-2OD-Based Organic Solar Cells. *Macromolecules* **51** (17), 6682–6691.
- [170] G. Sini, M. Schubert, C. Risko, S. Roland, O. P. Lee, Z. Chen, T. V. Richter, D. Dolfen, V. Coropceanu, S. Ludwigs, U. Scherf, A. Facchetti, J. M. J. Fréchet, and D. Neher (2018). On the Molecular Origin of Charge Separation at the Donor-Acceptor Interface. *Advanced Energy Materials* **8** (12), 1702232.
- [171] F. C. Krebs (2009). Fabrication and Processing of Polymer Solar Cells: A Review of Printing and Coating Techniques. *Solar Energy Materials and Solar Cells* **93** (4), 394–412.
- [172] R. Hildner, A. Köhler, P. Müller-Buschbaum, F. Panzer, and M. Thelakkat (2017). π -Conjugated Donor Polymers: Structure Formation and Morphology in Solution, Bulk and Photovoltaic Blends. *Advanced Energy Materials* **7** (16), 1700314.
- [173] F. C. Krebs, T. Tromholt, and M. Jørgensen (2010). Upscaling of Polymer Solar Cell Fabrication Using Full Roll-to-Roll Processing. *Nanoscale* **2** (6), 873–886.
- [174] J.-F. Chang, B. Sun, D. W. Breiby, M. M. Nielsen, T. I. Sölling, M. Giles, I. McCulloch, and H. Sirringhaus (2004). Enhanced Mobility of Poly(3-Hexylthiophene) Transistors by Spin-Coating from High-Boiling-Point Solvents. *Chemistry of Materials* **16** (23), 4772–4776.
- [175] M. Sanyal, B. Schmidt-Hansberg, M. F. G. Klein, A. Colsmann, C. Munuera, A. Vorobiev, U. Lemmer, W. Schabel, H. Dosch, and E. Barrena (2011). In Situ X-Ray Study of Drying-Temperature Influence on the Structural Evolution of Bulk-Heterojunction Polymer-Fullerene Solar Cells Processed by Doctor-Blading. *Advanced Energy Materials* **1** (3), 363–367.
- [176] M. Abdelsamie, K. Zhao, M. R. Niazi, K. W. Chou, and A. Amassian (2014). In Situ UV-Visible Absorption during Spin-Coating of Organic Semiconductors: A New Probe for Organic Electronics and Photovoltaics. *Journal of Materials Chemistry C* **2** (17), 3373–3381.
- [177] J. Y. Na, B. Kang, D. H. Sin, K. Cho, and Y. D. Park (2015). Understanding Solidification of Polythiophene Thin Films during Spin-Coating: Effects of Spin-Coating Time and Processing Additives. *Scientific Reports* **5** (1), 13288.
- [178] K. Zhao, X. Yu, R. Li, A. Amassian, and Y. Han (2015). Solvent-Dependent Self-Assembly and Ordering in Slow-Drying Drop-Cast Conjugated Polymer Films. *Journal of Materials Chemistry C* **3** (38), 9842–9848.

-
- [179] S. Pröllner, D. Moseguí González, C. Zhu, E. Schaible, C. Wang, P. Müller-Buschbaum, A. Hexemer, and E. M. Herzig (2017). Note: Setup for Chemical Atmospheric Control during in Situ Grazing Incidence X-Ray Scattering of Printed Thin Films. *Review of Scientific Instruments* **88** (6), 066101.
- [180] C. McDowell, M. Abdelsamie, K. Zhao, D.-M. Smilgies, G. C. Bazan, and A. Amassian (2015). Synergistic Impact of Solvent and Polymer Additives on the Film Formation of Small Molecule Blend Films for Bulk Heterojunction Solar Cells. *Advanced Energy Materials* **5** (18), 1501121.
- [181] J. Peet, N. S. Cho, S. K. Lee, and G. C. Bazan (2008). Transition from Solution to the Solid State in Polymer Solar Cells Cast from Mixed Solvents. *Macromolecules* **41** (22), 8655–8659.
- [182] J. Peet, E. Brocker, Y. Xu, and G. C. Bazan (2008). Controlled β -Phase Formation in Poly(9,9-Di-n-Octylfluorene) by Processing with Alkyl Additives. *Advanced Materials* **20** (10), 1882–1885.
- [183] Y. Sun, G. C. Welch, W. L. Leong, C. J. Takacs, G. C. Bazan, and A. J. Heeger (2012). Solution-Processed Small-Molecule Solar Cells with 6.7% Efficiency. *Nature Materials* **11** (1), 44–48.
- [184] S. D. Collins, N. A. Ran, M. C. Heiber, and T.-Q. Nguyen (2017). Small Is Powerful: Recent Progress in Solution-Processed Small Molecule Solar Cells. *Advanced Energy Materials* **7** (10), 1602242.
- [185] Y. Huang, E. J. Kramer, A. J. Heeger, and G. C. Bazan (2014). Bulk Heterojunction Solar Cells: Morphology and Performance Relationships. *Chemical Reviews* **114** (14), 7006–7043.
- [186] L. A. Perez, K. W. Chou, J. A. Love, T. S. VAN DER Poll, D.-M. Smilgies, T.-Q. Nguyen, E. J. Kramer, A. Amassian, and G. C. Bazan (2013). Solvent Additive Effects on Small Molecule Crystallization in Bulk Heterojunction Solar Cells Probed During Spin Casting. *Advanced Materials* **25** (44), 6380–6384.
- [187] L. J. Richter, D. M. DeLongchamp, F. A. Bokel, S. Engmann, K. W. Chou, A. Amassian, E. Schaible, and A. Hexemer (2015). In Situ Morphology Studies of the Mechanism for Solution Additive Effects on the Formation of Bulk Heterojunction Films. *Advanced Energy Materials* **5** (3), 1400975.
- [188] M. Abdelsamie, N. D. Treat, K. Zhao, C. McDowell, M. A. Burgers, R. Li, D.-M. Smilgies, N. Stingelin, G. C. Bazan, and A. Amassian (2015). Toward Additive-Free Small-Molecule Organic Solar Cells: Roles of the Donor Crystallization Pathway and Dynamics. *Advanced Materials* **27** (45), 7285–7292.
- [189] M. Reichenberger, S. Baderschneider, D. Kroh, S. Grauf, J. Köhler, R. Hildner, and A. Köhler (2016). Watching Paint Dry: The Impact of Diiodooctane on the Kinetics of Aggregate Formation in Thin Films of Poly(3-Hexylthiophene). *Macromolecules* **49** (17), 6420–6430.
- [190] E. F. Manley, J. Strzalka, T. J. Fauvell, T. J. Marks, and L. X. Chen (2018). In Situ Analysis of Solvent and Additive Effects on Film Morphology Evolution in Spin-Cast Small-Molecule and Polymer Photovoltaic Materials. *Advanced Energy Materials* **8** (23), 1800611.

- [191] B. W. Boudouris, V. Ho, L. H. Jimison, M. F. Toney, A. Salleo, and R. A. Segalman (2011). Real-Time Observation of Poly(3-Alkylthiophene) Crystallization and Correlation with Transient Optoelectronic Properties. *Macromolecules* **44** (17), 6653–6658.
- [192] G. C. Welch, L. A. Perez, C. V. Hoven, Y. Zhang, X.-D. Dang, A. Sharenko, M. F. Toney, E. J. Kramer, T.-Q. Nguyen, and G. C. Bazan (2011). A Modular Molecular Framework for Utility in Small-Molecule Solution-Processed Organic Photovoltaic Devices. *Journal of Materials Chemistry* **21** (34), 12700–12709.
- [193] B. Lin, X. Zhou, H. Zhao, J. Yuan, K. Zhou, K. Chen, H. Wu, R. Guo, M. A. Scheel, A. Chumakov, S. V. Roth, Y. Mao, L. Wang, Z. Tang, P. Müller-Buschbaum, and W. Ma (2020). Balancing the Pre-Aggregation and Crystallization Kinetics Enables High Efficiency Slot-Die Coated Organic Solar Cells with Reduced Non-Radiative Recombination Losses. *Energy & Environmental Science* **13** (8), 2467–2479.
- [194] H. Zhao, H. B. Naveed, B. Lin, X. Zhou, J. Yuan, K. Zhou, H. Wu, R. Guo, M. A. Scheel, A. Chumakov, S. V. Roth, Z. Tang, P. Müller-Buschbaum, and W. Ma (2020). Hot Hydrocarbon-Solvent Slot-Die Coating Enables High-Efficiency Organic Solar Cells with Temperature-Dependent Aggregation Behavior. *Advanced Materials* **32** (39), 2002302.
- [195] K. H. Hendriks, A. S. G. Wijpkema, J. J. van Franeker, M. M. Wienk, and R. A. J. Janssen (2016). Dichotomous Role of Exciting the Donor or the Acceptor on Charge Generation in Organic Solar Cells. *Journal of the American Chemical Society* **138** (31), 10026–10031.
- [196] B. M. Savoie, A. Rao, A. A. Bakulin, S. Gelinas, B. Movaghar, R. H. Friend, T. J. Marks, and M. A. Ratner (2014). Unequal Partnership: Asymmetric Roles of Polymeric Donor and Fullerene Acceptor in Generating Free Charge. *Journal of the American Chemical Society* **136** (7), 2876–2884.
- [197] J.-L. Brédas, D. Beljonne, V. Coropceanu, and J. Cornil (2004). Charge-Transfer and Energy-Transfer Processes in π -Conjugated Oligomers and Polymers: A Molecular Picture. *Chemical Reviews* **104** (11), 4971–5004.
- [198] H. Tamura, R. Martinazzo, M. Ruckebauer, and I. Burghardt (2012). Quantum Dynamics of Ultrafast Charge Transfer at an Oligothiophene-Fullerene Heterojunction. *The Journal of Chemical Physics* **137** (22), 22A540.
- [199] E. R. Bittner and C. Silva (2014). Noise-Induced Quantum Coherence Drives Photo-Carrier Generation Dynamics at Polymeric Semiconductor Heterojunctions. *Nature Communications* **5** (1), 3119.
- [200] D. Veldman, S. C. J. Meskers, and R. A. J. Janssen (2009). The Energy of Charge-Transfer States in Electron Donor-Acceptor Blends: Insight into the Energy Losses in Organic Solar Cells. *Advanced Functional Materials* **19** (12), 1939–1948.
- [201] C. Zhou, Q. Cui, C. McDowell, M. Seifrid, X. Chen, J.-L. Brédas, M. Wang, F. Huang, and G. C. Bazan (2017). Topological Transformation of π -Conjugated Molecules Reduces Resistance to Crystallization. *Angewandte Chemie* **129** (32), 9446–9449.

- [202] M. T. Seifrid, G. N. M. Reddy, C. Zhou, B. F. Chmelka, and G. C. Bazan (2019). Direct Observation of the Relationship between Molecular Topology and Bulk Morphology for a π -Conjugated Material. *Journal of the American Chemical Society* **141** (13), 5078–5082.
- [203] G. Macchi, B. M. Medina, M. Zambianchi, R. Tubino, J. Cornil, G. Barbarella, J. Gierschner, and F. Meinardi (2009). Spectroscopic Signatures for Planar Equilibrium Geometries in Methyl-Substituted Oligothiophenes. *Physical Chemistry Chemical Physics* **11** (6), 984–990.
- [204] N. S. Güldal, T. Kassar, M. Berlinghof, T. Ameri, A. Osvet, R. Pacios, G. L. Destri, T. Unruh, and C. J. Brabec (2016). Real-Time Evaluation of Thin Film Drying Kinetics Using an Advanced, Multi-Probe Optical Setup. *Journal of Materials Chemistry C* **4** (11), 2178–2186.
- [205] S. Engmann, F. A. Bokel, H. W. Ro, D. M. DeLongchamp, and L. J. Richter (2016). Real-Time Photoluminescence Studies of Structure Evolution in Organic Solar Cells. *Advanced Energy Materials* **6** (10), 1502011.
- [206] S. Cook, A. Furube, and R. Katoh (2008). Analysis of the Excited States of Regioregular Polythiophene P3HT. *Energy & Environmental Science* **1** (2), 294–299.
- [207] M. Chauhan, Y. Zhong, K. Schötz, B. Tripathi, A. Köhler, S. Huettnner, and F. Panzer (2020). Investigating Two-Step MAPbI₃ Thin Film Formation during Spin Coating by Simultaneous in Situ Absorption and Photoluminescence Spectroscopy. *Journal of Materials Chemistry A* **8** (10), 5086–5094.
- [208] I. Botiz, S. Astilean, and N. Stingelin (2016). Altering the Emission Properties of Conjugated Polymers. *Polymer International* **65** (2), 157–163.
- [209] S. Han, X. Yu, W. Shi, X. Zhuang, and J. Yu (2015). Solvent-Dependent Electrical Properties Improvement of Organic Field-Effect Transistor Based on Disordered Conjugated Polymer/Insulator Blends. *Organic Electronics* **27**, 160–166.
- [210] A. Kumar, M. A. Baklar, K. Scott, T. Kreouzis, and N. Stingelin-Stutzmann (2009). Efficient, Stable Bulk Charge Transport in Crystalline/Crystalline Semiconductor-Insulator Blends. *Advanced Materials* **21** (44), 4447–4451.
- [211] S. Pröller, F. Liu, C. Zhu, C. Wang, T. P. Russell, A. Hexemer, P. Müller-Buschbaum, and E. M. Herzig (2016). Following the Morphology Formation In Situ in Printed Active Layers for Organic Solar Cells. *Advanced Energy Materials* **6** (1), 1501580.
- [212] Y.-J. Kim, S. Lee, M. R. Niazi, K. Hwang, M.-C. Tang, D.-H. Lim, J.-S. Kang, D.-M. Smilgies, A. Amassian, and D.-Y. Kim (2020). Systematic Study on the Morphological Development of Blade-Coated Conjugated Polymer Thin Films via In Situ Measurements. *ACS Applied Materials & Interfaces* **12** (32), 36417–36427.
- [213] D. T. Duong, B. Walker, J. Lin, C. Kim, J. Love, B. Purushothaman, J. E. Anthony, and T.-Q. Nguyen (2012). Molecular Solubility and Hansen Solubility Parameters for the Analysis of Phase Separation in Bulk Heterojunctions. *Journal of Polymer Science Part B: Polymer Physics* **50** (20), 1405–1413.

- [214] J. Gierschner, Y.-S. Huang, B. Van Averbeke, J. Cornil, R. H. Friend, and D. Beljonne (2009). Excitonic versus Electronic Couplings in Molecular Assemblies: The Importance of Non-Nearest Neighbor Interactions. *The Journal of Chemical Physics* **130** (4), 044105.
- [215] F. Kanal, S. Keiber, R. Eck, and T. Brixner (2014). 100-kHz Shot-to-Shot Broadband Data Acquisition for High-Repetition-Rate Pump-Probe Spectroscopy. *Optics Express* **22** (14), 16965.
- [216] T. Unger (2017). Ultraschnelle transiente Spektroskopie zur Untersuchung des Einflusses der Morphologie auf die Dynamik von Anregungen in organischen und hybriden Halbleitern. PhD Thesis. University of Bayreuth.
- [217] S. Wedler (2016). Ultrafast Dynamics of Charge Transfer in Polymer-Fullerene Systems. Master Thesis. University of Bayreuth.
- [218] K. Schötz (2017). Spectroscopic Signature of Temperature Induced Phase Transitions. Master Thesis. Bayreuth: University of Bayreuth.
- [219] G. Angulo, G. Grampp, and A. Rosspeintner (2006). Recalling the Appropriate Representation of Electronic Spectra. *Spectrochimica Acta Part A: Molecular and Biomolecular Spectroscopy* **65** (3), 727–731.
- [220] J. Mooney and P. Kambhampati (2013). Get the Basics Right: Jacobian Conversion of Wavelength and Energy Scales for Quantitative Analysis of Emission Spectra. *The Journal of Physical Chemistry Letters* **4** (19), 3316–3318.
- [221] T. Kumrey (2019). Verbesserung eines Aufbaus zur Messung von Absorption und Photolumineszenz und dessen Verwendung zur in-Situ-Untersuchung der Filmbildung von MAPbI₃. Bachelor Thesis. University of Bayreuth.

Part II

Publications

The Impact of Driving Force and Temperature on the Electron Transfer in Donor–Acceptor Blend Systems

Thomas Unger,^{†,||} Stefan Wedler,^{†,||} Frank-Julian Kahle,[†] Ullrich Scherf,[§] Heinz Bässler,[‡] and Anna Köhler^{*,†,‡,||}

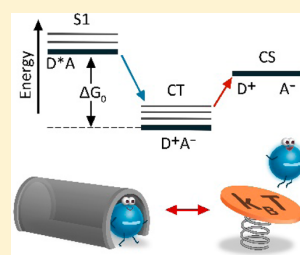
[†]Experimental Physics II, University of Bayreuth, 95447 Bayreuth, Germany

[‡]Bayreuth Institut of Macromolecular Research (BIMF), University of Bayreuth, 95447 Bayreuth, Germany

[§]Makromolekulare Chemie, Bergische Universität Wuppertal, 42119 Wuppertal, Germany

Supporting Information

ABSTRACT: We discuss whether electron transfer from a photoexcited polymer donor to a fullerene acceptor in an organic solar cell is tractable in terms of Marcus theory, and whether the driving force ΔG_0 is crucial in this process. Considering that Marcus rates are presumed to be thermally activated, we measured the appearance time of the polaron (i.e., the radical-cation) signal between 12 and 295 K for the representative donor polymers PTB7, PCPDTBT, and Me-LPPP in a blend with PCBM as acceptor. In all cases, the dissociation process was completed within the temporal resolution of our experimental setup (220–400 fs), suggesting that the charge transfer is independent of ΔG_0 . We find that for the PCPDTBT:PCBM ($\Delta G_0 \approx -0.2$ eV) and PTB7:PCBM ($\Delta G_0 \approx -0.3$ eV) the data is mathematically consistent with Marcus theory, yet the condition of thermal equilibrium is not satisfied. For MeLPPP:PCBM, for which electron transfer occurs in the inverted regime ($\Delta G_0 \approx -1.1$ eV), the dissociation rate is inconsistent with Marcus theory but formally tractable using the Marcus–Levich–Jortner tunneling formalism which also requires thermal equilibrium. This is inconsistent with the short transfer times we observed and implies that coherent effects need to be considered. Our results imply that any dependence of the total yield of the photogeneration process must be ascribed to the secondary escape of the initially generated charge transfer state from its Coulomb potential.



1. INTRODUCTION

The conversion of optical energy into electrical energy in organic solar cells is meanwhile established to occur as a two-step process.¹ The initial step is the transfer of an electron from a photoexcited donor chromophore to an acceptor chromophore. This leads to the formation of a charge-transfer state, or, more generally, a Coulomb-bound electron–hole (eh) pair, that separates into free charges in a subsequent step.^{2,3} The initial electron transfer step is exothermic, while the subsequent charge separation step is endothermic. A key parameter here is the “driving force ΔG_0 ” of the process, commonly considered to be the difference in the energies of the initial and final states of the system. More precisely, the driving force is the difference in Gibbs free energy (also known as free enthalpy) between the initial and final states, $\Delta G_0 = \Delta H - T\Delta S$, with H being the enthalpy, T the temperature, and S the entropy.⁴ It is an intuitively attractive idea that the overall process may be more efficient when more energy is released during the initial electron transfer from the excited donor to the acceptor. Furthermore, when ΔG_0 becomes more negative, then the excess energy might be used to facilitate overcoming the Coulomb barrier of the initially created electron–hole pair.^{5,6} On the other hand, there is growing evidence that this subsequent dissociation process starts from a “cold” eh pair.² If so, would a high driving force still be of advantage for the cell efficiency irrespective of the fact that a high driving force

implies a lower open circuit voltage of the solar cell?⁷ Evidently, to clarify the role of the driving force is a crucial question for understanding the operation of organic solar cells.^{7,8}

Our current study was stimulated by the work of Ward et al.⁹ They conducted time-resolved photoluminescence measurements on donor–acceptor blends, in which the LUMO energies of the acceptor were varied systematically. From their studies, they inferred the rate of charge transfer in the donor–acceptor pair and found an apparent correlation between the driving force and the charge transfer rate that they interpreted to be in agreement with the classical Marcus theory. Specifically, they concluded that the charge transfer rate is maximal when the driving force is $\Delta G_0 = -0.4$ eV but that the rate decreases significantly for driving forces above and below this optimum value. However, recent experiments on non-fullerene-type acceptors have been shown to lead to efficient solar cells, even if the driving force, measured as the energy difference between the donor LUMO and the acceptor LUMO, is close to zero.^{10,11}

These considerations and the unclear role of ΔG_0 result from an approach where the electron transfer is a priori considered treatable in a classical Marcus type framework. Marcus’ theory was originally developed and proved successful to describe

Received: September 15, 2017

Published: September 20, 2017

energy or electron transfer between an individual molecular donor and an individual molecular acceptor in solution.^{12–14} However, in its original, classical form, it is not generally suitable to describe the transport of charges through a thin film of an organic semiconductor.^{15–17} The latter may be seen as a sequence of electron transfer events between chemically identical donor and acceptor sites. The reason for this shortcoming is that in disordered systems the direct quantum mechanical tunneling between initial and final states takes more weight compared to the thermally activated process than predicted by classical Marcus theory.^{18–20} It is therefore uncertain whether classical Marcus theory is the most appropriate approach to describe the electron transfer from a donor material to an acceptor material when the two materials form a disordered thin film in an organic solar cell. In fact, more sophisticated quantum mechanical descriptions have recently been suggested.^{21–26} Nevertheless, Marcus theory is frequently used to account for the photogeneration of charges.^{8,27–29} The question that we are discussing in this paper is, therefore, *whether classical Marcus theory gives a suitable description for electron transfer in a thin donor–acceptor type film and, associated with this, what the role of the driving force ΔG_0 is in promoting the electron transfer.*

We address this issue by measuring the electron transfer rate through time-resolved photoinduced absorption of thin films made of blends of a polymer donor and the fullerene acceptor PCBM over a broad range of temperatures. The measured rates (or their lower limits) are compared with the transfer rates that are expected on the basis of the molecular parameters. For our study, we employed PCBM as a prototypical, widely used acceptor and combined it with the donor polymer PTB7 that was also investigated by Ward et al.⁹ As a second, representative donor polymer, we chose PCPDTBT.^{30,31} Both PTB7 and PCPDTBT have moderate driving forces when combined with PCBM. As an example of a polymer with a high driving force, we also investigated the rigid MeLPPP. All chemical structures are shown in Figure 1.

2. EXPERIMENTAL SECTION

2.1. Materials and Sample Preparation. PTB7 (poly-({4,8-bis[(2-ethylhexyl)oxy]benzo[1,2-*b*:4,5-*b'*]dithiophene-2,6-diyl}-{3-fluoro-2-[(2-ethylhexyl)carbonyl]thieno[3,4-*b*]thiophene-2,5-diyl})) was purchased from 1-Material and has a molecular weight M_w of 23 kDa. The solvents, PC₆₀BM and PCPDTBT (poly{[4,4-bis(2-ethylhexyl)-cyclopenta(2,1-*b*;3,4-*b'*)dithiophene-2,6-diyl]-*alt*-(2,1,3-benzothiadiazole-4,7-diyl)}) were obtained from Sigma-Aldrich. Methylated ladder-type poly(para-phenylene) polymer (MeLPPP) ($M_w = 83$ kDa) was synthesized in the group of U. Scherf.^{32,33} To prepare thin films for optical measurements, a 36 g/L chloroform solution of MeLPPP blended with PCBM (1:1 by weight) and of neat MeLPPP was spin-coated under a nitrogen atmosphere onto spectroil B substrates at 700 and 800 rpm, respectively. PCPDTBT and PTB7 films were spin-coated onto quartz substrates at 700 rpm from 20 g/L chlorobenzene solutions. No further annealing step was performed in order to keep phase separation as low as possible. Doped films were obtained by immersing the neat polymer films in acetonitrile solution of FeCl₃ (0.1%) for about 10 min. In Figure 1, we display the difference in absorption between the film prior to and after the doping process. The UV/vis absorption was measured using a Cary 5000 UV–vis-NIR spectrophotometer. Photolumines-

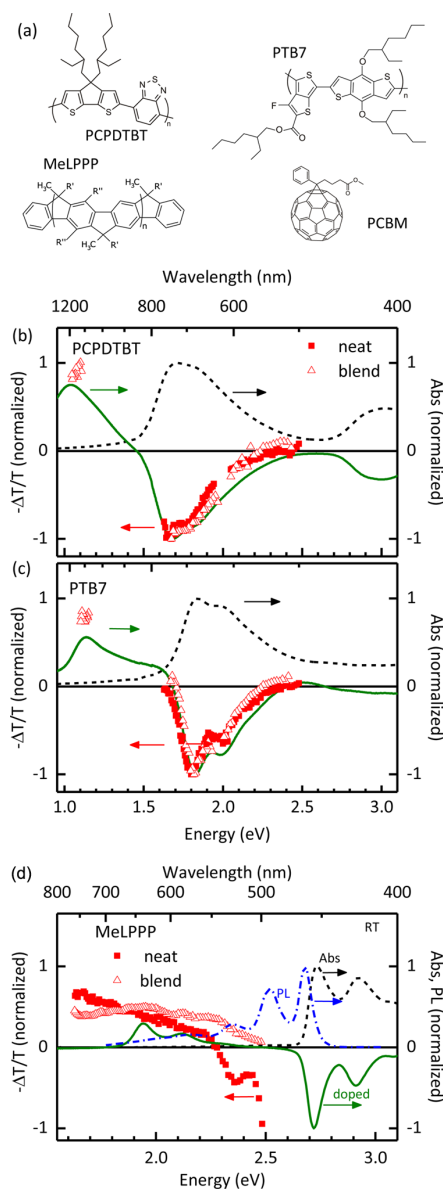


Figure 1. (a) Chemical structures of the donor polymers and the fullerene acceptor. (b–d) Spectra of blends and neat films of PCPDTBT, PTB7, and MeLPPP. The black dashed line shows the absorption of the neat neutral donor, and the green solid line indicates the changes obtained in absorption upon doping the neat donor. The symbols show the photoinduced absorption obtained for the neat donor film (solid squares) and for the blend (open triangles) at 2 ps after the excitation pulse (1 ps for neat PTB7). For MeLPPP, the photoluminescence (PL) is also indicated as a blue dash-dotted line.

cence spectra (PL) are recorded with a JASCO FP-8600 spectrofluorometer.

2.2. Femtosecond Transient Absorption Measurements. Transient absorption measurements were performed using a RegA9000 regenerative amplifier system from Coherent Inc. (pulse length 210 fs) with a 100 kHz repetition rate. About 12% of the output intensity is used for generation of the probe light between 480 and 750 nm in a YAG-crystal. The remaining

intensity of the output intensity is used to pump an OPA (Coherent Inc.) for the pump beam at 3.1 eV (400 nm) and 1.94 eV (640 nm). The pump fluence is in the range 10–30 $\mu\text{J}/\text{cm}^2$. The spectra are recorded by using a lock-in amplifier (SR830, Stanford Research) and a monochromator (spectral resolution 3 nm) with a Si-diode for the Vis region or a InGaAs-diode for the NIR region. The measurements were performed on thin films placed in a cryostat under a helium atmosphere and at temperatures as indicated in the figure captions.

2.3. CT Measurements. In order to determine the energy of the charge transfer (CT) state and the associated reorganization energy in MeLPPP:PCBM blends, we measured the external quantum efficiency (EQE) and electroluminescence (EL) in bulk heterojunction solar cell devices of the structure ITO-covered glass/ MoO_3 (15 nm)/blend or neat film/Al (100 nm). Blends had a thickness of 110 nm, spun from chloroform at 15 mg mL^{-1} . For reference, solar cells with pristine MeLPPP (chloroform, 7.5 mg mL^{-1}) and PCBM layers (chloroform, 15 mg mL^{-1}), respectively, were fabricated accordingly. The thicknesses of the MeLPPP and PCBM films were 60 and 30 nm, respectively. The thicknesses of the active layer of the solar cells were controlled with a Dektak (Veeco) profilometer directly on a device.

EQE measurements were performed using a lock-in amplifier (SR830) at a reference frequency of 130 Hz and using monochromatic illumination from a 150 W tungsten lamp (Osram). For EL measurements, the solar cells were biased at 3V using a Keithley source-measure unit (SMU 237). The luminescence of the sample was recorded by a CCD camera (Andor iDus) coupled to a monochromator (Oriol). For both EQE and EL measurements, the sample was kept in an appropriate vacuum condition sample holder at room temperature. CT and reorganization energies were determined from a simultaneous Gaussian fit to the reduced EQE and EL spectra according to Vandewal et al.³⁴ The reduced EQE and EL are given by reduced EQE = $E \cdot \text{EQE}(E)$ and reduced EL = $\text{EL}(E)/E$.

3. RESULTS

3.1. Experimentally Determined Transfer Rates. In order to compare theoretically predicted rates with experimentally observed ones, the rates of charge transfer—or their lower bounds—need to be determined. We focused therefore on measuring the appearance of the absorption due to the cation that forms on the donor when the electron transfers onto the acceptor. Thus, a first step is to determine the spectral position of this absorption. For this, we measured the absorption of the respective neat donor polymer films after oxidizing them chemically using FeCl_3 . The spectra and the other optical properties of the used materials are shown in Figure 1. The low-bandgap polymers PCPDTBT and PTB7 (Figure 1b,c) have their main absorption peak between 2.5 eV (500 nm) and 1.6 eV (800 nm). It is straightforward to assign the reduction of absorption in the spectra of the chemically oxidized neat samples as well as in the pump–probe spectra of the neat samples and blends to the ground state bleach (GSB) of the respective donor polymers. The difference in the absorption of the neat films before and after the chemical oxidation process is the absorption due to the thus formed cations on the polymers. The cation spectra show broad absorption bands centered at 1.0 eV (1200 nm) for PCPDTBT and 1.1 eV (1100 nm) for PTB7, which is also in agreement

with literature.^{35–37} At these energies, we can also observe a clear pump–probe signal with positive sign in the blends, yet not in the neat films, which we can therefore attribute to the absorption of the polymer cation formed after photoinduced electron transfer to PCBM.

Figure 1d contains the corresponding spectra for MeLPPP. The absorption is structured and lies in the blue part of the visible spectrum, with the first absorption peak situated at 2.7 eV (454 nm). In addition to the GSB at the same energy, there is a structured absorption with a 0–0 peak at about 1.9 eV (640 nm) and a vibronic replica at 2.1 eV (580 nm) in the cation absorption spectra obtained from the chemically oxidized films. The pump–probe spectrum at early times (2 ps) for the neat film consists of a stimulated emission (SE) band above 2.25 eV (below 550 nm) corresponding to the photoluminescence (PL) spectrum (blue line, in Figure 1d). A broad induced absorption band appears below 2.25 eV (above 550 nm) further increasing into the NIR beyond the investigated spectral range, which we attribute to the excited state absorption of the singlet exciton.³⁸ The SE contribution is nearly absent in the pump–probe spectrum of the blend. Instead, there is an additional absorption feature at the position of the polymer cation absorption with a maximum at about 1.9 eV (650 nm), which is also in accordance with the literature.^{38,39}

Having identified the spectral position of the cation absorption, we can now monitor its evolution. Figure 2 shows charge transfer dynamics of the cation absorption at room temperature and at 12 K in the low-bandgap polymers and in their blends with PCBM. For control purposes, the appearance of the GSB is also monitored. For both blends, we observe that the appearance of the cation absorption occurs within our temporal resolution (220 fs in vis, 400 fs in NIR due to technical reasons, indicated by the gray and red shaded areas around time zero position) for room temperature measurement as well as at low temperatures. The same holds for the neat polymer films, yet the signals decay faster than in the blend. Conversely, the cation absorption signals of the blend films at 12 K show an additional offset due to an increased lifetime⁴⁰ that exceeds the laser repetition time of 10 μs .

Figure 3 displays the dynamics of the MeLPPP:PCBM system at early times for different temperatures between 250 and 12 K. The transients are taken at the wavelength of the cation absorption signal at 640 nm (1.9 eV). Within the entire temperature range probed, we see an ultrafast charge transfer which is faster than our temporal resolution. Furthermore, there is no initial offset. The exciton signal probed at 730 nm (1.7 eV) decays with a time constant of about 5 ps, which is mainly assigned to the diffusion of singlets to the interface which are not directly created at the interface. Small contributions of this 5 ps decay can also be seen in the cation signal at 250 and 200 K. We attribute this to a contribution from the overlapping exciton signal leaking into the cation signal, which disappears at lower temperatures (see Figure 3).

From these data, we can nominally derive the rise time for the cation signal. We find that the corresponding rate is in the range of $(2\text{--}5) \times 10^{12} \text{ s}^{-1}$. Thus, for all three materials and all temperatures probed, the rise time is within the resolution limit of our instrument. This resolution limit varies slightly for different probe wavelengths.

3.2. Transfer Rates according to Marcus Theory. We now consider whether our experimental values are consistent with Marcus theory. The Marcus transfer rate is given by^{41,42}

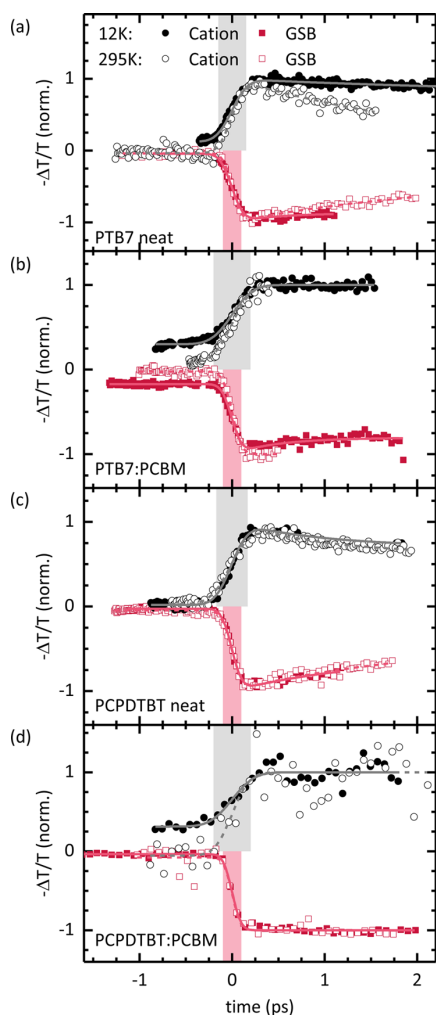


Figure 2. Normalized pump–probe transients in thin films, taken at the wavelength of the ground state bleach (GSB) and the cation absorption. The temporal resolution is indicated by the colored boxes at zero time delay; the solid lines correspond to fits. (a) Neat PTB7; (b) PTB7:PCBM, both GSB at 1.77 eV (700 nm), cation at 1.11 eV (1120 nm); (c) neat PCPDTBT; (d) PCPDTBT:PCBM, both GSB at 1.75 eV (710 nm), cation at 1.11 eV (1120 nm).

$$k_{\text{Marcus}}(T) = \frac{|J_{\text{DA}}|^2}{\hbar} \sqrt{\frac{\pi}{\lambda k_{\text{B}} T}} \exp\left[-\frac{(\lambda + \Delta G_0)^2}{4\lambda k_{\text{B}} T}\right] \quad (1)$$

with the electronic coupling strength J_{DA} , reorganization energy λ , and driving force ΔG_0 . This equation is based on thermal equilibrium under the assumption that the quantum nature of the acoustic phonons (with energies of a few meV) does not need to be considered explicitly, i.e., $k_{\text{B}}T \gg \hbar\omega$, and can be treated classically.⁴³ This is typically the case for temperatures above 100 K.

In order to calculate the rate, we therefore require knowledge of the driving force ΔG_0 , the reorganization energy λ , and the electronic coupling J_{DA} between donor and acceptor molecules. The rate is particularly sensitive to the relative magnitude of λ and ΔG_0 , as the two quantities tend to have different signs, so that their difference enters the argument of the exponential function. As a simple approximation for the driving force, it is

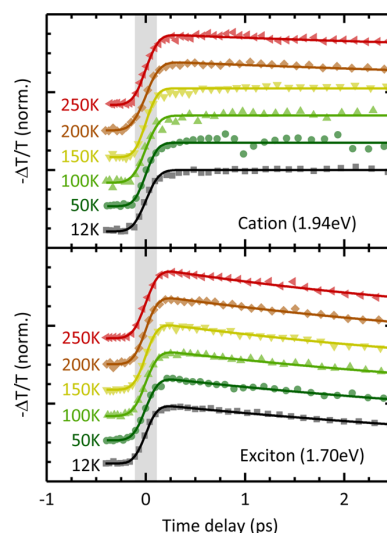


Figure 3. Normalized pump–probe transients of the cation absorption and the exciton absorption in MeLPPP:PCBM blend films excited at 3.1 eV (400 nm) at different temperatures.

common to take the difference in electron affinities.⁴⁴ This is sufficient for many cases. Here, we would like to determine ΔG_0 as accurately as possible. Therefore, we consider the difference between the energy of the photoexcited donor and the final charge-transfer state to be ΔG_0 :⁴⁵

$$-\Delta G_0 = E_{\text{S1}} - E_{\text{CT}} \quad (2)$$

This is illustrated in Figure 4 for ease of reference for the cases of $\Delta G_0 = 0$, $\Delta G_0 = -\lambda$, and $\Delta G_0 \ll -\lambda$. To find the values of ΔG_0 for our compounds, we determined E_{S1} from the intersection between the absorption and emission spectra, each normalized to unity at the peak of the first band. For PCPDTBT and PTB7, we took the values for E_{CT} and λ from

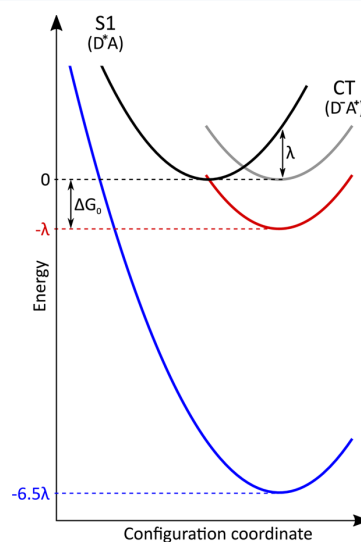


Figure 4. Energy diagram for an electron transfer process in the Marcus picture with vanishing driving force (gray), $\Delta G_0 \approx -\lambda$ (red) and $\Delta G_0 \approx -6.5 \lambda$ (blue).

Table 1. Summary of the Input Parameters Used to Calculate the Charge Transfer Rate according to eq 1 for the Three Blends Considered^a

	PCPDTBT:PCBM	PTB7:PCBM	MeLPPP:PCBM
E_{S1} (eV)	$1.50 \pm 0.10^{47,48}$	$1.67 \pm 0.05^{49-51}$	2.70 ± 0.05^{52}
E_{CT} (eV)	1.30 ± 0.05^b	$1.35 \pm 0.05^{49,53,54}$	1.57 ± 0.05
$-\Delta G_0$ (eV)	0.21 ± 0.11	0.32 ± 0.07	1.13 ± 0.07
λ (eV)	$0.30 \pm 0.10^{b,45}$	$0.35 \pm 0.05^{9,45}$	0.17 ± 0.03
$\lambda + \Delta G_0$ (eV)	0.09 ± 0.15	0.03 ± 0.09	-0.96 ± 0.08
J_{DA} (eV) ^{45,55}	0.03 ± 0.02	0.03 ± 0.02	0.03 ± 0.02

^a E_{S1} is the energy of the singlet excited state, E_{CT} is the energy of the CT state, $-\Delta G_0$ denotes the driving force, λ is the reorganization energy associated with the charge transfer, and J_{DA} is the electronic coupling. ^bSee the Supporting Information, Figure S3.

published data as listed in Table 1. These values result from fitting the photocurrent spectra (EQE) and electroluminescence (EL) as outlined by Vandewal,^{34,46} where 2λ then corresponds to the difference between the maxima in the CT state absorption and emission and E_{CT} is taken from their intersection. Static disorder can contribute to the width of these bands, so that the obtained values are an upper limit. This method determines the reorganization energy between the neutral ground state and the CT state, whereas we consider the formation of the CT state via the excited state. In principle, these values are different. However, they are expected to be very similar, as the reorganization energy for the fullerene acceptor is small due to its rigidity.^{56,57}

Table 1 lists the driving force thus obtained, along with the pertaining parameters. For the MeLPPP system, we needed to experimentally determine E_{CT} and λ . Therefore, we measured the EL of the MeLPPP:PCBM blend to compare against the EL spectrum of the neat MeLPPP and PCBM. The EL of neat MeLPPP was consistent with ref 58. It is more than 1 eV separated from the blend EL and therefore does not need to be considered further. Figure 5a shows the EL of the blend along with the EL from neat PCBM, taken from ref 59 and normalized to fit the high energy tail. The difference between the two spectra, shown as a blue line, is assigned to the EL of the CT state. In Figure 5b, the CT EL is compared to the EQE spectrum of the blend. We fitted the CT emission and the low energy tail of the EQE, respectively, according to

$$EL(E) \propto \frac{1}{E\sqrt{4\pi\lambda k_B T}} \exp\left(-\frac{(E_{CT} - \lambda - E)^2}{4\lambda k_B T}\right) \quad \text{and}$$

$$EQE(E) \propto \frac{1}{E\sqrt{4\pi\lambda k_B T}} \exp\left(-\frac{(E_{CT} + \lambda - E)^2}{4\lambda k_B T}\right),$$

as outlined in ref 34, using identical parameters for the CT emission and the fit to the low energy tails of the EQE. Here, E denotes the photon energy and $k_B T$ denotes the product of Boltzmann constant and temperature. From this procedure, we arrive at $E_{CT} = 1.57 \pm 0.05$ eV and $\lambda = 0.17 \pm 0.03$ eV.

To calculate the charge transfer rate according to Marcus, we still require the value of the electronic coupling. This can only be derived by calculations. Leng and co-workers report a value of 30 meV for PCPDTBT:PCBM,⁴⁵ and Liu and co-workers report 20–30 meV for P3HT:PCBM.⁵⁵ On the basis of these studies, we adopt a value of $J = 30 \pm 20$ meV for all compounds. All values required to calculate the transfer rate are summarized in Table 1. A detailed discussion to each value and its error margin is given in the Supporting Information (SI 1.1). For reference, we have also considered which driving force ΔG_0^{IP} , and concomitantly which transfer rate, would result if the

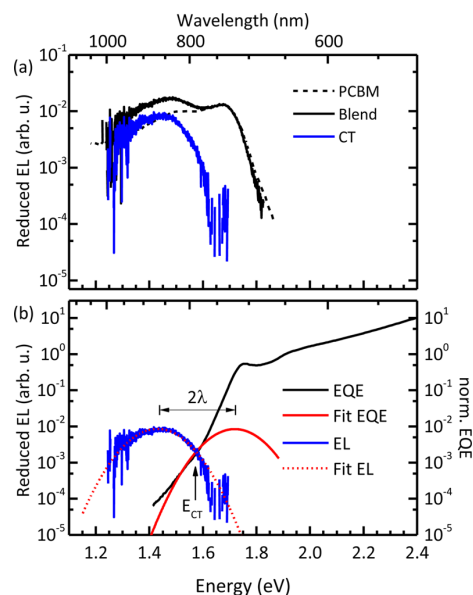


Figure 5. (a) Reduced EL of MeLPPP:PCBM (black solid line) and pristine PCBM (black dashed line). The difference of the two spectra corresponds to the CT emission (blue solid line). The spectra of pristine PCBM were reprinted with permission from ref 59. Copyright (2009) American Chemical Society. (b) Reduced EQE and EL spectra of MeLPPP:PCBM (black solid lines). The blue line corresponds to the CT-EL spectrum, as shown in part a. Red lines indicate simultaneous Gaussian fits to the CT region of EQE (solid) and EL (dotted) according to Vandewal et al.³⁴

difference in the ionization potential of the donors, derived from refs 45 and 60 for PCPDTBT, as well as ref 50 for PTB7, and the fullerene EA of 3.8 ± 0.1 eV was considered.^{2,61,62} It turns out that this does not impact the overall conclusions, as detailed in the Supporting Information (SI 1.2).

By comparing the values of ΔG_0 and λ , one can see that for PCPDTBT:PCBM and PTB7:PCBM $\Delta G_0 \cong -\lambda$, whereas for MeLPPP:PCBM $\Delta G_0 \cong -6.5\lambda$. These two cases are illustrated in Figure 4. Evidently, rather high transfer rates can be expected in the former case, while transfer should become difficult in the latter case, which is the Marcus inverted regime. Table 2 summarizes the transfer rates calculated according to eq 1 with the mean values of parameters of Table 1.

4. ANALYSIS

4.1. Electron Transfer in the Marcus Normal Regime.

It is worthwhile to discuss the range of values that may be obtained by using eq 1 from the experimentally found input parameters. We shall first focus on PCPDTBT and PTB7. The usual preconception is that a thermally activated charge transfer can be described by Marcus theory,^{8,27} and that the expected charge transfer rate slows down upon cooling due to the exponential term. It turns out that, for the low-bandgap polymers we investigated, PCPDTBT and PTB7, the magnitude of the reorganization energy λ and of the driving force ΔG_0 are, within the experimental error, about equal, while their signs are opposite. As a result, the argument of the exponential function is close to zero, with some variation on both sides of zero due to the experimental error margins. The fact that $\Delta G_0 + \lambda \approx \pm 0$ has two consequences. First, it results in a rather large range of values that can be obtained within the

Table 2. Transfer Rates Determined according to eq 1 for Different Temperatures, along with the Experimentally Measured Lower Limits for the Transfer Rates^a

temperature (K)	PCPDTBT	PTB7	MeLPPP
		Expected from Marcus Theory in s ⁻¹	
295	2 × 10 ¹³	3 × 10 ¹³	3 × 10 ⁻¹⁰
200	2 × 10 ¹³	3 × 10 ¹³	3 × 10 ⁻²¹
150	2 × 10 ¹³	3 × 10 ¹³	2 × 10 ⁻³²
100	2 × 10 ¹³	4 × 10 ¹³	3 × 10 ⁻⁵⁵
12	4 × 10 ¹⁰	7 × 10 ¹³	<10 ⁻³⁰⁰
		Experimental Values in s ⁻¹ (Lower Limits)	
295	(2.9 ± 1.8) × 10 ¹²	(2.6 ± 0.2) × 10 ¹²	(4.1 ± 0.2) × 10 ¹²
12	(2.2 ± 0.7) × 10 ¹²	(2.4 ± 0.1) × 10 ¹²	(4.5 ± 0.2) × 10 ¹²

^aMinimum and maximum transfer rates resulting from the uncertainties of the parameters are given in the Supporting Information (Table S2).

limits of the input parameters. Second, the temperature dependence of the transfer rate does not necessarily reduce upon cooling, in contrast to the common expectation. Rather, it may be nearly independent of temperature or even increase upon cooling, when the overall temperature dependence is controlled by the nonexponential prefactor. Figure 6 illustrates the temperature dependence that results from eq 1 for PCPDTBT and for PTB7 in addition to the temperature dependence obtained when using the mean values for the input parameters λ , ΔG_0 , and J_{DA} . Figure 6 also shows, as shaded areas, the range of accessible values when the input parameters λ , ΔG_0 , and J_{DA} are varied within their range of uncertainty

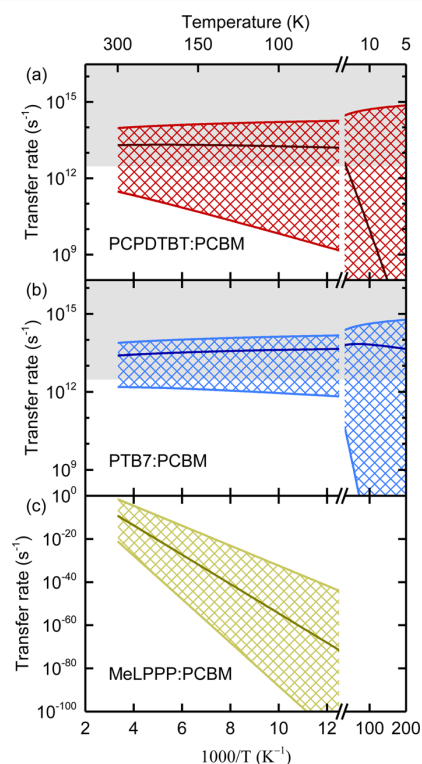


Figure 6. Arrhenius plots of the Marcus-type electron transfer rate according to eq 1, calculated using the mean values for each parameter (dark solid line). The fastest and slowest rates accessible within the error range of the parameters are shown as light solid lines bordering the patterned range of accessible values. The gray shaded area indicates values that are beyond our instrumental resolution.

(compare Table S2 in the Supporting Information). While we show the functional dependence of eq 1 for values down to 10 K, one needs to bear in mind that the *mathematical* application of eq 1 below about 100 K does not necessarily carry any *physical* meaning as detailed below. The gray shaded area indicates the range of rates that are beyond our instrumental time resolution.

The values of the singlet energy, CT state energy, and reorganization energy found for PCPDTBT and PTB7 in combination with PCBM are typical for many low-bandgap polymers. It is therefore instructive to consider how sensitively the transfer rates depend on the driving force and reorganization energy. Figure 7 shows calculated Marcus rates (eq 1) as a function of driving force for an electronic coupling of $J_{DA} = 30$ meV and two different values of reorganization energy, $\lambda = 0.30$ eV and $\lambda = 0.35$ eV. This corresponds to the

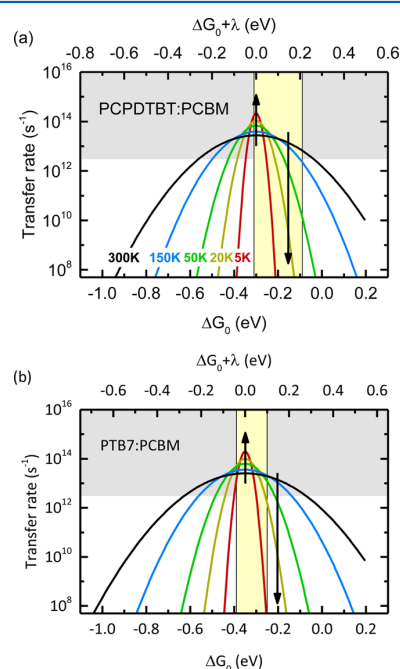


Figure 7. Marcus-type electron transfer rates according to eq 1 as a function of driving force for temperatures of 300, 150, 50, 20, and 5 K (a) for PCPDTBT:PCBM and (b) for PTB7:PCBM. The gray shaded area indicates values that are beyond our instrumental resolution. The yellow shaded area indicates the parameter range for the driving force.

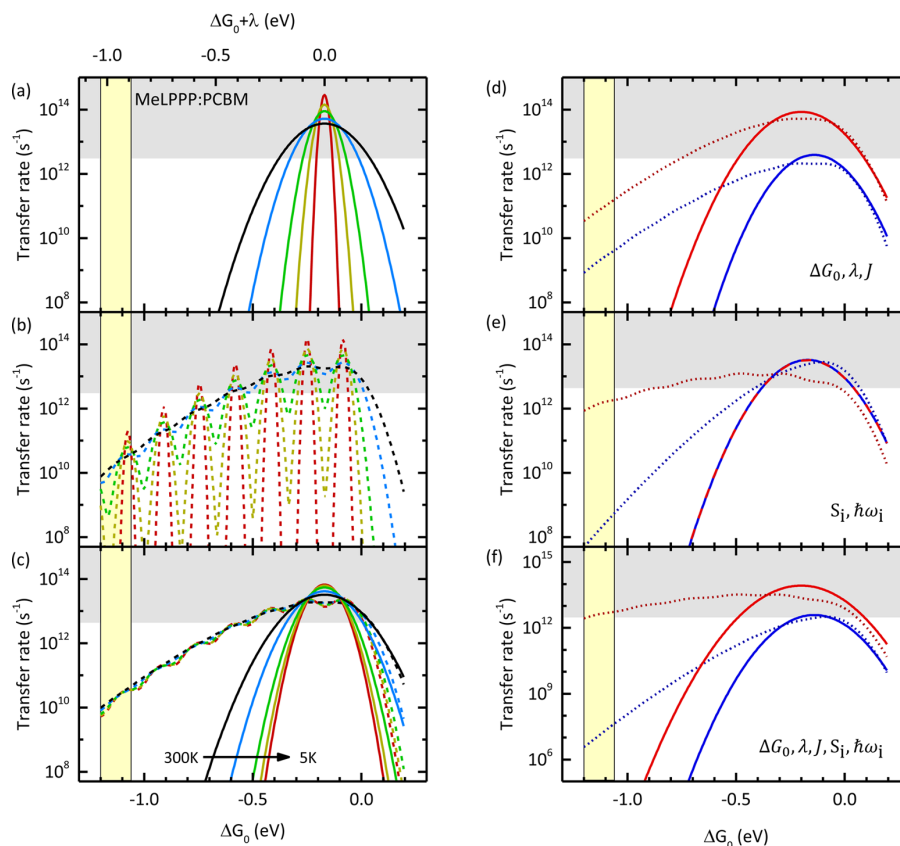


Figure 8. Electron transfer rates for MeLPPP:PCBM calculated with $\lambda = 0.17$ eV and $J_{DA} = 30$ meV for different temperatures (300, 150, 50, 20, and 5 K). The gray shaded area indicates values that are beyond our instrumental resolution. The yellow shaded area indicates the parameter range for the driving force. (a) Using Marcus theory (eq 1), (b) using MLJ theory (eq 3), (c) including disorder in eq 1 (solid lines) and in eq 3 (dashed lines). (d–f) Maximizing (red lines) and minimizing (blue lines) electron transfer rates at 300 K including disorder using Marcus theory (solid lines) and MLJ theory (dotted lines) by varying (d) ΔG_0 , λ , and J_{DA} , (e) S_i and $\hbar\omega_i$, and (f) all parameters.

parameter sets for PCPDTBT:PCBM and PTB7:PCBM. The resulting rates are displayed for different temperatures in the range from 300 to 5 K. Evidently, for a driving force close to zero, Marcus theory predicts a strong reduction of the transfer rate with decreasing temperature and values that are accessible with many pump–probe setups. This temperature dependence agrees with the notion one has when considering the corresponding energy levels in Figure 4. However, for driving forces close to λ , the transfer rate increases upon cooling. This is because the exponential term in eq 1 vanishes, so that the $T^{-0.5}$ dependence in the prefactor dominates. Furthermore, the rate increases to values that push the time resolution of common pump–probe setups to their limits. In Figure 7, the yellow area indicates the error range we found for the driving force ΔG_0 . This illustrates how for PCPDTBT:PCBM both an increasing as well as a decreasing transfer rate upon cooling would be consistent with the experimental data. Essentially the same applies for PTB7:PCBM. It becomes further evident that, for both materials, the rate dependence according to Marcus as well as its temperature dependence should exceed our experimental resolution. While this is indeed what we observe (cf. Table 2), it can neither confirm nor disprove the applicability of eq 1.

The lower limit we experimentally find by pump–probe spectroscopy for the transfer rate in PTB7:PCBM, about $2.6 \times$

10^{12} s^{-1} , is at variance with the transfer rate of $8 \times 10^{11} \text{ s}^{-1}$ reported by Ward et al. on the basis of photoluminescence quenching experiments.⁹ The latter value would have been well within our experimental range. Ward et al. find their value can be fitted with Marcus theory, using values of $\lambda = 0.4$ eV and $\Delta G_0 = -0.2$ eV. From their data, we calculate a corresponding coupling strength J_{DA} of 9 meV. While their reorganization energy and driving force are close to the ones we found of $\lambda = 0.35 \pm 0.05$ eV and $\Delta G_0 = -0.32 \pm 0.07$ eV, their required electronic coupling is low compared to the value range of $J_{DA} = 0.03 \pm 0.02$ eV that is reported in other publications.^{45,55}

In summary, while PCPDTBT and PTB7 are donor materials which are widely used for solar cells and have values for ΔG_0 and λ that are typical for the low bandgap polymer/fullerene couples used in solar cells, they are not suitable to assess the validity of the Marcus approach in thin films as well as similar donor–acceptor systems. The reason for this lies in the fact that ΔG_0 and λ are approximately of equal magnitude yet opposite sign, so that the resulting rate may rise, remain constant, or decrease with decreasing temperature, depending sensitively on whether the two parameters sum up to the positive or negative side of zero. In addition, for a moderate coupling strength of $J_{DA} = 30$ meV, the resulting transfer times are below 100 fs, thus rendering detection difficult. From Figure 7, it is also evident that the applicability of Marcus

theory may be probed more reliably for donor–acceptor systems that have a driving force close to zero, as has been reported for some blends made with nonfullerene acceptors.^{10,11} There, slower transfer rates, in particular upon cooling, can be expected if Marcus theory applies.

4.2. Electron Transfer in the Marcus Inverted Regime.

We now turn to the material system with a more significant difference between ΔG_0 and λ , that is MeLPPP combined with PCBM. We compare the values expected on the basis of Marcus theory against the experimental value. Figure 8a shows the transfer rates calculated using eq 1 for the values given in Table 1, with the yellow shaded area indicating the error range of ΔG_0 . Evidently, for MeLPPP:PCBM, the transfer should be very slow, at most near 10^{-2} s^{-1} (see Figure 6 and Table S2 in the Supporting Information). However, from solar cell measurements, we know that the transfer actually occurs with a finite yield.⁶³ Furthermore, if the transfer occurred indeed on a long time scale, we should see some signal at negative delay times from the previous pulse, as the laser repetition rate is 100 kHz. This is not the case (see Figure 3). Rather, we observe that the signal for MeLPPP appears within the rise-time of the laser. Therefore, we conclude that the electron transfer is indeed many orders of magnitude faster than what classical Marcus theory would predict (see also Table 2).

This can be understood when considering Figure 4. For MeLPPP, the driving force is more than 6 times larger than the reorganization energy. Thus, the system is well into the so-called Marcus inverted regime. Under such conditions, the probability of tunneling from the D^*A to the D^+A^- potential energy surface can become significant.^{64,65} This tunneling process is taken into account in the extension of Marcus theory by Marcus, Levich, and Jortner (MLJ). We have therefore considered whether our results are consistent with the MLJ equation⁴³

$$k_{\text{LJ}}(T) = \frac{|J_{\text{DA}}|^2}{\hbar} \sqrt{\frac{\pi}{\lambda_o k_{\text{B}} T}} \sum_{\nu=0}^{\infty} \frac{e^{-S_i} S_i^{\nu}}{\nu!} \times \exp\left[-\frac{(\Delta G_0 + \lambda_o + \nu \hbar \omega_i)^2}{4\lambda_o k_{\text{B}} T}\right] \quad (3)$$

In this approach, one differentiates between the high-frequency intramolecular vibrations $\hbar\omega_i$, for which $\hbar\omega_i \gg k_{\text{B}}T$, and the low-frequency, environmental phonons with $\hbar\omega_o \ll k_{\text{B}}T$. We adopt the subscripts *i* and *o* to differentiate the inner (=intramolecular) and outer (=environmental) contributions. While the contributions of the intramolecular vibrations are explicitly included with their associated Huang–Rhys parameter S_i , the influence of the surrounding medium is incorporated through the reorganization energy λ_o .

Figure 8b shows the rates calculated by eq 3 assuming a mean vibrational energy of $\hbar\omega_i = 165 \text{ meV}$ for donor and acceptor, a Huang–Rhys parameter S_i of 1, and an estimated outer reorganization energy $\lambda_o \approx 0.5\lambda \approx 0.09 \text{ meV}$. Estimating the outer reorganization energy is not trivial.^{65,66} Theoretical calculations for similar systems show that this estimate gives reasonable results.²⁸ The dependence of eq 3 on these parameters will be discussed further below. Two features are noteworthy. First, the dependence of the transfer rates on the driving force ΔG_0 is significantly reduced compared to Figure 8a. Second, there is a resonance (of 165 meV) on the energy dependence of the rate with a narrowing line width at lower temperatures. Thus, at lower temperatures, the transfer rate

would be very sensitive to small energy variations. Furthermore, there would be a temperature dependence of the transfer rates, in contrast to what we experimentally observe (see Figure 3), unless by chance a stationary point on the curve is hit.

So far, we have neglected that there is some statistical energetic disorder in the sample, so that ΔG_0 may feature a statistical distribution. We have therefore considered how the rates obtained by eqs 1 and 3 change if we allow for a statistical variation in ΔG_0 . We implemented disorder by convoluting eqs 1 and 3 below with a Gaussian disorder distribution $g(\epsilon) = \frac{1}{\sqrt{2\pi}\sigma} \exp\left(-\frac{\epsilon^2}{2\sigma^2}\right)$ with a width of $\sigma = 50 \text{ meV}$ according to

$$k(T) = \int_{-\infty}^{\infty} \frac{|J_{\text{DA}}|^2}{\hbar} \sqrt{\frac{\pi}{\lambda k_{\text{B}} T}} \exp\left[-\frac{(\lambda + \Delta G_0 - \epsilon)^2}{4\lambda k_{\text{B}} T}\right] \times \frac{1}{\sqrt{2\pi}\sigma} \exp\left[-\frac{\epsilon^2}{2\sigma^2}\right] d\epsilon \quad (4)$$

for eq 1 and a corresponding expression for eq 3. This results in

$$k(T) = \frac{|J_{\text{DA}}|^2}{\hbar} \sqrt{\frac{2\pi}{2\lambda k_{\text{B}} T + \sigma^2}} \exp\left[-\frac{(\lambda + \Delta G_0)^2}{4\lambda k_{\text{B}} T + 2\sigma^2}\right] \quad (5)$$

for eq 1 and an analogous expression for eq 3. This procedure corresponds to considering the statistical mean over many individual single electron transfer events that differ slightly in ΔG_0 . In passing, we note that this differs in nature from considering a sequence of electron transfer rates at thermal equilibrium in a Gaussian density of states, where a different expression results for the ensemble average as detailed in refs 18–20. As can be seen in Figure 8c, energetic disorder results in a weaker temperature dependence of the Marcus-based transfer rates at lower temperatures (eq 1). For the MLJ-based transfer rates (eq 3), the inclusion of disorder first smears out the oscillatory dependence of k on ΔG_0 , and second, it removes the temperature dependence almost entirely, consistent with our experimental findings. From this first evaluation, it seems that a MLJ-type approach that includes the effects of statistical disorder seems more appropriate to account for the experimental rate.

We now consider how the MLJ rates at room temperature depend on the choice of input parameters. The curves in Figure 8a–c were obtained using the mean values in Table 1 for ΔG_0 and λ , as well as an effective vibrational frequency $\hbar\omega_i$ of 165 meV with $S_i = 1$, and the approximation of $\lambda_o \approx 0.5\lambda$. Changing the values of the reorganization energy λ , driving force ΔG_0 , and coupling strength J_{DA} to the maximum and minimum values in Table 1 shifts both the MLJ rates and the Marcus rates on the ordinate and abscissa yet causes only very minor changes in the slope of the curves (Figure 8d). In contrast, considering a different vibrational energy and vibrational coupling by varying $\hbar\omega_i$ from 150 to 200 meV and S_i from 0.5 to 2 modifies the dependence of the MLJ rate on the driving force (Figure 8e). Both the slope and the ΔG_0 value for which the MLJ rate is at maximum are modified. In particular, the slope is rather sensitive to the value of S_i , so that an increase in S_i leads to high transfer rates in the Marcus inverted regime. The reason for this is that the dissipation of the excess energy between the S_i and the CT state is enhanced for larger vibrational energies and stronger coupling to the vibrations, which increases the electron transfer rate. This is akin to the energy gap law for nonradiative

decay.^{67,68} The maximum range of transfer rates that is consistent with the most fortunate or unfortunate combination of input parameters is shown in Figure 8f. When considering Figure 8d–f, one can see that the measured transfer rate for the MeLPPP:PCBM system is consistent with MLJ theory, provided that the vibrational dissipation of energy is not too weak, i.e., $S_i \geq 1$, and disorder is included. We recall that the yellow bar in Figure 8 indicates the ΔG_0 range for the MeLPPP:PCBM system, and that we found the electron transfer to occur with a rate that exceeds $4 \times 10^{12} \text{ s}^{-1}$. It is somewhat disconcerting that such a fast rate is only in agreement with the MLJ rate if all parameters combine in the most advantageous way within their error range, and we furthermore take $S_i = 1$. This is larger than the effective Huang–Rhys parameter observed in the absorption or emission spectra of MeLPPP, which is around 0.6.^{69,70} This suggests that there may be further contributions that facilitate such a fast rate, such as particularly strong electronic or vibrational coupling between the photoexcited, initial S_1 state and the charge separated, final CT state.^{21,22,29,71,72} Another contribution could be ultrafast hole transfer from photoexcited PCBM molecules, as their absorbance at the pump energy (3.1 eV) is in a similar range to that of MeLPPP. Fullerenes have a tightly bound S_1 state at about 1.7 eV, as well as a sequence of charge-transfer states from about 2.3 eV onward.⁷³ After absorption at 3.1 eV, fast internal conversion will occur within the manifold of CT states down to 2.3 eV, or even down to the Frenkel-type 1.7 eV state. If hole transfer takes place from the more delocalized interfullerene charge transfer state at 2.3 eV, the associated driving force is approximately 0.7 eV (see the Supporting Information). While this is well in the Marcus inverted regime, an ultrafast transfer is reasonable within the boundaries predicted by the MLJ equation, as evident by considering the upper and lower limits for the transfer rates in Figure 8f. Alternatively, hole transfer could occur from the 1.7 eV state, where the driving force of 0.1–0.2 eV is rather low, so that an ultrafast transfer is even compatible with a Marcus-type process.

It is therefore instructive to consider other systems such as P3HT:PCBM, where both electron and hole transfer are reported to occur on ultrafast time scales (50 fs for electron transfer²¹ and less than 250 fs for hole transfer⁷⁴), although these processes are well in the Marcus inverted regime, as detailed in the Supporting Information, implying that these fast processes cannot be described by Marcus theory. Figure 9 shows the dependence of the transfer rate for electron and hole transfer for P3HT:PCBM calculated according to the Marcus and Marcus–Levich–Jortner equations. The effect of disorder is already implemented, as described above with $\sigma = 75 \text{ meV}$, and we used $J_{\text{DA}} = 0.02 \text{ eV}$, $\lambda_0 = 0.27 \text{ eV}$, $S_i = 1$, and $\hbar\omega_i = 180 \text{ meV}$ as detailed in the Supporting Information.

Regarding the temperature dependence of the electron transfer, we did not observe any significant reduction for the rate of electron transfer from MeLPPP to PCBM upon cooling. This is in good agreement with a description in the framework of the MLJ theory for a disordered system. The use of the MLJ theory is required for the MeLPPP:PCBM system, as its large driving force places this donor–acceptor couple well into the Marcus inverted regime. Regarding the low-bandgap donors PCPDTBT and PTB7 with the acceptor PCBM, all three cases of an accelerating, constant, and decreasing rate with temperature are, in principle, compatible with Marcus theory and the range of experimentally determined input parameters.

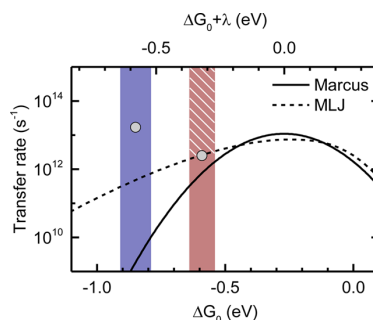


Figure 9. Calculated transfer rates for P3HT:PCBM in the framework of Marcus theory (solid line) and MLJ (dashed line). The boxes indicate the driving force for electron transfer (blue) and hole transfer (red). The gray dots indicate measured transfer rates from refs 21 and 74 in which the value for hole transfer is resolution limited (indicated by the dashed area).

If MLJ theory is applied to these materials (see Figures S1 and S2 in the Supporting Information) and a statistical energetic disorder is considered, no temperature dependence should result. Experimentally, we observed rates faster than our detection limit, which is consistent with theoretical expectations.

5. DISCUSSION

5.1. The Role of the Driving Force, Based on Marcus and MLJ Theory. Thus, in summary, we find temperature-independent electron transfer rates in excess of $2 \times 10^{12} \text{ s}^{-1}$ for all three donor:fullerene blends investigated. For PCPDTBT:PCBM and PTB7:PCBM, this experimental lower limit is consistent with the values that can be expected mathematically from Marcus theory on the basis of the input parameters. However, as shall be discussed in detail below, this fast rate renders the applicability of Marcus theory (as well as MLJ theory) itself questionable. However, for MeLPPP:PCBM, the experimentally observed lower limit for the transfer rate cannot be accounted for by Marcus theory. It can be reconciled with the value expected from Marcus–Levich–Jortner theory, which considers tunneling from the S_1 state to the CT-state surface followed by dissipation of energy through coupling to high-frequency vibrations. Numerically, the experimental rate just about agrees with the value predicted by MLJ theory provided that the errors of all input parameters combine most fortunately and a strong vibrational coupling is assumed. Alternatively, ultrafast hole transfer from PCBM to MeLPPP could account for the experimental data, in agreement with MLJ theory if the transfer takes place from a more delocalized CT state on the fullerene, or in numerical agreement with Marcus theory if the hole transfers from the S_1 of the PCBM. Therefore, we finally considered the P3HT:PCBM system, where the reported values for electron transfer disagree with both Marcus or MLJ theory. Hole transfer can also not be reconciled with Marcus theory yet can just about be brought in numerical agreement with rates predicted by MLJ theory.

These results raise two issues. First, if we presume that the mixed classical/quantum-chemical description by Marcus, Levich, and Jortner is a suitable framework to describe the electron transfer in thin donor–acceptor blend films, what could be concluded regarding the importance of the driving force? Second, do the fast rates that we observed, and that have been observed by many others for similar systems

before,^{10,21,35,75–77} actually allow for a description as a nonadiabatic transfer? We shall address these questions in sequence.

Figure 10 shows how the electron transfer rates evolve with driving force for a MLJ equation and, for comparison, a Marcus

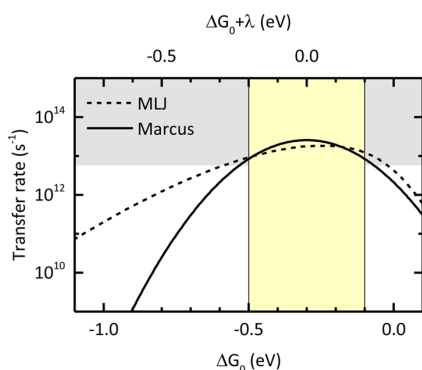


Figure 10. Electron transfer rates for eq 1 (Marcus) and eq 3 (MLJ) for PCPDTBT:PCBM with energetic disorder using $J_{\text{DA}} = 30$ meV, $\lambda = 0.3$ eV, $S_1 = 1$, $\hbar\omega_i = 165$ meV, and $\sigma = 50$ meV. The gray shaded area indicates values that are beyond our instrumental resolution. The yellow shaded area indicates the parameter range for the driving force.

equation. We include disorder and take a typical value of 0.3 eV for the reorganization energy λ in donor polymer:fullerene systems. For donor–acceptor combinations, a typical driving force ΔG_0 is in the range from -0.1 to -0.5 eV, indicated by yellow shading in Figure 10. Larger values are not common, as they compromise the open circuit voltage.^{7,8} It is evident that (i) $\Delta G_0 \approx -\lambda$, (ii) the transfer rate is only weakly dependent on ΔG_0 , and (iii) it occurs faster than 10^{13} s⁻¹. How does this impact the efficiency of electron transfer? The efficiency of electron transfer from the photoexcited donor can be calculated as $\phi_{\text{ET}} = k_{\text{ET}}/(k_{\text{ET}} + \tau_s^{-1})$, with τ_s being the lifetime of the photoexcited donor in the absence of the acceptor. If we take 0.5 ns to be a typical lifetime for a S_1 state in the donor, we find that electron transfer occurs with essentially 99.98% efficiency for $k_{\text{ET}} = 10^{13}$ s⁻¹, i.e., for any ΔG_0 in the range from -0.1 to -0.5 eV. For driving forces exceeding -0.6 eV, i.e., 2λ , the dependence of the forward transfer rate on ΔG_0 is still weak to moderate due to the fairly flat slope of the MLJ curve. Even for an electron transfer rate of 10^{11} s⁻¹, obtained with the MLJ curve for $\Delta G_0 = -1$ eV, the resulting electron transfer efficiency is still 83%. Thus, on the basis of a MLJ equation, *the driving force is irrelevant for the forward electron transfer from donor to acceptor* which occurs with virtually 100% efficiency for ΔG_0 in the range from -0.1 to -0.5 eV.

This conclusion appears to be at variance with some experimental results indicating that the yield of photogeneration does depend on driving force and is—at least qualitatively—in agreement with Marcus theory.^{8,27} This paradox is solved by considering that the overall yield of photogeneration is the product of the primary yield of the formation of the CT state and the yield of its subsequent dissociation into free charges. The latter is controlled by the competition between CT separation and loss. The loss rate may include several pathways, such as direct radiative or non-radiative recombination to the ground state,^{78,79} recombination via an intermediate triplet state,^{80,81} or back transfer to the initial singlet state.⁸² The yield of CT separation is then

determined by the trade-off between the processes of endothermic escape and exothermic geminate recombination, which both can depend on the released excess energies but in a counteracting way. For example, when comparing the transfer from one donor to different acceptors, an increase in ΔG_0 implies a reduction of the CT state energy and concomitantly a higher nonradiative decay rate from the CT state.⁷⁹ On the other hand, a large ΔG_0 can be of advantage for the escape from the CT state. It has been suggested that this allows for the generation of (vibrationally cold) states at the top of the disorder-controlled density of CT states, with associated high initial electron/hole mobility that have a faster rate of CT state dissociation.⁸³ *As a result of these competing processes, there can seem to be an apparent optimal driving force that is, however, not related to the actual charge transfer rate from the photoexcited donor to the acceptor and a description in terms of Marcus theory.*

5.2. Implications of Fast Transfer Rates Regarding

Marcus and MLJ Theory. We now turn to the second issue, the implications of the fast transfer rate. Both the Marcus and MLJ equations consider a nonadiabatic electron transfer; i.e., the frequency of vibrations is fast compared to the time required for the electron transfer.⁸⁴ Essentially, this corresponds to the requirement that thermal equilibrium is established. At room temperature, low energy vibrations can be easily excited, e.g., with a thermal energy of 26 meV. This energy corresponds to a vibrational frequency of about 6.3×10^{12} Hz, implying that a time well in excess of $(6.3 \times 10^{12} \text{ Hz})^{-1} = 160$ fs is required for nonadiabatic electron transfer. At lower temperatures, this time increases accordingly. Processes with transfer times shorter than a few 100 fs (i.e., rates larger than 10^{12} – 10^{13} s⁻¹) are therefore not suitably described by a Marcus or Marcus–Levich–Jortner type picture. In fact, donor–acceptor systems where Marcus theory was experimentally confirmed to apply had electron transfer rates in the range 10^6 – 10^{10} s⁻¹.¹⁴ These were donor and acceptor couples separated by a spacer and measured in solution. The donor–acceptor couples investigated here are neither separated by a spacer nor measured in solution, where the outer reorganization energy can be significant. Rather, our samples are in a solid film, which reduces external reorganization effects. In all cases, including the P3HT:PCBM system, the transfer rates were experimentally found in excess of 3×10^{12} s⁻¹.

This is at variance with the value of 8×10^{11} s⁻¹ reported by Ward et al. for the PTB7:PCBM system,⁹ yet it agrees with frequent literature reports that electron transfer in thin film conjugated polymer:fullerene systems frequently occurs in less than a couple of hundred femtoseconds.^{35,76,85,86}

Thus, even if these transfer rates may, for example, be numerically consistent with nonadiabatic electron transfer rates such as those by Marcus or MLJ, the thermal equilibrium which is presumed in deriving these expressions cannot be established on the fast time scales that are observed. Consequently, it is necessary to look beyond such descriptions and to apply models that include adiabatic and coherent mechanisms of electron transfer.^{21–23,76,86–88} On these short time scales, coupling to nuclear motion is an essential part to the description of electron transfer in solid state donor–acceptor blends.²¹ Similarly, the delocalization of the electron wave function over the acceptor molecules and the associated density of accepting states become crucial.^{86–88} That density of states can also depend on the morphology of the donor–acceptor blend. The importance of high intermolecular coupling and

charge delocalization has recently been highlighted by Jakowetz et al. in experiments involving pump–push–probe spectroscopy.⁷⁶ Also, suitable quantum chemical approaches are being developed in contemporary theoretical work.^{21–23}

CONCLUSION

In summary, we have shown that forward charge transfer from donor to acceptor occurs at time scales below 250 fs for PCPDTBT, PTB7, and MeLPPP blended with PCBM, even though the temperature range was varied from 300 to 12 K and the driving force ranges from -0.2 to -1.1 eV. This corresponds to the regimes from $\Delta G_0 \approx -\lambda$, where Marcus-type electron transfer rates are at maximum to the Marcus-inverted regime $\Delta G_0 \approx -6.5\lambda$. At such fast time scales, the efficiency of electron transfer exceeds 99.9%, presuming a lifetime of the donor singlet state of about 500 ps. By carefully considering the experimentally determined range of input parameters to eqs 1 and 3, we find that (i) these transfer rates can be numerically consistent with Marcus theory for PCPDTBT:PCBM and PTB7:PCBM, even at low temperatures. In contrast, for MeLPPP:PCBM, tunneling and coupling to vibrations would need to be included explicitly by MLJ theory. An analysis of values reported for P3HT:PCBM confirms this further. (ii) For realistic input parameters, ΔG_0 has no significant impact on the rate or efficiency of electron transfer from the photoexcited donor to the cold CT state. Overall, however, we note that, at such short time scales, theoretical approaches beyond the nonadiabatic transfer are required.

Our findings suggest that the most promising strategy for the design of efficient solar cells may be to accept a low driving force in favor of optimizing the open-circuit voltage, and then to aim at enhancing the subsequent charge separation rate from the relaxed CT state. Approaches for that include optimizing the packing between the acceptor or donor molecules so as to enhance interchromophore coupling, charge delocalization, and charge mobility as well as reducing the reorganization energy.^{66,72,73,76,89}

ASSOCIATED CONTENT

Supporting Information

The Supporting Information is available free of charge on the ACS Publications website at DOI: 10.1021/acs.jpcc.7b09213.

- (i) A detailed discussion of input parameters for evaluation of eqs 1 and 3, (ii) an extension of Table 2 including maximum and minimum calculated transfer rates, (iii) additional figures comparing transfer rates using eqs 1 and 3 for PCPDTBT:PCBM and PTB7:PCBM, (iv) an evaluation of transfer rates for hole transfer in the MeLPPP:PCBM system, and for both electron and hole transfer in the P3HT:PCBM system, and (v) reorganization energy and CT state energy for PCPDTBT:PCBM (PDF)

AUTHOR INFORMATION

Corresponding Author

*E-mail: Anna.Koehler@uni-bayreuth.de.

ORCID

Anna Köhler: 0000-0001-5029-4420

Author Contributions

^{||}T.U., S.W.: Both authors contributed equally.

Notes

The authors declare no competing financial interest.

ACKNOWLEDGMENTS

We are grateful to Stavros Athanasopoulos for helpful discussions and suggestions. We further thank Dieter Neher and his research group for providing the reorganization energy and CT state energy for PCPDTBT:PCBM, shown as Figure S3 in the Supporting Information. Financial support is acknowledged from the Deutsche Forschungsgemeinschaft through GRK1640 (Photophysics of Synthetic and Biological Multichromophoric Systems), from the Marie-Curie Innovative Training Network (ITN) INFORM, and from the Bayerisches Staatsministerium für Bildung und Kultus, Wissenschaft und Kunst through the grant “Solar Technologies go Hybrid” as well as the program “MINT-Lehramt plus”.

REFERENCES

- (1) Bässler, H.; Köhler, A. “Hot or Cold”: How Do Charge Transfer States at the Donor-Acceptor Interface of an Organic Solar Cell Dissociate? *Phys. Chem. Chem. Phys.* **2015**, *17*, 28451–28462.
- (2) Albrecht, S.; Vandewal, K.; Tumbleston, J. R.; Fischer, F. S.; Douglas, J. D.; Frechet, J. M.; Ludwigs, S.; Ade, H.; Salleo, A.; Neher, D. On the Efficiency of Charge Transfer State Splitting in Polymer:Fullerene Solar Cells. *Adv. Mater.* **2014**, *26*, 2533–2539.
- (3) Deibel, C.; Strobel, T.; Dyakonov, V. Role of the Charge Transfer State in Organic Donor–Acceptor Solar Cells. *Adv. Mater.* **2010**, *22*, 4097–4111.
- (4) Hood, S. N.; Kassal, I. Entropy and Disorder Enable Charge Separation in Organic Solar Cells. *J. Phys. Chem. Lett.* **2016**, *7*, 4495–4500.
- (5) Shoaee, S.; Clarke, T. M.; Huang, C.; Barlow, S.; Marder, S. R.; Heeney, M.; McCulloch, I.; Durrant, J. R. Acceptor Energy Level Control of Charge Photogeneration in Organic Donor/Acceptor Blends. *J. Am. Chem. Soc.* **2010**, *132*, 12919–12926.
- (6) Pensack, R. D.; Asbury, J. B. Barrierless Free Carrier Formation in an Organic Photovoltaic Material Measured with Ultrafast Vibrational Spectroscopy. *J. Am. Chem. Soc.* **2009**, *131*, 15986–15987.
- (7) Veldman, D.; Meskers, S. C. J.; Janssen, R. A. J. The Energy of Charge-Transfer States in Electron Donor-Acceptor Blends: Insight into the Energy Losses in Organic Solar Cells. *Adv. Funct. Mater.* **2009**, *19*, 1939–1948.
- (8) Hendriks, K. H.; Wijkema, A. S.; van Franeker, J. J.; Wienk, M. M.; Janssen, R. A. Dichotomous Role of Exciting the Donor or the Acceptor on Charge Generation in Organic Solar Cells. *J. Am. Chem. Soc.* **2016**, *138*, 10026–10031.
- (9) Ward, A. J.; Ruseckas, A.; Kareem, M. M.; Ebenhoch, B.; Serrano, L. A.; Al-Eid, M.; Fitzpatrick, B.; Rotello, V. M.; Cooke, G.; Samuel, I. D. W. The Impact of Driving Force on Electron Transfer Rates in Photovoltaic Donor-Acceptor Blends. *Adv. Mater.* **2015**, *27*, 2496–2500.
- (10) Liu, J.; Chen, S.; Qian, D.; Gautam, B.; Yang, G.; Zhao, J.; Bergqvist, J.; Zhang, F.; Ma, W.; Ade, H.; et al. Fast Charge Separation in a Non-Fullerene Organic Solar Cell with a Small Driving Force. *Nat. Energy* **2016**, *1*, 16089.
- (11) Kawashima, K.; Tamai, Y.; Ohkita, H.; Osaka, I.; Takimiya, K. High-Efficiency Polymer Solar Cells with Small Photon Energy Loss. *Nat. Commun.* **2015**, *6*, 10085.
- (12) Marcus, R. A.; Sutin, N. Electron Transfers in Chemistry and Biology. *Biochim. Biophys. Acta, Rev. Bioenerg.* **1985**, *811*, 265–322.
- (13) Marcus, R. A. Exchange Reactions and Electron Transfer Reactions Including Isotopic Exchange. Theory of Oxidation-Reduction Reactions Involving Electron Transfer. Part 4.-a Statistical-Mechanical Basis for Treating Contributions from Solvent, Ligands, and Inert Salt. *Discuss. Faraday Soc.* **1960**, *29*, 21–31.
- (14) Miller, J. R.; Calcaterra, L. T.; Closs, G. L. Intramolecular Long-Distance Electron Transfer in Radical Anions. The Effects of Free

- Energy and Solvent on the Reaction Rates. *J. Am. Chem. Soc.* **1984**, *106*, 3047–3049.
- (15) Hoffmann, S. T.; Athanasopoulos, S.; Beljonne, D.; Bäessler, H.; Köhler, A. How Do Triplets and Charges Move in Disordered Organic Semiconductors? A Monte Carlo Study Comprising the Equilibrium and Nonequilibrium Regime. *J. Phys. Chem. C* **2012**, *116*, 16371–16383.
- (16) Bäessler, H.; Köhler, A. Charge Transport in Organic Semiconductors. In *Unimolecular and Supramolecular Electronics I: Chemistry and Physics Meet at Metal-Molecule Interfaces*; Metzger, R. M., Ed.; Springer: Berlin, Heidelberg, 2012; pp 1–65.
- (17) Köhler, A.; Bäessler, H. Electronic and Optical Processes of Organic Semiconductors. *Electronic Processes in Organic Semiconductors*; Wiley-VCH: Weinheim, Germany, 2015; pp 193–305.
- (18) Fishchuk, I. I.; Kadashchuk, A.; Hoffmann, S. T.; Athanasopoulos, S.; Genoe, J.; Bäessler, H.; Köhler, A. Unified Description for Hopping Transport in Organic Semiconductors Including Both Energetic Disorder and Polaronic Contributions. *Phys. Rev. B: Condens. Matter Mater. Phys.* **2013**, *88*, 125202.
- (19) Fishchuk, I. I.; Kadashchuk, A.; Sudha Devi, L.; Heremans, P.; Bäessler, H.; Köhler, A. Triplet Energy Transfer in Conjugated Polymers. II. A Polaron Theory Description Addressing the Influence of Disorder. *Phys. Rev. B: Condens. Matter Mater. Phys.* **2008**, *78*, 045211.
- (20) Sudha Devi, L.; Al-Suti, M. K.; Dosche, C.; Khan, M. S.; Friend, R. H.; Köhler, A. Triplet Energy Transfer in Conjugated Polymers. I. Experimental Investigation of a Weakly Disordered Compound. *Phys. Rev. B: Condens. Matter Mater. Phys.* **2008**, *78*, 045210.
- (21) Falke, S. M.; Rozzi, C. A.; Brida, D.; Maiuri, M.; Amato, M.; Sommer, E.; De Sio, A.; Rubio, A.; Cerullo, G.; Molinari, E.; et al. Coherent Ultrafast Charge Transfer in an Organic Photovoltaic Blend. *Science* **2014**, *344*, 1001–1005.
- (22) Bredas, J.-L.; Sargent, E. H.; Scholes, G. D. Photovoltaic Concepts Inspired by Coherence Effects in Photosynthetic Systems. *Nat. Mater.* **2016**, *16*, 35–44.
- (23) Bittner, E. R.; Silva, C. Noise-Induced Quantum Coherence Drives Photo-Carrier Generation Dynamics at Polymeric Semiconductor Heterojunctions. *Nat. Commun.* **2014**, *5*, 3119.
- (24) Tamura, H.; Burghardt, I. Potential Barrier and Excess Energy for Electron–Hole Separation from the Charge-Transfer Exciton at Donor–Acceptor Heterojunctions of Organic Solar Cells. *J. Phys. Chem. C* **2013**, *117*, 15020–15025.
- (25) Tamura, H.; Burghardt, I.; Tsukada, M. Exciton Dissociation at Thiophene/Fullerene Interfaces: The Electronic Structures and Quantum Dynamics. *J. Phys. Chem. C* **2011**, *115*, 10205–10210.
- (26) Tamura, H.; Martinazzo, R.; Ruckebauer, M.; Burghardt, I. Quantum Dynamics of Ultrafast Charge Transfer at an Oligothiophene–Fullerene Heterojunction. *J. Chem. Phys.* **2012**, *137*, 22A540.
- (27) Coffey, D. C.; Larson, B. W.; Hains, A. W.; Whitaker, J. B.; Kopidakis, N.; Boltalina, O. V.; Strauss, S. H.; Rumbles, G. An Optimal Driving Force for Converting Excitons into Free Carriers in Excitonic Solar Cells. *J. Phys. Chem. C* **2012**, *116*, 8916–8923.
- (28) Liu, T.; Troisi, A. Absolute Rate of Charge Separation and Recombination in a Molecular Model of the P3ht/Pcbm Interface. *J. Phys. Chem. C* **2011**, *115*, 2406–2415.
- (29) Savoie, B. M.; Rao, A.; Bakulin, A. A.; Gelinis, S.; Movaghar, B.; Friend, R. H.; Marks, T. J.; Ratner, M. A. Unequal Partnership: Asymmetric Roles of Polymeric Donor and Fullerene Acceptor in Generating Free Charge. *J. Am. Chem. Soc.* **2014**, *136*, 2876–2884.
- (30) Peet, J.; Kim, J. Y.; Coates, N. E.; Ma, W. L.; Moses, D.; Heeger, A. J.; Bazan, G. C. Efficiency Enhancement in Low-Bandgap Polymer Solar Cells by Processing with Alkane Dithiols. *Nat. Mater.* **2007**, *6*, 497–500.
- (31) Boland, P.; Lee, K.; Namkoong, G. Device Optimization in Pcpdttb:Pcbm Plastic Solar Cells. *Sol. Energy Mater. Sol. Cells* **2010**, *94*, 915–920.
- (32) Scherf, U.; Müllen, K. Polyarylenes and Poly(Arylenevinylenes), 7. A Soluble Ladder Polymer Via Bridging of Functionalized Poly(P-Phenylene)-Precursors. *Makromol. Chem., Rapid Commun.* **1991**, *12*, 489–497.
- (33) Scherf, U.; Bohnen, A.; Müllen, K. Polyarylenes and Poly(Arylenevinylene)S, 9 the Oxidized States of a (1,4-Phenylene) Ladder Polymer. *Makromol. Chem.* **1992**, *193*, 1127–1133.
- (34) Vandewal, K.; Tvingstedt, K.; Gadisa, A.; Inganäs, O.; Manca, J. V. Relating the Open-Circuit Voltage to Interface Molecular Properties of Donor:Acceptor Bulk Heterojunction Solar Cells. *Phys. Rev. B: Condens. Matter Mater. Phys.* **2010**, *81*, 125204.
- (35) Grancini, G.; Maiuri, M.; Fazzi, D.; Petrozza, A.; Egelhaaf, H. J.; Brida, D.; Cerullo, G.; Lanzani, G. Hot Exciton Dissociation in Polymer Solar Cells. *Nat. Mater.* **2012**, *12*, 29–33.
- (36) Szarko, J. M.; Rolczynski, B. S.; Lou, S. J.; Xu, T.; Strzalka, J.; Marks, T. J.; Yu, L.; Chen, L. X. Photovoltaic Function and Exciton/Charge Transfer Dynamics in a Highly Efficient Semiconducting Copolymer. *Adv. Funct. Mater.* **2014**, *24*, 10–26.
- (37) Etzold, F.; Howard, I. A.; Forler, N.; Cho, D. M.; Meister, M.; Mangold, H.; Shu, J.; Hansen, M. R.; Müllen, K.; Laquai, F. The Effect of Solvent Additives on Morphology and Excited-State Dynamics in Pcpdttb:Pcbm Photovoltaic Blends. *J. Am. Chem. Soc.* **2012**, *134*, 10569–10583.
- (38) Müller, J. G.; Lupton, J. M.; Feldmann, J.; Lemmer, U.; Scharber, M. C.; Sariciftci, N. S.; Brabec, C. J.; Scherf, U. Ultrafast Dynamics of Charge Carrier Photogeneration and Geminate Recombination in Conjugated Polymer:Fullerene Solar Cells. *Phys. Rev. B: Condens. Matter Mater. Phys.* **2005**, *72*, 195208.
- (39) Wohlgenannt, M.; Jiang, X. M.; Vardeny, Z. V. Spin-Dependent Exciton Formation Rates in Π -Conjugated Oligomers and Polymers. *Synth. Synth. Met.* **2003**, *137*, 1069–1071.
- (40) Luzzati, S.; Scharber, M.; Catellani, M.; Giacalone, F.; Segura, J. L.; Martin, N.; Neugebauer, H.; Sariciftci, N. S. Long-Lived Photoinduced Charges in Donor–Acceptor Anthraquinone-Substituted Thiophene Copolymers. *J. Phys. Chem. B* **2006**, *110*, 5351–5358.
- (41) Marcus, R. A. Electron Transfer Reactions in Chemistry. Theory and Experiment. *Rev. Mod. Phys.* **1993**, *65*, 599–610.
- (42) Kestner, N. R.; Logan, J.; Jortner, J. Thermal Electron Transfer Reactions in Polar Solvents. *J. Phys. Chem.* **1974**, *78*, 2148–2166.
- (43) Jortner, J. Temperature Dependent Activation Energy for Electron Transfer between Biological Molecules. *J. Chem. Phys.* **1976**, *64*, 4860–4867.
- (44) Dennler, G.; Scharber, M. C.; Brabec, C. J. Polymer–Fullerene Bulk-Heterojunction Solar Cells. *Adv. Mater.* **2009**, *21*, 1323–1338.
- (45) Leng, C.; Qin, H.; Si, Y.; Zhao, Y. Theoretical Prediction of the Rate Constants for Exciton Dissociation and Charge Recombination to a Triplet State in Pcpdttb with Different Fullerene Derivatives. *J. Phys. Chem. C* **2014**, *118*, 1843–1855.
- (46) Vandewal, K.; Tvingstedt, K.; Gadisa, A.; Inganäs, O.; Manca, J. V. On the Origin of the Open-Circuit Voltage of Polymer–Fullerene Solar Cells. *Nat. Mater.* **2009**, *8*, 904–909.
- (47) Scharsich, C.; Fischer, F. S. U.; Wilma, K.; Hildner, R.; Ludwigs, S.; Köhler, A. Revealing Structure Formation in Pcpdttb by Optical Spectroscopy. *J. Polym. Sci., Part B: Polym. Phys.* **2015**, *53*, 1416–1430.
- (48) Jarzab, D.; Cordella, F.; Gao, J.; Scharber, M.; Egelhaaf, H.-J.; Loi, M. A. Low-Temperature Behaviour of Charge Transfer Excitons in Narrow-Bandgap Polymer-Based Bulk Heterojunctions. *Adv. Energy Mater.* **2011**, *1*, 604–609.
- (49) Kraus, H.; Heiber, M. C.; Vath, S.; Kern, J.; Deibel, C.; Sperlich, A.; Dyakonov, V. Analysis of Triplet Exciton Loss Pathways in Ptb7:Pc71bm Bulk Heterojunction Solar Cells. *Sci. Rep.* **2016**, *6*, 29158.
- (50) Carsten, B.; Szarko, J. M.; Son, H. J.; Wang, W.; Lu, L.; He, F.; Rolczynski, B. S.; Lou, S. J.; Chen, L. X.; Yu, L. Examining the Effect of the Dipole Moment on Charge Separation in Donor–Acceptor Polymers for Organic Photovoltaic Applications. *J. Am. Chem. Soc.* **2011**, *133*, 20468–20475.
- (51) Liang, Y.; Xu, Z.; Xia, J.; Tsai, S. T.; Wu, Y.; Li, G.; Ray, C.; Yu, L. For the Bright Future–Bulk Heterojunction Polymer Solar Cells with Power Conversion Efficiency of 7.4%. *Adv. Mater.* **2010**, *22*, E135–E138.

- (52) Hoffmann, S. T.; Scheler, E.; Koenen, J.-M.; Forster, M.; Scherf, U.; Strohriegel, P.; Bäessler, H.; Köhler, A. Triplet Energy Transfer in Conjugated Polymers. Iii. An Experimental Assessment Regarding the Influence of Disorder on Polaronic Transport. *Phys. Rev. B: Condens. Matter Mater. Phys.* **2010**, *81*, 165208.
- (53) Peng, Z.; Xia, Y.; Gao, F.; Xiong, K.; Hu, Z.; James, D. I.; Chen, J.; Wang, E.; Hou, L. A Dual Ternary System for Highly Efficient Ito-Free Inverted Polymer Solar Cells. *J. Mater. Chem. A* **2015**, *3*, 18365–18371.
- (54) Gerhard, M.; Arndt, A. P.; Howard, I. A.; Rahimi-Iman, A.; Lemmer, U.; Koch, M. Temperature- and Energy-Dependent Separation of Charge-Transfer States in Ptb7-Based Organic Solar Cells. *J. Phys. Chem. C* **2015**, *119*, 28309–28318.
- (55) Liu, T.; Cheung, D. L.; Troisi, A. Structural Variability and Dynamics of the P3ht/Pcbm Interface and Its Effects on the Electronic Structure and the Charge-Transfer Rates in Solar Cells. *Phys. Chem. Chem. Phys.* **2011**, *13*, 21461–21470.
- (56) Hoke, E. T.; Vandewal, K.; Bartelt, J. A.; Mateker, W. R.; Douglas, J. D.; Noriega, R.; Graham, K. R.; Fréchet, J. M. J.; Salleo, A.; McGehee, M. D. Recombination in Polymer:Fullerene Solar Cells with Open-Circuit Voltages Approaching and Exceeding 1.0 V. *Adv. Energy Mater.* **2013**, *3*, 220–230.
- (57) Guldi, D. M.; Prato, M. Excited-State Properties of C60 Fullerene Derivatives. *Acc. Chem. Res.* **2000**, *33*, 695–703.
- (58) Tasch, S.; Niko, A.; Leising, G.; Scherf, U. Highly Efficient Electroluminescence of New Wide Band Gap Ladder-Type Poly(Para-Phenylenes). *Appl. Phys. Lett.* **1996**, *68*, 1090–1092.
- (59) Tvingstedt, K.; Vandewal, K.; Gadisa, A.; Zhang, F.; Manca, J.; Inganäs, O. Electroluminescence from Charge Transfer States in Polymer Solar Cells. *J. Am. Chem. Soc.* **2009**, *131*, 11819–11824.
- (60) Clarke, T.; Ballantyne, A.; Jamieson, F.; Brabec, C.; Nelson, J.; Durrant, J. Transient Absorption Spectroscopy of Charge Photogeneration Yields and Lifetimes in a Low Bandgap Polymer/Fullerene Film. *Chem. Commun.* **2008**, *1*, 89–91.
- (61) Faist, M. A.; Kirchartz, T.; Gong, W.; Ashraf, R. S.; McCulloch, I.; de Mello, J. C.; Ekins-Daukes, N. J.; Bradley, D. D. C.; Nelson, J. Competition between the Charge Transfer State and the Singlet States of Donor or Acceptor Limiting the Efficiency in Polymer:Fullerene Solar Cells. *J. Am. Chem. Soc.* **2012**, *134*, 685–692.
- (62) He, Y.; Chen, H.-Y.; Hou, J.; Li, Y. Indene-C60 Bisadduct: A New Acceptor for High-Performance Polymer Solar Cells. *J. Am. Chem. Soc.* **2010**, *132*, 1377–1382.
- (63) Arif, M.; Yang, K.; Li, L.; Yu, P.; Guha, S.; Gangopadhyay, S.; Förster, M.; Scherf, U. Harvesting Triplet Excitons for Application in Polymer Solar Cells. *Appl. Phys. Lett.* **2009**, *94*, 063307.
- (64) Coropceanu, V.; Cornil, J.; da Silva Filho, D. A.; Olivier, Y.; Silbey, R.; Brédas, J.-L. Charge Transport in Organic Semiconductors. *Chem. Rev.* **2007**, *107*, 926–952.
- (65) Brédas, J.-L.; Beljonne, D.; Coropceanu, V.; Cornil, J. Charge-Transfer and Energy-Transfer Processes in π -Conjugated Oligomers and Polymers: A Molecular Picture. *Chem. Rev.* **2004**, *104*, 4971–5004.
- (66) Vandewal, K.; Benduhn, J.; Schellhammer, K. S.; Vangerven, T.; Rückert, J. E.; Piersimoni, F.; Scholz, R.; Zeika, O.; Fan, Y.; Barlow, S.; et al. Absorption Tails of Donor:C60 Blends Provide Insight into Thermally Activated Charge-Transfer Processes and Polaron Relaxation. *J. Am. Chem. Soc.* **2017**, *139*, 1699–1704.
- (67) Freed, K. F.; Jortner, J. Multiphonon Processes in the Nonradiative Decay of Large Molecules. *J. Chem. Phys.* **1970**, *52*, 6272–6291.
- (68) Englman, R.; Jortner, J. The Energy Gap Law for Radiationless Transitions in Large Molecules. *Mol. Phys.* **1970**, *18*, 145–164.
- (69) Hoffmann, S. T.; Bäessler, H.; Köhler, A. What Determines Inhomogeneous Broadening of Electronic Transitions in Conjugated Polymers? *J. Phys. Chem. B* **2010**, *114*, 17037–17048.
- (70) Khan, A. L. T.; Sreearunothai, P.; Herz, L. M.; Banach, M. J.; Köhler, A. Morphology-Dependent Energy Transfer within Polyfluorene Thin Films. *Phys. Rev. B: Condens. Matter Mater. Phys.* **2004**, *69*, 085201.
- (71) Janković, V.; Vukmirović, N. Origin of Space-Separated Charges in Photoexcited Organic Heterojunctions on Ultrafast Time Scales. *Phys. Rev. B: Condens. Matter Mater. Phys.* **2017**, *95*, 075308.
- (72) Kocherzhenko, A. A.; Lee, D.; Forsuelo, M. A.; Whaley, K. B. Coherent and Incoherent Contributions to Charge Separation in Multichromophore Systems. *J. Phys. Chem. C* **2015**, *119*, 7590–7603.
- (73) Hahn, T.; Tscheuschner, S.; Saller, C.; Strohriegel, P.; Boregowda, P.; Mukhopadhyay, T.; Patil, S.; Neher, D.; Bäessler, H.; Köhler, A. Role of Intrinsic Photogeneration in Single Layer and Bilayer Solar Cells with C60 and Pcbm. *J. Phys. Chem. C* **2016**, *120*, 25083–25091.
- (74) Cook, S.; Katoh, R.; Furube, A. Ultrafast Studies of Charge Generation in Pcbm:P3ht Blend Films Following Excitation of the Fullerene Pcbm. *J. Phys. Chem. C* **2009**, *113*, 2547–2552.
- (75) Chen, K.; Barker, A. J.; Reish, M. E.; Gordon, K. C.; Hodgkiss, J. M. Broadband Ultrafast Photoluminescence Spectroscopy Resolves Charge Photogeneration Via Delocalized Hot Excitons in Polymer:Fullerene Photovoltaic Blends. *J. Am. Chem. Soc.* **2013**, *135*, 18502–18512.
- (76) Jakowetz, A. C.; Bohm, M. L.; Zhang, J.; Sadhanala, A.; Huettnner, S.; Bakulin, A. A.; Rao, A.; Friend, R. H. What Controls the Rate of Ultrafast Charge Transfer and Charge Separation Efficiency in Organic Photovoltaic Blends. *J. Am. Chem. Soc.* **2016**, *138*, 11672–11679.
- (77) Kozlov, O. V.; Pavelyev Vlad, G.; de Gier Hilde, D.; Remco Havenith, W. A.; van Loosdrecht Paul, H. M.; Hummelen Jan, C.; Pshenichnikov Maxim, S. Ultrafast Electron and Hole Transfer in Bulk Heterojunctions of Low-Bandgap Polymers. *Org. Photonics Photovolt.* **2016**, *4*, 24–34.
- (78) Vandewal, K.; Albrecht, S.; Hoke, E. T.; Graham, K. R.; Widmer, J.; Douglas, J. D.; Schubert, M.; Mateker, W. R.; Bloking, J. T.; Burkhard, G. F.; et al. Efficient Charge Generation by Relaxed Charge-Transfer States at Organic Interfaces. *Nat. Mater.* **2013**, *13*, 63–68.
- (79) Benduhn, J.; Tvingstedt, K.; Piersimoni, F.; Ullbrich, S.; Fan, Y.; Tropiano, M.; McGarry, K. A.; Zeika, O.; Riede, M. K.; Douglas, C. J.; et al. Intrinsic Non-Radiative Voltage Losses in Fullerene-Based Organic Solar Cells. *Nat. Energy* **2017**, *2*, 17053.
- (80) Kraffert, F.; Steyrlleuthner, R.; Albrecht, S.; Neher, D.; Scharber, M. C.; Bittl, R.; Behrends, J. Charge Separation in Pcpdttb:Pcbm Blends from an Epr Perspective. *J. Phys. Chem. C* **2014**, *118*, 28482–28493.
- (81) Rao, A.; Chow, P. C. Y.; Gelinas, S.; Schlenker, C. W.; Li, C.-Z.; Yip, H.-L.; Jen, A. K. Y.; Ginger, D. S.; Friend, R. H. The Role of Spin in the Kinetic Control of Recombination in Organic Photovoltaics. *Nature* **2013**, *500*, 435–439.
- (82) Morteani, A. C.; Sreearunothai, P.; Herz, L. M.; Friend, R. H.; Silva, C. Exciton Regeneration at Polymeric Semiconductor Heterojunctions. *Phys. Rev. Lett.* **2004**, *92*, 247402.
- (83) Melianas, A.; Pranculis, V.; Xia, Y.; Felekidis, N.; Inganäs, O.; Gulbinas, V.; Kemerink, M. Photogenerated Carrier Mobility Significantly Exceeds Injected Carrier Mobility in Organic Solar Cells. *Adv. Energy Mater.* **2017**, *7*, 1602143.
- (84) May, V.; Kühn, O. *Electron Transfer. Charge and Energy Transfer Dynamics in Molecular Systems*; Wiley-VCH Verlag GmbH & Co. KGaA: Berlin, Germany, 2011; pp 309–433.
- (85) Bakulin, A. A.; Rao, A.; Pavelyev, V. G.; van Loosdrecht, P. H. M.; Pshenichnikov, M. S.; Niedzialek, D.; Cornil, J.; Beljonne, D.; Friend, R. H. The Role of Driving Energy and Delocalized States for Charge Separation in Organic Semiconductors. *Science* **2012**, *335*, 1340–1344.
- (86) Herrmann, D.; Niesar, S.; Scharsich, C.; Köhler, A.; Stutzmann, M.; Riedle, E. Role of Structural Order and Excess Energy on Ultrafast Free Charge Generation in Hybrid Polythiophene/Si Photovoltaics Probed in Real Time by near-Infrared Broadband Transient Absorption. *J. Am. Chem. Soc.* **2011**, *133*, 18220–18233.
- (87) Kästner, C.; Vandewal, K.; Egbe, D. A. M.; Hoppe, H. Revelation of Interfacial Energetics in Organic Multiheterojunctions. *Adv. Sci.* **2017**, *4*, 1600331.

(88) Zimmerman, J. D.; Xiao, X.; Renshaw, C. K.; Wang, S.; Diev, V. V.; Thompson, M. E.; Forrest, S. R. Independent Control of Bulk and Interfacial Morphologies of Small Molecular Weight Organic Heterojunction Solar Cells. *Nano Lett.* **2012**, *12*, 4366–4371.

(89) Tscheuschner, S.; Bäessler, H.; Huber, K.; Köhler, A. A Combined Theoretical and Experimental Study of Dissociation of Charge Transfer States at the Donor–Acceptor Interface of Organic Solar Cells. *J. Phys. Chem. B* **2015**, *119*, 10359–10371.

Supporting Information

The Impact of Driving Force and Temperature on the Electron Transfer in Donor-Acceptor Blend Systems

Thomas Unger^{1#}, Stefan Wedler^{1#}, Frank-Julian Kahle¹, Ullrich Scherf³, Heinz Bässler², Anna
Köhler^{1,2*}

¹Experimental Physics II, University of Bayreuth, 95447 Bayreuth, Germany.

²Bayreuth Institut of Macromolecular Research (BIMF), University of Bayreuth, 95447
Bayreuth, Germany.

³Makromolekulare Chemie, Bergische Universität Wuppertal, 42119 Wuppertal

*e-Mail: Anna.Koehler@uni-bayreuth.de

both authors contributed equally

I Energy levels from literature

1.1 Parameters for Marcus theory

The description of electron transfer rates in the framework of classical Marcus theory is based on the driving force ΔG_0 , the reorganization energy λ and the electronic coupling J_{DA} . We estimate the driving force ΔG_0 as the difference between the energy of the singlet state E_{S1} and the energy of the charge transfer state E_{CT} . In what follows we shall discuss the values we used for these energies, which are summarized in Table 1 in the main text.

Singlet energy E_{S1}

PCPDTBT: We take a value of 1.5 ± 0.10 eV, consistent with the spectra and calculations reported by Scharsich et al.¹ and Jarzab et al.² In both cases the value is taken from the intersection of absorption and emission spectra.

PTB7: We take a value of 1.67 ± 0.05 eV. Kraus et al. reported 1.65 eV³ (from the intersection of absorption and emission spectra), while 1.68 eV are reported by Son et al.⁴ (taken from the onset of absorption), and Liang et al.⁵ (taken from the onset of absorption).

MeLPPP: We take a value of 2.7 eV ± 0.05 eV from the intersection of absorption and emission spectra reported by Hoffmann et al.⁶

Energy of the charge transfer state E_{CT}

PCPDTBT: For PCPDTBT, Kurpiers et al. reported the CT-Energy in blends with PCBM to be 1.30 eV (see section V). We thus consider a CT energy of 1.30 ± 0.05 eV to be a reliable estimate.

PTB7: Peng et al. fitted the EQE data to give a CT energy of about 1.4 eV.⁷ Based on the open-circuit voltage, Kraus et al. estimate a CT energy of 1.3 eV,³ consistent with a value of 1.32 eV reported by Gerhard et al.⁸ We thus consider a mean value of 1.35 ± 0.05 eV

MeLPPP: There are no reports in literature to the best of our knowledge. We performed EQE- and EL-measurements to determine E_{CT} as detailed in the manuscript.

Reorganization energy λ

PCPDTBT: For PCPDTBT, Kurpiers et al. reported the reorganization energy to be 0.22 eV from fitting the EQE and EL and considering the Stokes' shift (see section V). As this DFT calculations by Leng et al. further yield a value of 0.4 eV for C-PCPDTBT.⁹ For our calculations, we adopted a value of 0.30 ± 0.10 eV.

PTB7: Fits to the EQE by Peng et al. give $\lambda = 0.3$ eV.⁷ This may be compared to a value of 0.4 eV that is reported by Ward et al.¹⁰ We consider thus that $\lambda = 0.35 \pm 0.05$ eV is a reasonable estimate.

MeLPPP: See main manuscript.

Electronic coupling J_{DA}

Leng and coworkers considered the electron transfer from PCPDTBT to PCBM. Their DFT calculations give a value of about 20 meV for J_{DA} .⁹ For other material systems, similar values are obtained. For example, for the combination of P3HT with PCBM, electronic couplings from 20 to 30 meV are reported, depending on the intermolecular distance.¹¹ We estimate thus that $J_{DA}=30\pm 20$ meV gives a reliable parameter range for all materials considered.

1.2 Alternative estimation for ΔG_0 from electronic frontier orbitals

A common estimate of the driving force is to take the ionization potential IP of the donor molecule, to subtract the electron affinity EA of the acceptor molecule and to subtract the singlet energy E_{S1} of the donor molecule, $-\Delta G_0 = (IP - EA) - E_{S1}$. In this section we estimate ΔG_0 by this method. First we discuss the energy values taken from literature before we summarize them and the resulting ΔG_0 in table S1. This method results in very similar values for ΔG_0 within the reported parameter ranges. In addition, the resulting transfer rates according to Marcus theory (eq 1 in the main text) and the possible range of their values are included in Table S1 as well.

EA PCBM

As detailed in Hahn et al.,¹² based on the gas phase electron affinity and the polarization energy, the value of the electron affinity of the fullerene C60 is expected to be at about 3.7 eV. Values reported for PCBM on the basis of cyclic voltammetry range around 3.7-3.9 eV.¹³⁻¹⁵ We therefore use a value of **3.8±0.1 eV**.

Ionization Potential IP

PCPDTBT: DFT calculations by Leng et al. using CAM-B3LYP results in 5.0 eV.⁹ UPS measurements with PCPDTBT on different substrates give values of 5.1 eV on PEDT:PSS, 4.9 eV on ITO and 4.8 eV on gold.¹⁶ In CV measurements, both oxidation and reduction are shown reversibly, giving a value of 5.3 eV.¹⁷ We consider that **5.05 ± 0.1 eV** is a realistic value for the IP of PCPDTBT, having taken the standard deviation of the values to estimate the error.

PTB7: A value of 5.15 eV is reported by cyclic voltammetry measurements.⁴ We estimate an error of 0.1 eV.

MeLPPP: The ionization potential of MeLPPP was determined to be 5.3 ± 0.05 eV by UPS.¹⁸

Table S1: Input parameters and the resulting Marcus transfer rate, based on considering $-\Delta G_0 = (\text{IP} - \text{EA}) - E_{\text{S1}}$. Values and estimated errors are taken from literature as described in the text.

		PCPDTBT	PTB7	MeLPPP
IP (eV)		5.05±0.10	5.15±0.05	5.3±0.1
E_{S1} (eV)		1.50 ± 0.10 ^[1,2]	1.67 ± 0.05 ^[3-5]	2.7±0.05
$-\Delta G_0$ (eV)		0.25±0.17	0.32±0.12	1.2±0.15
Temperature (K)		Marcus transfer rate (s ⁻¹)		
295	min	2.2×10^{11}	1.0×10^{12}	9.8×10^{-33}
	mean	2.6×10^{13}	2.5×10^{13}	8.2×10^{-14}
	max	9.4×10^{13}	7.7×10^{13}	3.5×10^{-2}
200	min	7.9×10^{10}	7.6×10^{11}	7.2×10^{-54}
	mean	3.0×10^{13}	3.0×10^{13}	2.2×10^{-26}
	max	1.1×10^{14}	9.4×10^{13}	2.0×10^{-9}
150	min	2.6×10^{10}	5.4×10^{11}	9.1×10^{-76}
	mean	3.3×10^{13}	3.4×10^{13}	2.0×10^{-39}
	max	1.3×10^{14}	1.1×10^{14}	6.0×10^{-17}
100	min	2.7×10^9	2.5×10^{11}	1.3×10^{-119}
	mean	3.7×10^{13}	4.1×10^{13}	1.5×10^{-65}
	max	1.6×10^{14}	1.3×10^{14}	4.9×10^{-32}
12	min	1.8×10^{-14}	4.2×10^2	
	mean	1.8×10^{13}	6.8×10^{13}	$< 10^{-300}$
	max	4.7×10^{14}	3.8×10^{14}	

II Minimum and maximum transfer rate in the framework of Marcus theory

Table S2: Transfer rates determined according to eq 1 in the manuscript for different temperatures, along with the experimentally measured lower limits for the transfer rates. The minimum and maximum values result from the parameter ranges as discussed above.

Temperature (K)		PCPDTBT	PTB7	MeLPPP
expected from Marcus theory in s ⁻¹				
295	min	2.9×10^{11}	1.5×10^{12}	2.4×10^{-22}
	mean	2.0×10^{13}	2.5×10^{13}	2.6×10^{-10}
	max	9.4×10^{13}	7.7×10^{13}	1.5×10^{-2}
200	min	1.2×10^{11}	1.4×10^{12}	1.5×10^{-38}
	mean	2.1×10^{13}	3.0×10^{13}	3.1×10^{-21}
	max	1.1×10^{14}	9.4×10^{13}	5.8×10^{-10}
150	min	4.8×10^{10}	1.3×10^{12}	2.4×10^{-55}
	mean	2.0×10^{13}	3.4×10^{13}	1.5×10^{-32}
	max	1.3×10^{14}	1.1×10^{14}	1.1×10^{-17}
100	min	6.7×10^9	9.0×10^{11}	5.9×10^{-89}
	mean	1.8×10^{13}	4.1×10^{13}	3.1×10^{-55}
	max	1.6×10^{14}	1.3×10^{14}	4.1×10^{-33}
12	min	3.1×10^{-11}	1.6×10^7	
	mean	4.4×10^{10}	6.8×10^{13}	$< 10^{-300}$
	max	4.7×10^{14}	3.8×10^{14}	
experimental values in s ⁻¹				
295		$(2.9 \pm 1.8) \times 10^{12}$	$(2.6 \pm 0.2) \times 10^{12}$	$(4.1 \pm 0.2) \times 10^{12}$
12		$(2.2 \pm 0.7) \times 10^{12}$	$(2.4 \pm 0.1) \times 10^{12}$	$(4.5 \pm 0.2) \times 10^{12}$

III Comparison of transfer rates for the low-bandgap polymer:PCBM blends

3.1 PCPDTBT:PCBM

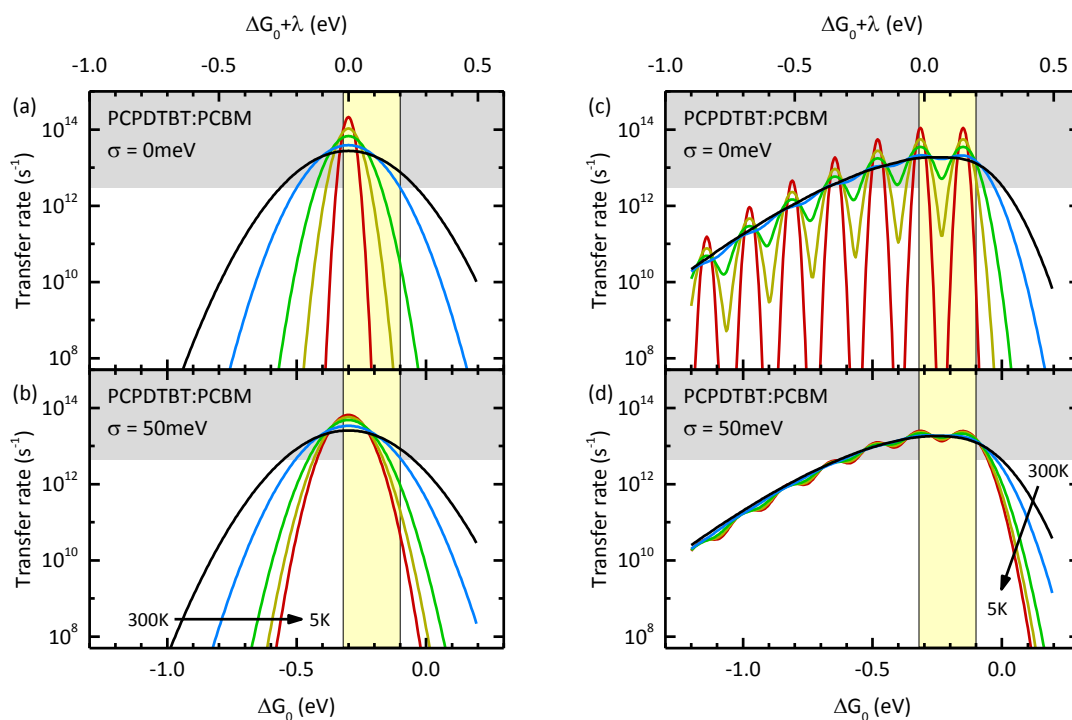


Fig. S1

Marcus rates (a,b) and Marcus-Levich-Jortner rates (c,d) of the PCPDTBT:PCBM blend as a function of driving force for different temperatures (300K, 150K, 50K, 20K and 5K) without disorder (a,c) and with energetic disorder of $\sigma = 50$ meV (b,d). The grey shaded area indicates values that are beyond our instrumental resolution. The yellow shaded indicates the parameter range for the driving force.

3.2 PTB7:PCBM

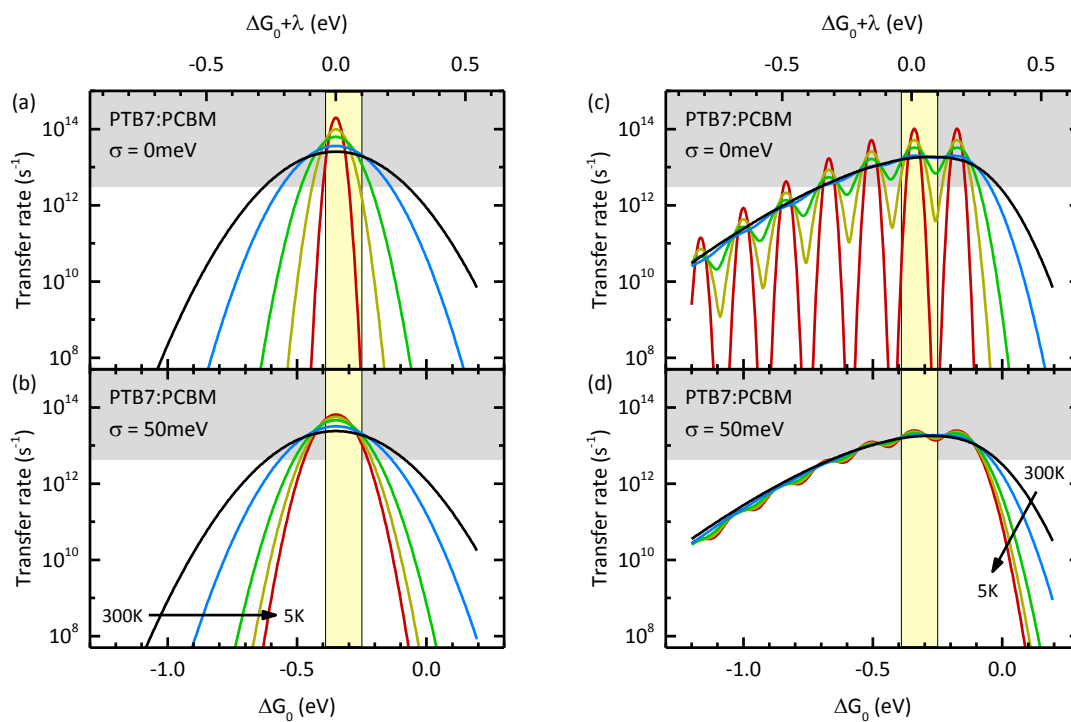


Fig. S2

Marcus rates (a,b) and Marcus-Levich-Jortner rates (c,d) of the PTB7:PCBM blend as a function of driving force for different temperatures (300K, 150K, 50K, 20K and 5K) without disorder (a,c) and with energetic disorder of $\sigma = 50$ meV (b,d). The grey shaded area indicates values that are beyond our instrumental resolution. The yellow shaded indicates the parameter range for the driving force.

IV Hole transfer from photoexcited acceptor to donor

4.1 MeLPPP:PCBM

We use the same method for the calculation of the driving force for hole transfer ΔG_0^{HT} as for electron transfer. For this purpose we need the singlet energy E_{S1} of PCBM. Veldman et al report a value of 1.70 eV taken from the onset of absorption.¹⁹ Coffey et al give a value of 1.76 eV determined by absorption and photoluminescence spectroscopy.²⁰ We therefore use a value of **1.73 ± 0.05 eV**. Using our measurement value of 1.57 ± 0.05 eV for the CT energy, we calculate the driving force to $-\Delta G_0^{\text{HT}} = 160 \pm 70$ meV.

If hole transfer takes place from the CT manifold with energies of 2.3 eV and above as detailed by Hahn et al,¹² the driving force increases to $-\Delta G_0^{\text{HT}} = 0.73$ eV, which is well in the Marcus inverted regime.

4.2 The case of P3HT:PCBM

We again need the energy values of the singlet state and the CT state to consider the expected transfer rates in the framework of Marcus and MLJ.

Reported values of the singlet energy are 2.06 eV using Franck Condon analysis of absorption by Herrman et al,²¹ 1.91 eV using the onset of absorption by Veldman et al¹⁹ and 2.0 eV using absorption and photoluminescence spectroscopy by Ohkita et al.²² We use a value of **$E_{S1} = 1.99 \pm 0.06$ eV**.

Vandewal et al performed EL/EQE measurements²³ and report a value of **1.14 eV** for the CT state energy as well as a **reorganization energy of 0.27 eV**. Their value for the reorganization energy matches with the result from Alberga et al, which was calculated using MD simulations.²⁴

The value of the **electronic coupling** is reported to be around 10 to 30 meV by Liu et al.^{11, 25} We use **20 ± 10 meV**.

Further parameters for calculations in the MLJ framework are **$\sigma = 75$ meV** for the energetic disorder, a **Huang Rhys parameter of 1** and a vibrational energy of **$\hbar\omega = 180$ meV** as reported by Hermann et al.²¹

Using the energies of the singlet state as well as the CT state as discussed above, we calculate the driving force for electron transfer $-\Delta G_0^{\text{ET}} = 850 \pm 60$ meV and for hole transfer $-\Delta G_0^{\text{HT}} = 590 \pm 50$ meV. Both transfer types take place well in the Marcus inverted regime, being triple (twice) the reorganization energy for electron (hole) transfer.

Having established the input values, we calculate the transfer rates for the P3HT:PCBM blend system in Figure 9 in the manuscript. The possible ranges for the driving forces are indicated by blue (electron transfer) and red (hole transfer) boxes. Falke et al measured an electron transfer time between 50 and 60 fs (sub-20 fs resolution),²⁶ and Cook et al give a resolution limited value of 250 fs for the hole transfer,²⁷ which are drawn in Figure 9 in the manuscript as well. Both transfer times are much too fast compared to the expectations of Marcus theory.

V Reorganisation energy and CT energy of PCPDTBT:PCBM

Figure S3 shows the electroluminescence and the external quantum efficiency for a blend solar cell made of PCPDTBT:PCBM. This Figure is part of the manuscript ‘On the Activation Energy of Free Charge Formation in Polymer-Fullerene Solar Cells and the Role of “Hot” Generation Pathways’ by Jona Kurpiers, Thomas Ferron, Steffen Roland, John A. Love, Tobias Thiede, Frank Jaiser, Steve Albrecht, Anne Katholing, Sylvia Janietz, Antonio Facchetti, Brian A. Collins and Dieter Neher., which was kindly provided to us by the authors prior to publication.

The EQE and EL measurements were performed and analysed as described for the MeLPPP:PCBM system.

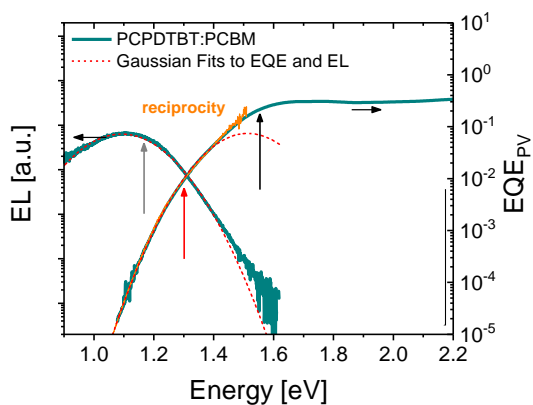


Fig S3:

EL and EQE measurements for PCPDTBT:PCBM. Red dotted lines indicate simultaneous Gaussian fits to the CT-region of EQE and EL according to Vandewal et al.²³ This results in a reorganization energy of 220 meV and a CT energy of 1.30 eV.

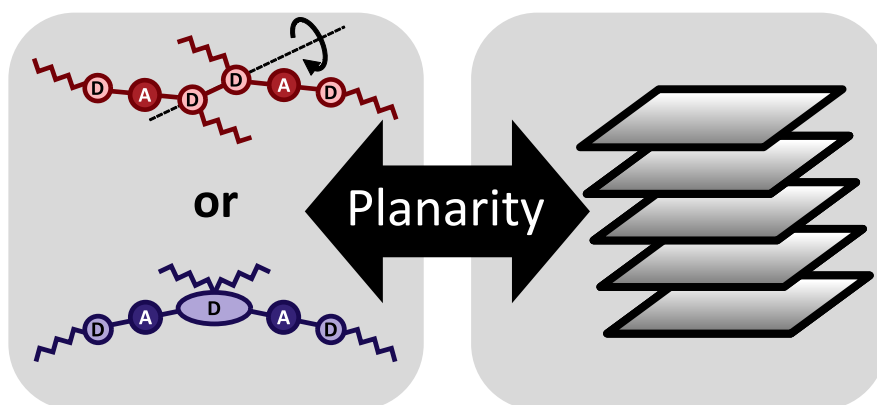
References

1. Scharsich, C.; Fischer, F. S. U.; Wilma, K.; Hildner, R.; Ludwigs, S.; Köhler, A., Revealing Structure Formation in Pcpdtdt by Optical Spectroscopy. *J. Polym. Sci. B Polym. Phys.* **2015**, *53*, 1416-1430.
2. Jarzab, D.; Cordella, F.; Gao, J.; Scharber, M.; Egelhaaf, H.-J.; Loi, M. A., Low-Temperature Behaviour of Charge Transfer Excitons in Narrow-Bandgap Polymer-Based Bulk Heterojunctions. *Adv. Energy Mater.* **2011**, *1*, 604-609.
3. Kraus, H.; Heiber, M. C.; Vath, S.; Kern, J.; Deibel, C.; Sperlich, A.; Dyakonov, V., Analysis of Triplet Exciton Loss Pathways in Ptb7:Pc71bm Bulk Heterojunction Solar Cells. *Sci. Rep.* **2016**, *6*.
4. Carsten, B.; Szarko, J. M.; Son, H. J.; Wang, W.; Lu, L.; He, F.; Rolczynski, B. S.; Lou, S. J.; Chen, L. X.; Yu, L., Examining the Effect of the Dipole Moment on Charge Separation in Donor-Acceptor Polymers for Organic Photovoltaic Applications. *J. Am. Chem. Soc.* **2011**, *133*, 20468-20475.
5. Liang, Y.; Xu, Z.; Xia, J.; Tsai, S. T.; Wu, Y.; Li, G.; Ray, C.; Yu, L., For the Bright Future-Bulk Heterojunction Polymer Solar Cells with Power Conversion Efficiency of 7.4%. *Adv. Mater.* **2010**, *22*, E135-E138.
6. Hoffmann, S. T.; Scheler, E.; Koenen, J.-M.; Forster, M.; Scherf, U.; Strohriegel, P.; Bäessler, H.; Köhler, A., Triplet Energy Transfer in Conjugated Polymers. ii. An Experimental Assessment Regarding the Influence of Disorder on Polaronic Transport. *Phys. Rev. B* **2010**, *81*.
7. Peng, Z.; Xia, Y.; Gao, F.; Xiong, K.; Hu, Z.; James, D. I.; Chen, J.; Wang, E.; Hou, L., A Dual Ternary System for Highly Efficient Ito-Free Inverted Polymer Solar Cells. *J. Mater. Chem. A* **2015**, *3*, 18365-18371.
8. Gerhard, M.; Arndt, A. P.; Howard, I. A.; Rahimi-Iman, A.; Lemmer, U.; Koch, M., Temperature- and Energy-Dependent Separation of Charge-Transfer States in Ptb7-Based Organic Solar Cells. *J. Phys. Chem. C* **2015**, *119*, 28309-28318.
9. Leng, C.; Qin, H.; Si, Y.; Zhao, Y., Theoretical Prediction of the Rate Constants for Exciton Dissociation and Charge Recombination to a Triplet State in Pcpdtdt with Different Fullerene Derivatives. *J. Phys. Chem. C* **2014**, *118*, 1843-1855.
10. Ward, A. J.; Ruseckas, A.; Kareem, M. M.; Ebenhoch, B.; Serrano, L. A.; Al-Eid, M.; Fitzpatrick, B.; Rotello, V. M.; Cooke, G.; Samuel, I. D. W., The Impact of Driving Force on Electron Transfer Rates in Photovoltaic Donor-Acceptor Blends. *Adv. Mater.* **2015**, *27*, 2496-2500.
11. Liu, T.; Cheung, D. L.; Troisi, A., Structural Variability and Dynamics of the P3ht/Pcbm Interface and Its Effects on the Electronic Structure and the Charge-Transfer Rates in Solar Cells. *Phys. Chem. Chem. Phys.* **2011**, *13*, 21461-21470.
12. Hahn, T.; Tscheuschner, S.; Saller, C.; Strohriegel, P.; Boregowda, P.; Mukhopadhyay, T.; Patil, S.; Neher, D.; Bäessler, H.; Köhler, A., Role of Intrinsic Photogeneration in Single Layer and Bilayer Solar Cells with C60 and Pcbm. *J. Phys. Chem. C* **2016**, *120*, 25083-25091.
13. Faist, M. A.; Kirchartz, T.; Gong, W.; Ashraf, R. S.; McCulloch, I.; de Mello, J. C.; Ekins-Daukes, N. J.; Bradley, D. D. C.; Nelson, J., Competition between the Charge Transfer State and the Singlet States of Donor or Acceptor Limiting the Efficiency in Polymer:Fullerene Solar Cells. *J. Am. Chem. Soc.* **2012**, *134*, 685-692.
14. He, Y.; Chen, H.-Y.; Hou, J.; Li, Y., Indene-C60 Bisadduct: A New Acceptor for High-Performance Polymer Solar Cells. *J. Am. Chem. Soc.* **2010**, *132*, 1377-1382.
15. Albrecht, S.; Vandewal, K.; Tumbleston, J. R.; Fischer, F. S.; Douglas, J. D.; Frechet, J. M.; Ludwigs, S.; Ade, H.; Salleo, A.; Neher, D., On the Efficiency of Charge Transfer State Splitting in Polymer:Fullerene Solar Cells. *Adv. Mater.* **2014**, *26*, 2533-2539.
16. Aygül, U.; Peisert, H.; Frisch, J.; Vollmer, A.; Koch, N.; Chassé, T., Electronic Properties of Interfaces between Pcpdtdt and Prototypical Electrodes Studied by Photoemission Spectroscopy. *ChemPhysChem* **2011**, *12*, 2345-2351.
17. Mühlbacher, D.; Scharber, M.; Morana, M.; Zhu, Z.; Waller, D.; Gaudiana, R.; Brabec, C., High Photovoltaic Performance of a Low-Bandgap Polymer. *Adv. Mater.* **2006**, *18*, 2884-2889.

18. Schwarz, C.; Tscheuschner, S.; Frisch, J.; Winkler, S.; Koch, N.; Bässler, H.; Köhler, A., Role of the Effective Mass and Interfacial Dipoles on Exciton Dissociation in Organic Donor-Acceptor Solar Cells. *Physical Review B* **2013**, *87*.
19. Veldman, D.; Meskers, S. C. J.; Janssen, R. A. J., The Energy of Charge-Transfer States in Electron Donor-Acceptor Blends: Insight into the Energy Losses in Organic Solar Cells. *Adv. Funct. Mater.* **2009**, *19*, 1939-1948.
20. Coffey, D. C.; Larson, B. W.; Hains, A. W.; Whitaker, J. B.; Kopidakis, N.; Boltalina, O. V.; Strauss, S. H.; Rumbles, G., An Optimal Driving Force for Converting Excitons into Free Carriers in Excitonic Solar Cells. *J. Phys. Chem. C* **2012**, *116*, 8916-8923.
21. Herrmann, D.; Niesar, S.; Scharsich, C.; Köhler, A.; Stutzmann, M.; Riedle, E., Role of Structural Order and Excess Energy on Ultrafast Free Charge Generation in Hybrid Polythiophene/Si Photovoltaics Probed in Real Time by near-Infrared Broadband Transient Absorption. *J. Am. Chem. Soc.* **2011**, *133*, 18220-18233.
22. Ohkita, H., et al., Charge Carrier Formation in Polythiophene/Fullerene Blend Films Studied by Transient Absorption Spectroscopy. *J. Am. Chem. Soc.* **2008**, *130*, 3030-3042.
23. Vandewal, K.; Tvingstedt, K.; Gadisa, A.; Inganäs, O.; Manca, J. V., Relating the Open-Circuit Voltage to Interface Molecular Properties of Donor:Acceptor Bulk Heterojunction Solar Cells. *Phys. Rev. B* **2010**, *81*.
24. Alberga, D.; Perrier, A.; Ciofini, I.; Mangiatordi, G. F.; Lattanzi, G.; Adamo, C., Morphological and Charge Transport Properties of Amorphous and Crystalline P3ht and Pbtbt: Insights from Theory. *Phys. Chem. Chem. Phys.* **2015**, *17*, 18742-18750.
25. Liu, T.; Troisi, A., Absolute Rate of Charge Separation and Recombination in a Molecular Model of the P3ht/Pcbm Interface. *J. Phys. Chem. C* **2011**, *115*, 2406-2415.
26. Falke, S. M., et al., Coherent Ultrafast Charge Transfer in an Organic Photovoltaic Blend. *Science* **2014**, *344*, 1001-1005.
27. Cook, S.; Katoh, R.; Furube, A., Ultrafast Studies of Charge Generation in Pcbm:P3ht Blend Films Following Excitation of the Fullerene Pcbm. *J. Phys. Chem. C* **2009**, *113*, 2547-2552.

7

What is the role of planarity and torsional freedom for aggregation in a π -conjugated donor–acceptor model oligomer?



Stefan Wedler, Axel Bourdick, Stavros Athanasopoulos, Stephan Gekle, Fabian Panzer, Caitlin McDowell, Thuc-Quyen Nguyen, Guillermo C. Bazan, and Anna Köhler.

Published in
Journal of Materials Chemistry C, **2020**, 8, 4944–4955
(DOI: 10.1039/D0TC00217H)

Reproduced by permission of
The Royal Society of Chemistry

Cite this: *J. Mater. Chem. C*, 2020, **8**, 4944

What is the role of planarity and torsional freedom for aggregation in a π -conjugated donor–acceptor model oligomer?†

Stefan Wedler,^a Axel Bourdick,^b Stavros Athanasopoulos,^c Stephan Gekle,^d Fabian Panzer,^a Caitlin McDowell,^d Thuc-Quyen Nguyen,^d Guillermo C. Bazan^e and Anna Köhler^{*af}

Ordered domains play a central role in determining the properties of organic semiconductors, and thereby the performance of their devices. The molecules in these ordered domains are often characterized by planar backbone conformations. We investigate the influence of backbone planarity on the propensity to form ordered structures using a pair of model oligomers with electron poor benzo-thiadiazole moieties and electron rich thiophene units. The two oligomers differ by their central unit, where a bithiophene unit either allows for flexible twists (“**TT**”), or where it is bridged as a cyclopentadithiophene to provide a rigid planar connection (“**CT**”). Temperature dependent absorption and luminescence spectroscopy in solution along with atomistic simulations show that the more flexible **TT** readily forms aggregates upon cooling, while **CT** instead first forms non-emissive excimers and only forms aggregates below 200 K. Molecular dynamics simulations reveal that aggregation in **TT** can only be accounted for if **TT** takes on a planar conformation in the course of the aggregation process. The stronger intermolecular interaction in **TT** compared to the banana-shaped **CT** can then be related to the larger number of attractive intermolecular interactions between the various subunits. Thus, molecular flexibility is an important design parameter, as it determines the accessibility of ordered intermolecular structures and ultimately device performance.

Received 13th January 2020,
Accepted 3rd March 2020

DOI: 10.1039/d0tc00217h

rsc.li/materials-c

1. Introduction

The performance of organic semiconductor devices such as organic solar cells (OSCs), transistors (OFETs) and light emitting diodes (OLEDs) depends not just on the chemical structure of the π -conjugated oligomers used. Rather, over the last decade we learned that the molecular self-assembly, and the resulting intermolecular interactions, as well as disorder can be decisive in controlling device performance.^{1–7} An attractive feature of organic semiconductors is that they can be processed from

solution, provided they are appropriately substituted,^{8–11} so that fabrication avenues such as printing or roll-to-roll processing are possible.^{12–17}

To understand the complex film formation processes that are involved in the fabrication of devices from solution, we need to first understand the interactions that prevail between chromophores in solution. A suitable means to examine the formation of structures with short-range or even long-range order, referred to as “aggregates”, is to cool down a solution.¹⁸ This approach keeps the concentration constant while the solvent quality gradually deteriorates. When such studies are carried out on π -conjugated polymers or oligomers, one finds the appearance of emission or absorption due to aggregates is preceded by a planarization process of the polymer or oligomer.^{19–23} Also, structural design to enhance the planarization of a polymer backbone by inserting heteroatoms with interactions that lead to conformational locks has been demonstrated to successfully increase the propensity to form ordered structures.^{24–27} For oligomers such as acenes or coronenes, it is well known that an extended planar π -system is conducive to aggregation.^{28–31} In fact, the challenge is frequently to suppress excessive aggregation by insertion of suitable sidechains or

^a *Soft Matter Optoelectronics, Experimentalphysik II, University of Bayreuth, Bayreuth 95440, Germany. E-mail: Anna.Koehler@uni-bayreuth.de*

^b *Biofluid Simulation and Modeling, Theoretische Physik VI, Universität Bayreuth, Bayreuth 95440, Germany*

^c *Departamento de Física, Universidad Carlos III de Madrid, Avenida Universidad 30, 28911 Leganés, Madrid, Spain*

^d *Center for Polymers and Organic Solids, Departments of Chemistry & Biochemistry and Materials, University of California, Santa Barbara, USA*

^e *Departments of Chemistry and Chemical Engineering, National University of Singapore, 119077, Singapore*

^f *Bayreuth Institute of Macromolecular Research (BIMF) and Bavarian Polymer Institute (BPI), University of Bayreuth, 95440 Bayreuth, Germany*

† Electronic supplementary information (ESI) available. See DOI: 10.1039/d0tc00217h

sterically demanding groups.^{32–36} From these studies one may infer that a rigidified planar backbone is a guiding principle to obtain compounds that can self-assemble into ordered structures.

However, there are reports that indicate that the aggregation process itself is inducing the planar conformation of the chromophore. For example, De Lener *et al.* studied how aggregates form for the polymer MEH-PPV.³⁷ In their quantum chemical studies, they found that the timescale for conformational fluctuations, notably rotations of the vinyl and phenyl units, are slowed down when two chain segments are brought close. This allows for the build-up of attractive interactions and the eventual formation of a planar, aggregated segment. Further, Kärnbratt *et al.* investigated the self-assembly process of linear porphyrin oligomers. From the very sudden onset of aggregation they conclude that a planar backbone structure has been induced by the assembly process, rather than *vice versa*.²⁹ In these cases one would expect that the molecules need to possess a certain degree of flexibility to eventually access the conformation required for ordered structures.

Here we address the question whether pre-existing backbone planarity is of advantage for the self-assembly process, or whether the required planarity may instead also be induced during the assembly process by considering two model oligomers referred to as “TT” and “CT”. Fig. 1 shows the chemical structures of these molecules. They differ only in their central unit. For TT, the central unit is a flexible bithiophene, marked in red. The hexyl sidechains induce a dihedral angle of 68°, as obtained from DFT calculations, while the flexibility is preserved. In particular, TT is able to planarize. The stiff molecule CT comprises a cyclopentadithiophene, marked in blue, forcing it to be planar. These model oligomers are very similar to compounds used in efficient solar cells, such as T1,^{38–41} which are frequently made in a D–A–D–A–D type structure with electron-rich (D) and electron-poor (A) subunits.^{31,42,43}

This paper is structured as follows. After introducing the methods in Section 2, we describe in Section 3 our observations and interpretation of the spectroscopic measurements taken in solution. In Section 4, these results are compared to and discussed against the predictions made by molecular dynamics simulations. Time dependent density functional theory (TD-DFT) calculations on the excited state structure in dimers are discussed in Section 5. Section 6 finally reports and discusses the observation of emission from *cis*- and *trans*-conformations of TT. A concluding summary is provided in Section 7.

2. Methods

Sample preparation

The molecules 7,7'-(3,3'-dihexyl-[2,2'-bithiophene]-5,5'-diyl)bis-(6-fluoro-4-(5-hexylthiophen-2-yl)benzo[*c*][1,2,5]thiadiazole) (TT)

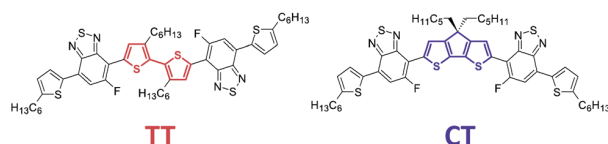


Fig. 1 Chemical structures of TT and CT.

and 7,7'-(4,4-dihexyl-4*H*-cyclopenta[2,1-*b*:3,4-*b'*]dithiophene-2,6-diyl)bis(6-fluoro-4-(5-hexylthiophen-2-yl)benzo[*c*][1,2,5]thiadiazole) (CT) were synthesized as reported previously,⁴⁴ their structures are shown in Fig. 1. Solutions with different concentrations were prepared inside a glovebox using O₂-free anhydrous hexane from Acros. To ensure complete dissolution, the solutions were heated to 50 °C and stirred up to one hour. We used quartz glass cuvettes with a thickness of 1.00 mm (10.00 mm) for solutions with concentrations of 5.0 × 10^{−5} M and higher (5.0 × 10^{−6} M and lower) for optical characterization.

Emission and absorption measurements

Temperature dependent absorption and emission spectra were measured with a home-built setup.²³ Detection was performed utilizing a CCD camera (Andor iDus 420) coupled to an Andor Shamrock 303 spectrograph. For excitation we used a 405 nm diode laser from Coherent for all CT measurements and a 485 nm diode laser from PicoQuant for all TT measurements, both operating in continuous wave mode. Emission spectra were corrected for the efficiencies of all optical components as well as for changes of the absorbance at the laser wavelength. All samples were put into a temperature controlled continuous-flow cryostat (Oxford Instruments) using liquid helium as the coolant. A waiting time of 15 minutes before measurement was sufficient after reaching each temperature to ensure thermal equilibration of the sample.

Time-correlated single photon counting measurements were performed using a FluoTime 200 spectrometer from PicoQuant and a 485 nm diode laser operating in pulsed mode for excitation. Signal acquisition was performed utilizing the counting module PicoHarp 300E (PicoQuant).

Quantum-chemical calculations

Ground state optimizations of the individual molecules with the side chains were performed at the density functional theory (DFT) level using the ωB97XD long-range corrected exchange–correlation functional⁴⁵ and a split valence 6-31G** polarized double zeta basis set. We have used a range separation parameter of ω = 0.13 a.u.^{−1} that has been previously obtained by tuning the fundamental gap of the TT molecule.⁴⁴ This functional provides comparable performance to coupled cluster CCSD(T) calculations in substituted bithiophenes.⁴⁶ Excited state geometry optimizations and vertical transition energies of the individual molecules and the dimers were obtained with linear response time dependent density functional theory (TD-DFT). All DFT and TD-DFT calculations were carried out with Gaussian 09 software.⁴⁷ Calculated absorption spectra for the single molecules as well as aggregated dimers can be found in the ESI† (Section S1) and show excellent agreement with experimental data.

To quantify the extent of intermolecular exciton delocalization on the CT and TT dimers we have computed the participation ratio of the dominant hole and electron natural transition orbitals (NTOs),⁷ defined as:

$$PR = (\rho_{\text{mol1}}^2 + \rho_{\text{mol2}}^2)^{-1}$$

with

$$\rho_{\text{moli}} = \sum_{j \in \text{moli}} C_j^2$$

C_j are the corresponding coefficients of the normalised NTOs. PR takes values between 1 and 2: when PR = 1 the natural transition orbital is fully localized on a single molecule while when PR = 2 it is equally delocalized between the two molecules. To obtain information on the intermolecular charge transfer character we define a CTC parameter as:

$$\text{CTC} = \left| \frac{\Delta h - \Delta e}{2} \right|$$

where

$$\Delta h = \sum_{j \in \text{mol1}} C_{j,\text{HOMO}}^2 - \sum_{j \in \text{mol2}} C_{j,\text{HOMO}}^2$$

$$\Delta e = \sum_{j \in \text{mol1}} C_{j,\text{LUMO}}^2 - \sum_{j \in \text{mol2}} C_{j,\text{LUMO}}^2$$

The CTC parameter takes values between 0 and 1: CTC = 0 indicates an excitation without intermolecular charge transfer character and CTC = 1 indicates an excitation with complete charge transfer character, meaning the hole (HOMO) NTO is completely localized over the first molecule and the electron (LUMO) NTO is completely localized over the opposite molecule.

MD-simulations

We performed molecular dynamics simulation with Gromacs^{48–51} using the Gromos 54a7 force field.⁵² The structure files were generated with JME.⁵³ The force field files for CT⁵⁴ and TT⁵⁵ were generated with the automated force field topology builder and repository.^{56–58}

In order to make the simulations more accurate we calculated the charge distribution and the potential energy surface (PES) of the dihedral angle between the various donor and acceptor parts of the molecules and between the two thiophene rings in the central donor unit of TT with DFT and adjusted our MD models to reproduce the behaviour calculated with DFT. Structure and topology files for the solvent hexane were taken from the ATB database.⁵⁹ More details about how the models were built are specified in the ESI,† Section S2. For the simulations all-atom force field topologies were used. We used a cubic box of two solute molecules and between 500 and 1100 solvent molecules. We defined the reaction coordinate as the distance between the center of mass of the central donor unit of TT and the center of mass of the middle ring of the central donor unit of CT. Starting configurations for the umbrella windows were generated from a random configuration from which we squeezed the solute molecules together and pulled them apart along the reaction coordinate. Configuration snapshots were saved in steps of 0.04 nm. Each simulation was equilibrated and conducted as NPT ensemble. To cover the whole configurational phase space, we sampled the reaction pathways independently eight times for

TT and eleven times for CT with hexyl sidechains. For the free energy graphs with CH₃ sidechains we sampled the reaction pathway of TT and CT four times each. The free energy graphs are averaged over all these runs. The simulation time varied from 60 ns to 800 ns per window. The free energy graphs were calculated with umbrella sampling⁶⁰ and the *Weighted Histogram Analysis Method*,⁶¹ which is implemented in Gromacs as *gmx wham*. Two-dimensional free energy surfaces were calculated with well-tempered metadynamics,^{62–65} which was carried out using the open-source community-developed PLUMED library version 2.2 integrated as a plugin to the Gromacs software.^{66,67} Visualisation was done with VMD.⁶⁸ All simulations were performed at $T = 300$ K. Further details about the simulation parameters and the used force constants can also be found in the ESI,† Section S2.

3. Optical spectroscopy

Results

We study the influence of torsional rigidity on the aggregation behaviour using the two molecules shown in Fig. 1. They consist of typical building blocks for donor-acceptor-type molecules used in organic solar cells and differ only in their central unit, which consists of connected thiophenes (“CT”) or twisted thiophenes (“TT”). The stiff molecule, thereafter referred to as CT, comprises a cyclopentadithiophene marked in blue. For the molecule called TT, the central unit is a flexible bithiophene, marked in red. Its alkyl sidechains result in a twisted geometry with a dihedral angle of 68° as determined by quantum chemical calculations (see Section 6) and in agreement with literature.⁴⁴

We conducted temperature dependent absorption and emission measurements in hexane between 300 K and 180 K to investigate their aggregation properties in solution and compare three different concentrations. Fig. 2 shows the absorption and emission of TT in hexane at 5.0×10^{-6} M, 5.0×10^{-5} M and 2.5×10^{-4} M. All emission spectra are normalized to coincide at the high energy side at about 2.1 eV. For the lowest concentration of 5.0×10^{-6} M, both absorption and emission only change little upon cooling. The unstructured absorption (Fig. 2b) increases in intensity and the peak position shifts from 2.53 eV at 300 K to 2.47 eV at 200 K. In emission (Fig. 2a) we also observe a redshift of the peak around 2.0 eV by 20 meV and a reduction of the linewidth upon cooling. Furthermore, an additional high-energy shoulder at 2.15 eV emerges upon cooling. We discuss the origin of this shoulder further below in Section 6.

For the intermediate concentration of 5.0×10^{-5} M (Fig. 2c and d) we again observe a redshift and increase in absorption until 230 K (solid yellow line) upon cooling. At 220 K and below, new spectral features emerge at lower energies both in absorption and emission. A structured absorption feature with the first peak at 1.95 eV and further vibronic replicas at 2.12 eV and 2.30 eV is observed. Concomitantly, the unstructured absorption band centered at 2.5 eV disappears, resulting in an isosbestic

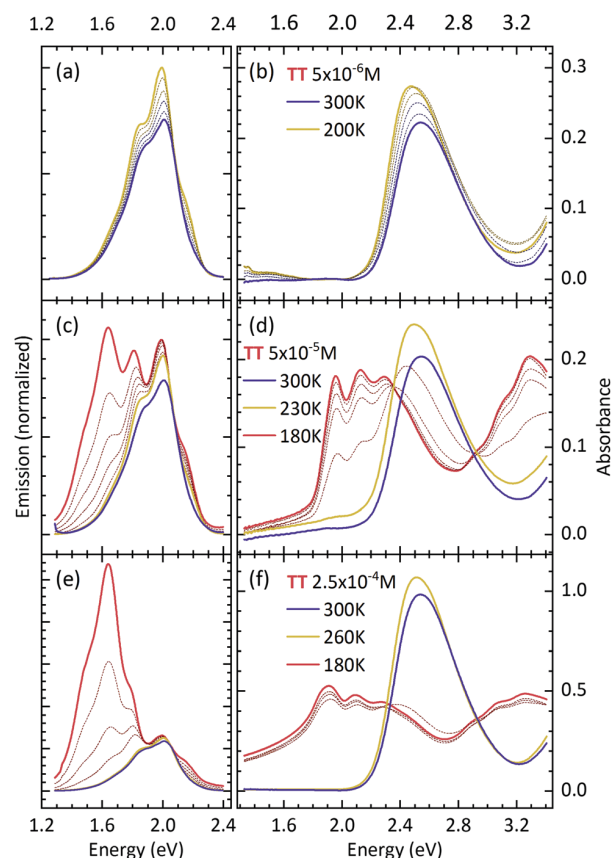


Fig. 2 Absorption (b, d and f) and emission (a, c and e) spectra of **TT** in hexane for different temperatures at a concentration of (a and b) 5.0×10^{-6} M, (c and d) 5.0×10^{-5} M and (e and f) 2.5×10^{-4} M. Emission spectra are normalized to about 2.08 eV. Spectra taken at characteristic temperatures are drawn with solid lines and given in the legend. Temperatures in between are shown in steps of 20 K for (a), (b) and between 180 K and 260 K in (e) and (f), and in steps of 10 K between 180 K and 230 K for (c) and (d).

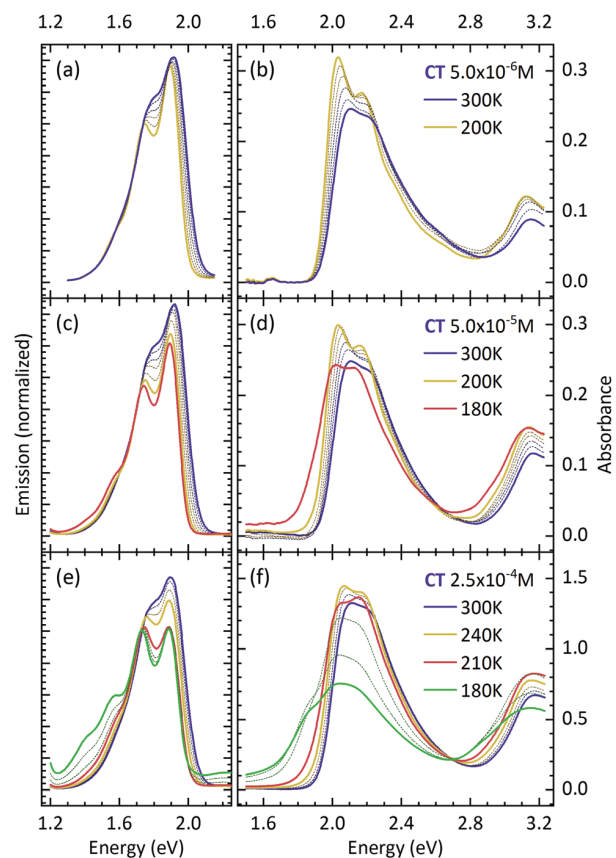


Fig. 3 Absorption (b, d and f) and emission (a, c and e) spectra of **CT** in hexane for different temperatures at a concentration of (a and b) 5.0×10^{-6} M, (c and d) 5.0×10^{-5} M and (e and f) 2.5×10^{-4} M. Emission spectra are normalized to about 1.7 eV. Spectra taken at characteristic temperatures are drawn with solid lines and given in the legend. Temperatures in between are shown in steps of 20 K for (a), (b), (c), (d) and between 240 K and 300 K in (e) and (f), and in steps of 10 K between 180 K and 210 K for (e) and (f).

point at 2.35 eV. The additional luminescence feature shows peaks at 1.81 eV and 1.64 eV, and a shoulder at 1.46 eV. Again, the high-energy shoulder at 2.15 eV emerges upon cooling.

The spectral changes upon cooling become more drastic when we increase the concentration further to 2.5×10^{-4} M (Fig. 2e and f). The absorption band reduces in intensity below 260 K. The emerging absorption feature shows a strong raising baseline and the structure is smeared out. This is characteristic for light scattering from small particles. Similarly, in emission, the peaks at 1.81 eV and 1.64 eV grow in from 260 K onwards and keep increasing. This is accompanied by a change in relative weight of the vibrational peaks, so that the peak at 1.64 eV eventually dominates and the overall shape is reminiscent of a classical excimer-type emission (except for being more structured).³⁰ In addition to this evolution at the red side of the spectrum, the already mentioned shoulder at 2.15 eV emerges at low temperatures, independent of concentration.

The changes of the more rigid **CT** with temperature and concentration are displayed in Fig. 3. The emission spectra are

normalized to coincide at the low energy side around 1.7 eV. For the lowest concentration (Fig. 3a and b), both absorption and emission change little upon cooling. Overall, the intensity of the absorption increases slightly, the spectra shift to the red by 40 meV and the linewidth (full width at half maximum) of the absorption narrows by 29 meV. A Franck-Condon analysis reveals that the apparent change of the peak ratios is due to the decreasing linewidth, as detailed in the ESI,[†] Section S3.

When increasing the concentration to 5.0×10^{-5} M (Fig. 3c and d), we notice a decrease in absorption intensity for the spectra taken at 200 K, 190 K and 180 K. This is accompanied by a reduction in the ratio between the 0–0 peak at about 2.03 eV and the 0–1 peak at about 2.18 eV as well as a broadening of the low energy tail. The emission spectra have a similar shape at lower concentration. However, the relative contribution of the 0–0 peak at 1.9 eV is less pronounced and at the lowest temperature (180 K) we observe an additional weak feature below 1.6 eV.

In absorption, at the highest concentration (Fig. 3f), there is a reduction of the 0–0 peak at about 2.05 eV from 280 K onwards compared to the 0–0 peak intensity observed for the

lower concentrations (for better comparison among different concentrations see ESI,† Section S4). The overall absorption intensity reduces from 240 K onwards, and the spectra exhibit a low energy shoulder at 1.85 eV for 200 K and below, as well as a scattering offset. In emission (Fig. 3e) the trends already observed for the intermediate concentration are more pronounced. In particular, we observe a clear low energy feature with peaks at 1.55 eV and 1.40 eV for 200 K and below.

We displayed the emission spectra in Fig. 2 and 3 in a normalized manner to allow for a good comparison of the spectral shapes. The relative emission intensities, integrated over the entire spectrum and normalized to unity at room temperature, are displayed in Fig. 4a and b. For **TT**, the overall intensity remains constant until the lower energy band appears (at 230 K and 260 K for the intermediate and higher concentration, respectively), and then reduces steeply. For **CT**, the emission intensity reduces for the intermediate and higher concentration from about 250 K onwards, which does not correlate in an obvious way with spectral changes.

More information on the low energy bands can be obtained from their spectral shapes. For the concentration of 2.5×10^{-4} M, we separated the low energy band in **TT** (**CT**) spectrally from the high energy band. For this, we took the emission spectrum at 260 K (210 K) that displays only the high energy feature, normalized it to the high energy side of the spectra taken at lower temperatures, and subtracted it. The resulting difference spectrum consists only of the low energy band and is shown in Fig. 4c. With decreasing temperature, there is a reduction of the 0-0 peak at 1.8 eV for the low energy band in **TT**. The energy of the 0-0 peak stays constant during the transition, in contrast to an ongoing bathochromic shift observed for aggregate emission in several polymers like P3HT or PCPDTBT.^{19,20} For **CT**, the separated spectra of the low energy band below 210 K are identical within experimental uncertainty and we only present the result for 180 K, which also shows a reduced intensity of the 0-0 peak.

Discussion

Cooling down a solution is a well-known means to reduce the quality of a solvent to promote aggregation phenomena while

keeping the overall concentration unchanged. The different spectral evolutions we observe for **CT** and **TT** seem to suggest that the nature of the connecting unit has a strong impact on their propensity to aggregate.

The evolution of the spectra for **TT** is comparatively straightforward to interpret, as it follows the pattern observed for other conjugated polymers or molecules such as P3HT.^{18,19,69} Consider for example the absorption at the intermediate concentration, 5×10^{-5} M. The bathochromic shift and increase in oscillator strength in absorption implies that the conjugation length in the molecule increases upon cooling, suggesting a freezing out of torsional motion between the various heterocyclic units and stronger planarization of the backbone. Changes in the refractive index and/or polarizability of the solvent upon cooling have minor impact on the spectral positions (see ESI,† Section S5).⁷⁰ The appearance of the isosbestic point below a critical temperature T_c of 230 K indicates the transition from individually solvated molecules into aggregates, and this is accompanied by the appearance of associated emission features. At higher concentrations, this transition sets in at higher temperatures. We attribute the appearance of an apparent long low energy tail in the absorption at the highest concentration to light-scattering due to a larger size of the aggregated conglomerates. The reduction in emission intensity upon aggregate formation, the reduction of the 0-0 peak upon cooling (Fig. 4a and c), and the increase of the non-radiative decay rate from 0.3 ns^{-1} at 300 K to 1.2 ns^{-1} at 180 K are characteristic for a predominantly H-type interaction (see ESI,† Section S6).⁷¹ Thus, we can conclude that **TT** forms weakly interacting H-type aggregates when reducing the solvent quality by cooling.

In contrast, the evolution of the **CT** spectra is more complex. The small redshift upon cooling in the absorption of the dilute solution indicates a freezing out of torsional modes in the vicinity of the benzothiadiazole that increases the overall conjugation length, which is less pronounced in emission, consistent with a typically already more planar geometry of the excited state.⁷² Despite the more planar, rigid character, signs of aggregate formation are less pronounced than for **TT**.

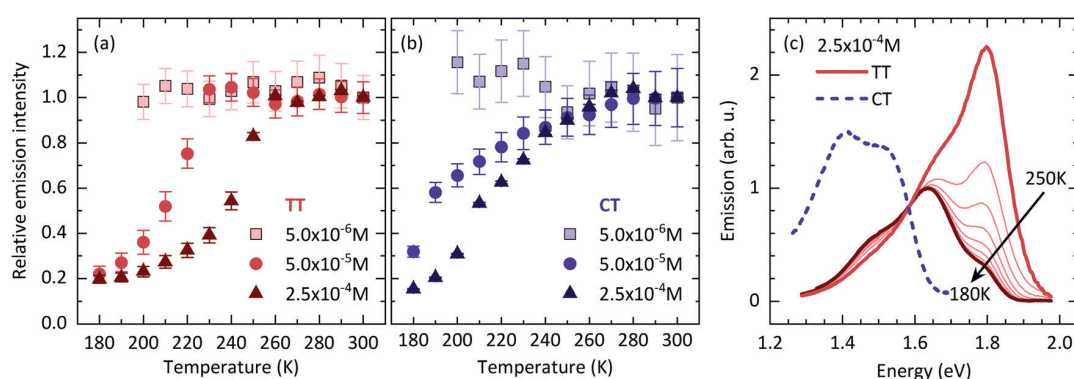


Fig. 4 Relative emission intensity as function of temperature for different concentrations for (a) **TT** and (b) **CT**. (c) Separated aggregate emission spectra at the concentration of 2.5×10^{-4} M. The spectra for **TT** are normalized to 1.6 eV and are taken in steps of 10 K as indicated by the arrow. For **CT** only the spectrum at 180 K is shown.

Clear signatures in absorption and emission for the formation of a weakly interacting aggregate prevail in the higher concentrated solution, *i.e.* at 2.5×10^{-4} M, only below 210 K, and for the intermediate concentration below 200 K. There are, however, more subtle spectral changes already below 240 K, notably in the ratios of the 0–0 to 0–1 absorption peaks. It is striking that there is a clear decrease in overall emission intensity below 250 K for the intermediate and higher concentrations, even though this is not accompanied by any emissive features. This suggests that, below 250 K, CT first forms some non-emissive species, and emissive aggregates are only formed at higher concentrations and lower temperatures. A similar observation has been made earlier for the aggregation process in pyrene-derivatives.⁷³

This is an unexpected result for CT. For the polymers and oligomers we investigated so far, including TT reported here, we always observed that a planarization of the backbone preceded the formation of aggregates, and that these aggregates had sufficient oscillator strength so that they could be identified in absorption and emission. Moreover, increasing the backbone planarity through conformational locks has previously been demonstrated to enhance the tendency to form ordered, even crystalline structures.^{24,74} In contrast, here, it seems that the rigid nature of the connection does not assist the formation of aggregates, but rather induces the formation of non-emissive excimer-like species.

4. Molecular dynamics simulations

Results

In previous work we found that reduced torsional motion precedes aggregation,¹⁸ and an initial planarization prior to aggregation is also what we observed here for CT and TT, as discussed in Section 3. It is thus not immediately clear why CT shows less signs of aggregation than TT. A possible explanation could be that the sidechains of the central CT unit might prevent approximation of adjacent molecules as these chains are pointing out of the molecular plane, whereas the sidechains lie in the molecular plane for TT. To test this hypothesis, we conducted molecular dynamics (MD) simulations for the molecules with the full hexyl sidechains, as well as for the molecules where the central sidechains are replaced by CH₃. Different rotamers, meaning different orientations of the benzothiadiazole unit, were sampled in the simulations, as their existence was observed for related compounds.^{75,76} We found no significant difference among the possible rotamers in our simulations. The key observable of the simulations is the free energy of the system, which consists of two single molecules surrounded by 500 to 1100 solvent molecules. Free energy curves are computed using Umbrella Sampling as detailed in the Method section and the ESI,† Section S2.

Fig. 5 compares the resulting average free energies as a function of intermolecular distance, defined as the center of mass distance for the central units, alongside with corresponding dimer geometries. These schematics serve to illustrate

the mean configurations of snapshots in the MD simulation at the different minima along the free energy curves. We find that upon approximation the free energy of two molecules decreases. For both, TT and CT, this pathway involves several minima. For TT, we find that the two molecules approach predominantly by successively sliding over each other along the long axis of the molecule. Due to the central twist, the two wings do not lie parallel on top of each other, but rather twist around each other (Fig. 5b, position 4, and movie clip deposited as ESI†). When the sidechains are replaced by CH₃ groups, it seems that this process becomes facilitated, resulting in a significantly deeper minimum at closest approximation.

For CT, we also observe predominantly a sliding process along the long axis. Due to the rigid central cyclopentadithiophene, CT has a banana shape. Correspondingly, there are two possible conformations, depending on the relative orientation of the central cyclopentadithiophene group (Fig. 5d, position 3, and movie clips deposited as ESI†). The two molecules may arrange with their curvature in opposite direction (type A) or in the same direction (type B). For type A, the sidechains on the two central units are also orientated opposite, thus not causing any steric effects. For type B, the final geometry contains an offset by one ring unit along the molecular long axis, thus avoiding direct interaction of the sidechains. The prevalence of two possible energetically favourable arrangements in CT as opposed to only one in TT is further supported by metadynamics calculations, as evident from Fig. 5e as well as Fig. S2.6 and S2.7 in the ESI.†

Replacing the hexyl side chains by CH₃ hardly affects this arrangement. As a result, there is very little increase in free energy gain when the long alkyl sidechains are replaced by CH₃. Importantly, we do not observe a significantly lower minimum of the free energy for CT without sidechains as compared to TT without sidechains. Thus, the sidechains do not seem to be the decisive factor that renders TT more prone to aggregation than CT.

From the free energy curves obtained for the molecules with sidechains, we would, in fact, expect a stronger propensity to aggregation from CT, at variance with experiment. However, in the MD calculation of Fig. 5a we considered a twisted dihedral potential in TT, which was derived from DFT calculations of a single molecule. In other words, the calculations did not take into account any possible planarization effects that may result from a change of the electronic structure caused by intermolecular interactions upon approximation. In fact, TT was found to planarize in the solid state^{44,77} while planarization has also been observed in substituted oligothiophenes.^{78,79} Therefore, it is conceivable that the molecule also planarizes when two of them approach in order to form an aggregate in solution, and this may need to be considered in the MD calculation. Thus we calculated the free energy between two TT molecules when the rotational potential of central bithiophene has a minimum for both sulphurs of the molecule pointing into the same direction (“*cis*”) or opposite direction (“*trans*”). The result is shown in Fig. 6. Allowing for a planarization of TT indeed results in significant energy gain upon aggregation. Compared to

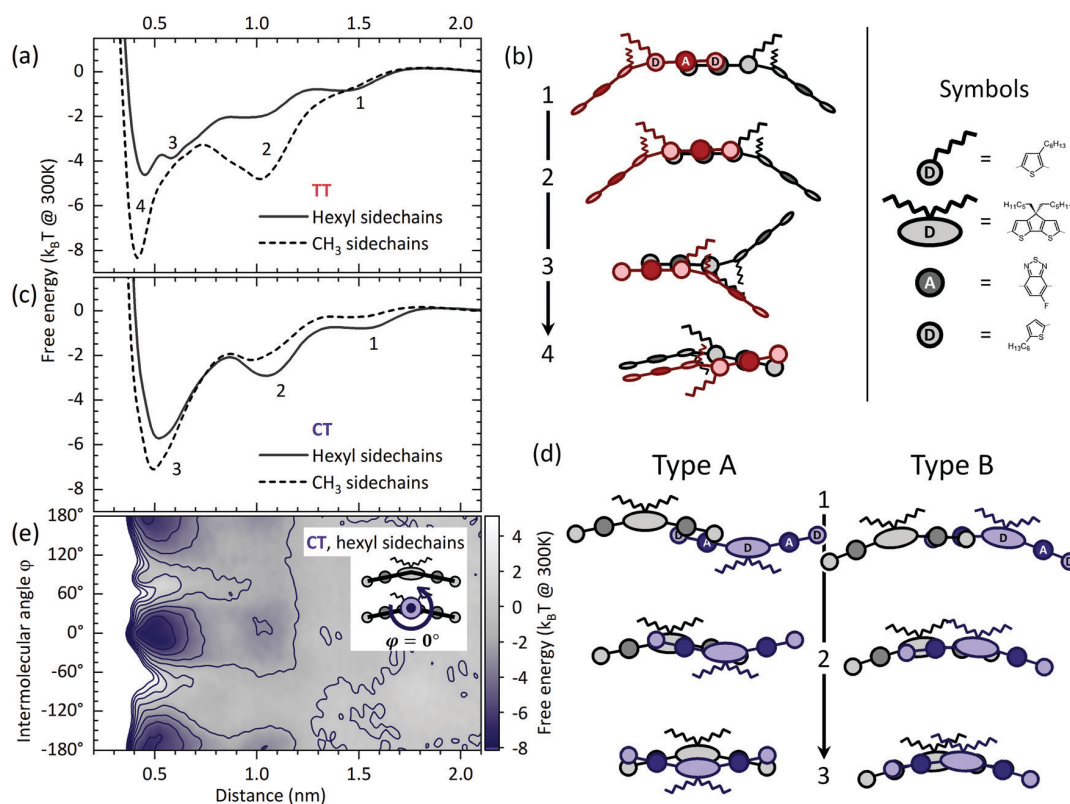


Fig. 5 (a) Free energy curves for the **TT** dimer with hexyl and CH_3 sidechains as function of the distance of the central bithiophenes. (b) Dimer geometries for the closest distance and along the free energy curve as indicated in (a). (c) Free energy curves for the **CT** dimer with hexyl and CH_3 sidechains as function of the distance of the central cyclopentadithiophenes. (d) Dimer geometries for the closest distance and along the free energy curve as indicated in (c). For **CT** there are two final conformations possible. (e) Two-dimensional free energy surface calculated by metadynamics for the **CT** dimer with hexyl side chains as function of intermolecular distance and intermolecular angle φ . The inset visualizes φ and shows the conformation for $\varphi = 0^\circ$.

the conformation with a twisted central bithiophene, the *cis* conformation is favoured by $3.5 k_B T$, and the *trans*-conformation is stabilized by $5.0 k_B T$. Importantly, for both planar conformations the free energy is lower for **TT** as compared to **CT**. The same conclusion still applies when the sidechains are replaced by CH_3 , as discussed in the ESI† (Section S7).

Allowing for a planarized central bithiophene unit thus results in a free energy curve that is consistent with the experimental observations of a higher critical temperature as well as clear aggregate signatures for **TT**. We also found that lack of steric hindrance by sidechains is not the reason for the strong tendency to aggregate that we see experimentally for **TT**. To understand in more detail what promotes the aggregation, we thus proceed to consider interactions between adjacent units in our model dimers. For **TT**, the final average configuration obtained by MD is illustrated as inset in Fig. 6. In the *trans*-configuration, the molecules adopt a slight zig-zag shape and they arrange offset by one unit along the long molecular axis. This comprises four pairs where an electron-rich thiophene is opposite an electron-poor benzothiadiazole, and one thiophene-thiophene pair. In contrast, for **CT**, there are less points of contact. For type A (Fig. 5), only two benzothiadiazole rings lie

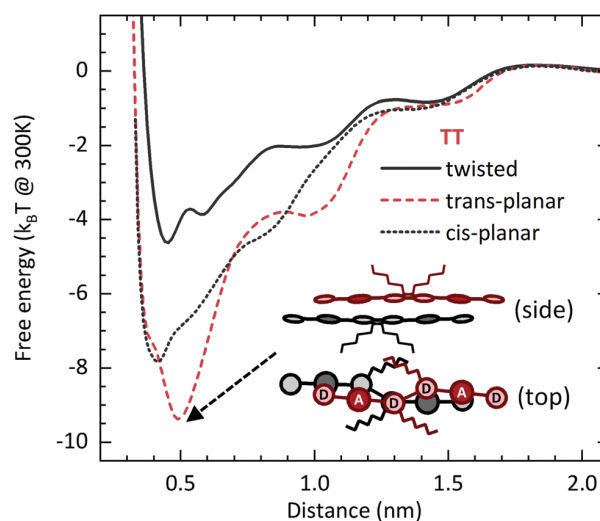


Fig. 6 Free energy simulations of **TT** for the twisted conformation and both planar conformations. The sketch shows the intermolecular geometry for the *trans*-planar dimer with highest energetic stabilisation.

opposite each other. For type B, there is slightly more interaction, that is, two thiophene-benzothiadiazole pairs form and the

central bithiophene–benzothiadiazole units lie adjacent such as to be able to interact. The interactions between these subunits is attractive, in particular for donor–acceptor type pairs, as already shown earlier⁴¹ and detailed further in the ESI† (Section S8). Thus, it appears that the stronger interaction in the **TT** dimer can be rationalized by its zig-zag like geometry that allows for more contact points where attractive interactions can take place.

Discussion

To summarize the insight gained from the MD simulations, we found that planarization of the **TT** molecule is essential to reproduce its strong propensity to form aggregates. We can therefore say that a more planar structure, preferably *trans*-planar, is needed to promote aggregation. This planar configuration may form *in situ* after an initial pairing of twisted molecules, *i.e.* through the sliding mechanism in Fig. 5b. There is evidence that a temporarily more planar structure can itself be induced by the proximity of two molecules. For example, De Leener *et al.* performed a combination of molecular dynamics and quantum chemistry calculations for the polymer MEH-PPV.³⁷ They could show that conformational fluctuations are large for isolated molecules on short timescales. However, these fluctuations happen on longer timescales in the bulk, making polymer chains more planar on average once they are surrounded by other chains. It is conceivable that a similar mechanism contributes here to render the **TT** molecule more planar when a second molecule comes close, in addition to the electronic-structure-induced planarization discussed above. This would result in the planarity required to allow for persistent aggregation.

The amount of interaction between two adjacent molecules depends on the number of units that come close, and thus it depends on its shape. The MD calculations indicate that the slight zig-zag geometry of **TT** leads to more contact points than the banana shape of **CT**, and this seems to advance the propensity for aggregation. At first sight, this seems to be at variance with the results by Welch *et al.*⁸⁰ for related banana-shaped oligomers. They reported that a stronger bend angle is favourable for crystallization, while according to our results, a weaker bend angle inducing more contact points should seem advantageous. The resolution to this apparent contradiction lies in the overall symmetry of the arrangement. The banana-shaped oligomers addressed by Welch *et al.* arrange in a type A conformation. Here, attractive interactions can result from the contacts between acceptor units. However, the central unit does not contribute to this at a close distance. Rather, there is an unfavourable need to repel solvent molecules between the central units, and the interaction between the central units is itself repulsive (see ESI,† Section S8).⁴¹ A stronger bend angle here indeed alleviates this constraint while still preserving the acceptor interactions. The situation is different for the zig-zag geometry of **TT**, where the attractive interactions between the four donor–acceptor pairs dominate, or for type B of **CT** where the central units are also attractive.

5. Quantum chemical calculations

Having established what causes the stronger propensity of **TT** to aggregate, we reconsider the spectral signatures of both molecules. For **TT**, additional features appear simultaneously upon cooling in the absorption and the emission spectra, consistent with our interpretation of an H-type aggregate. The continuous reduction of the 0–0 peak with cooling in the aggregate emission (compare Fig. 4c) can be understood as a sign of increasing strength of electronic interaction, as observed earlier for instance in P3HT or PCPDTBT.^{19,20} In contrast, for **CT**, signs of aggregation emerged in the absorption spectra only below 200 K (Fig. 3). The emission from the aggregate has a broad shape with a 0–0 peak that is slightly lower than the 0–1 peak, indicative of some H-like electronic interaction (Fig. 4). However, the emission intensity in **CT** reduces already from 250 K onwards, even though no additional features appear in absorption or emission. The reduction of emission intensity suggests that an additional non-radiative decay channel opens up. We already mentioned that the most likely candidate for this is the formation of a non-emissive excimer. Such species that form as a precursor to aggregates have been reported before by Haedler *et al.* for pyrene-derivatives.⁷³ The formation of more weakly bound precursor species such as excimers would be consistent with the lower number of attractive contact points formed for **CT**. We have conducted time dependent density functional theory (TD-DFT) calculations to consider the electronic nature of possible dimers formed for **TT** and **CT**.

For this, we averaged the dimer structures from the MD simulations, focusing on the relevant conformations with minimal intermolecular distance. For **TT** we used only the *trans*-planar aggregate, while for **CT** we considered both, type A and type B conformers separately. Based on these, we have prepared dimers with one of the molecules on the ground state geometry and the other molecule on the first excited state geometry. These conformations served as starting points for TD-DFT geometry optimizations of the first excited state of the dimer without imposing any symmetry constraints. We thus monitor the structural relaxation of the dimer upon photo-excitation and internal conversion of one of the molecules and therefore the propensity of the aggregate to form excimer states.

Table 1 shows the optimized geometries for all three dimers and the corresponding electron–hole pair natural transition orbitals. The relaxed excited state geometry for the **TT** dimer has a plane-to-plane distance of 3.66 Å, which is close to the ground state plane-to-plane distance of 3.63 Å. The natural transition orbitals delocalize over the whole dimer, yielding a small charge transfer character of 0.23, and the oscillator strength is low. This is consistent with experiment, as the emission intensity decreases significantly upon aggregation.

The picture is different for **CT**. Upon excitation, the dimer geometry relaxes such that the plane-to-plane distance decreases significantly. This is most pronounced for the type A conformation where the plane-to-plane distance reduces by 0.20 Å.

Table 1 TD-DFT results for the optimized S_1 state of each dimer for **TT** in the trans-planar conformation and **CT** type A and type B. We display visualizations of the dominant electron-hole pair natural transition orbitals, the corresponding transition energy, the oscillator strength (f), the charge transfer character (CTC), and the plane-to-plane distances for ground state and excited state

	TT (<i>trans</i>)	CT (type A)	CT (type B)
Electron			
Hole			
Energy (eV)	1.69	1.56	1.68
f	0.0014	0.0000	0.21
CTC	0.23	0.00	0.39
Plane-to-plane distance (Å)			
Ground state	3.63	3.68	3.64
Excited state	3.66	3.48	3.52
Difference	+0.03	-0.20	-0.12

The excitation is delocalized equally over both molecules of the dimer. Emission from this excited state has no charge transfer character, yet also no oscillator strength. The significant geometry change upon excitation, lack of charge transfer character and lack of oscillator strength imply that this is quasi a textbook example for a non-emissive excimer.⁸¹ Moreover, it is also at lower energy than the type B conformation. For the type B dimer, we find a reduction in plane-to-plane distance still by 0.12 Å. The transition has a large charge transfer character, where the electron is localized mainly on one molecule and the hole is equally delocalized over both molecules of the dimer. The transition to the ground state has a finite oscillator strength. Between 250 K and 200 K we have not observed any emission feature that could be assigned to emission from type B dimers. Evidently, energy is funnelled to a type A excimer-like precursor, which accounts for the reduction in emission intensity, until emissive aggregates can form below 200 K.

6. High energy peak in TT

As a final point we consider briefly the emission feature observed in **TT** at 2.15 eV for all temperatures and all concentrations, even when diluting further to 5.0×10^{-7} M (see ESI,† Section S9). The fact that this shoulder is independent of concentration excludes intermolecular origins for this spectral feature. We note that this feature does not allow for a description of the overall emission spectra in terms of a single Franck-Condon-transition (see ESI,† Section S10). However, assuming two very similar progressions at different energies gives a satisfactory description of the spectral shape. This is shown in Fig. 7a exemplary for the 200 K emission spectrum. For both progressions, we used a Gaussian linewidth of $\sigma = 59$ meV and the same 3 vibrational energies at 55 meV, 135 meV and 180 meV as observed in the Raman spectra, that we tentatively associated with librations or rotations, C-H in plane bending modes on the rings and C=C stretching modes, respectively.⁸¹ A detailed description of the fitting procedure

and parameters is given in the ESI† (Section S10). To identify the origin of the two features, we performed time-correlated single photon counting measurements at two energies at 200 K. Fig. 7b shows the decay curves at 2.23 eV and at 1.89 eV as well as the instrument response function. Both features show about the same exponential decay of $\tau = 2.2 \pm 0.2$ ns from about 1 ns onward. At shorter times, the signal at 2.23 eV is dominated by different contributions from the instrument response function. More precisely, Raman scattering of the 2850 cm^{-1} mode from the solvent takes place and contributes at very short times.⁸² The same decay time at both energies excludes a transition from a possible higher energy state into a lower energy state. Rather, both features seem to pertain to very similar excited states. Dual emission from two states on the same chromophore such as S_1 and S_2 can be safely excluded as origin since the two features differ by only 150 meV. After excitation into a S_2 state, internal conversion into S_1 would be very fast and outcompete radiative decay due to the energy gap law (Kasha's rule). Furthermore, identical emission spectra upon different excitation energies (3.06 eV and 2.56 eV) as well as DFT calculations safely exclude different rotamers as the origin of the high energy feature.

A further possibility is to consider that both conformations can be accessed after excitation. Fig. 7c shows the potential energy surface for **TT** as a function of the dihedral angle between the two central thiophenes for the ground state (GS) and lowest excited state (ES) before and after relaxation subsequent to a transition. The S_0 to S_1 transition (absorption) occurs vertically from the $\text{GS}_{\text{relaxed}}$ curve to the ES_{GS} curve. In the relaxed GS, the conformation has a *cis*-like character. After the vertical transition, the molecule relaxes into the $\text{ES}_{\text{relaxed}}$ curve. In this process, it can relax to the *cis*-like minimum in the $\text{ES}_{\text{relaxed}}$ curve at 50° or to the *trans*-like minimum above 140° , from where they can decay to the GS_{ES} curve with a slightly larger (*cis*-like) or smaller (*trans*-like) transition energy. Keeping in mind the limitations of DFT calculations for quantitative values for donor-acceptor type compounds, and recalling the case of polyacetylene,⁸³ we can

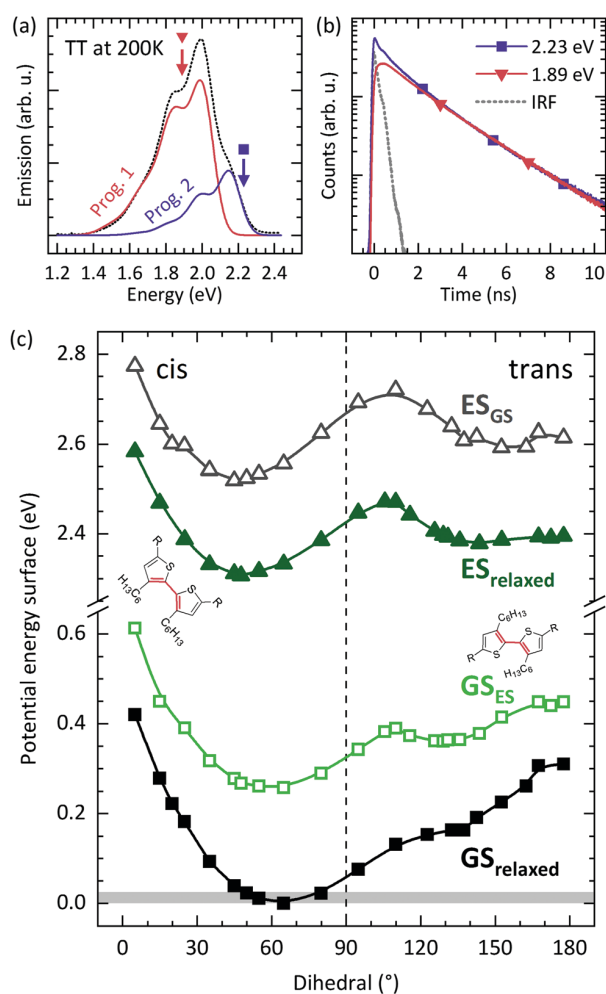


Fig. 7 (a) Decomposition of the **TT** emission spectrum at 200 K into a low energy progression (progression 1) and a high energy progression (progression 2). The symbols mark the spectral positions of the decay curves. (b) Decay curves at 200 K monitored at the energies marked in (a). The grey broken line shows the instrumental response measured at the excitation energy. (c) Potential energy surface of the central thiophene–thiophene dihedral angle in **TT** for ground state (GS) and excited state (ES) obtained by DFT and TD-DFT. The calculations are performed in the relaxed geometries (filled symbols) and in the non-relaxed geometries after electronic transition (open symbols). The grey area indicates $k_B T$ at room temperature. The dashed line serves to separate the *cis*-like conformations visually from the *trans*-like configurations.

still safely associate the *cis*-like configuration with the higher energy transition and the *trans*-like configuration with the lower energy transition. Thus, the high-energy shoulder we observe in **TT** is attributed to emission from molecules where a *cis*-like configuration of the central bithiophene still prevails.

When wondering why there is no energy transfer to molecules in the *trans*-like configuration it is worth recalling that the minimum in the GS geometry is for the *cis*-like configuration, and the *trans*-like configuration is mostly accessed through the excited state. This explains why emission from both configurations can be observed.

7. Conclusions

In this study we address the role of backbone torsion and planarity in the formation of ordered structures using a pair of model oligomers with a twisted central bithiophene unit (**TT**) or a rigid central cyclopentadithiophene (**CT**). Unexpectedly, the more flexible **TT** is found more disposed to form weakly emissive H-type aggregates than planar **CT**. It turns out that the propensity of these oligomers to form ordered structures is not controlled by steric demands of their sidechains. Rather, it can be rationalized by considering the number of attractive interactions that can take place between the various subunits along the oligomer. A certain flexibility of the backbone assists in establishing these intermolecular contact points. In the MD calculations we find that the experimentally observed aggregation in **TT** can only be explained when **TT** is allowed to adopt planar conformation. In this case, the more zig-zag like backbone conformation of **TT** leads to a larger number of attractive interactions than the banana-shape of **CT**. This larger interaction accounts not only for the stronger tendency of **TT** to aggregate, but also can elucidate why **TT** directly forms emissive aggregates while **CT**, upon cooling, first forms non-emissive excimer-type precursors until aggregate formation sets in below 200 K.

Conflicts of interest

There are no conflicts of interest to declare.

Acknowledgements

We acknowledge financial support by the Bavarian State Ministry of Science, Research, and the Arts (StMWK) through the Collaborative Research Network “Solar Technologies go Hybrid” and through the Bavarian Center “BaCaTec”. S. W. was supported by the Elite Network Bavaria (ENB) in the framework of the Elite Study Program “Macromolecular Science” and “MINT Lehramt plus”. A. B. was supported by the German Science Foundation (GRK1640 “Photophysics of Synthetic and Biological Multichromophoric Systems”). We acknowledge support through the computational resources provided by the Bavarian Polymer Institute and the Jülich Supercomputing Center. S. G. thanks the Volkswagen Foundation. This work was also supported by the Universidad Carlos III de Madrid, the European Union’s Seventh Framework Programme for research, technological development and demonstration under grant agreement No. 600371, el Ministerio de Economía, Industria y Competitividad (COFUND2014-51509), el Ministerio de Educación, cultura y Deporte (CEI-15-17), Banco Santander and el Ministerio de Ciencia, Innovación y Universidades (RTI2018-101020-B-I00). This work was supported by the Office of Naval Research Award No. N00014-14-1-0580. A. B. and S. G. were supported by the (DFG, German Research Foundation) – project number 391977956-SFB1357/B04.

References

- 1 D. Moseguí González, C. J. Schaffer, S. Pröller, J. Schlipf, L. Song, S. Bernstorff, E. M. Herzig and P. Müller-Buschbaum, *ACS Appl. Mater. Interfaces*, 2017, **9**, 3282–3287.
- 2 F.-J. Kahle, C. Saller, S. Olthof, C. Li, J. Lebert, S. Weiß, E. M. Herzig, S. Hüttner, K. Meerholz, P. Strohmriegel and A. Köhler, *J. Phys. Chem. C*, 2018, **122**, 21792–21802.
- 3 G. Feng, J. Li, Y. He, W. Zheng, J. Wang, C. Li, Z. Tang, A. Osvet, N. Li, C. J. Brabec, Y. Yi, H. Yan and W. Li, *Joule*, 2019, **3**, 1765–1781.
- 4 N. Gasparini, S. Kahmann, M. Salvador, J. D. Perea, A. Sperlich, A. Baumann, N. Li, S. Rechberger, E. Spiecker, V. Dyakonov, G. Portale, M. A. Loi, C. J. Brabec and T. Ameri, *Adv. Energy Mater.*, 2019, **9**, 1803394.
- 5 Y.-s. Huang, S. Westenhoff, I. Avilov, P. Sreearunothai, J. M. Hodgkiss, C. Deleener, R. H. Friend and D. Beljonne, *Nat. Mater.*, 2008, **7**, 483–489.
- 6 T. A. Papadopoulos, L. Muccioli, S. Athanasopoulos, A. B. Walker, C. Zannoni and D. Beljonne, *Chem. Sci.*, 2011, **2**, 1025–1032.
- 7 A. Sharma, S. Athanasopoulos, P. C. Tapping, R. P. Sabatini, O. F. McRae, M. Müllner, T. W. Kee and G. Lakhwani, *J. Phys. Chem. C*, 2018, **122**, 23910–23916.
- 8 Y. Lin, Y. Li and X. Zhan, *Chem. Soc. Rev.*, 2012, **41**, 4245–4272.
- 9 Y. Chen, X. Wan and G. Long, *Acc. Chem. Res.*, 2013, **46**, 2645–2655.
- 10 A. a. F. Eftaiha, J.-P. Sun, I. G. Hill and G. C. Welch, *J. Mater. Chem. A*, 2013, **2**, 1201–1213.
- 11 S. D. Collins, N. A. Ran, M. C. Heiber and T.-Q. Nguyen, *Adv. Energy Mater.*, 2017, **7**, 1602242.
- 12 F. C. Krebs, S. A. Gevorgyan and J. Alstrup, *J. Mater. Chem.*, 2009, **19**, 5442–5451.
- 13 F. C. Krebs, T. Tromholt and M. Jørgensen, *Nanoscale*, 2010, **2**, 873–886.
- 14 R. Søndergaard, M. Hösel, D. Angmo, T. T. Larsen-Olsen and F. C. Krebs, *Mater. Today*, 2012, **15**, 36–49.
- 15 B. Qu and S. R. Forrest, *Appl. Phys. Lett.*, 2018, **113**, 053302.
- 16 J. Yang, Y. Lin, W. Zheng, A. Liu, W. Cai, X. Yu, F. Zhang, Q. Liang, H. Wu, D. Qin and L. Hou, *ACS Appl. Mater. Interfaces*, 2018, **10**, 22485–22494.
- 17 K. S. Wienhold, V. Körstgens, S. Grott, X. Jiang, M. Schwartzkopf, S. V. Roth and P. Müller-Buschbaum, *ACS Appl. Mater. Interfaces*, 2019, **11**, 42313–42321.
- 18 F. Panzer, H. Bässler and A. Köhler, *J. Phys. Chem. Lett.*, 2017, **8**, 114–125.
- 19 F. Panzer, M. Sommer, H. Bässler, M. Thelakktat and A. Köhler, *Macromolecules*, 2015, **48**, 1543–1553.
- 20 C. Scharsich, F. S. U. Fischer, K. Wilma, R. Hildner, S. Ludwigs and A. Köhler, *J. Polym. Sci., Part B: Polym. Phys.*, 2015, **53**, 1416–1430.
- 21 D. Raithel, S. Baderschneider, T. B. de Queiroz, R. Lohwasser, J. Köhler, M. Thelakktat, S. Kümmel and R. Hildner, *Macromolecules*, 2016, **49**, 9553–9560.
- 22 M. Reichenberger, J. A. Love, A. Rudnick, S. Bagnich, F. Panzer, A. Stradomska, G. C. Bazan, T.-Q. Nguyen and A. Köhler, *J. Chem. Phys.*, 2016, **144**, 074904.
- 23 M. Reichenberger, D. Kroh, G. M. M. Matrone, K. Schötz, S. Pröller, O. Filonik, M. E. Thordardottir, E. M. Herzig, H. Bässler, N. Stingelin and A. Köhler, *J. Polym. Sci., Part B: Polym. Phys.*, 2018, **56**, 532–542.
- 24 H. Huang, L. Yang, A. Facchetti and T. J. Marks, *Chem. Rev.*, 2017, **117**, 10291–10318.
- 25 N. E. Jackson, B. M. Savoie, K. L. Kohlstedt, M. Olvera de la Cruz, G. C. Schatz, L. X. Chen and M. A. Ratner, *J. Am. Chem. Soc.*, 2013, **135**, 10475–10483.
- 26 K. J. Thorley and I. McCulloch, *J. Mater. Chem. C*, 2018, **6**, 12413–12421.
- 27 W. Zhang, Z. Mao, N. Zheng, J. Zou, L. Wang, C. Wei, J. Huang, D. Gao and G. Yu, *J. Mater. Chem. C*, 2016, **4**, 9266–9275.
- 28 M. Levitus, K. Schmieder, H. Ricks, K. D. Shimizu, U. H. F. Bunz and M. A. Garcia-Garibay, *J. Am. Chem. Soc.*, 2001, **123**, 4259–4265.
- 29 J. Kärnbratt, M. Gilbert, J. K. Sprafke, H. L. Anderson and B. Albinsson, *J. Phys. Chem. C*, 2012, **116**, 19630–19635.
- 30 J. Gierschner and S. Y. Park, *J. Mater. Chem. C*, 2013, **1**, 5818.
- 31 A. Mishra and P. Bäuerle, *Angew. Chem., Int. Ed.*, 2012, **51**, 2020–2067.
- 32 Q. Yan, Y. Zhou, Y.-Q. Zheng, J. Pei and D. Zhao, *Chem. Sci.*, 2013, **4**, 4389.
- 33 Y. Liu, C. Mu, K. Jiang, J. Zhao, Y. Li, L. Zhang, Z. Li, J. Y. L. Lai, H. Hu, T. Ma, R. Hu, D. Yu, X. Huang, B. Z. Tang and H. Yan, *Adv. Mater.*, 2015, **27**, 1015–1020.
- 34 W. Chen, X. Yang, G. Long, X. Wan, Y. Chen and Q. Zhang, *J. Mater. Chem. C*, 2015, **3**, 4698–4705.
- 35 W. Chen and Q. Zhang, *J. Mater. Chem. C*, 2017, **5**, 1275–1302.
- 36 C. B. Nielsen, S. Holliday, H.-Y. Chen, S. J. Cryer and I. McCulloch, *Acc. Chem. Res.*, 2015, **48**, 2803–2812.
- 37 C. De Leener, E. Hennebicq, J.-C. Sancho-Garcia and D. Beljonne, *J. Phys. Chem. B*, 2009, **113**, 1311–1322.
- 38 Y. Sun, G. C. Welch, W. L. Leong, C. J. Takacs, G. C. Bazan and A. J. Heeger, *Nat. Mater.*, 2012, **11**, 44–48.
- 39 J. A. Love, C. M. Proctor, J. Liu, C. J. Takacs, A. Sharenko, T. S. V. D. Poll, A. J. Heeger, G. C. Bazan and T.-Q. Nguyen, *Adv. Funct. Mater.*, 2013, **23**, 5019–5026.
- 40 J. A. Love, I. Nagao, Y. Huang, M. Kuik, V. Gupta, C. J. Takacs, J. E. Coughlin, L. Qi, T. S. van der Poll, E. J. Kramer, A. J. Heeger, T.-Q. Nguyen and G. C. Bazan, *J. Am. Chem. Soc.*, 2014, **136**, 3597–3606.
- 41 A. Bourdick, M. Reichenberger, A. Stradomska, G. C. Bazan, T.-Q. Nguyen, A. Köhler and S. Gekle, *J. Phys. Chem. B*, 2018, **122**, 9191–9201.
- 42 J. E. Coughlin, A. Zhugayevych, I. Bakus, C. Ronald, T. S. van der Poll, G. C. Welch, S. J. Teat, G. C. Bazan and S. Tretiak, *J. Phys. Chem. C*, 2014, **118**, 15610–15623.
- 43 G. C. Welch, L. A. Perez, C. V. Hoven, Y. Zhang, X.-D. Dang, A. Sharenko, M. F. Toney, E. J. Kramer, T.-Q. Nguyen and G. C. Bazan, *J. Mater. Chem.*, 2011, **21**, 12700.

- 44 C. Zhou, Q. Cui, C. McDowell, M. Seifrid, X. Chen, J.-L. Brédas, M. Wang, F. Huang and G. C. Bazan, *Angew. Chem.*, 2017, **129**, 9446–9449.
- 45 J.-D. Chai and M. Head-Gordon, *J. Chem. Phys.*, 2008, **128**, 084106.
- 46 T.-J. Lin and S.-T. Lin, *Phys. Chem. Chem. Phys.*, 2015, **17**, 4127–4136.
- 47 M. J. Frisch, G. W. Trucks, H. B. Schlegel, G. E. Scuseria, M. A. Robb, J. R. Cheeseman, G. Scalmani, V. Barone, B. Mennucci, G. A. Petersson, H. Nakatsuji, M. Caricato, X. Li, H. P. Hratchian, A. F. Izmaylov, J. Bloino, G. Zheng, J. L. Sonnenberg, M. Hada, M. Ehara, K. Toyota, R. Fukuda, J. Hasegawa, M. Ishida, T. Nakajima, Y. Honda, O. Kitao, H. Nakai, T. Vreven, J. A. Montgomery, Jr., J. E. Peralta, F. Ogliaro, M. Bearpark, J. J. Heyd, E. Brothers, K. N. Kudin, V. N. Staroverov, T. Keith, R. Kobayashi, J. Normand, K. Raghavachari, A. Rendell, J. C. Burant, S. S. Iyengar, J. Tomasi, M. Cossi, N. Rega, J. M. Millam, M. Klene, J. E. Knox, J. B. Cross, V. Bakken, C. Adamo, J. Jaramillo, R. Gomperts, R. E. Stratmann, O. Yazyev, A. J. Austin, R. Cammi, C. Pomelli, J. W. Ochterski, R. L. Martin, K. Morokuma, V. G. Zakrzewski, G. A. Voth, P. Salvador, J. J. Dannenberg, S. Dapprich, A. D. Daniels, O. Farkas, J. B. Foresman, J. V. Ortiz, J. Cioslowski and D. J. Fox, *Gaussian 09, Revision E.01*, Gaussian, Inc., Wallingford CT, 2013.
- 48 S. Pronk, S. Páll, R. Schulz, P. Larsson, P. Bjelkmar, R. Apostolov, M. R. Shirts, J. C. Smith, P. M. Kasson, D. van der Spoel, B. Hess and E. Lindahl, *Bioinformatics*, 2013, **29**, 845–854.
- 49 M. J. Abraham, T. Murtola, R. Schulz, S. Páll, J. C. Smith, B. Hess and E. Lindahl, *SoftwareX*, 2015, **1-2**, 19–25.
- 50 S. Páll, M. J. Abraham, C. Kutzner, B. Hess and E. Lindahl, in *Solving Software Challenges for Exascale*, ed. S. Markidis and E. Laure, Springer International Publishing, 2015, pp. 3–27.
- 51 B. Hess, C. Kutzner, D. van der Spoel and E. Lindahl, *J. Chem. Theory Comput.*, 2008, **4**, 435–447.
- 52 N. Schmid, A. P. Eichenberger, A. Choutko, S. Riniker, M. Winger, A. E. Mark and W. F. van Gunsteren, *Eur. Biophys. J.*, 2011, **40**, 843.
- 53 P. Ertl, *J. Cheminf.*, 2010, **2**, 1.
- 54 ATB Database: CT Structure and Toplogy Files, <https://atb.uq.edu.au/molecule.py?molid=285451>, accessed June 2019.
- 55 ATB Database: TF Structure and Toplogy Files, <https://atb.uq.edu.au/molecule.py?molid=285450>, accessed June 2019.
- 56 A. K. Malde, L. Zuo, M. Breeze, M. Stroet, D. Poger, P. C. Nair, C. Oostenbrink and A. E. Mark, *J. Chem. Theory Comput.*, 2011, **7**, 4026–4037.
- 57 S. Canzar, M. El-Kebir, R. Pool, K. Elbassioni, A. K. Malde, A. E. Mark, D. P. Geerke, L. Stougie and G. W. Klau, *J. Comput. Biol.*, 2013, **20**, 188–198.
- 58 K. B. Koziara, M. Stroet, A. K. Malde and A. E. Mark, *J. Comput. – Aided Mol. Des.*, 2014, **28**, 221–233.
- 59 ATB Database: Hexane Structure and Toplogy Files, <https://atb.uq.edu.au/molecule.py?molid=467>, accessed June 2019.
- 60 J. Kästner, *WIREs Comput. Mol. Sci.*, 2011, **1**, 932–942.
- 61 J. S. Hub, B. L. de Groot and D. van der Spoel, *J. Chem. Theory Comput.*, 2010, **6**, 3713–3720.
- 62 A. Barducci, G. Bussi and M. Parrinello, *Phys. Rev. Lett.*, 2008, **100**, 020603.
- 63 B. M. Dickson, *Phys. Rev. E: Stat., Nonlinear, Soft Matter Phys.*, 2011, **84**, 037701.
- 64 A. Laio and M. Parrinello, *Proc. Natl. Acad. Sci. U. S. A.*, 2002, **99**, 12562–12566.
- 65 A. Barducci, M. Bonomi and M. Parrinello, *WIREs Comput. Mol. Sci.*, 2011, **1**, 826–843.
- 66 G. A. Tribello, M. Bonomi, D. Branduardi, C. Camilloni and G. Bussi, *Comput. Phys. Commun.*, 2014, **185**, 604–613.
- 67 The PLUMED consortium, *Nat. Methods*, 2019, **16**, 670–673.
- 68 W. Humphrey, A. Dalke and K. Schulten, *J. Mol. Graphics Modell.*, 1996, **14**, 33–38.
- 69 A. Köhler, S. T. Hoffmann and H. Bässler, *J. Am. Chem. Soc.*, 2012, **134**, 11594–11601.
- 70 J. Gierschner, H.-G. Mack, L. Lüer and D. Oelkrug, *J. Chem. Phys.*, 2002, **116**, 8596.
- 71 N. J. Hestand and F. C. Spano, *Chem. Rev.*, 2018, **118**, 7069–7163.
- 72 D. Raitchel, L. Simine, S. Pickel, K. Schötz, F. Panzer, S. Baderschneider, D. Schiefer, R. Lohwasser, J. Köhler, M. Thelakkat, M. Sommer, A. Köhler, P. J. Rossky and R. Hildner, *Proc. Natl. Acad. Sci. U. S. A.*, 2018, **115**, 2699–2704.
- 73 A. T. Haedler, H. Misslitz, C. Buehlmeier, R. Q. Albuquerque, A. Köhler and H.-W. Schmidt, *ChemPhysChem*, 2013, **14**, 1818–1829.
- 74 H. Hu, P. C. Y. Chow, G. Zhang, T. Ma, J. Liu, G. Yang and H. Yan, *Acc. Chem. Res.*, 2017, **50**, 2519–2528.
- 75 C. McDowell, K. Narayanaswamy, B. Yadagiri, T. Gayathri, M. Seifrid, R. Datt, S. M. Ryno, M. C. Heifner, V. Gupta, C. Risko, S. P. Singh and G. C. Bazan, *J. Mater. Chem. A*, 2018, **6**, 383–394.
- 76 J. Shi, A. Isakova, A. Abudulimu, M. V. D. Berg, O. K. Kwon, A. J. Meixner, S. Y. Park, D. Zhang, J. Gierschner and L. Lüer, *Energy Environ. Sci.*, 2018, **11**, 211–220.
- 77 M. T. Seifrid, G. N. M. Reddy, C. Zhou, B. F. Chmelka and G. C. Bazan, *J. Am. Chem. Soc.*, 2019, **141**, 5078–5082.
- 78 G. Barbarella, M. Zambianchi, A. Bongini and L. Antolini, *Adv. Mater.*, 1992, **4**, 282–285.
- 79 G. Macchi, B. M. Medina, M. Zambianchi, R. Tubino, J. Cornil, G. Barbarella, J. Gierschner and F. Meinardi, *Phys. Chem. Chem. Phys.*, 2009, **11**, 984–990.
- 80 G. C. Welch, I. Bakus, C. Ronald, S. J. Teat and G. C. Bazan, *J. Am. Chem. Soc.*, 2013, **135**, 2298–2305.
- 81 A. Köhler and H. Bässler, *Electronic Processes in Organic Semiconductors: An Introduction*, Wiley-VCH Verlag GmbH & Co. KGaA, Weinheim, Germany, 2015.
- 82 F. F. Cleveland and P. Porcelli, *J. Chem. Phys.*, 1950, **18**, 1459–1461.
- 83 H. Eckhardt, *J. Chem. Phys.*, 1983, **79**, 2085–2086.

Electronic Supporting Information

What is the role of planarity and torsional freedom for aggregation in a π -conjugated donor-acceptor model oligomer?

Stefan Wedler¹, Axel Bourdick², Stavros Athanasopoulos³, Stephan Gekle², Fabian Panzer¹, Caitlin McDowell⁴, Thuc-Quyen Nguyen⁴, Guillermo C. Bazan⁵, Anna Köhler^{1,6*}

¹ Soft Matter Optoelectronics, Experimentalphysik II, University of Bayreuth, Bayreuth 95440, Germany.

²Biofluid Simulation and Modeling, Theoretische Physik VI, Universität Bayreuth, Bayreuth 95440, Germany

³Departamento de Física, Universidad Carlos III de Madrid, Avenida Universidad 30, 28911 Leganés, Madrid, Spain.

⁴Center for Polymers and Organic Solids, Departments of Chemistry & Biochemistry and Materials, University of California, Santa Barbara

⁵Departments of Chemistry and Chemical Engineering, National University of Singapore, Singapore, 119077

⁶Bayreuth Institute of Macromolecular Research (BIMF) and Bavarian Polymer Institute (BPI), University of Bayreuth, 95440 Bayreuth, Germany.

*e-mail: Anna.Koehler@uni-bayreuth.de

1 Simulated spectra

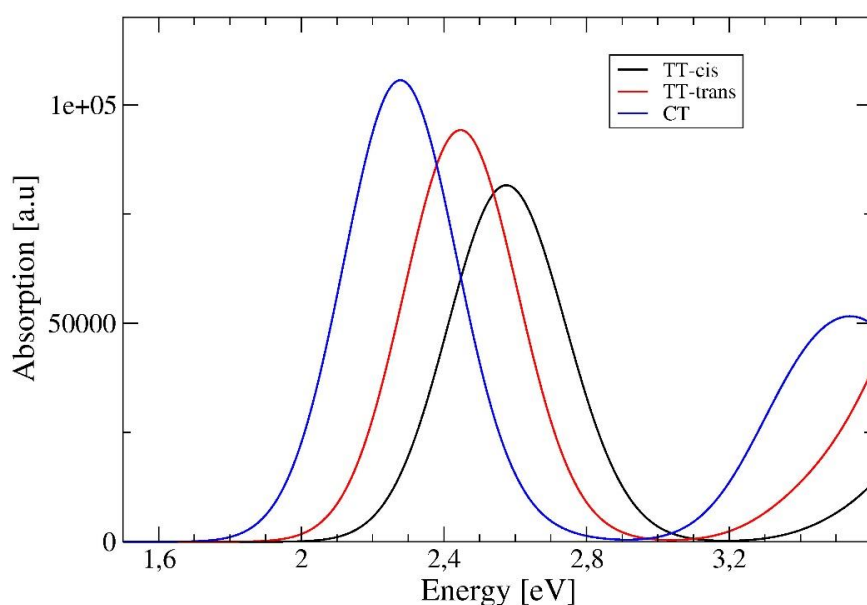


Figure S1.1: Single molecule TD-DFT simulated absorption spectra at the wB97XD/6-31G** level for the TT and CT molecules. TT absorption at the ground state twisted cis and trans configurations is depicted. Vertical transition energies have been broadened by a Gaussian function with a half-width at half-height of 1500cm^{-1} .

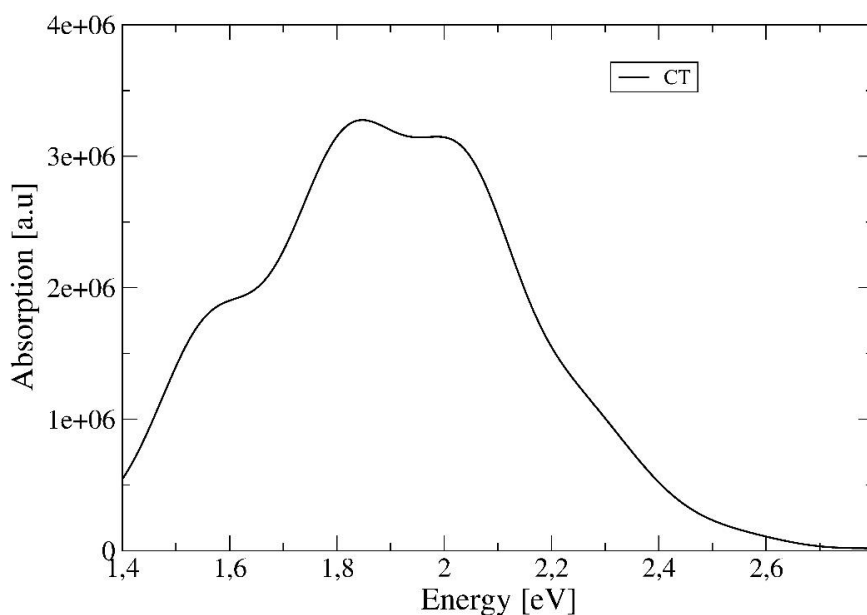


Figure S1.2: Simulated average CT aggregate absorption spectrum. The six lowest vertical transition transition energies for CT dimer configurations taken from the MD simulations have been computed with TD-DFT at the wB97XD/6-31G** level. Vertical transition energies have been broadened by a Gaussian function with a half-width at half-height of 1500cm^{-1} . A total of 60 snapshot configurations corresponding to type A and type B conformations from the three minima of the free energy curve (Figure 5) was used.

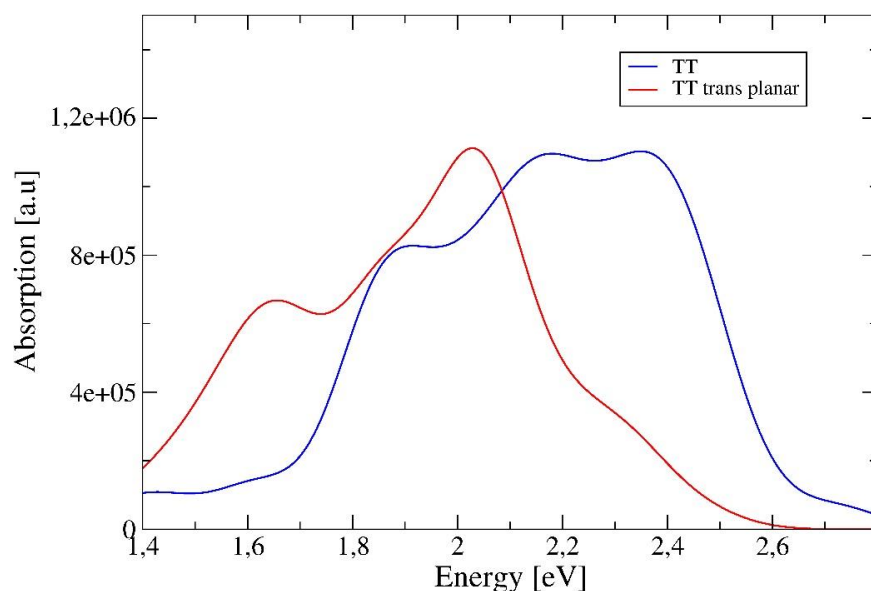


Figure S1.3: Simulated average TT aggregate absorption spectra. The six lowest vertical transition transition energies for TT dimer configurations taken from the MD simulations have been computed with TD-DFT at the wB97XD/6-31G** level. Vertical transition energies have been broadened by a Gaussian function with a half-width at half-height of 1500cm^{-1} . A total of 40 snapshot configurations for the four minima of the free energy curve (Figure 5) was used for the twisted TT aggregates. A total of 30 snapshot configurations from the lowest energy minima of the free energy curve (Figure 6) for the trans planar TT aggregates was used.

2 Methodical details of Simulations

As described in the main text, we used the *automated force field topology builder and repository*¹⁻³ to get starting force field models for CT⁴ and TT⁵ which we refined with our own calculations to better reflect the physical properties of the molecules. The model for the solvent Hexane⁴ was taken from ATB directly. We used non-polarizable force fields. As we investigate aggregation in a nonpolar solvent, we expect no major difference of our results if a polarizable force field is used.

Determination of partial charges

To make the models more accurate we calculated the charge distribution for CT and TT with Gaussian09, Revision E.01.⁶ We requested tight convergence in geometry optimization and used an ultrafine integration grid. We refined the charge distribution by incorporating charges which were calculated via ground state structure optimization with the Mullikan fitting scheme with the help of Gaussian.

Determination of dihedral potential energy surfaces

The donor and acceptor units of the molecules CT and TT consist of aromatic rings, which are connected via single C-C bonds. To accurately reproduce the aggregation properties, we calculated the potential energy surfaces (PES) of the dihedral angles between the donor and acceptor units for

the relevant fragments with quantum chemical calculations. Relaxed potential energy scans were used. We scanned from 0° to 180° in intervals of 5°. We reused the PES data from our previous work,⁷ because the fragments in question are the same as for previously investigated systems, for which we used the CAM-B3LYP long-range corrected functional with the 6-31G** basis set. We adjusted our MD models to reproduce the calculated PES by implementing Ryckaert-Bellemans Potentials.

The defining characteristic of TT lies in its twisted geometry. The central donor unit consists of two thiophene units with a hexane side-chain attached to both which determines the resulting structure. To accurately describe the central dihedral, we used the long-range corrected functional *wB97xD*. We determined the long-range correction parameter to be 0.13 bohr⁻¹ via the condition

$$IP = -\epsilon_{HOMO}$$

where IP denotes the ionization energy for the ground state geometry and ϵ_{HOMO} is the energy of the highest occupied molecular orbital and used that value for the PES scan. The calculated PES is displayed in Figure 7 in the main text ($GS_{relaxed}$). We also calculated the PES for the first excited state (GS_{ES}). For each configuration we also calculated the vertical transition energies in order to obtain the graphs for $ES_{relaxed}$ and ES_{GS} in Figure 7.

The models without side chains were made based on the models of the full systems. The side chains were cut off and replaced by CH₃ groups. The charge distribution was adjusted near the points of intersection to ensure a vanishing net charge.

The planarized TT models were constructed by replacing the twisted central potential in order to force the molecule in the desired orientation with the potential:

$$V(\varphi) = k(1 + \cos(n\varphi - \varphi_s))$$

The intramolecular dihedral angle is denoted as φ . The multiplicity n was set to 1, the force constant k was chosen to be 100 kJ/mol and φ_s was chosen to get a cis- or trans-planar configuration accordingly.

We extracted average configurations from our MD simulations. Because the molecules rotate and move during the simulation, for each time frame we constructed a coordinate system inside the reference frame of the molecule, then transformed the whole simulation box to this coordinate system in which we averaged the position of the solute molecule. This approach works, as long as no aromatic rings flip, because then one would average two different configurations which would skew the final structure. We therefore chose a suitable window for the averaging process in which no flips occur.

To better visualize the dimer conformations, we created rotating video clips of these average configurations of the most stable dimers. For this, the structures are averaged over 10 ns. For clarity of presentation, the sidechains have been replaced with CH₃ groups. For orientation, sulfur atoms are marked in yellow, nitrogen in blue.

Parameters for MD simulations and free energy calculations

The parameters used for all MD simulations are displayed in Table S2.1.

Table S2.1: The Gromacs parameters used for the MD simulations.

Option	Value
Integrator	Md
dt	0.002
Nstxout	200
constraint_algorithm	lincs
constraints	h-bonds
lincs_iter	1
lincs_order	4
ns_type	Grid
nstlist	15
rlist	1.0
rcoulomb	1.0
rvdw	1.0
coulombtype	PME
tcoupl	v-rescale
tau_t	0.1
pcoupl	Berendsen
pcoupltype	isotropic
tau_p	2.0
ref_p	1.0
compressibility	4.5e-5
pcbc	xyz
DispCorr	EnerPres
gen_seed	-1

For all free energy graphs shown in the main text, which were made with umbrella sampling, we swept the reaction pathway multiple times independently to ensure a sufficient sampling of the whole configurational phase space. All free energy graphs shown in the main text were made with umbrella sampling by sampling the reaction pathway multiple times independently to ensure a sufficient sampling of the whole configurational phase space. The details for the individual simulations are presented in the following. To give the system time to equilibrate, we cut off the first 200 ps of each window for each simulation.

To calculate the distance between two molecules during an aggregation process, we used the distance between the two molecules as the reaction coordinate. For TT, we defined this as the distance of the center of mass of the central donor units, for CT we used the center of mass of the central ring of the central donor units.

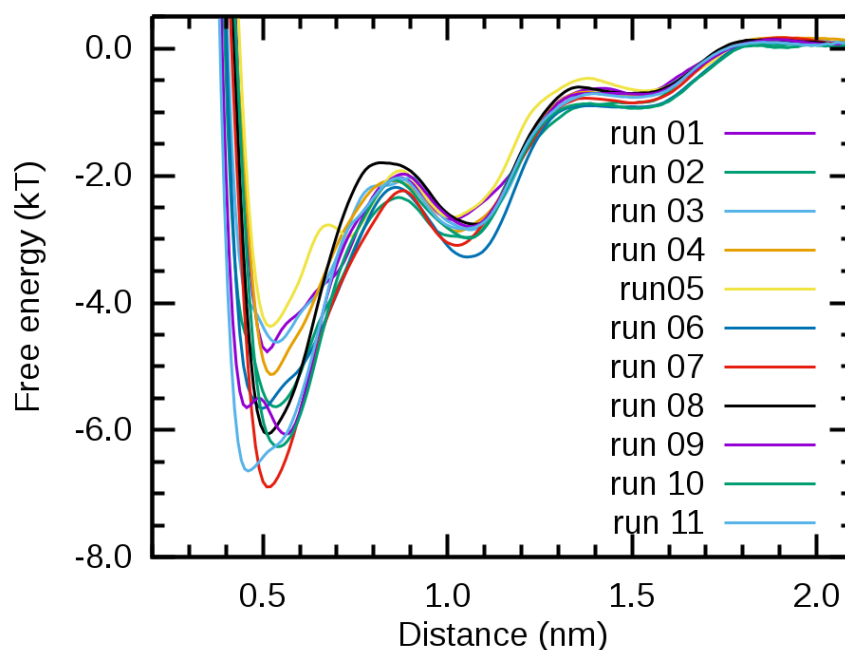


Figure S2.1: All individual free energy graphs for CT. The number of the run corresponds to the parameters defined in Table S2.2.

The free energy of CT with sidechains as displayed in Figure 5c in the main text was made from eleven individual simulations, in all of which the reaction coordinate was sampled independently. The parameters for the individual simulations are shown in Table S2.2. The individual free energy graphs are displayed in Figure S2.1.

Table S2.2: Parameters used in the individual free energy simulations for CT, which are combined to the free energy in Figure 5c in the main text.

Number	Time per window (ns)	Number of windows	Force constant (kJ/mol)	Number hexane molecules
1	60 – 80	44	1200	1100
2	60 – 120	33	1100 - 1200	500
3	60 - 120	33	1100 – 1200	500
4	450	33	1000 – 1200	500
5	100 - 140	33	1000 – 1200	500
6	200	35	800	600
7	200	35	800	600
8	200	34	1000	500
9	380	35	1000	500
10	200	32	1000	450
11	200	33	1000	450

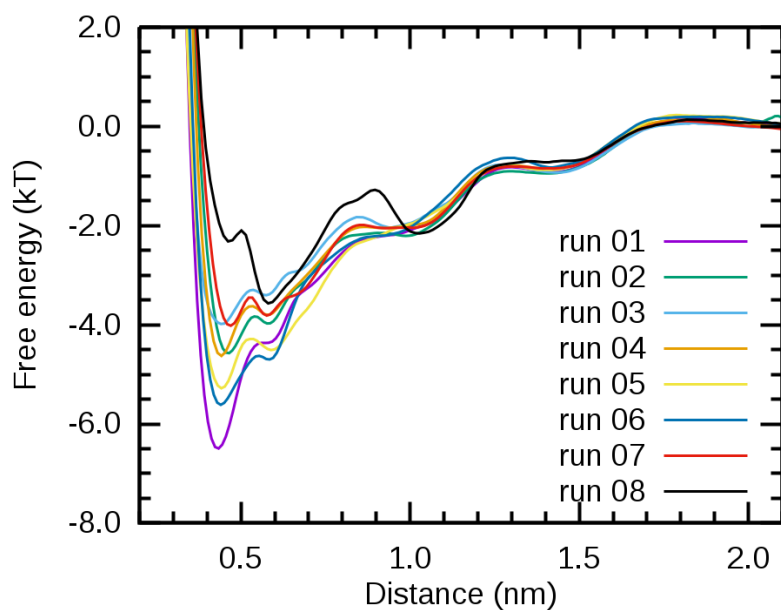


Figure S2.2: The curves used in the individual free energy calculations for TT are displayed here. They are combined to get the full free energy profile displayed in Figure 5a in the main text.

For TT, we combined eight individual free energy calculations. The parameters for each run are shown in Table S2.3 and the corresponding graphs in Figure S2.2. All these simulations were combined to yield the full free energy graph shown in Figure 5a in the main text.

Table S2.3: The parameters used in the individual free energy calculations for TT. They are combined to get the full free energy profile displayed in Figure 5a in the main text.

Number	Time per window (ns)	Number of windows	Force constant (kJ/mol)	Number hexane molecules
1	300	41	1000	600
2	300	34	1000	500
3	200	35	1000	500
4	800	42	1000	800
5	100 – 200	30	1000 – 1200	600
6	80 – 100	34	1000 – 1200	600
7	200 – 760	32	1000 – 1200	600
8	80	47	1200	1100

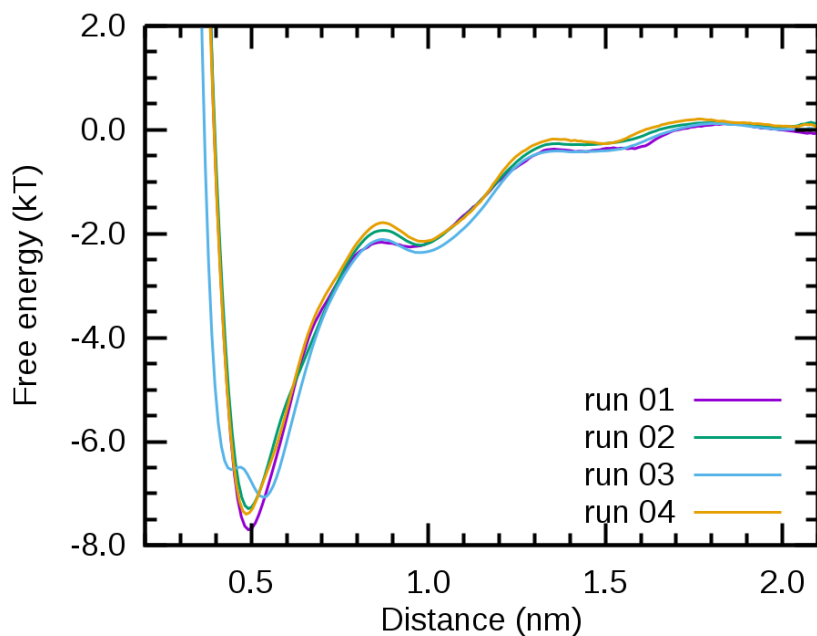


Figure S2.3: Individual free energy calculations used for CT with CH₃ sidechains.

The models without side-chains required less intense sampling, because the absence of them significantly reduces the possible configurational phase space of the system resulting in faster convergence. For CT without side-chains (shown in Figure 5c in the main text) we combined four independent free energy samplings, the parameters of which are displayed in Table S2.4 with their graphs shown in Figure S2.3.

Table S2.4: For CT with CH₃ sidechains we combined four individual free energy calculations, the parameters of which are shown here.

Number	Time per window (ns)	Number of windows	Force constant (kJ/mol)	Number hexane molecules
1	400	33	1000	600
2	180	32	1000	450
3	200	32	1000	450
4	200	30	1000	450

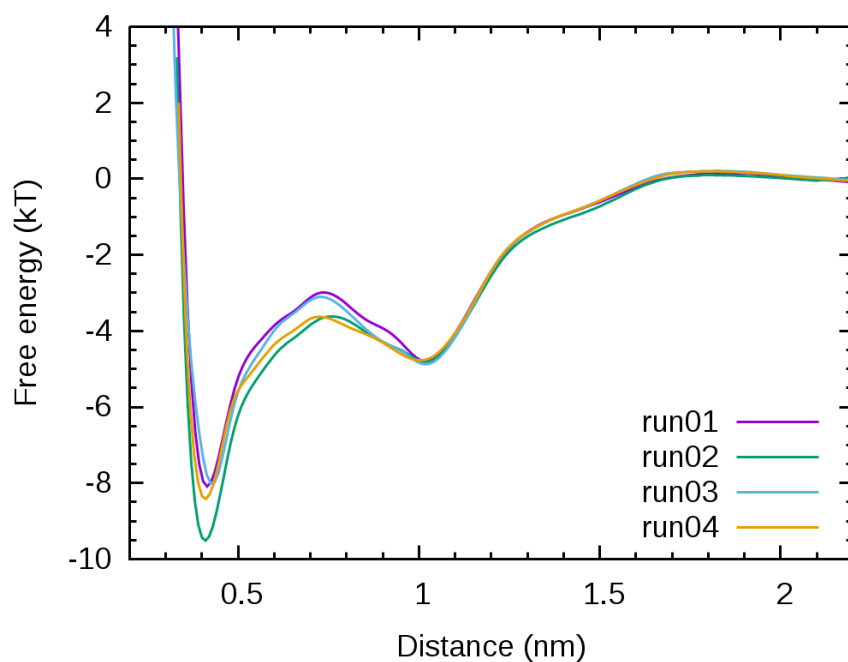


Figure S2.4: Individual free energy calculations used for TT with CH₃ sidechains.

For TT without side-chains we also combined four individual samplings of the reaction coordinate to yield the whole free energy graph shown in Figure 5a of the main text. The parameters are shown in Table S2.5 with their corresponding graphs displayed in Figure S2.4.

Table S2.5: Parameters used in the individual free energy calculations for TT with CH₃ sidechains. They are combined to get the full free energy profile displayed in Figure 5a in the main text.

Number	Time per window (ns)	Number of windows	Force constant (kJ/mol)	Number hexane molecules
1	400	34	800	650
2	220	35	800	600
3	400	35	900	650
4	250	37	800	650

Free energy error analysis

With the *Weighted Histogram Analysis Method* (WHAM), the free energy is calculated for small windows individually, after which they are combined to span the whole parameter space of the reaction coordinate. The statistical error of this recombination process can be estimated with a bootstrap analysis.⁸ The results from the error analysis are shown in Figure S2.5

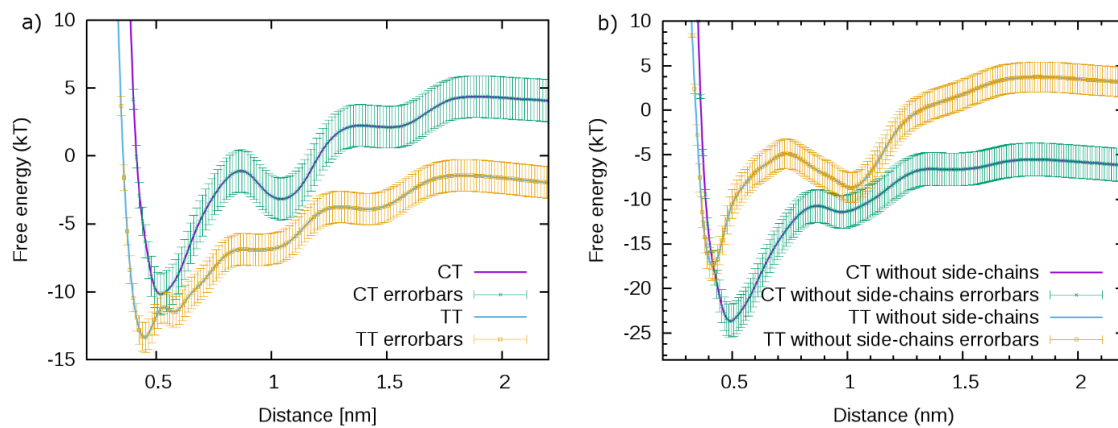


Figure S2.5: a) Free energy of CT and TT with hexyl sidechains with error bars from bootstrap analysis. b) Free energy of CT and TT with CH₃ sidechains with error bars from bootstrap analysis.

Metadynamics results

To distinguish the free energy of type A and type B aggregation in CT we employed well-tempered metadynamics to calculate the free energy in dependence of the distance between the molecule and their relative intermolecular orientation simultaneously. The result is presented in Figure S2.6. The offset can be chosen arbitrarily as only free energy differences determine which process can happen spontaneously. For the metadynamics plots we set the zero point to the global minimum. To describe the relative orientation of the two molecules, we defined a dihedral angle consisting of the outer most C atoms of the central donor units for both molecules.

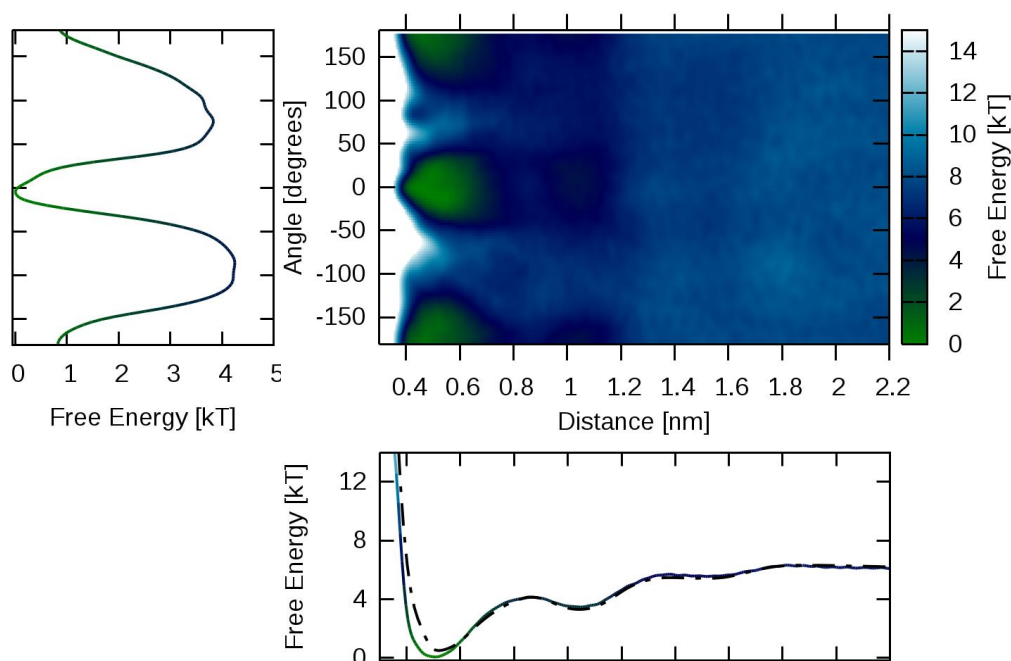


Figure S2.6: Two-dimensional free energy surface of two CT molecules in Hexane in dependence of distance and intermolecular angle calculated with metadynamics. The projections on the one-dimensional reaction coordinates are shown. The dashed line in the distance plot corresponds to the free energy calculated by umbrella sampling (Figure 5c in the main text). Here we placed zero energy to the potential minimum rather than at infinity.

The minima for type A and type B aggregates are at the same energy in the two-dimensional plot. When integrating out over all distances to get the global angular dependence, there is a small energetic difference between type A and type A aggregates of about 0.7 kT.

For the sake of completeness, we also calculated the free energy with metadynamics for TT in Hexane, shown in Figure S2.7. The angular dependence between the molecules is more complicated, probably due to the intramolecular rotational degree of freedom. There is a clear global minimum at about 180°, which corresponds to the configuration we identified in the main text. The comparison with the free energy in dependence of distance calculated with umbrella sampling shows excellent agreement.

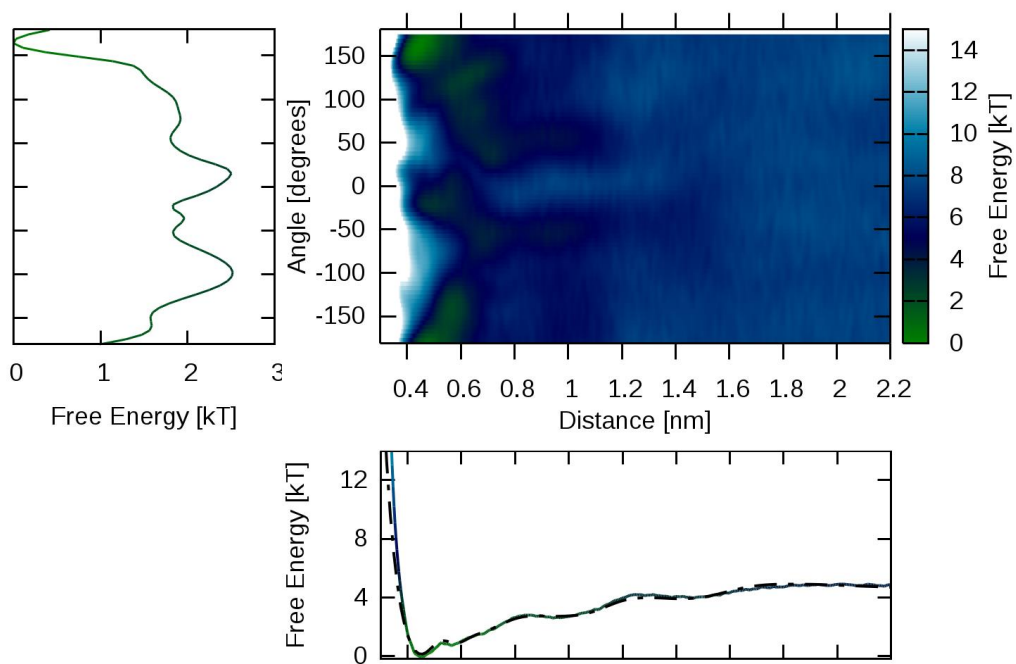


Figure S2.7: Two-dimensional free energy surface of two TT molecules in Hexane in dependence of distance and intermolecular angle calculated with metadynamics. The projections on the one-dimensional reaction coordinates are shown. The dashed line in the distance plot corresponds to the free energy calculated by umbrella sampling (Figure 5a in the main text). Here we placed zero energy to the potential minimum rather than at infinity.

3 Franck-Condon analysis of CT absorption spectra

Fitting procedure

Absorption and emission spectra can be modelled using a simple Franck-Condon description. This allows determining the energetic position of the 0-0 transition, the linewidth and the coupling of the transition to intramolecular vibrations. The intensity of emission I_{PL} and absorption I_{Abs} for several contributing vibrational modes is the sum of all transitions from the vibrational level $(0, 0, \dots) \rightarrow (m_1, m_2, \dots)$ and given by⁹

$$\frac{I_{PL}(E)}{(n \cdot E)^3} \propto \sum_{m_i} \prod_i \frac{S_i^{m_i} \exp(-S_i)}{m_i!} \Gamma \left[\left(E - \left(E_0 - \sum_i m_i E_i^{vib} \right) \right) \right]$$

$$\frac{I_{Abs}(E)}{n \cdot E} \propto \sum_{m_i} \prod_i \frac{S_i^{m_i} \exp(-S_i)}{m_i!} \Gamma \left[\left(E - \left(E_0 + \sum_i m_i E_i^{vib} \right) \right) \right]$$

with photon energy E , refractive index n of the surrounding medium (assumed to be constant for dilute solutions), energy of the 0-0 transition E_0 , vibrational energy E_i^{vib} and Huang-Rhys factor S_i of the i -th contributing vibrational mode. The factors $(n \cdot E)^3$ in emission and $n \cdot E$ in absorption take the photon density of states into account. $\Gamma(E)$ is the line shape function and assumed as purely Gaussian:

$$\Gamma(E) = \exp \left(-\frac{(E)^2}{2\sigma^2} \right)$$

We get the energies of the vibrational modes from the Raman spectra of both molecules, which are shown in Figure S3.1.

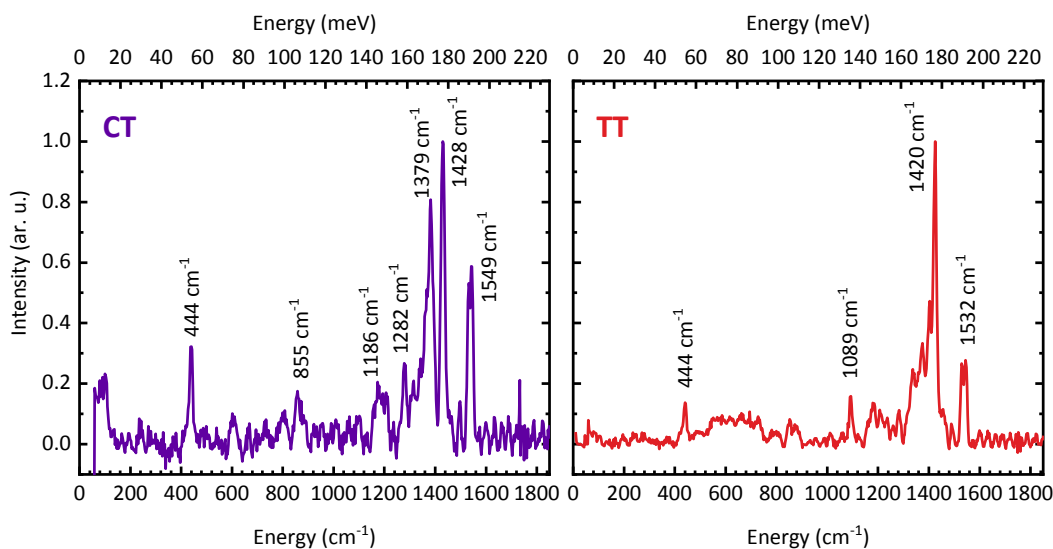


Figure S3.1: Raman spectra of CT and TT. The most prominent modes are labelled with their energies.

For CT we use the modes at 444 cm^{-1} (55 meV), 855 cm^{-1} (106 meV), 1412 cm^{-1} (175 meV) and 1549 cm^{-1} (192 meV), for TT in section 10 we use the modes at 444 cm^{-1} (55 meV), 1089 cm^{-1} (135 meV) and 1452 cm^{-1} (180 meV). Close-by vibrational modes are treated as effective modes in both cases.

Fitting results of the absorption of CT in hexane ($5.0 \cdot 10^{-6}$ M)

We start modelling the spectrum at 200 K. The resulting parameters are then used as starting point for the next temperature, where we mainly varied the energy of the 0-0 transition and the width of the Gaussian line shape. This procedure is then sequentially repeated for all remaining temperatures, varying the Huang-Rhys parameters as little as possible. The final parameters are shown in Table S3, the spectra with the modelled curves are displayed in Figure S3.2 along with the 0-0 transition and the first vibronic transitions. The results clearly show that the linewidth varies strongly with temperature, in contrast to the Huang-Rhys parameters, which mostly remain constant. Therefore, the changes in σ can account for the apparent change in peak ratios. We also give the linewidth as FWHM, which is calculated to $\text{FWHM} = 2\sqrt{2 \ln 2} \cdot \sigma$ for Gaussian lineshapes.

Table S3: Fitting parameters and resulting reorganization energies of absorption spectra of CT in hexane ($5.0 \cdot 10^{-6}$ M)

Temperature (K)	E_0 (eV)	σ (meV)	FWHM (meV)	S 55 meV	S 106 meV	S 175 meV	S 192 meV	λ (meV)
200	2.014	52.00	122.4	0.1141	0.5273	0.1262	0.3420	149.9
210	2.020	53.12	125.1	0.1141	0.5273	0.1262	0.3420	149.9
220	2.024	54.31	127.9	0.1176	0.5299	0.1269	0.3420	150.5
230	2.029	55.96	131.8	0.1314	0.5299	0.1269	0.3419	151.2
240	2.032	57.13	134.5	0.1314	0.5382	0.1269	0.3530	154.3
250	2.037	58.38	137.5	0.1314	0.5382	0.1269	0.3530	154.3
260	2.040	60.19	141.7	0.1314	0.5407	0.1269	0.3670	157.2
270	2.046	61.49	144.8	0.1314	0.5407	0.1269	0.3670	157.2
280	2.050	62.22	146.5	0.1314	0.5407	0.1269	0.3670	157.2
290	2.054	63.82	150.3	0.1314	0.5611	0.1269	0.3714	160.2
300	2.057	64.29	151.4	0.1314	0.5643	0.1269	0.3714	160.6

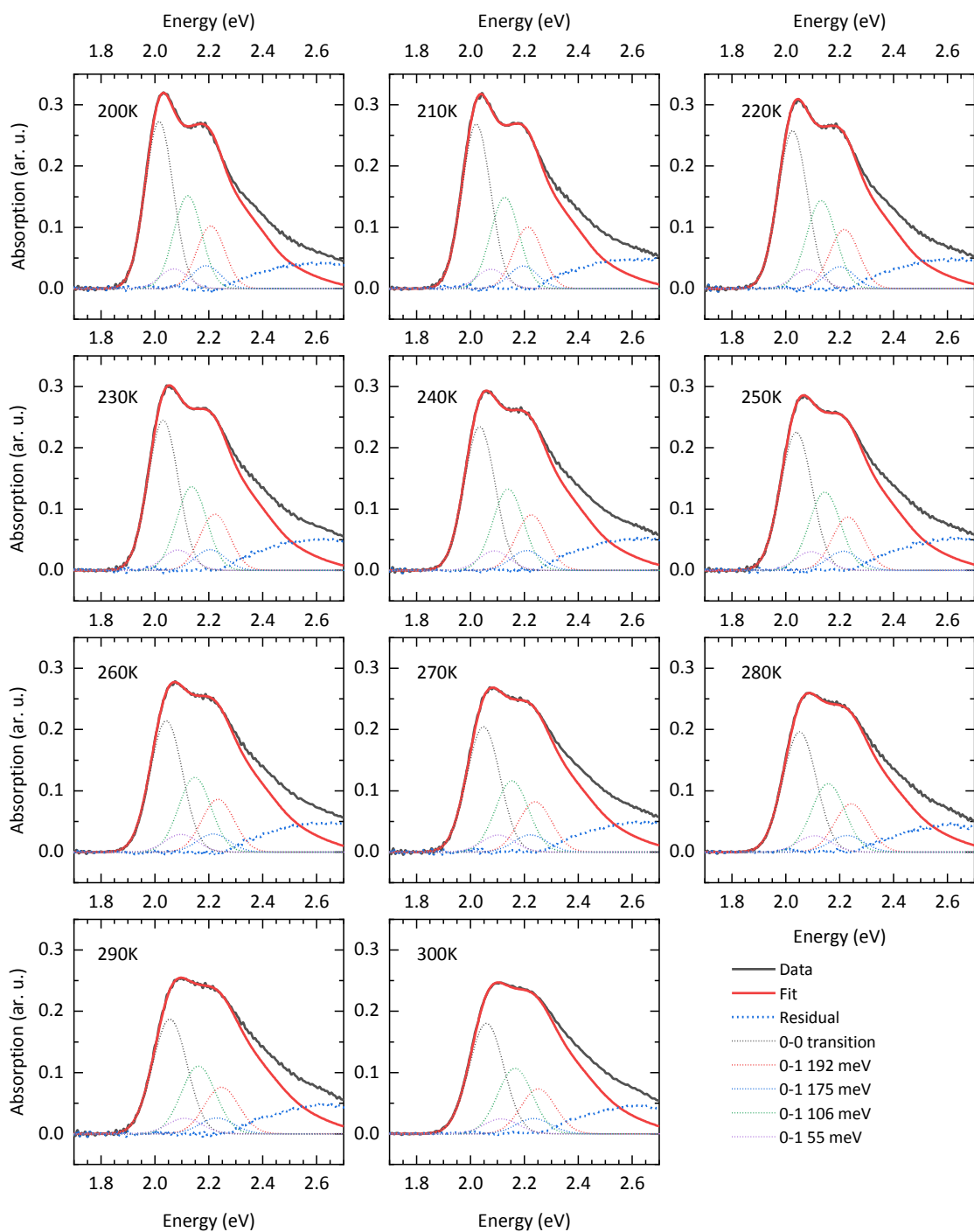


Figure S3.2: Franck-Condon fits of CT absorption spectra in hexane ($5.0 \cdot 10^{-6}$ M) for different temperatures. The position of the 0-0 transition as well as the first vibronic transitions are shown in dotted lines.

4 CT absorption and emission spectra in separate graphs

In the manuscript we compare the spectral shapes at fixed temperatures for different concentrations. We showed them in a tidy and compact format. However, direct comparison may be difficult. Here we show the same data, but plot spectra for different concentrations at the same temperature in a joint graph.

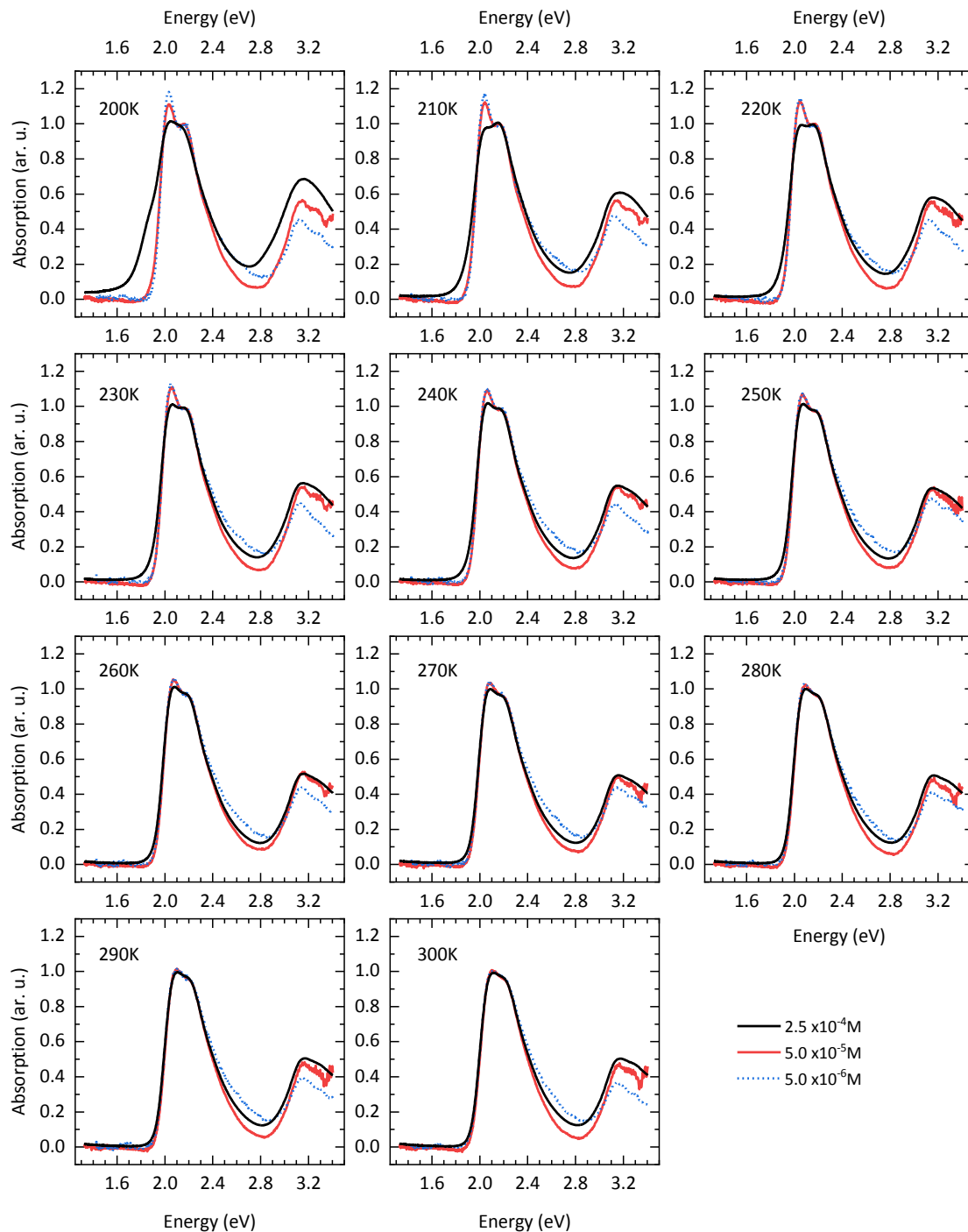


Figure S4.1: Absorption of CT in hexane at different temperatures and concentrations normalized to the vibronic 0-1 transition.

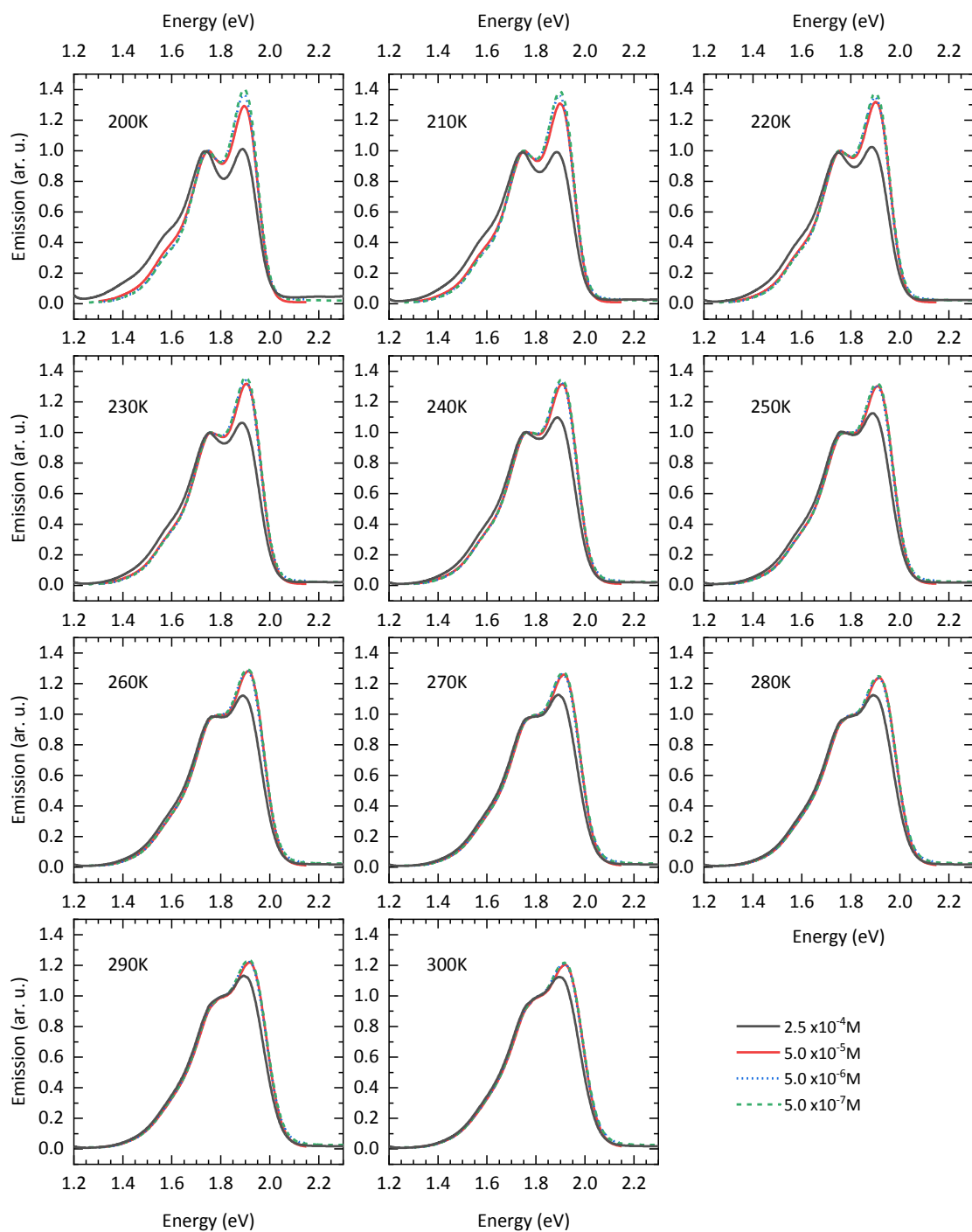


Figure S4.2: Emission of CT in hexane at different temperatures and concentrations normalized to the vibronic 0-1 transition. We additionally measured at a concentration of 5.0×10^{-7} M to safely exclude the possibility of aggregation for all higher concentrations.

5 Absorption and emission using different solvents

Figure S5.1 shows the emission and absorption spectra of CT and TT at room temperature in solvents with increasing polarities (hexane [0.009], toluene [0.099], mTHF [0.179], chlorobenzene [0.188], chloroform [0.259]; relative polarities in squared brackets¹⁰). Both CT and TT behave similarly. The spectral position of the absorption spectra remains unchanged. For CT, the weak structure of the absorption in hexane disappears. All other absorption spectra are broad and unstructured. The emission spectra become increasingly unstructured with increasing solvent polarity, in accordance to the absorption spectra. However, the emission spectra undergo an increasing bathochromic shift with increasing solvent polarity, This is consistent with a charge transfer character of the excited state, as the energy associated with solvent reorganization is larger for more polar solvents.¹¹

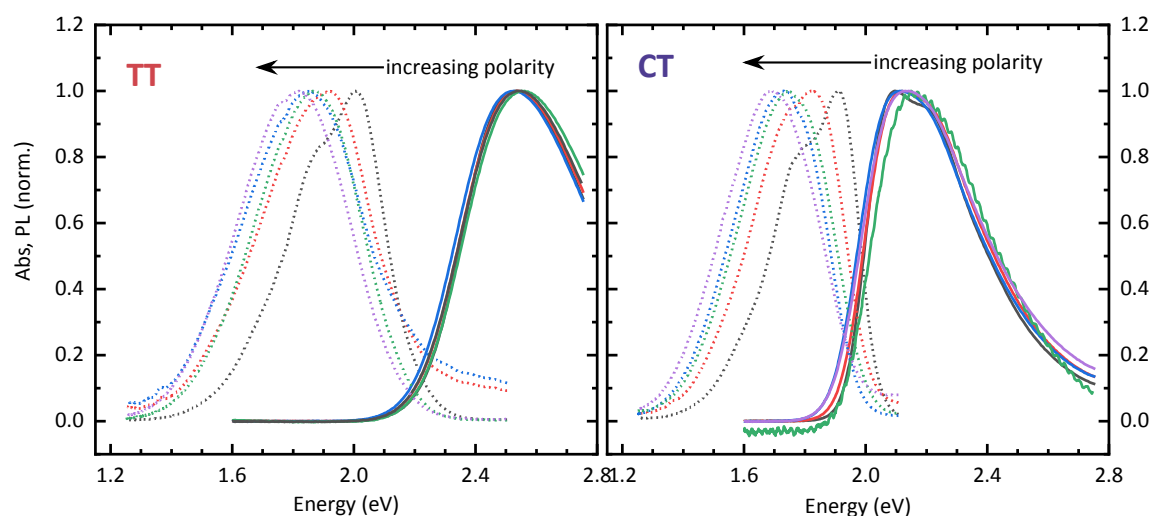


Figure S5.1: Absorption and emission spectra of CT and TT in solvents with different polarities (hexane, toluene, mTHF, chlorobenzene, chloroform).

We further performed temperature dependent absorption and emission measurements for both molecules in solutions of chloroform and mTHF, see Figure S5.2. The trends are similar to the corresponding evolution in hexane solutions at the lowest concentration investigated in the main manuscript. The absorption spectra increase and shift to lower energies upon cooling. Pronounced spectral structures are missing with CT in mTHF below 200 K as an exception.

The emission spectra also shift to lower energies upon cooling while remaining unstructured. However, the amount of bathochromic shift is larger than for hexane, which is consistent with the larger Stokes' shift in more polar solvents. For TT in mTHF one may suspect a shoulder on the high energy side of the emission at low temperatures. In accordance with the arguments we elaborated in the main manuscript (section 6) for the high energy shoulder in hexane, we assign this shoulder to emission from cis- and trans-planar conformations of TT in the excited state. However, here it is mostly masked by the large broadening.

Importantly, we do not observe any spectral signs of aggregation in both chloroform and mTHF at all spectroscopic accessible concentrations.

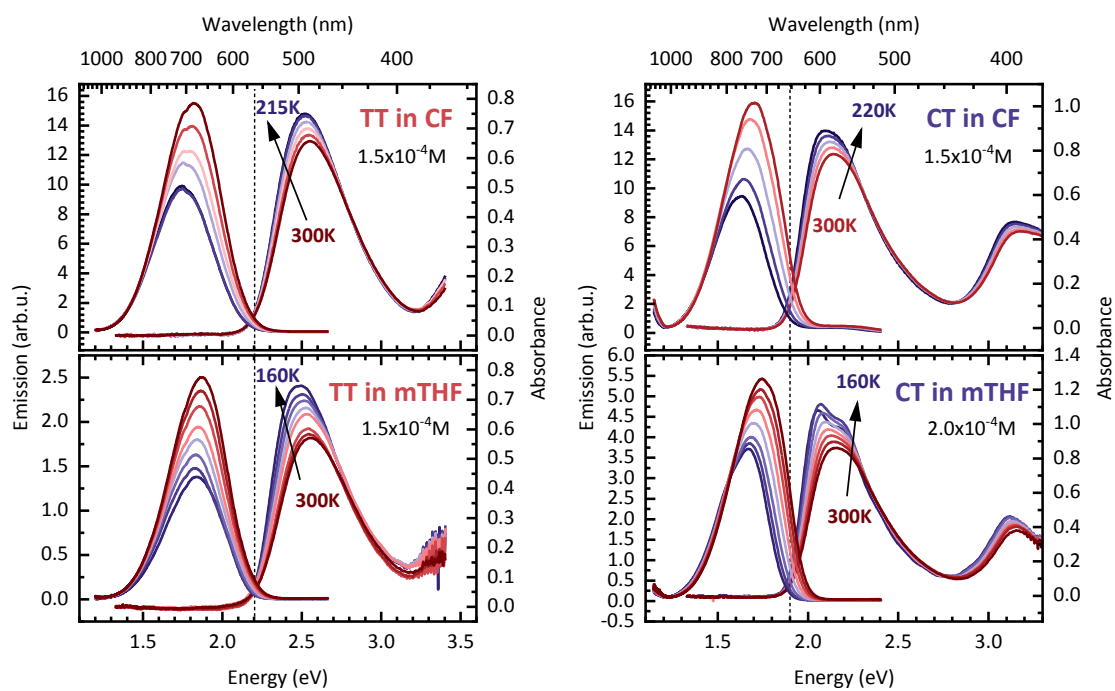


Figure S5.2: Absorption and emission spectra of CT and TT in solvents with different polarities (hexane, toluene, mTHF, chlorobenzene, chloroform). Spectra are shown in steps of 20 K, the dashed line marks the onset of absorption and serves as guide to the eye.

6 Radiative and non-radiative decay rates for TT

We performed TCSPC measurements for TT in hexane ($2.5 \cdot 10^{-4} \text{M}$) at 300 K and at 180 K. We performed a reconvolution fit with the measured instrument response function (IRF) to extract the lifetime of the excited state. Data, IRF and fit are shown in Figure S6. At 300 K the decay is perfectly monoexponential with a decay time of 2.2 ns. The decay of the emission at 180 K can be described by a stretched exponential with a characteristic time constant of 0.8 ns, indicating a distribution of decay times.

The photoluminescence quantum yield (PLQY) at 300 K was determined as 0.31 using an integrating sphere.¹² The PLQY at 180 K was estimated to 0.06 from the data presented in Figure 4a in the main manuscript.

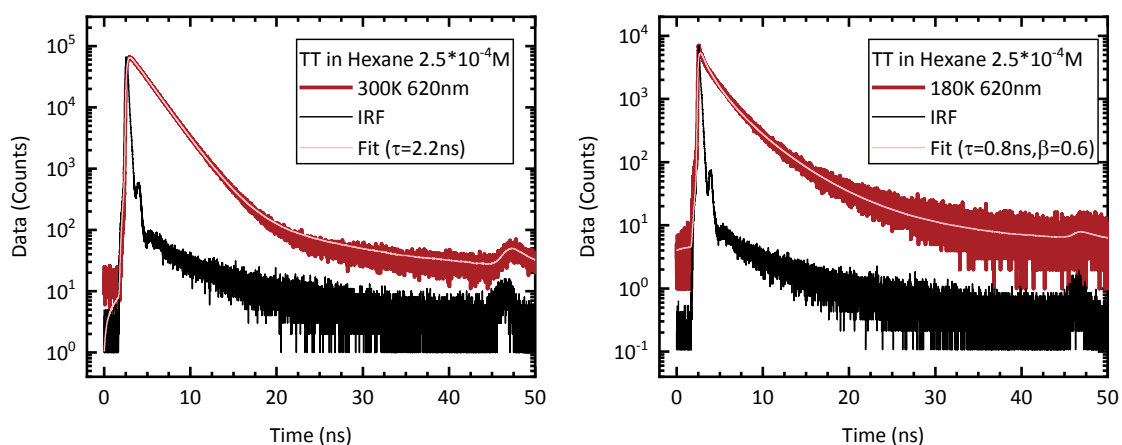


Figure S6: TCSPC measurements for TT in hexane at 300 K and 180 K, IRF and reconvolution fit.

Using

$$PLQY = \frac{k_r}{k_r + k_{nr}}$$

and

$$\frac{1}{\tau} = k_r + k_{nr}$$

the radiative and nonradiative decay rates k_r and k_{nr} can be calculated to

$$k_r(300 \text{ K}) = 0.08 \text{ ns}^{-1}, k_{nr}(300 \text{ K}) = 0.3 \text{ ns}^{-1}, k_r(180 \text{ K}) = 0.1 \text{ ns}^{-1}, k_{nr}(180 \text{ K}) = 1.2 \text{ ns}^{-1}.$$

7 Comparison of planarized TT with CH₃ sidechains

In the main text we compared TT with full hexyl sidechains and CT with full hexyl sidechains when TT is allowed to adopt a planar conformation. We concluded that planarization in TT can account for the strong aggregation behaviour as observed experimentally. For CT, a possible steric influence of the central sidechains on the weak preference was excluded in the manuscript as well. To round off the picture, we performed free energy calculations for TT dimers with CH₃ sidechains, allowing the molecules to planarize either into the cis conformation or the trans conformation. Figure S7 shows the result. Again, allowing both molecules to planarize simultaneously results in a strong energetic preference of the planar dimer. Interestingly, now the cis conformation is strongly preferred by 6 k_BT, whereas the trans conformation becomes less favoured by 2 k_BT. The depth of the global minimum of the free energy for the trans conformation is comparable to the corresponding global minimum for CT with CH₃ sidechains. This means that TT still has an enormous energetic advantage to form dimers when allowed to adopt planar conformations, compared to CT.

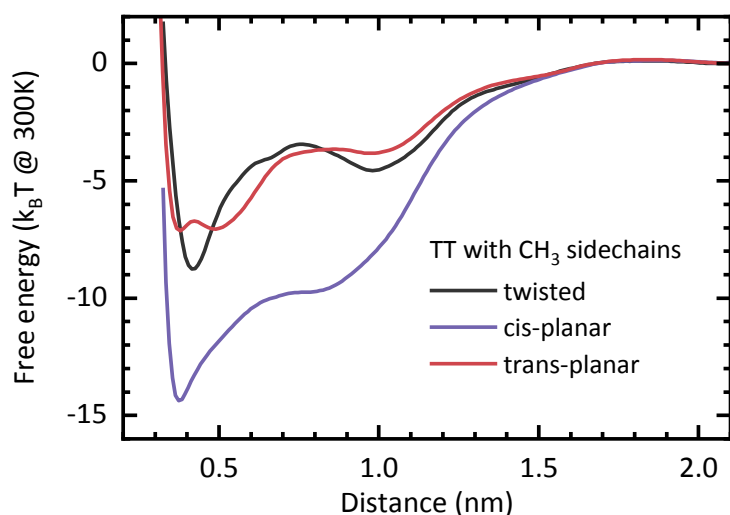


Figure S7: Free energy calculations for the TT dimer with CH₃ sidechains. Both molecules of the dimer adopt either a twisted dihedral angle, a cis-planar conformation or a trans-planar conformation.

8 Interactions between the molecular subunits

Following earlier work⁷ we discuss the mutual interactions between the different building blocks of the molecules. Bourdick et al. conducted their calculations in the solvent MTHF. We repeat the calculations in the solvent hexane for the subunits, which are relevant for CT and TT. The results are shown in Figure S8. For clarity of presentation and in order to have a constant reference point at infinity, we removed the ideal contribution of $2k_B T \cdot \ln r$, which is due to an increase in volume. As the configurational phase space of the individual parts is small, the graphs presented only consist of a single sweeping of the reaction coordinate. We simulated each window between 200 ns and 300 ns.

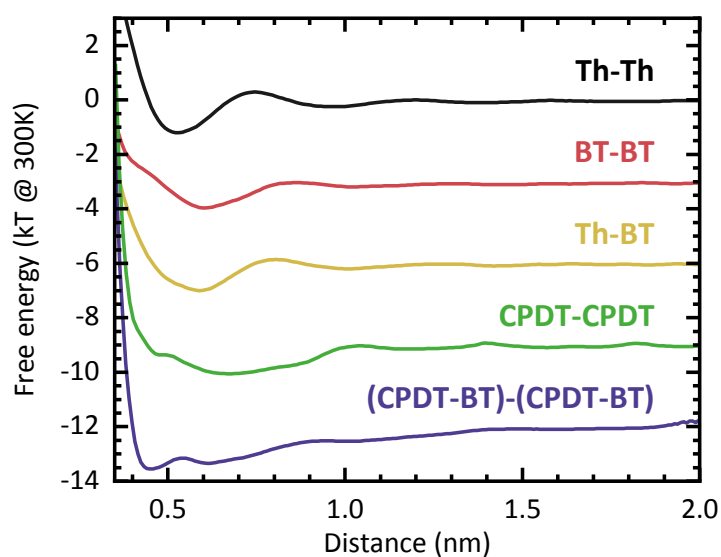


Figure S8: Free energy calculations between the different building blocks in hexane. The units are thiophenes (Th), fluorinated benzothiadiazole (BT), cyclopentadithiophene (CPDT) and a combination of the latter two (CPDT-BT).

9 TT Emission spectra in separate graphs

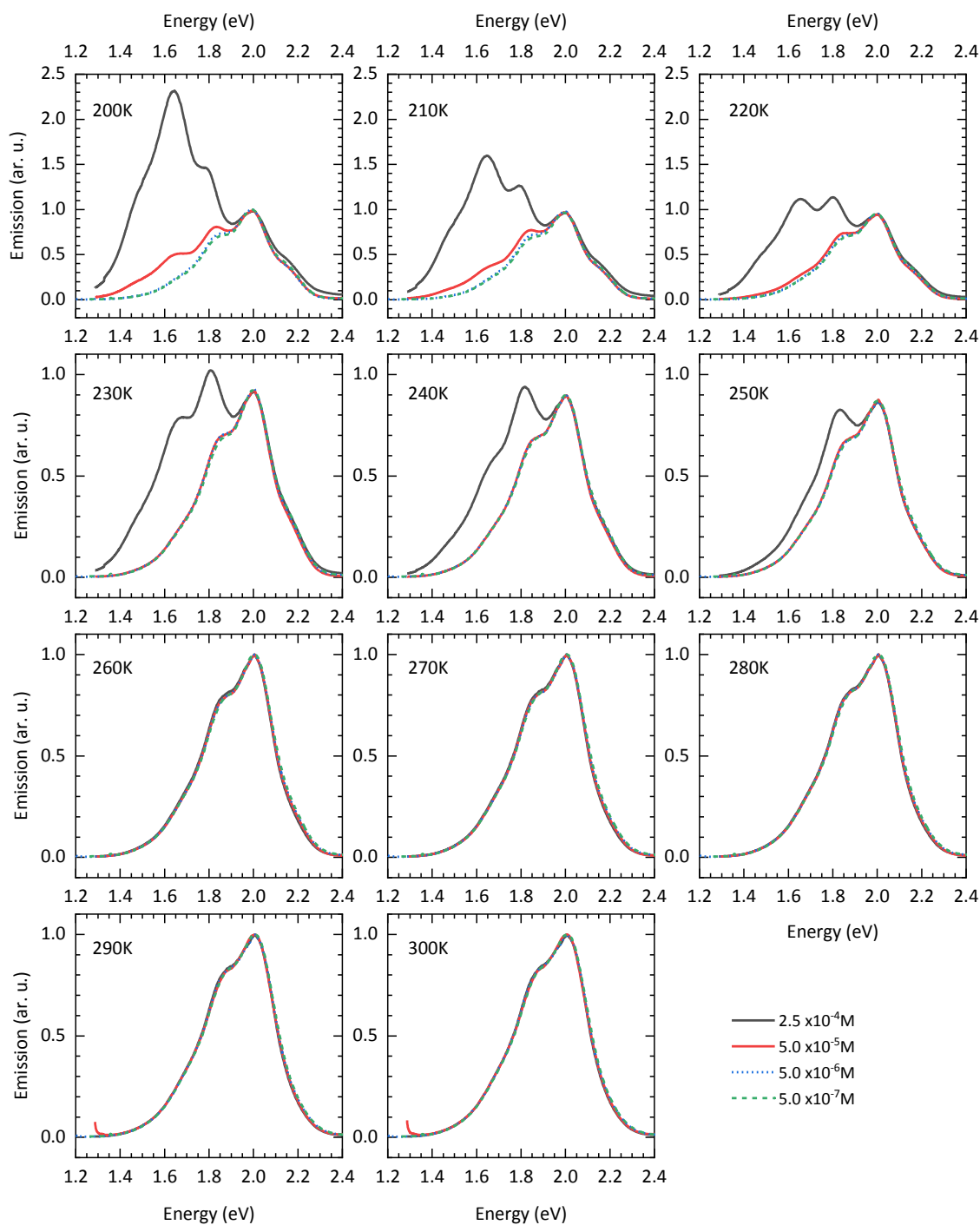


Figure S9: Emission of TT in hexane at different temperatures and concentrations normalized to the peak at 2.0 eV. We additionally measured at a concentration of $5.0 \times 10^{-7} \text{M}$ to safely exclude the possibility of aggregation for all higher concentrations.

10 Franck-Condon analysis for emission spectra of TT

The emission of TT in hexane features a shoulder on the blue side of the spectra, even for the lowest concentration as shown in the previous section. A description of the spectra utilizing a single vibronic progression is incompatible with this spectral feature, as shown in Figure S10.1 for different cases exemplarily at 200 K.

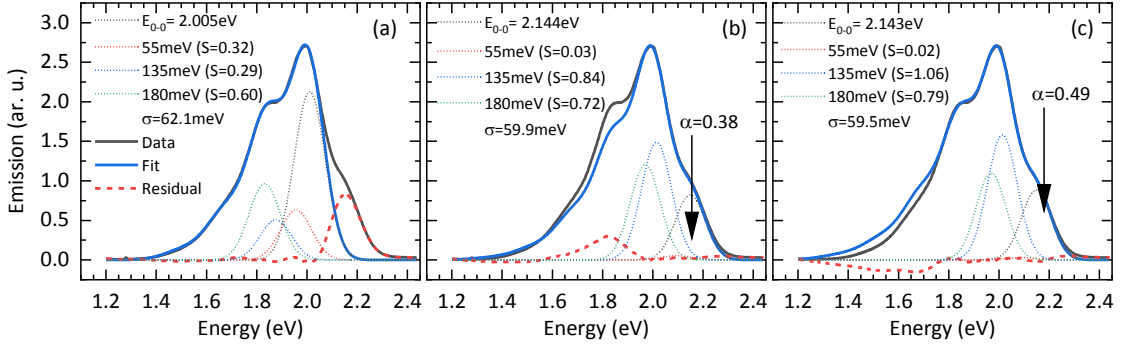


Figure S10.1: Emission of TT in hexane ($5.0 \cdot 10^{-6}$ M) at 200 K with best fits using a single Franck-Condon progression with (a) the 0-0 transition at the dominant peak, (b) with suppressed 0-0 transition and best fit of the red side, and (c) with suppressed 0-0 transition and best fit up to the second vibronic peak at 1.8 eV. The caption contains the fitting parameters. For (b) and (c) the 0-0 suppression factor α is indicated. For details see text.

In case (a) we chose the 0-0 transition energy that it matches the dominant peak at 2.0 eV. This approach entirely fails to describe the blue shoulder. In the other cases we chose a modified Franck-Condon progression, where the amplitude of the 0-0 transition is multiplied with the factor α to account for suppression effects due to H-type interactions:¹³

$$\frac{I_{PL}(E)}{(n \cdot E)^3} \propto e^{-S} \cdot \left(\alpha \Gamma(E - E_0) + \sum_{m_i \neq 0} \prod_i \frac{S_i^{m_i}}{m_i!} \Gamma \left[\left(E - \left(E_0 - \sum_i m_i E_i^{vib} \right) \right) \right] \right)$$

where S is the sum of the Huang-Rhys parameters of all vibrational modes. For fitting, we first adjusted E_0 and σ to reproduce the shoulder at 2.15 eV. Then we iteratively varied α and all S_i to reproduce the dominant peak at 2.0 eV.

It is not possible to get a parameter set where good description for the complete spectrum is achieved. We can either reproduce the red side at energies lower than 1.65 eV as shown in Figure S10.1 b, which results in an underestimation of the peak at 1.8 eV. On the other hand, if this peak is reproduced satisfactorily (Figure S10.1 c), the fit overestimates the spectrum at 1.7 eV and below. Furthermore, the 0-0 transition is suppressed artificially to get an apparent good description of the spectra. This procedure is physically unreasonable, as the shape of the emission spectra remains the same even when decreasing the concentration by an order of magnitude to $5.0 \cdot 10^{-7}$ M, excluding any intermolecular interactions between the chromophores.

However, modelling is possible using two separate progressions. We again started with the spectrum at 200 K. First we used the vibrational modes of TT to perform a Franck-Condon fit onto the emission of CT at 200 K, as the emitting states should in principle be similar. We then used this approximation as a starting point for both the high energy progression (HEP) as well as the low energy progression

(LEP) of the TT emission and iteratively changed the fitting parameters to achieve good agreement between model and data. The other temperatures were then fitted consecutively, varying mainly the Gaussian line widths, the amplitudes and the energetic positions of both contributions. Table S10.1 contains the final parameters and figure S10.2 shows the spectra and the calculated progressions for each temperature.

Table S10.1: Fitting parameters and resulting reorganization energies for low energy progression (LEP) and high energy progression (HEP) of TT in hexane ($5.0 \cdot 10^{-6}$ M) at different temperatures.

Temperature (K)		E_0 (eV)	σ (meV)	S 55 meV	S 135 meV	S 180 meV	λ (meV)
200	LEP	2.006	59.3	0.42	0.406	0.614	188.4
	HEP	2.148	59.3	0.09	0.341	0.478	137.0
210	LEP	2.009	59.6	0.417	0.406	0.614	188.3
	HEP	2.151	61.1	0.09	0.341	0.478	137.0
220	LEP	2.013	59.9	0.411	0.415	0.611	188.6
	HEP	2.153	61.7	0.09	0.341	0.478	137.0
230	LEP	2.016	60.2	0.408	0.439	0.602	190.1
	HEP	2.155	62.3	0.09	0.341	0.478	137.0
240	LEP	2.017	60.8	0.387	0.472	0.581	189.6
	HEP	2.155	63.5	0.09	0.341	0.478	137.0
250	LEP	2.019	61.1	0.378	0.472	0.581	189.1
	HEP	2.157	64.1	0.09	0.341	0.478	137.0
260	LEP	2.021	62.3	0.354	0.49	0.575	189.1
	HEP	2.157	67.7	0.09	0.341	0.478	137.0
270	LEP	2.022	62.9	0.354	0.49	0.575	189.1
	HEP	2.157	68.3	0.09	0.341	0.478	137.0
280	LEP	2.025	62.9	0.354	0.523	0.563	191.4
	HEP	2.158	68.3	0.09	0.386	0.478	143.1
290	LEP	2.028	64.1	0.345	0.523	0.578	193.6
	HEP	2.159	69.8	0.09	0.386	0.478	143.1
300	LEP	2.027	64.7	0.321	0.523	0.572	191.2
	HEP	2.159	71.9	0.09	0.386	0.478	143.1

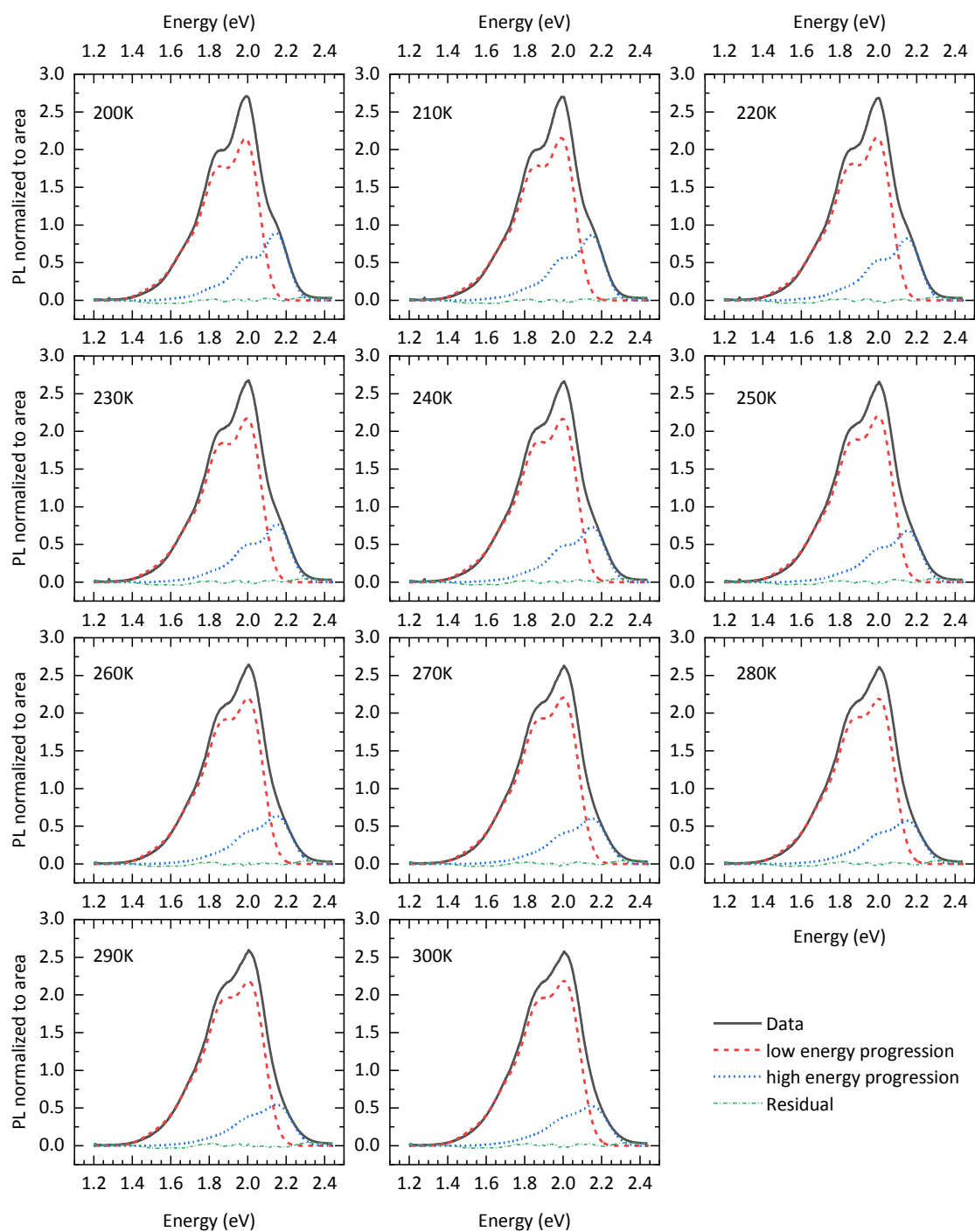


Figure S10.2: Emission of TT in hexane ($5.0 \cdot 10^{-6}$ M) with decomposition into low energy progression and high energy progression at different temperatures.

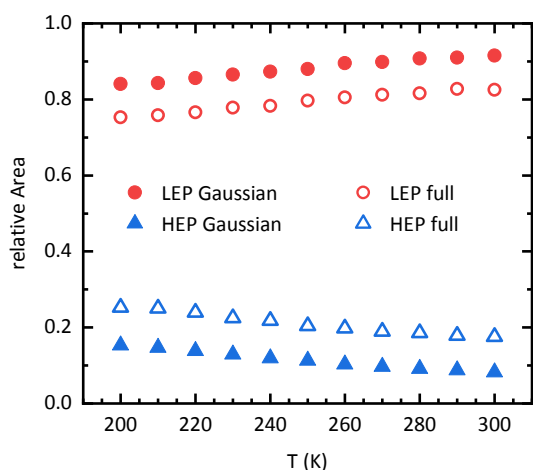


Figure S10.3: Distribution of the total area of high energy and low energy contribution for different decomposition methods

We note that the decomposition is ambiguous, as the high energy progression can also be modelled by a single Gaussian. However, this only affects the intensity ratio between both contributions and not the physical meaning. Figure S10.3 shows the difference for the relative area of both contributions between a high energy Gaussian and a full high energy progression. Table S10.2 contains the corresponding fitting parameters and the related decompositions of the spectra are shown in Figure S10.4.

Table S10.2: Fitting parameters and resulting reorganization energies for low energy progression and high energy Gaussian of TT in hexane ($5.0 \cdot 10^{-6}$ M) at different temperatures.

Temperature (K)		E_0 (eV)	σ (meV)	S 55 meV	S 135 meV	S 180 meV	λ (meV)
200	progression	1.995	59.9	0.26	0.453	0.478	161.5
	Gaussian	2.133	66.7				
210	progression	1.998	60.5	0.26	0.453	0.478	161.5
	Gaussian	2.138	67.5				
220	progression	2.003	62.5	0.26	0.453	0.481	162.0
	Gaussian	2.142	67.8				
230	progression	2.004	64.0	0.204	0.471	0.487	162.5
	Gaussian	2.146	69.0				
240	progression	2.007	65.0	0.204	0.471	0.493	163.5
	Gaussian	2.148	70.2				
250	progression	2.009	65.4	0.204	0.483	0.493	165.2
	Gaussian	2.147	71.0				
260	progression	2.013	66.7	0.204	0.483	0.511	168.4
	Gaussian	2.153	72.2				
270	progression	2.015	67.5	0.204	0.483	0.517	169.5
	Gaussian	2.153	74.1				
280	progression	2.018	68.0	0.204	0.489	0.517	170.3
	Gaussian	2.157	74.3				
290	progression	2.019	68.3	0.198	0.495	0.52	171.3
	Gaussian	2.156	74.3				
300	progression	2.022	69.9	0.198	0.495	0.529	172.9
	Gaussian	2.156	74.0				

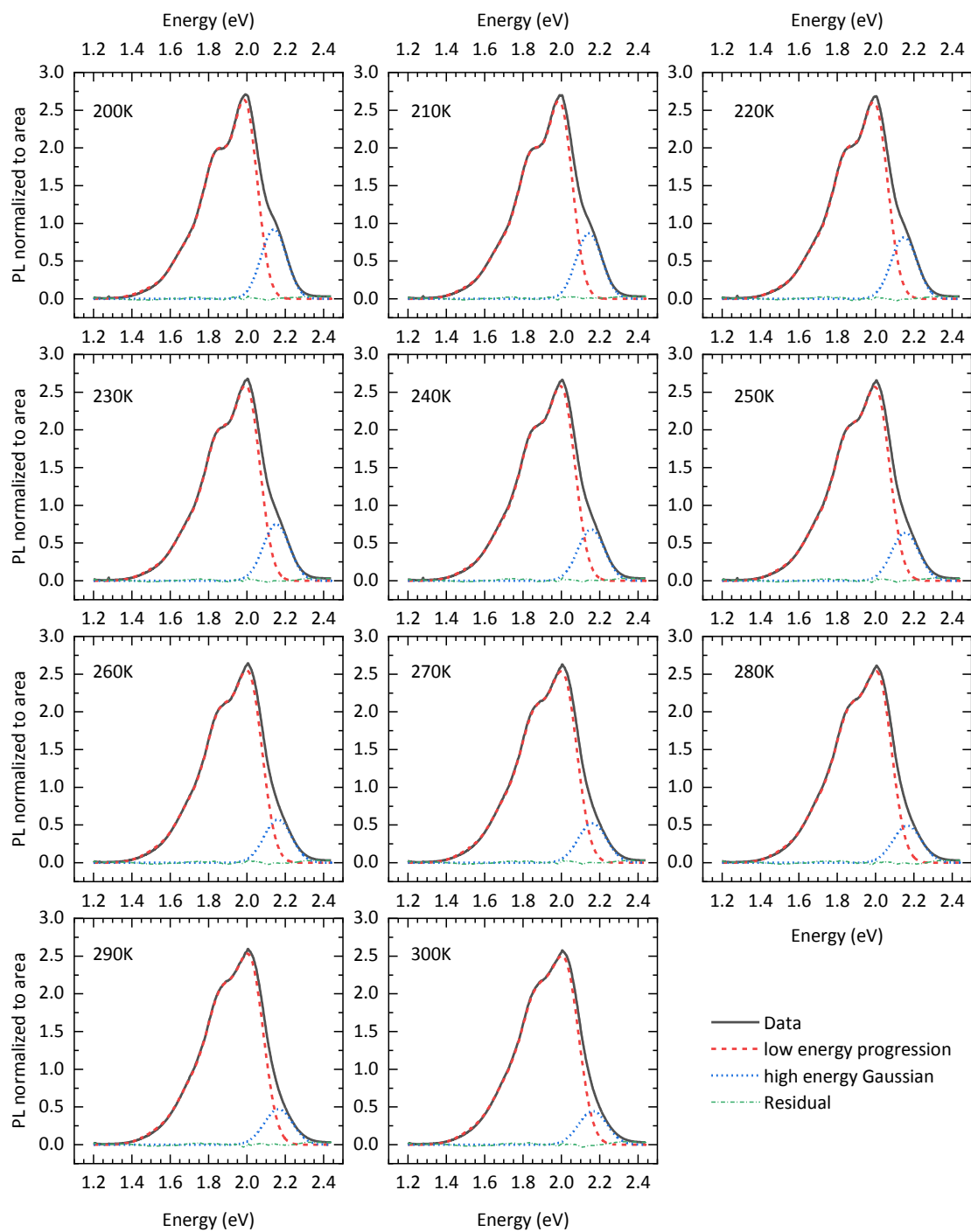


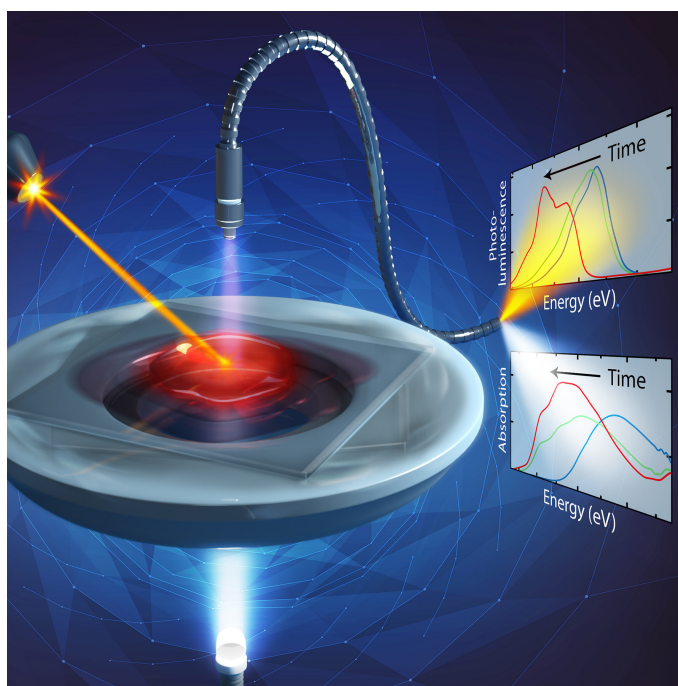
Figure S10.4: Emission of TT in hexane ($5.0 \cdot 10^{-6}$ M) with alternative decomposition into low energy progression and high energy Gaussian at different temperatures.

11 Literature

1. A. K. Malde, L. Zuo, M. Breeze, M. Stroet, D. Poger, P. C. Nair, C. Oostenbrink and A. E. Mark, *J. Chem. Theory Comput.*, 2011, **7**, 4026-4037.
2. S. Canzar, M. El-Kebir, R. Pool, K. Elbassioni, A. K. Malde, A. E. Mark, D. P. Geerke, L. Stougie and G. W. Klau, *J. Comput. Biol.*, 2013, **20**, 188-198.
3. K. B. Koziara, M. Stroet, A. K. Malde and A. E. Mark, *J. Comput. Aided Mol. Des.*, 2014, **28**, 221-233.
4. ATB Database: CT Structure and Toplogy Files, <https://atb.uq.edu.au/molecule.py?molid=285451>, (accessed June 2019).
5. ATB Database: TT Structure and Toplogy Files, <https://atb.uq.edu.au/molecule.py?molid=285450>, (accessed June 2019).
6. M. J. Frisch, G. W. Trucks, H. B. Schlegel, G. E. Scuseria, M. A. Robb, J. R. Cheeseman, G. Scalmani, V. Barone, G. A. Petersson, H. Nakatsuji, X. Li, M. Caricato, A. V. Marenich, J. Bloino, B. G. Janesko, R. Gomperts, B. Mennucci, H. P. Hratchian, J. V. Ortiz, A. F. Izmaylov, J. L. Sonnenberg, Williams, F. Ding, F. Lipparini, F. Egidi, J. Goings, B. Peng, A. Petrone, T. Henderson, D. Ranasinghe, V. G. Zakrzewski, J. Gao, N. Rega, G. Zheng, W. Liang, M. Hada, M. Ehara, K. Toyota, R. Fukuda, J. Hasegawa, M. Ishida, T. Nakajima, Y. Honda, O. Kitao, H. Nakai, T. Vreven, K. Throssell, J. A. Montgomery Jr., J. E. Peralta, F. Ogliaro, M. J. Bearpark, J. J. Heyd, E. N. Brothers, K. N. Kudin, V. N. Staroverov, T. A. Keith, R. Kobayashi, J. Normand, K. Raghavachari, A. P. Rendell, J. C. Burant, S. S. Iyengar, J. Tomasi, M. Cossi, J. M. Millam, M. Klene, C. Adamo, R. Cammi, J. W. Ochterski, R. L. Martin, K. Morokuma, O. Farkas, J. B. Foresman and D. J. Fox, Gaussian 09 Rev. E.01, Gaussian, Inc., Wallingford, CT, 2013
7. A. Bourdick, M. Reichenberger, A. Stradomska, G. C. Bazan, T.-Q. Nguyen, A. Köhler and S. Gekle, *J. Phys. Chem. B*, 2018, **122**, 9191-9201.
8. J. S. Hub, B. L. de Groot and D. van der Spoel, *J. Chem. Theory Comput.*, 2010, **6**, 3713-3720.
9. P. K. H. Ho, J.-S. Kim, N. Tessler and R. H. Friend, *J. Chem. Phys.*, 2001, **115**, 2709-2720.
10. C. Reichardt and T. Welton, *Solvents and Solvent Effects in Organic Chemistry*, Wiley-VCH Verlag GmbH & Co. KGaA, Weinheim, Germany, Fourth Edition edn., 2010.
11. J. W. Baur, M. D. Alexander, M. Banach, L. R. Denny, B. A. Reinhardt, R. A. Vaia, P. A. Fleitz and S. M. Kirkpatrick, *Chem. Mater.*, 1999, **11**, 2899-2906.
12. J. C. d. Mello, H. F. Wittmann and R. H. Friend, *Adv. Mater.*, 1997, **9**, 230-232.
13. J. Clark, C. Silva, R. H. Friend and F. C. Spano, *Phys. Rev. Lett.*, 2007, **98**, 206406.

8

Setup to Study the in Situ Evolution of Both Photoluminescence and Absorption during the Processing of Organic or Hybrid Semiconductors



Michael Buchhorn, Stefan Wedler, and Fabian Panzer.

Published in

The Journal of Physical Chemistry A, **2018**, 122, 9115–9122

(DOI: 10.1021/acs.jpca.8b07495)

Reprinted with permission from the American Chemical Society

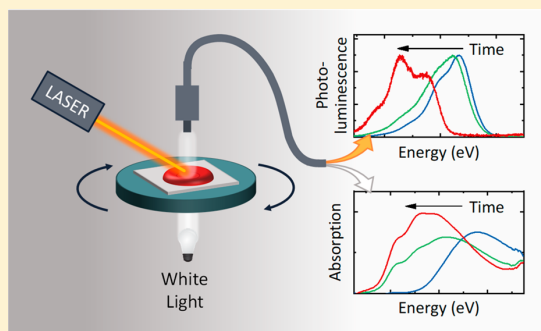
Copyright (2018) American Chemical Society

Setup to Study the in Situ Evolution of Both Photoluminescence and Absorption during the Processing of Organic or Hybrid Semiconductors

Michael Buchhorn, Stefan Wedler, and Fabian Panzer*

Soft Matter Optoelectronics, University of Bayreuth, Bayreuth 95440, Germany

ABSTRACT: In situ measurement techniques, applied during the solution processing of novel semiconductors such as organic semiconductors or hybrid perovskites, have become more and more important to understand their film formation. In that context, it is crucial to determine how the optical properties, namely photoluminescence (PL) and absorption, evolve during processing. However, until now PL and absorption have mostly been investigated independently, significantly reducing the potential insights into film formation dynamics. To tackle this issue we present the development of a detection system that allows simultaneous measurement of full absorption and PL spectra during solution processing of the investigated film. We also present a spin-coater system attachable to the detection system, where the temperature of the substrate on which the film is processed can be changed. We performed test measurements by spin coating the well-known conjugated polymer P3HT demonstrating the potential of this technique. By considering absorption and corresponding PL, we extract the PL quantum yield (PLQY) during processing, which decreases with substrate temperature. Furthermore, we identify a significant red shift of the PL just prior to the onset of the aggregation process, indicating the importance of chain planarization prior to solid film formation.



INTRODUCTION

Organic semiconductors and hybrid perovskites have emerged as highly important semiconductor materials, used as active layers in next-generation optoelectronic devices including photovoltaics,^{1,2} field effect transistors,^{3,4} lighting and display devices,^{5,6} and photodiodes for UV, visible,^{7,8} and high-energy photons (e.g., X-ray, γ -ray).^{9–11} For both types of semiconductors, changes in their local microstructure or morphology also impact their electronic structure, which significantly impacts the resulting performance of optoelectronic devices.^{12–16} Such changes in structure and morphology naturally occur during the film formation from solution.^{17,18} As electronic structure is highly dependent on local microstructure, optical properties also change. In recent years, this has led to the aim to track the optical properties of these materials during processing to monitor, better understand, and finally control and optimize the film formation mechanisms.^{19,20} This was achieved by controlling and systematically changing processing conditions such as atmosphere,²¹ solvent,^{22,23} or temperature.²⁴ The latter has an especially critical impact on film formation, as it not only influences the solvent drying rate but also can dictate the conformational phase of the material prior to and during film formation.²⁵

In previous works, optical in situ detection was usually carried out by measuring absorption during processing. From these measurements it was possible to extract basic parameters,

such as absorption coefficients and vibronic peak ratios, and to analyze how they evolve over time.^{26,27}

However, within the last years, several theoretical models and methodologies were developed that yield fundamental insights into underlying electronic structure requiring concurrent full absorption and photoluminescence (PL) spectra, ideally probing the same chromophore ensemble.^{28–31} These studies could also provide fundamental insights on how changes in the electronic structure of the material correlate with their conformational and structural properties, even when they undergo significant changes, as is typically the case during processing or upon changing the temperature.^{28–32} However, these theoretical models cannot be readily applied to unravelling how interdependent processing conditions influence local microstructure and contingent optoelectronic properties, due to the difficulty inherent in collecting simultaneous PL and absorption spectra of the same region at a sufficiently high frequency (>10 Hz) to track the transition from solution to film. Pertinently, although such capability has been demonstrated for blade coating (albeit with absorption and PL probing adjacent locations),³³ this is not the case for the ubiquitous spin-coating film deposition method, limiting

Received: August 2, 2018

Revised: October 11, 2018

Published: October 25, 2018

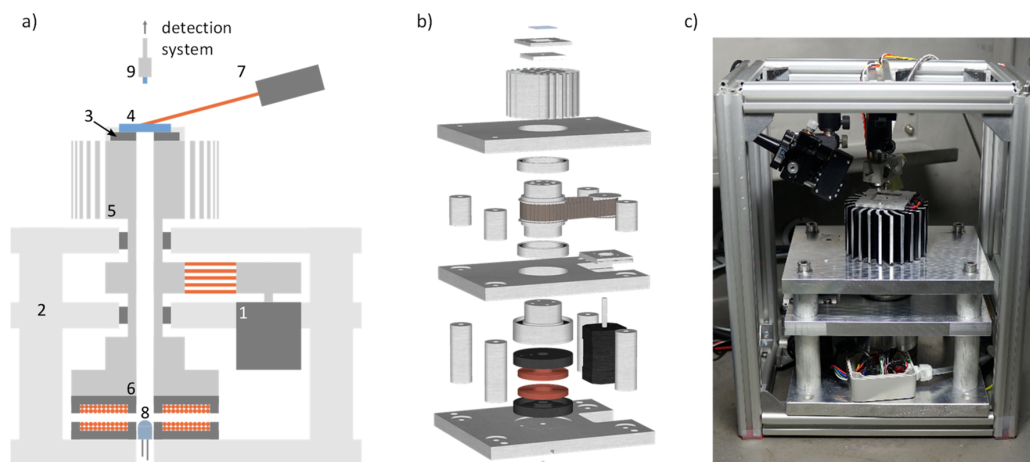


Figure 1. (a) Schematic representation of the spin-coater device. Relevant components are labeled by numbers and described in more detail in the main text. (b) Exploded View drawing of the spin-coater device. (c) Photograph of the assembled spin coater.

the scope of investigation into establishing the processing–structure–property relations essential in controlling device-relevant optoelectronic properties.

In this work, we present an easy-to-use system for the quasi-simultaneous detection of absorption and photoluminescence during solution processing, including spin coating, of novel semiconductor materials such as π -conjugated polymers or hybrid perovskites. The system is designed to consist of only a few common optomechanical components and uses only one CCD spectrograph for detection, which makes it portable, so it can easily be combined with other in situ measurement techniques. Associated with this detection system, we also present a spin coater that allows for the detection of both absorption and PL during processing, probing the same region on the sample substrate. Furthermore, it is possible to control the substrate temperature during processing between 0 and 150 °C. With that, valuable insights on aggregate formation during the solution processing of the investigated material can be gained, which we demonstrate using the example of the polymer P3HT. This will help to tailor the route for processing next-generation optoelectronic devices more expeditiously.

■ EXPERIMENTAL SETUP

Figure 1a shows a schematic representation of the spin-coater device, and in Figure 1b an exploded view drawing of its 3D model is shown.

The main components are a brushless DC motor (1) (Trinamic BLDC4208) which is connected with the rotatable chuck via a cogged V-belt. In combination with a motor driver (Trinamic TMC1640) it is possible to set the rotation speed of up to 2300 rpm and control it via serial connection to a computer. To ensure balanced rotation, the chuck is mounted on two ball bearings, which are each edged into a robust aluminum structure (2). We use a Peltier element (3) to control the temperature of the substrate (4) on which the sample solution is deposited. It is located on a heat diffusor (5) in the upper part of the chuck. This passive heat exchanging geometry allows setting the substrate temperature between 0 and 150 °C and ensures quick thermal equilibration at the substrate. To allow heating and also cooling from room temperature, the Peltier's polarity can be changed by a switch that is integrated in the chunk. The Peltier element can draw

up to 60 W electrical power from a rotary transformer (6) after rectification, which is located at the lower part of the chuck. This approach reduces maintenance compared to the usage of slip rings, as no abrasion or corrosion can occur.

To allow quasi-simultaneous detection of both absorption and PL during processing, the spin-coater setup is supplemented with a diode laser (7) above the substrate and a white LED (8). The latter is static and placed below the chuck. The type of the white LED can easily be changed, while we used a generic cold white LED covering a spectral range from 415 to about 820 nm (i.e., 1.51–2.99 eV) for our test measurements (vide infra). A bore along the rotation axis of the chuck with a diameter of 4 mm at the Peltier element allows the emitted white light to reach the substrate. Finally, the light transmitted through the substrate (and eventually the sample material) enters an optical fiber (9) above the sample that leads to the detection system.

The diode laser is attached to a frame made of common aluminum profiles. The laser's position can be chosen to ensure that the laser beam excites the top of the sample under a shallow angle to minimize self-absorption effects. We use a laser system that is based on exchangeable TO Can laser diodes, allowing us to choose excitation wavelengths between 405 and 820 nm (i.e., 1.51–3.07 eV). The emitted light from the sample enters the same optical fiber that is also used for the transmitted white light. Figure 1c shows a photograph of the entire spin-coater device, including the frame with the diode laser.

The detection system to measure absorption and PL alternately is shown in Figure 2 and described below. To ensure a sufficient time resolution for tracking the optical properties during processing, we used only one spectrograph with a CCD camera and kept the spectral range between consecutive absorption and PL frames unchanged. We used a sufficiently large spectral range that includes the wavelength of the excitation laser, the absorption, and the emission spectrum. This allows to subsequently also calculate the photoluminescence quantum yield (PLQY) as a function of film-processing time, yet it requires to filter the signal of the laser during the PL measurement to prevent damage of the CCD. For this purpose, we used two beam paths depending on whether absorption or PL is measured. In our detection system

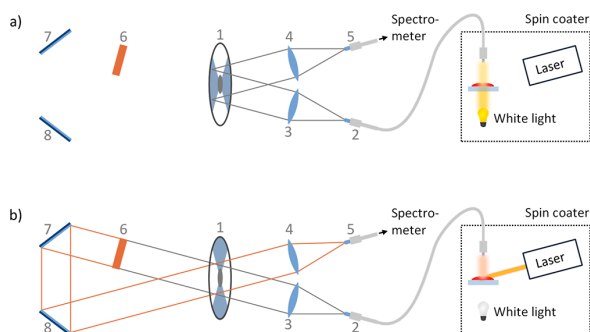


Figure 2. Schematic illustration of the main components of the detection system and corresponding operation states of the laser and white light during an absorption (a) and a PL (b) measurement. Different components are labeled by numbers and described in the main text.

this is implemented by using a mechanical chopper with blades that have been coated to act as a mirror. Depending on the orientation of the chopper wheel (1), a beam path either for absorption (Figure 2a) or for PL (Figure 2b) is realized. For absorption, the transmitted light enters the detection system via the optical fiber (2) that is connected to the spin coater. A lens (3) collimates the light, which reaches the chopper wheel. The latter consists of two slots, and the areas between them have a mirrored surface to reflect incident light. During an absorption measurement, the chopper wheel's orientation ensures a complete reflection of the collimated light. A lens (4) couples this reflected light into an optical fiber (5) connected to a spectrograph equipped with a CCD camera. For PL measurements, analogous to absorption, the emitted light from the sample enters the detection system through the optical fiber (2), is collimated by the lens (3), and reaches the chopper wheel (1). In contrast to absorption, the orientation of the chopper wheel ensures that incident light passes through a slot during a PL measurement. It further passes a filter (6) which is suitably selected to block the laser light. Using two mirrors (7 and 8), the filtered PL is then reflected back through the same

slot of the chopper wheel, so that it matches the reflected light from the absorption measurement in terms of direction and position. This allows using the same lens (4) and optical fiber (5) to guide the PL signal to the same spectrograph. Due to its modular design, individual components of the detection system can easily be modified or exchanged to match particular sample requirements. This can, for example, concern the white light source to provide white light intensity over the relevant spectral range or the CCD spectrograph to meet the required sensitivity for detection when investigating different material systems with different optical properties.

A microcontroller (Atmel ATmega328P) ensures smooth interaction between the components that change their states depending on whether absorption or PL is measured. The microcontroller triggers absorption and PL measurements based on the orientation of the chopper wheel. During absorption measurements, the white LED is switched on while the laser diode is off and vice versa for PL measurements. In each case, after LED and laser are set, the CCD camera is triggered to capture the corresponding spectrum. The maximum frame rate for data collection is limited by the acquisition time of the CCD camera. It needs to be suitably chosen to ensure sufficient intensities for PL and absorption. We use homemade computer software to set acquisition settings of the CCD camera, to collect and visualize the data, and to perform first analysis. The system proves to give excellent stabilities with fluctuations better than 0.3% rms for the white LED intensity and 0.8% rms for excitation intensity under typical measurement conditions.

TEST MEASUREMENTS

To demonstrate the kind of information that can be obtained with this setup, we measured the absorption and emission during the drying process of the π -conjugated polymer poly(3-hexylthiophene) (P3HT), which is a well-established model system and has emerged as the workhorse in the organic semiconductor field over recent years. We spin coated P3HT from chlorobenzene solution with a concentration of 10 mg/mL at a speed of 1000 rpm in a glovebox and measured the

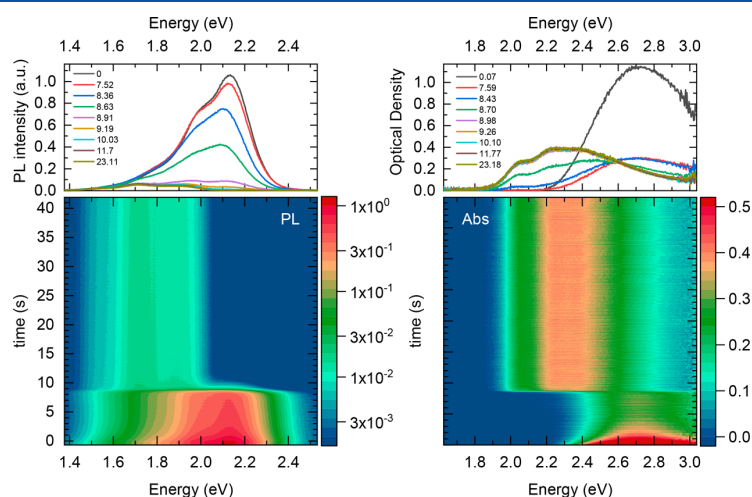


Figure 3. Photoluminescence (left) and absorbance (right) heat maps of P3HT taken at different times during spin coating from chlorobenzene solution at room temperature. In both cases time is displayed as the ordinate and energy is displayed as the abscissa. PL intensity and optical density are color coded. Horizontal cuts at the top of each heat map show spectra at certain times during processing.

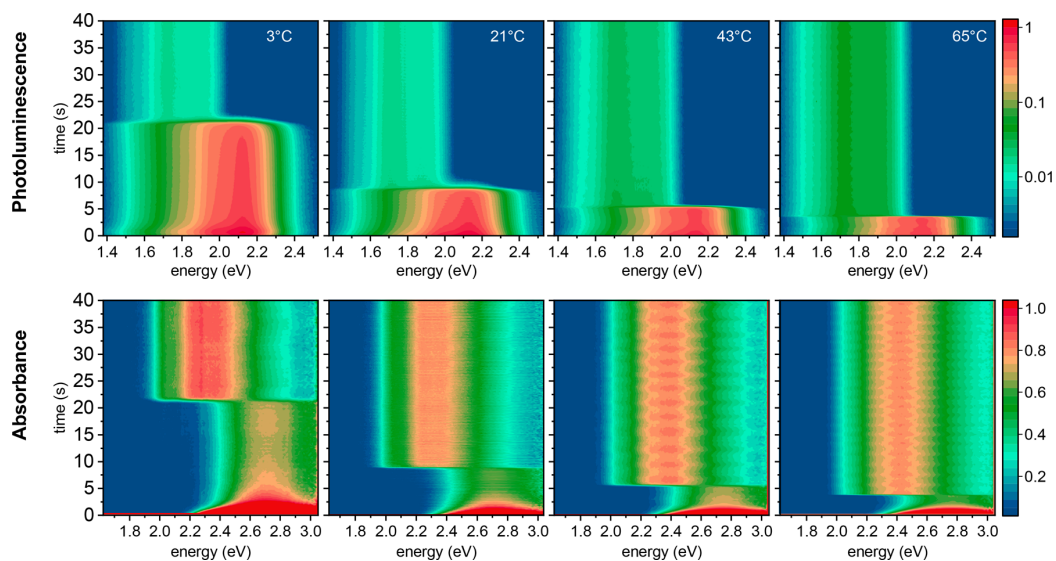


Figure 4. Normalized photoluminescence (top) and absorbance (bottom) heat maps of P3HT taken at different times during spin coating from chlorobenzene solution at 3, 21, 43, and 65 °C (from left to right). In each map time is displayed as the ordinate and energy is displayed as the abscissa. PL intensity and optical density are color coded. Time-dependent fluctuations in the absorption intensity for 43 and 65 °C occur from an inhomogeneous film distribution during spin coating.

optical properties in situ using our detection system (excitation intensity of 25 mW/cm² for PL) and spin coater. Figure 3 shows color-coded 2D maps of time-resolved absorption and corresponding PL spectra together with spectral slices at different times within the first 40 s of spin coating at room temperature (time resolution between two consecutive detection frames 0.07 s). The intensities of the PL spectra are corrected for the changes of absorption at the laser excitation energy of 3.06 eV. Significant changes in both absorption and PL occur after 8–9 s, which are associated with the optical signatures of the well-known order–disorder transition, typically occurring upon P3HT film formation.^{17,34} This transition can also occur in solution upon lowering the quality of the solvent either by altering the temperature^{25,35,36} or by systematically changing the ratio of good and bad solvents in solvent mixtures.^{37,38}

Before the transition, i.e. within the first 8–9 s of spin coating, a broad and featureless absorption spectrum that is associated with the disordered phase of P3HT is observed, which reduces in intensity within the first 2 s of spin coating due to slinging away of excess solution upon rotation. Corresponding PL spectra within the first 8–9 s of spin coating are structured with a dominant peak at 2.13 eV that is attributed to PL from the disordered phase. This peak fully disappears in the course of the order–disorder transition between 8 and 10 s. This is accompanied by the appearance of a red-shifted PL spectrum of the aggregated phase with a nondominant $S_1 \rightarrow S_0$ 0–0 peak at about 1.85 eV and by a significant reduction in overall PL intensity (note the logarithmic color code used in the 2D map of the PL). Both spectral changes are known spectroscopic signatures for the formation of an H-type intermolecular coupling within this phase.³⁹ In absorption, a red-shifted, better-structured spectrum is the signature for the appearance of the aggregated phase. After 10 s, no significant spectral changes in both PL and absorption are observed from thereon until the end of the spin coating, indicating that the phase transition is complete.

We spin coated P3HT from CB solution also at 3, 43, and 65 °C substrate temperature, while all other processing parameters were unchanged. We note that for the used temperatures the substrate temperature between the stationary state and upon rotation changes not more than 4 °C. 2D maps of PL and absorption at the different processing temperatures during the spin coating are shown in Figure 4. The impact of substrate temperature on the onset time of the phase transition is obvious, with higher substrate temperatures leading to an earlier occurrence of the phase transition due to more rapid solvent evaporation.

This is consistent with a recent work from our group on in situ absorption measurements during spin coating of P3HT.²⁴ Furthermore, at higher temperatures, the initial drop in absorbance, due to the removal of material during spin coating, occurs more rapidly, which can be understood by considering the decreasing viscosity of chlorobenzene with temperature.⁴⁰

As a first step, we extract parameters to identify and quantify the impact of processing temperature on the evolution of the optical properties. For this we do not need to apply sophisticated models to the measured data. Rather, we exploit the fact that the absorption spectrum of the aggregated phase does not overlap with the absorption of the disordered phase at lower photon energies ($\lesssim 2.3$ eV). Therefore, the intensity of the peak at lowest energy, i.e., 2.03 eV (associated with the $S_1 \leftarrow S_0$ 0–0 transition of the aggregated phase), can be taken to monitor the appearance and, to some extent, the amount of aggregated phase within the solution or film.^{24,26,27} Figure 5 (top) shows the normalized intensities at 2.03 eV for all four processing temperatures. From this we find the change of the onset time for the transition shifting from 21.1, 8.6, 5.3, to 3.6 s for 3, 21, 43, to 65 °C, respectively. We take the last frame before the steep increase of OD intensity at 2.03 eV (indicated as dashed lines in Figure 5) to determine the onset times for the film formation at each processing temperature. Furthermore, for 3 and 21 °C we find a small increase of the

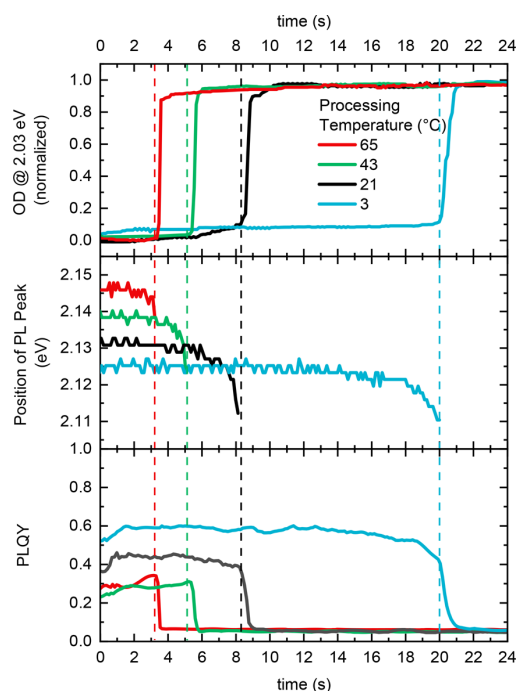


Figure 5. Evolution of relevant parameters during spin coating at different temperatures, extracted from the time-resolved absorption and PL data. (Top) Optical density at 2.03 eV, which is associated with absorption from aggregated phase. (Middle) PL peak position in the time range prior to film formation. (Bottom) PLQY, calculated from the evolution of integrated PL intensity, corrected for the changes of optical density at 3.05 eV and scaled with absolute PLQY values of the final thin films. Onset times are shown as dashed vertical lines.

absorption intensity at 2.03 eV (to about 10% of the maximum value) prior to the actual main transition, which indicates the formation of aggregates already in the solution drop on the substrate. Such a behavior can occur when the processing temperature is in the region of the critical order–disorder transition temperature T_c in solution,²⁴ where the longest polymer chains already aggregate due to the chain length dependence of T_c .^{35,41}

At first sight the time-dependent spectral changes of the PL spectra appear to correspond to the absorption spectra, as expected from temperature-dependent spectroscopic studies in solution.^{17,25} However, plotting the energetic position of the $S_1 \rightarrow S_0$ 0–0 PL peak of the disordered phase as a function of spin-coating time for all four processing temperatures (Figure 5, middle) reveals unexpected insights. First, the peak position at the beginning of spin coating increases with substrate temperature from 2.125 eV at 3 °C to 2.146 eV at 65 °C. In the framework of the so-called oligomer approach, this shift is associated with a decrease in effective conjugation length. It is a known behavior for conjugated polymers in solution,⁴² and the slope of this shift is in accordance with a recent publication.⁴³ As a function of processing time, the peak positions stay almost constant at the beginning but start to shift to lower energies close before the onset of each phase transition. We could clearly determine each onset from the analysis of the absorption spectra as described above (indicated with dashed lines in Figure 5).

We find that the amount of red shift of the PL spectrum between the start of spin coating and the onset of the phase transition is lower for higher processing temperatures. The reason for the red shift could be due to an increase in the conjugation length of the disordered chains in the course of a chain planarization (preaggregation) prior to the main order–disorder transition. It could also be influenced by a changing polarization environment of the polymer chains close before the phase transition, which would also impact on the electronic structure and result in a spectral shift.¹⁷

Additionally, the quasi-simultaneous detection of absorption and PL further allows extracting the relative change of absorbed light at the laser excitation wavelength during processing, which then can be used to scale the time-dependent integrated PL intensity. The resulting value represents the relative change of the PLQY. In addition, we determined the absolute PLQY values following the approach by de Mello et al.⁴⁴ We find them to be in the range between 3% and 5% for all films, which is consistent with typical values for P3HT thin films.⁴⁵ Using the absolute values of the PLQY of each final film also enables the absolute change of the PLQY during spin coating to be determined for the different processing temperatures (Figure 5, bottom).

We followed this approach and found that the PLQY reduces significantly during film formation for all investigated samples. Prior to the formation of aggregates we find that the PLQY values reduce from almost 60% for 3 °C to about 40% at room temperature and about 30% for both 43 and 65 °C. This temperature dependence of PLQY of the disordered phase was also observed for different π -conjugated material systems in the past. It results from an increased conjugation length due to a reduction of (thermally activated) torsional disorder and a decreased solubility at lower temperatures.²⁵ Furthermore, the absolute value of about 40% at room temperature is consistent with literature values reported for disordered P3HT in solution.⁴⁵ The PLQYs at room temperature and 3 °C stay relatively constant until film formation sets in, while the PLQYs for 43 and 65 °C show an additional increase shortly before the phase transition. We speculate that an efficient energy transfer from disordered chains to the small fraction of already existing aggregated chains might mask this increase in PLQY for the lower processing temperatures. However, a full investigation of this behavior and the physical origin of the spectral red shift prior to aggregation will be the focus of an in-depth study in the future.

CONCLUSION AND OUTLOOK

In conclusion, we have presented a detection system that is able to measure the absorption and the PL of semiconductor materials during their solution processing in an alternating shot-by-shot manner, probing the same sample region. Furthermore, we presented a newly designed spin coater compatible with the detection system, where the substrate temperature can be set or changed even while spinning. Together, this system allows correlating the time evolution of absorption and PL spectra during processing at different substrate temperatures, allowing, for example, the extraction of important optoelectronic parameters such as PLQY. Using this setup allowed us to identify a significant red shift of the PL spectrum of the disordered phase prior to aggregate formation in test measurements of the polymer P3HT. This underlines the importance of chain planarization before the main

aggregation process. We could extract the evolution of the PLQY during processing of P3HT for different substrate temperatures in the range between 3 and 65 °C, where we find increased PLQY values for lower processing temperatures in the time range before film formation. These results demonstrate the high potential of the setup to gain new fundamental insights into the film formation processes of solution-processed novel semiconductors, which will help to optimize their film formation.

As an outlook, our approach to simultaneous in situ PL and absorption measurement could be easily extended to other thin film processing techniques, particularly those relevant for large-area production such as blade coating, slot-dye coating, or inkjet printing. Systematically comparing film formation dynamics across processing methods will assist in understanding why local microstructure and resulting macroscopic optoelectronic properties show such a pronounced deposition method dependence, an especially important goal given that organic or hybrid optoelectronic devices produced with scalable methods are typically significantly less efficient than those with a spin-coated active layer. To extract more information about the electronic structure from the PL and absorption spectra, theoretical models such as multimode Franck–Condon analysis could be globally applied. The setup also easily allows investigating the changes of optical properties that occur when a semiconductor material undergoes a crystallization process upon cooling from the melt or vice versa. Furthermore, as the presented spin coater provides electrical power even during rotation, extensions regarding additional sensing on the chuck could be realized easily and electrical fields could be provided during processing, where the positive impact of the latter on film formation has been proven recently.^{46–48} The aim to combine different in situ measurement techniques during the processing has gained momentum within the past few years,^{49,50} especially involving in situ scattering techniques such as GIWAXS or GISAXS.^{51–54} As the latter can yield detailed information about structure formation on the micro- and mesoscale, a combination of these techniques with the detection system presented here would yield the possibility to directly correlate conformational changes with changes in the optical properties of the investigated material and is a promising future direction for in situ real-time investigations during processing.

AUTHOR INFORMATION

Corresponding Author

*E-mail: fabian.panzer@uni-bayreuth.de.

ORCID

Fabian Panzer: 0000-0002-2191-9011

Notes

The authors declare no competing financial interest.

ACKNOWLEDGMENTS

We thank Frank Schirmer and Thomas Dabisch for technical help with the setup, Anna Köhler, Eva Herzig, and Matt Dyson for fruitful discussions, and the mechanic and the electronic workshop of the university for supporting the development of the setup. F.P. acknowledges support from the Marie-Curie Innovative Training Network (ITN) INFORM. Financial support is acknowledged from the Deutsche Forschungsgemeinschaft through GRK1640 (Photophysics of Synthetic and Biological Multichromophoric Systems) and from the

Bayerisches Staatsministerium für Bildung und Kultus, Wissenschaft und Kunst, through the grant “Solar Technologies go Hybrid” as well as the program “MINT-Lehramt plus”.

REFERENCES

- (1) Brabec, C. J.; Gowrisanker, S.; Halls, J. J.; Laird, D.; Jia, S.; Williams, S. P. Polymer-Fullerene Bulk-Heterojunction Solar Cells. *Adv. Mater.* **2010**, *22*, 3839–3856.
- (2) Hedley, G. J.; Ruseckas, A.; Samuel, I. D. W. Light Harvesting for Organic Photovoltaics. *Chem. Rev.* **2017**, *117*, 796–837.
- (3) Sirringhaus, H. 25th Anniversary Article: Organic Field-Effect Transistors: The Path Beyond Amorphous Silicon. *Adv. Mater.* **2014**, *26*, 1319–1335.
- (4) Torsi, L.; Magliulo, M.; Manoli, K.; Palazzo, G. Organic Field-Effect Transistor Sensors: A Tutorial Review. *Chem. Soc. Rev.* **2013**, *42*, 8612–8628.
- (5) Bhatnagar, P. K. Organic Light-Emitting Diodes—A Review. In *Nanomaterials and Their Applications*; Khan, Z. H., Ed.; Springer Singapore: Singapore, 2018; pp 261–287.
- (6) Xu, R.-P.; Li, Y.-Q.; Tang, J.-X. Recent Advances in Flexible Organic Light-Emitting Diodes. *J. Mater. Chem. C* **2016**, *4*, 9116–9142.
- (7) Jansen-van Vuuren, R. D.; Armin, A.; Pandey, A. K.; Burn, P. L.; Meredith, P. Organic Photodiodes: the Future of Full Color Detection and Image Sensing. *Adv. Mater.* **2016**, *28*, 4766–4802.
- (8) Baeg, K. J.; Binda, M.; Natali, D.; Caironi, M.; Noh, Y. Y. Organic Light Detectors: Photodiodes and Phototransistors. *Adv. Mater.* **2013**, *25*, 4267–4295.
- (9) Shrestha, S.; Fischer, R.; Matt, G. J.; Feldner, P.; Michel, T.; Osvet, A.; Levchuk, I.; Merle, B.; Golkar, S.; Chen, H.; et al. High-Performance Direct Conversion X-Ray Detectors Based on Sintered Hybrid Lead Triiodide Perovskite Wafers. *Nat. Photonics* **2017**, *11*, 436.
- (10) Benavides, C. M.; Murto, P.; Chochos, C. L.; Gregoriou, V. G.; Avgeropoulos, A.; Xu, X.; Bini, K.; Sharma, A.; Andersson, M. R.; Schmidt, O.; et al. High-Performance Organic Photodetectors from a High-Bandgap Indacenodithiophene-Based π -Conjugated Donor–Acceptor Polymer. *ACS Appl. Mater. Interfaces* **2018**, *10*, 12937–12946.
- (11) Büchele, P.; Richter, M.; Tedde, S. F.; Matt, G. J.; Ankah, G. N.; Fischer, R.; Biele, M.; Metzger, W.; Lilliu, S.; Bikondoa, O.; et al. X-ray Imaging with Scintillator-Sensitized Hybrid Organic Photodetectors. *Nat. Photonics* **2015**, *9*, 843.
- (12) Sirringhaus, H.; Brown, P. J.; Friend, R. H.; Nielsen, M. M.; Bechgaard, K.; Langeveld-Voss, B. M. W.; Spiering, A. J. H.; Janssen, R. A. J.; Meijer, E. W.; Herwig, P.; et al. Two-Dimensional Charge Transport in Self-Organized, High-Mobility Conjugated Polymers. *Nature* **1999**, *401*, 685.
- (13) Schubert, M.; Dölfen, D.; Frisch, J.; Roland, S.; Steyrlleuthner, R.; Stiller, B.; Chen, Z.; Scherf, U.; Koch, N.; Facchetti, A.; et al. Influence of Aggregation on the Performance of All-Polymer Solar Cells Containing Low-Bandgap Naphthalenediimide Copolymers. *Adv. Energy Mater.* **2012**, *2*, 369–380.
- (14) Duong, D. T.; Ho, V.; Shang, Z.; Mollinger, S.; Mannsfeld, S. C. B.; Dacuna, J.; Toney, M. F.; Segalman, R.; Salleo, A. Mechanism of Crystallization and Implications for Charge Transport in Poly(3-ethylhexylthiophene) Thin Films. *Adv. Funct. Mater.* **2014**, *24*, 4515–4521.
- (15) Liu, Y.; Zhao, J.; Li, Z.; Mu, C.; Ma, W.; Hu, H.; Jiang, K.; Lin, H.; Ade, H.; Yan, H. Aggregation and Morphology Control Enables Multiple Cases of High-Efficiency Polymer Solar Cells. *Nat. Commun.* **2014**, *5*, 5293.
- (16) Noriega, R.; Rivnay, J.; Vandewal, K.; Koch, F. P. V.; Stingelin, N.; Smith, P.; Toney, M. F.; Salleo, A. A General Relationship Between Disorder, Aggregation and Charge Transport in Conjugated Polymers. *Nat. Mater.* **2013**, *12*, 1038.
- (17) Hildner, R.; Köhler, A.; Müller-Buschbaum, P.; Panzer, F.; Thelakkat, M. π -Conjugated Donor Polymers: Structure Formation

and Morphology in Solution, Bulk and Photovoltaic Blends. *Adv. Energy Mater.* **2017**, *7*, 1700314.

(18) Guilbert, A. A. Y.; Cabral, J. T. Impact of Solution Phase Behaviour and External Fields on Thin Film Morphology: PCBM and RRa-P3HT Model System. *Soft Matter* **2017**, *13*, 827–835.

(19) Güldal, N. S.; Kassar, T.; Berlinghof, M.; Unruh, T.; Brabec, C. J. In Situ Characterization Methods for Evaluating Microstructure Formation and Drying Kinetics of Solution-Processed Organic Bulk-Heterojunction Films. *J. Mater. Res.* **2017**, *32*, 1855–1879.

(20) Richter, L. J.; DeLongchamp, D. M.; Amassian, A. Morphology Development in Solution-Processed Functional Organic Blend Films: An In Situ Viewpoint. *Chem. Rev.* **2017**, *117*, 6332–6366.

(21) Pröller, S.; Mosegui Gonzalez, D.; Zhu, C.; Schaible, E.; Wang, C.; Müller-Buschbaum, P.; Hexemer, A.; Herzig, E. M. Note: Setup for Chemical Atmospheric Control During In Situ Grazing Incidence X-Ray Scattering of Printed Tin Films. *Rev. Sci. Instrum.* **2017**, *88*, 066101.

(22) Chang, J.-F.; Sun, B.; Breiby, D. W.; Nielsen, M. M.; Sölling, T. I.; Giles, M.; McCulloch, I.; Sringhaus, H. Enhanced Mobility of Poly(3-hexylthiophene) Transistors by Spin-Coating from High-Boiling-Point Solvents. *Chem. Mater.* **2004**, *16*, 4772–4776.

(23) Park, Y. D.; Lee, H. S.; Choi, Y. J.; Kwak, D.; Cho, J. H.; Lee, S.; Cho, K. Solubility-Induced Ordered Polythiophene Precursors for High-Performance Organic Thin-Film Transistors. *Adv. Funct. Mater.* **2009**, *19*, 1200–1206.

(24) Reichenberger, M.; Kroh, D.; Matrone, G. M. M.; Schötz, K.; Pröller, S.; Filonik, O.; Thordardottir, M. E.; Herzig, E. M.; Bässler, H.; Stingelin, N.; et al. Controlling Aggregate Formation in Conjugated Polymers by Spin-Coating Below the Critical Temperature of the Disorder-Order Transition. *J. Polym. Sci., Part B: Polym. Phys.* **2018**, *56*, 532–542.

(25) Panzer, F.; Bässler, H.; Köhler, A. Temperature Induced Order-Disorder Transition in Solutions of Conjugated Polymers Probed by Optical Spectroscopy. *J. Phys. Chem. Lett.* **2017**, *8*, 114–125.

(26) Abdelsamie, M.; Zhao, K.; Niazi, M. R.; Chou, K. W.; Amassian, A. In Situ UV-Visible Absorption During Spin-Coating of Organic Semiconductors: A New Probe for Organic Electronics and Photovoltaics. *J. Mater. Chem. C* **2014**, *2*, 3373–3381.

(27) Reichenberger, M.; Baderschneider, S.; Kroh, D.; Grauf, S.; Köhler, J.; Hildner, R.; Köhler, A. Watching Paint Dry: The Impact of Diiodooctane on the Kinetics of Aggregate Formation in Thin Films of Poly(3-hexylthiophene). *Macromolecules* **2016**, *49*, 6420–6430.

(28) Spano, F. C.; Silva, C. H- and J-Aggregate Behavior in Polymeric Semiconductors. *Annu. Rev. Phys. Chem.* **2014**, *65*, 477–500.

(29) Yamagata, H.; Spano, F. C. Interplay Between Intrachain and Interchain Interactions in Semiconducting Polymer Assemblies: The HJ-Aggregate Model. *J. Chem. Phys.* **2012**, *136*, 184901.

(30) Spano, F. C. The Spectral Signatures of Frenkel Polarons in H- and J-Aggregates. *Acc. Chem. Res.* **2010**, *43*, 429–439.

(31) Barford, W.; Marcus, M. Perspective: Optical Spectroscopy in π -conjugated Polymers and How it can be Used to Determine Multiscale Polymer Structures. *J. Chem. Phys.* **2017**, *146*, 130902.

(32) Köhler, A.; Bässler, H. In *Electronic Processes in Organic Semiconductors*; Köhler, A.; Bässler, H., Eds.; Wiley-VCH, 2015; pp 1–86.

(33) Engmann, S.; Bokel, F. A.; Ro, H. W.; DeLongchamp, D. M.; Richter, L. J. Real-Time Photoluminescence Studies of Structure Evolution in Organic Solar Cells. *Adv. Energy Mater.* **2016**, *6*, 1502011.

(34) Brown, P. J.; Thomas, D. S.; Köhler, A.; Wilson, J. S.; Kim, J.-S.; Ramsdale, C. M.; Sringhaus, H.; Friend, R. H. Effect of Interchain Interactions on the Absorption and Emission of Poly(3-hexylthiophene). *Phys. Rev. B: Condens. Matter Mater. Phys.* **2003**, *67*, No. e064203.

(35) Panzer, F.; Bässler, H.; Lohwasser, R.; Thelakkat, M.; Köhler, A. The Impact of Polydispersity and Molecular Weight on the Order-Disorder Transition in Poly(3-hexylthiophene). *J. Phys. Chem. Lett.* **2014**, *5*, 2742–2747.

(36) Panzer, F.; Sommer, M.; Bässler, H.; Thelakkat, M.; Köhler, A. Spectroscopic Signature of Two Distinct H-Aggregate Species in Poly(3-hexylthiophene). *Macromolecules* **2015**, *48*, 1543–1553.

(37) Bockmann, M.; Schemme, T.; de Jong, D. H.; Denz, C.; Heuer, A.; Doltsinis, N. L. Structure of P3HT Crystals, Thin Films, and Solutions by UV/Vis Spectral Analysis. *Phys. Chem. Chem. Phys.* **2015**, *17*, 28616–28625.

(38) Scharlich, C.; Lohwasser, R. H.; Sommer, M.; Asawapirom, U.; Scherf, U.; Thelakkat, M.; Neher, D.; Köhler, A. Control of Aggregate Formation in Poly(3-hexylthiophene) by Solvent, Molecular Weight, and Synthetic Method. *J. Polym. Sci., Part B: Polym. Phys.* **2012**, *50*, 442–453.

(39) Clark, J.; Silva, C.; Friend, R. H.; Spano, F. C. Role of Intermolecular Coupling in the Photophysics of Disordered Organic Semiconductors: Aggregate Emission in Regioregular Polythiophene. *Phys. Rev. Lett.* **2007**, *98*, 206406.

(40) Haase, R.; Lethen, M.; Dücker, K. H. Viskosität des flüssigen Systems Chlorbenzol + Brombenzol. *Z. Naturforsch., A: Phys. Sci.* **1975**, *30*, 916.

(41) Cone, C. W.; Cheng, R. R.; Makarov, D. E.; Vanden Bout, D. A. Molecular Weight Effect on the Formation of β Phase Poly(9,9'-dioctylfluorene) in Dilute Solutions. *J. Phys. Chem. B* **2011**, *115*, 12380–12385.

(42) Köhler, A.; Bässler, H. In *Electronic Processes in Organic Semiconductors*; Köhler, A.; Bässler, H., Eds.; Wiley-VCH, 2015; pp 87–191.

(43) Raithel, D.; Simine, L.; Pickel, S.; Schötz, K.; Panzer, F.; Baderschneider, S.; Schiefer, D.; Lohwasser, R.; Köhler, J.; Thelakkat, M.; et al. Direct Observation of Backbone Planarization via Side-Chain Alignment in Single Bulky-Substituted Polythiophenes. *Proc. Natl. Acad. Sci. U. S. A.* **2018**, *115*, 2699–2704.

(44) de Mello, J. C.; Wittmann, H. F.; Friend, R. H. An Improved Experimental Determination of External Photoluminescence Quantum Efficiency. *Adv. Mater.* **1997**, *9*, 230–232.

(45) Cook, S.; Furube, A.; Katoh, R. Analysis of the Excited States of Regioregular Polythiophene P3HT. *Energy Environ. Sci.* **2008**, *1*, 294–299.

(46) Solanki, A.; Bagui, A.; Long, G.; Wu, B.; Salim, T.; Chen, Y.; Lam, Y. M.; Sum, T. C. Effectiveness of External Electric Field Treatment of Conjugated Polymers in Bulk-Heterojunction Solar Cells. *ACS Appl. Mater. Interfaces* **2016**, *8*, 32282–32291.

(47) Elshobaki, M.; Gebhardt, R.; Carr, J.; Lindemann, W.; Wang, W.; Grieser, E.; Venkatesan, S.; Ngo, E.; Bhattacharjee, U.; Strzalka, J.; et al. Tailoring Nanoscale Morphology of Polymer:Fullerene Blends Using Electrostatic Field. *ACS Appl. Mater. Interfaces* **2017**, *9*, 2678–2685.

(48) Molina-Lopez, F.; Yan, H.; Gu, X.; Kim, Y.; Toney, M. F.; Bao, Z. Electric Field Tuning Molecular Packing and Electrical Properties of Solution-Shearing Coated Organic Semiconducting Thin Films. *Adv. Funct. Mater.* **2017**, *27*, 1605503.

(49) Güldal, N. S.; Kassar, T.; Berlinghof, M.; Ameri, T.; Osvet, A.; Pacios, R.; Li Destri, G.; Unruh, T.; Brabec, C. J. Real-Time Evaluation of Thin Film Drying Kinetics Using an Advanced, Multi-Probe Optical Setup. *J. Mater. Chem. C* **2016**, *4*, 2178–2186.

(50) Alsari, M.; Bikondoa, O.; Bishop, J.; Abdi-Jalebi, M.; Ozer, Y. L.; Hampton, M.; Thompson, P.; Horantner, M. T.; Mahesh, S.; Greenland, C.; et al. In Situ Simultaneous Photovoltaic and Structural Evolution of Perovskite Solar Cells During Film Formation. *Energy Environ. Sci.* **2018**, *11*, 383–393.

(51) Yoo, E. J.; Lyu, M.; Yun, J. H.; Kang, C. J.; Choi, Y. J.; Wang, L. Resistive Switching Behavior in Organic-Inorganic Hybrid $\text{CH}_3\text{NH}_3\text{Pb}_{1-x}\text{Cl}_x$ Perovskite for Resistive Random Access Memory Devices. *Adv. Mater.* **2015**, *27*, 6170–6175.

(52) Pröller, S.; Liu, F.; Zhu, C.; Wang, C.; Russell, T. P.; Hexemer, A.; Müller-Buschbaum, P.; Herzig, E. M. Following the Morphology Formation In Situ in Printed Active Layers for Organic Solar Cells. *Adv. Energy Mater.* **2016**, *6*, 1501580.

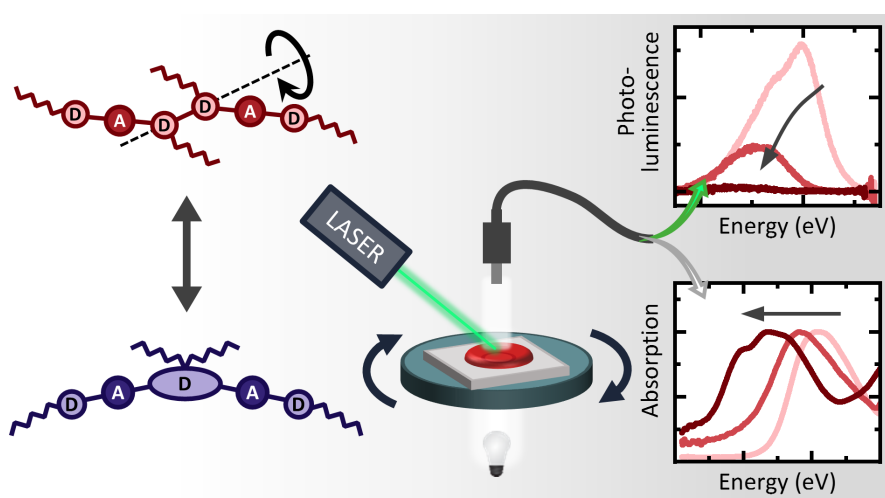
(53) van Franeker, J. J.; Hermida-Merino, D.; Gommès, C.; Arapov, K.; Michels, J. J.; Janssen, R. A. J.; Portale, G. Sub-Micrometer

Structure Formation during Spin Coating Revealed by Time-Resolved In Situ Laser and X-Ray Scattering. *Adv. Funct. Mater.* **2017**, *27*, 1702516.

(54) Manley, E. F.; Strzalka, J.; Fauvell, T. J.; Jackson, N. E.; Leonardi, M. J.; Eastham, N. D.; Marks, T. J.; Chen, L. X. In Situ GIWAXS Analysis of Solvent and Additive Effects on PTB7 Thin Film Microstructure Evolution during Spin Coating. *Adv. Mater.* **2017**, *29*, 1703933.

9

Role of Torsional Flexibility in the Film Formation Process in Two π -Conjugated Model Oligomers



Stefan Wedler, Cheng Zhou, Guillermo C. Bazan,
Fabian Panzer, and Anna Köhler.

Published in

The Journal of Physical Chemistry Letters, **2018**, 11, 9379–9386
(DOI: 10.1021/acs.jpcclett.0c02778)

Reprinted with permission from the American Chemical Society
Copyright(2020) American Chemical Society

Role of Torsional Flexibility in the Film Formation Process in Two π -Conjugated Model Oligomers

Stefan Wedler, Cheng Zhou, Guillermo C. Bazan, Fabian Panzer, and Anna Köhler*



Cite This: *J. Phys. Chem. Lett.* 2020, 11, 9379–9386



Read Online

ACCESS |



Metrics & More

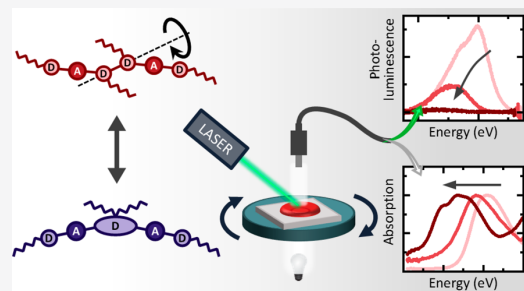


Article Recommendations



Supporting Information

ABSTRACT: The performance of solution-processed organic semiconductor devices is heavily influenced by the morphology of the active layer. Film formation is a complex process, with the final morphology being the result of the interplay between processing parameters and molecular properties, which is only poorly understood. Here, we investigate the influence of molecular stiffness by using two model oligomers, TT and CT, which differ only in the rotational flexibility of their central building block. We monitor absorption and emission simultaneously *in situ* during spin coating. We find that film formation takes place in four similar stages for both compounds. However, the time scales are remarkably different during the third stage, where electronically interacting aggregates are created. While this process is fast for the stiff CT, it takes minutes for the flexible TT. By comparing with previously determined aggregation properties in solution, we conclude that even though aggregate formation concurs with a planarization process, a certain amount of backbone flexibility is beneficial for establishing ordered structures during film formation. Here, the elongated time window in the case of the flexible compound can further allow for better processing control.



Organic solar cells are becoming more efficient, with power conversion efficiencies exceeding 17%.¹ One key insight on the way to this impressive performance was that the morphology of the active layer impacts strongly the performance of such devices, as it determines the amount of intermolecular coupling and hence charge generation and transport properties.^{2–15} Under ideal circumstances, the desired morphology is achieved during film formation. However, this is difficult to control, as different processing conditions make an impact on different time and length scales during the film evolution. These conditions include, for example, the choice of the solvent^{16–19} and possibly solvent additives,^{20–22} in particular regarding solubility parameter and boiling point, choice of processing temperature,^{23,24} solvent saturation of the atmosphere,^{25,26} and deposition conditions.²⁷

In addition, molecular parameters like backbone planarity and stiffness seem to be important. Studies conducted on macromolecules in solution upon cooling showed that, usually, a planarization process precedes the formation of aggregates, i.e. electronically interacting ensembles of chromophores, which takes place at a critical temperature T_c . This behavior has been observed for donor molecules such as p-DTF-(FBTTh₂)₂ as well as oligomers and polymers of PFO, MEH-PPV, P3HT, and PCPDTBT.^{28–33} Similarly, macromolecules where specific heteroatoms or halide substitutions enhance the planarity of the backbone have also been reported to be more likely to aggregate.^{33–39} Thus, the question arises of whether planar structures are beneficial for generating electronically

interacting ensembles, and how this leads to the establishment of different morphologies, including ordered phases, during film formation.

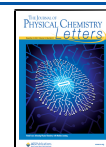
Postprocessing structural analysis gives only limited insight into the complex processes involved. It is more insightful to monitor suitable properties *in situ* during film formation to identify and manipulate relevant phases. There are several studies where the evolution of morphology during film formation was investigated using X-ray scattering (GIWAXS, GISAXS), optical methods (UV–vis absorption, ellipsometry), or combinations of these techniques.^{3,20,24,26,40–44} While they can monitor crystalline properties and film thickness, they cannot give a complete picture about intermolecular electronic interactions.

We recently developed an experimental setup capable of measuring absorption and emission simultaneously,²³ as in particular the emission is highly sensitive to intermolecular interactions.⁴⁵ This approach already gave valuable insight into the film formation of the hybrid lead perovskite MAPbI₃ when processed using a two-step method.⁴⁶ Here, we use this

Received: September 11, 2020

Accepted: October 12, 2020

Published: October 23, 2020



approach to address how the torsional flexibility of the central unit in two organic model compounds impacts the formation of ordered structures during film formation. Figure 1 shows the

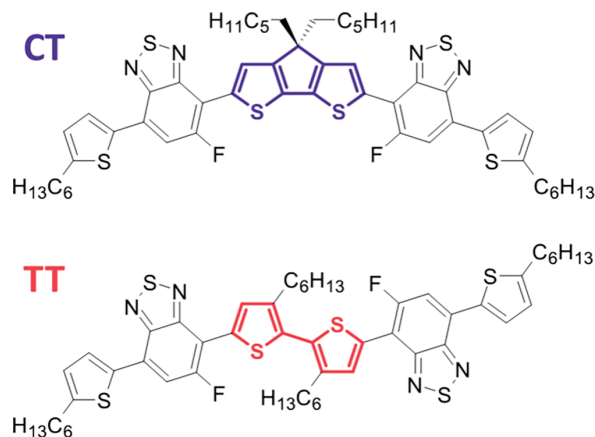


Figure 1. Chemical structures of CT and TT.

chemical structure of these molecules that make up the core of many typical donor molecules used for organic solar cell applications. They are constructed in a D–A–D′–A–D-type architecture, where electron rich units (donor, D) alternate with electron deficient units (acceptor, A). They differ only in their central building block. CT comprises a cyclopentadithiophene, making it planar and stiff. In contrast, TT has two thiophenes with hexyl side chains connected in a more flexible head-to-head fashion, which induces a twist of about 70° in the otherwise planar structure.^{47,48}

We have previously studied the aggregation behavior for CT and TT in hexane solution. We found that the more flexible and twisted TT readily forms aggregates upon cooling, while the tendency to aggregate is significantly less pronounced for the rigid, planar CT.⁴⁸ This was, at first, counterintuitive, as planarization has been observed to occur usually prior to aggregate formation.^{24,32,49} Closer inspection revealed the critical role of the formation pathway. In solution, the rigidity of CT inhibits the formation of optimum contact points between molecular subunits. Hence, a small amount of aggregates formed only for the highest concentration investigated close to the freezing point of the hexane solvent, where intermolecular contact and proximity is enforced. In contrast, the flexibility of TT allows two molecules to wrap around each other and optimize their mutual arrangement to allow for a concomitant planarization process. This eventually results in a large number of aggregates already at moderate concentrations and temperatures.

To explore how the behavior observed in solution affects the process of forming a thin film, we prepared thin films by spin coating and monitored absorption and emission simultaneously *in situ* during processing. The processing temperature for both solution and substrate was chosen to be above the critical temperature for aggregation, as the existence of preaggregates in the spin coating solution can affect the final morphology.^{3,24} From our measurements, from comparison between the film and solution data taken from the same solvent and from comparison with published GIWAXS data, we find that in contrast to the case in solution, the rigid CT readily forms films containing aggregates with some degree of

electronic interaction and local order between the molecules. In contrast, TT films seem to be amorphous right after solvent evaporation and evolve into structures with local order and electronic interaction only subsequently on a time scale of minutes. Nevertheless, both compounds evolve in similar stages, and though aggregation was associated with planarization in the past, our findings suggest that the flexible backbone of TT is still beneficial for the formation of aggregated structures.

For our investigation, we prepared hexane solutions of both compounds, and films were cast. The absorption and emission spectra were recorded simultaneously during spin-coating *in situ*. Details of the experiment are detailed in the Supporting Information. We first consider the film formation properties of CT during processing at room temperature, which is well above the critical temperature of −18 °C for aggregation in hexane (see Figure S1). Figures 2a and b show the emission and absorption spectra, respectively, as a function of processing time displayed as 2D heat maps (bottom) or as spectra at distinct time steps (top). As detailed below, the processing time is structured into four distinct temporal regimes.

We consider the temporal evolution of different spectral features to analyze the transition. Figure 2c shows the energy positions for the maxima of absorption and emission as well as the position of the low energy edge in absorption. We define this as the energy where the absorption reaches $1/e \approx 0.37$ of its maximum value compared to the baseline. We further indicate the optical density at the center of the initial broad CT absorption at 2.15 eV and at 1.90 eV, where an additional shoulder emerges. Also shown is the evolution of the absolute photoluminescence quantum yield (PLQY), calculated by integrating the emission spectra after correcting for changes in absorption at the excitation energy of 2.38 eV and comparing to the PLQYs for a dilute solution, as detailed in the Supporting Information. The color of filled circles indicates the temporal position of the spectra shown in the top panels of Figure 2a and b.

From a closer inspection of these features, we can identify four time ranges of the transition. Range I goes up to about 1.2 s. Here, the shapes and energetic positions of absorption and emission remain largely constant. The loss of OD at 2.15 eV in this time range is due to throw-off of excess solution. The shape of the emission spectra differs from the spectra of a dilute solution.⁴⁸ This is due to significant overlap of absorption and emission, which results in strong reabsorption. While the spectra are unchanged during range I, the PLQY already reduces. This implies the formation of a nonemissive decay channel. Evidently, the continuous increase in concentration due to ongoing solvent evaporation increases proximity between the molecules. This promotes the formation of nonemissive preaggregate species, as observed previously.^{48,50} Range II comprises the time from 1.2 to 1.8 s, where the energy of the broad emission peak reduces from 1.75 to 1.55 eV, accompanied by a further reduction in PLQY. Considering the entire evolution of the PL spectra over time, we attribute this to a reduction of the monomeric emission at higher energies, so that a remaining weak and broad lower energy emission dominates the spectral position of the peak. The concomitant absorption in range II changes only little in shape and intensity. The peak position remains constant though the low energy edge shifts slightly to lower energies, implying an increase in broadening.

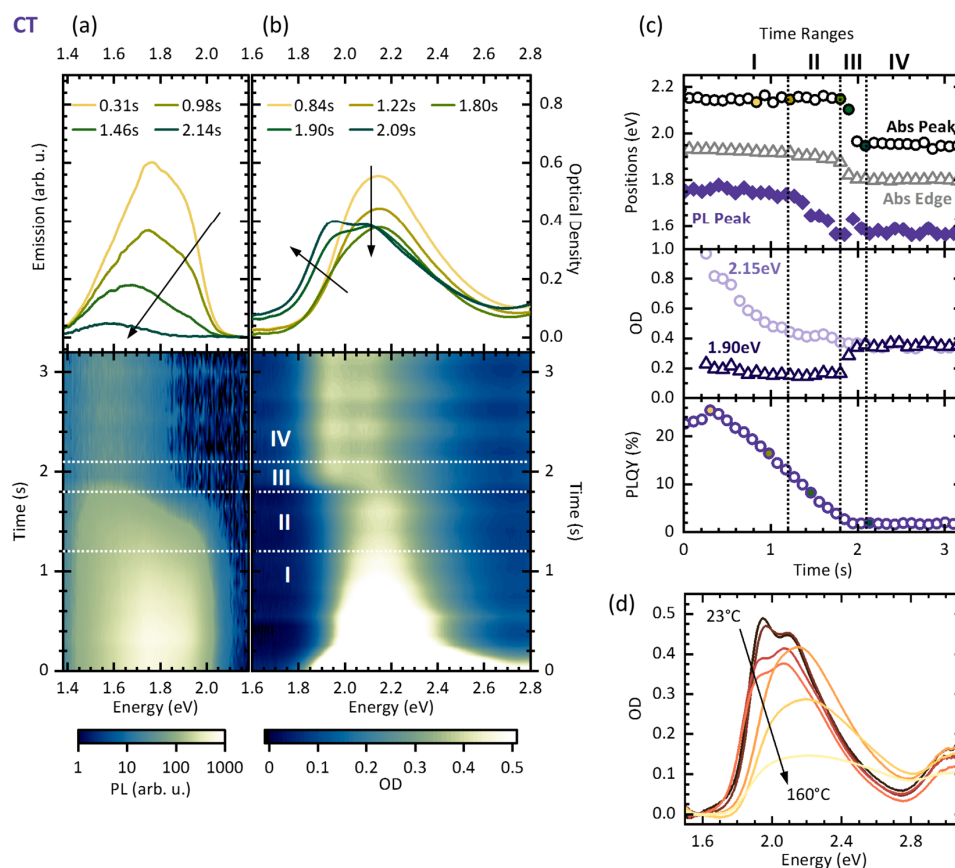


Figure 2. (a) Emission and (b) absorption spectra of a CT film during spin-casting from hexane solution at room temperature. The panels on top show spectra at fixed times after starting the spin coater rotation. The heat maps on the bottom show the evolution in the first 3 s. The white dotted lines indicate four different time ranges of film formation. (c) Temporal evolution of (top) the peak positions for absorption and emission as well as the low energy edge of absorption, (middle) the optical density at 2.15 and 1.90 eV, and (bottom) the PLQY. The filled circles correspond to the spectra shown in the top panels of (a) and (b). (d) Absorption spectra of a CT film upon heating at temperatures of 23, 52, 74, 96, 117, 138, and 160 °C.

The fast change in the energy positions of the absorption peak and edge occurring between 1.8 and 2.1 s defines range III. In absorption, the baseline rises and an additional structured feature appears with a main peak at 1.95 eV and a shoulder at 2.12 eV. Simultaneously, the broad unstructured part decreases in intensity, resulting in an isosbestic point at 2.11 eV. This isosbestic point also remains after baseline subtraction (see Figure S2). During this time, the PLQY reduces further, while the PL peak position has already reached its final position. Range IV, which starts at 2.1 s, denotes the end of the film formation process, as all photophysical parameters remain constant for processing times up to 95 s (see Figure S3). Overall, the process of film formation reduced the PLQY continuously from 25% to 2%, and the absorption changed to a more structured feature with a 0–0 peak located at 1.95 eV.

The formation of a lower-energy structured feature, accompanied by a reduction in PLQY and a redshift and broadening in emission strongly points to the formation of aggregates. To further investigate this, we measured the absorption spectra of a CT film upon heating above its melting point at around 140 °C (Figure 2d).⁴⁷ If the structured feature is of monomeric origin, we would expect an overall broadening

of all vibrational peaks and thus of the entire structure upon melting due to increased conformational freedom. Instead, we observe that the line width remains unchanged upon heating up to 96 °C, yet the peak at 1.95 eV decreases until it finally disappears at 117 °C. Concomitant with the disappearance of the 1.95 eV peak, the extinction of the remaining broad band centered at 2.15 eV increases discontinuously and then reduces subsequently while it broadens as expected from increased torsional motion. This is clear spectroscopic evidence that the structured feature at 1.95 eV can be assigned to an aggregate, consistent with the one observed in a CT hexane solution of 2.5×10^{-4} M at 1.85 eV and 180 K.⁴⁸

We now turn to the results for TT upon film formation, which are summarized in Figure 3. To ensure processing above the critical temperature for aggregation in solution of 42 °C (see Figure S1), processing was performed on a substrate heated to 51 °C. We observe that the evolution of absorption and emission takes place in two separate stages. The first stage, shown in Figure 3a, comprises the initial 3 s, where, as for CT, the transition from solution to a solid film takes place. This is followed by the second stage (Figure 3b) that is characterized by a subsequent slow crystallization process, as already reported by Zhou et al.⁴⁷ The entire evolution of absorption

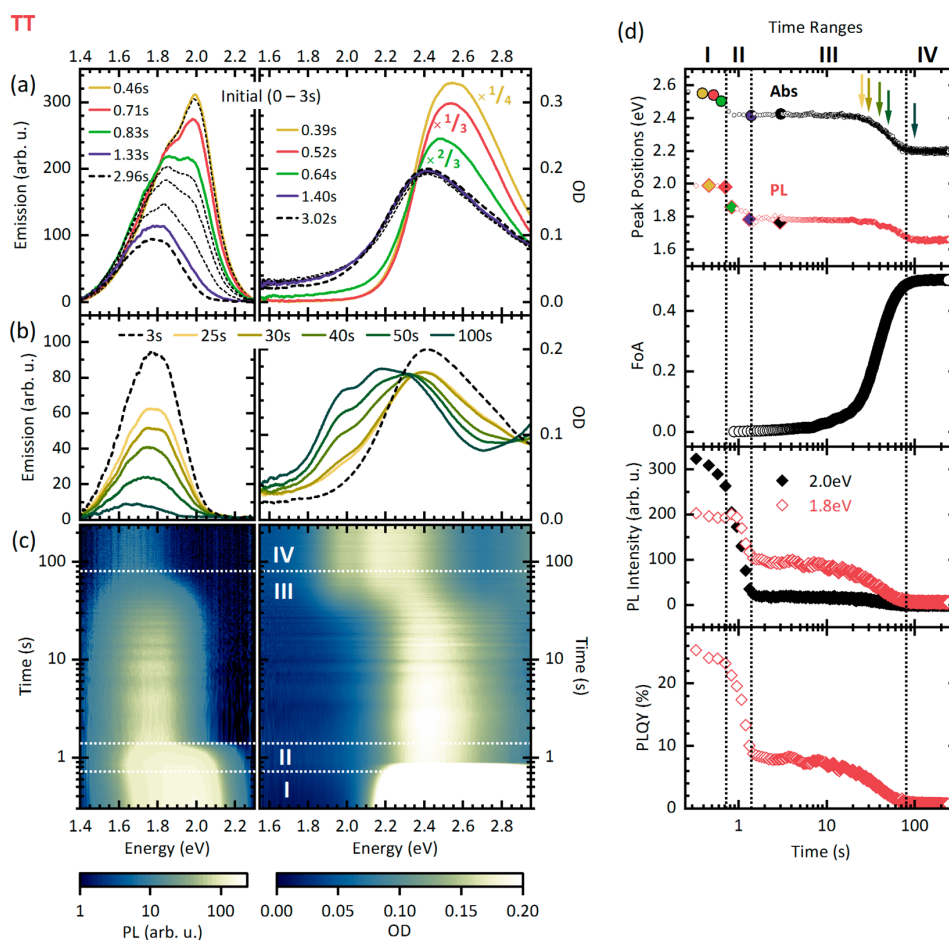


Figure 3. (a–c) Emission (left) and absorption (right) spectra of a TT film during spin-casting from hexane solution at a substrate temperature of 51 °C in (a) the first 3 s and (b) subsequently. The spectra in (a) between 0.39 and 1.40 s are shown in steps of 0.125 s, corresponding to the acquisition rate of 8.0 Hz. The complete evolution is shown as a 2D heat map in (c). The white dotted lines indicate four different time ranges of film formation. (d) Temporal evolution of the energy peak positions, the fraction of aggregates (FoA) in absorption, the emission intensity at 2.0 and 1.8 eV, and the PLQY. The colored symbols and arrows indicate the temporal positions of the spectra shown in (a) and (b).

and emission spectra is shown as a heat map with a logarithmic time scale in Figure 3c. While Figures 3a and 3b show the pertaining spectra at distinct time steps, Figure 3d highlights the temporal evolution of specific spectral features. Similar to CT, we can again identify four distinct stages, yet they occur on different time scales.

As in the case for CT, the initial time range is characterized by unchanged spectral features and a throw-off of solution. For TT, this lasts up to 0.72 s. In this period, solvent also evaporates so that the solution concentration increases. Even though absorption and emission appear unchanged, the PLQY decreases, suggesting the formation of some nonemissive or self-quenching interacting species similar to the case of CT. Time range II is also similar for both compounds, insofar that it happens in less than one second (from 0.72 to 1.40 s for TT, and from 1.2 to 1.8 s for CT), and there is no change in the absorption spectra during range II, while in emission the high energy peak (at 2.0 eV for TT, 1.9 eV for CT), associated with the dissolved monomeric species, disappears. What remains at the end of range II is a broad emission at lower energies with only poor PLQY that is indicative of some intermolecular interactions, yet without any long-range order as absorption

appears still unstructured. One clear difference compared to CT is the change in absorption for TT right at the transition from range I to II. Concomitant with the disappearance of the emission from the dissolved monomeric species, we note a rise in the absorption baseline, suggesting light scattering, and a sudden shift of the broad absorption to lower energies by 150 meV, along with some broadening. This indicates that the actual film formation is finished by the end of time range II and all further evolution takes place in the dry film. Time range III also differs significantly for the two compounds. For TT, this time range starts with a plateau of the PLQY, followed by a further slow decrease. Moreover, in absorption, a structured spectral contribution emerges continuously at lower energies as the broad feature at higher photon energies disappears. While this change takes place within only 0.25 s for CT, it is drawn out over about 80 s for TT. It is followed by time range IV, where no further spectral changes can be observed.

In our previous study, we observed a high tendency for TT in hexane to aggregate, while CT was significantly less prone to aggregate formation. This was attributed to its banana shape that limits the number of stabilizing intermolecular contact points. This is also reflected in the different critical

temperatures for aggregation of the two molecules, which is larger for TT. It is therefore striking to observe an apparently opposite behavior when spin coating films from hexane solution. This seeming contradiction between aggregate formation in solution and film can be resolved through closer inspection. First, we note that both compounds show the same four time ranges, corresponding to four stages, during film formation, albeit at a different time scale for the third stage. For both compounds, the first stage comprises about the first second after depositing the solution on the substrate. As the concentration of the solution increases due to solvent evaporation, absorption and emission remain unchanged, yet the overall PLQY reduces, indicating the formation of nonemissive species such as excimer-like molecular ensembles. This phenomenon has previously been noted for pyrene-derivatives.⁵⁰ The formation of nonemissive species is not uncommon and has been reported early on in the field, for example for the polymer MEH-PPV, where it was referred to as polaron pairs.⁵¹ Such species can particularly easily form at certain geometries when donor and acceptor units are brought into proximity and can evolve into excitons or charge transfer states through corresponding changes in the intermolecular arrangement.^{52,53} These geometrical changes take place during the second film formation stage, where the excitonic emission from the dissolved molecules is quenched in both compounds. Evidently, the closer proximity between molecules now allows for facile energy transfer to nonemissive species. In contrast to CT, for the flexible TT, this closer proximity manifests itself also in a bathochromic shift in absorption and line broadening, accompanied by a rising baseline, as if scattering conglomerates are formed.

The formation of aggregates takes place during the third stage, and this is where the different torsional flexibility has a pronounced influence. Our previous study showed that CT prefers to arrange in two dimer conformations that form with equal probability upon molecular approximation. In the type A conformation, the side chains of the two molecules comprising the dimer lie on opposite sites. This conformation supports nonemissive excimers that do not feature in the absorption spectra. In the type B conformations, the two molecules comprising the dimer arrange with the side chains on the same side, and this conformation allows for emissive excitons as well as dimer absorption (or absorption from a larger interacting ensemble, i.e. aggregates). Evidently, some of these aggregates form during the third stage, as indicated by the sudden rise of the aggregate absorption at 1.9 eV in CT, and are fixed in their positions thereafter due to the rigid nature of CT. This implies that intermolecular order is established only on a short-range length scale, which is confirmed by previous grazing incidence wide-angle X-ray scattering (GIWAXS) measurements showing scattering rings instead of distinct diffraction peaks for CT thin films.⁴⁷ In contrast, as detailed above, in our solution study we found that TT forms aggregates by a more complex pathway. Two approaching molecules seem to wrap around each other and planarize into a trans-planar structure. In hexane solution, this wrapping and planarization is not strictly subsequent but concurs to some extent. We envisage that the kinetically quenched molecular arrangement of TT will be located somewhere along the aggregate formation pathway, yet can continue to evolve due to the flexibility of the TT molecule. More specifically, a partially or fully wrapped dimer-like conformation can still planarize in the course of time, thus enabling the formation of electronically interacting chromo-

phores that give rise to the aggregate absorption emerging during the third stage. Corresponding GIWAXS measurements from a previous study on TT thin films prove the long-range character of this aggregate interaction.⁴⁷

We emphasize that the delayed crystallization in TT is a kinetic effect. The molecular geometry in solution is strongly twisted, as the central dihedral angle is about 70°. ^{47,48} The energetic barrier to planarization is around 0.3 eV, which is too large to be overcome spontaneously. However, the molecules adopt a planar conformation in the solid state,^{47,54} as well as in solution upon aggregation.⁴⁸ The decisive difference between aggregate formation in solution at low temperatures and film formation upon spin coating is the temporal duration of these processes. In solution, the molecules have enough time to approach each other and subsequently planarize sufficiently due to the intermolecular interaction. This is impossible during film processing within the temporal range of the solvent evaporation, which is finished in less than two seconds. Either, at the early stages, the molecules are too far apart to each other to induce the planar conformation, or, later on, they are forced close to each other too quickly, resulting in a kinetically quenched amorphous morphology, from which the planar structure can only emerge slowly. This resolves the apparent discrepancy between the aggregation behavior during film formation and what we observed before in solution.

The implication of this study is that a torsional flexible center, as opposed to a rigid one, is not necessarily a disadvantage to the formation of ordered structures. Nevertheless, our study demonstrates that a tendency to planarize is associated with the formation of locally ordered interacting structures. Hence, it will be of advantage to incorporate features that enhance the driving force toward planarization of the backbone, such as suitable heteroatoms or side chain engineering. Regarding the question whether a rigid center might be more advantageous a priori, we point out that for the rigid CT, the film formation process occurs very fast and precludes any intervention possibility. While this may not matter when the resulting structure is the one desired anyway, the kinetic lock can become relevant for larger molecules with a CT-like core, or polymers, where the desired structure is not immediately achieved. We envisage that, in contrast, the more elongated third stage in the film formation process that is associated with the flexible TT center may allow for user invention and process control with the aim to modify the resulting structure during deposition. This can take the form of controlling the solvent vapor pressure or the temperature of substrate and solution during deposition.

In conclusion, we compared the film formation during spin coating for two oligomer compounds, which consist of typical solar cell materials building blocks, and which differ only in the stiffness of their central unit. Both molecules show the same four time ranges upon film formation. During the first two stages, which is within the first two seconds, excess solution slips off, solvent evaporates, and precursors to aggregates already form. The third stage is important for the establishment of ground state interaction before film formation is finished in the fourth stage. The molecular flexibility largely impacts this critical third stage. For the rigid CT, it is fast, and thus, the molecules are kinetically locked in the conformations in which they happen to end up. Changes in morphology would require post-treatment of the final film. In contrast, stage III lasts around 80 s for the flexible TT, where we observed a continuous transformation into ordered structures.

Comparison to our previous study of aggregation in the same solvent hexane allowed us to attribute this behavior to conformational changes of the TT molecule from twisted to planar in the dry film. This enables the TT molecules to reorient into arrangements with strong intermolecular interaction. More importantly, the elongated aggregation period would allow for user intervention during deposition, thus opening up possibilities to fine-tune and tailor the desired morphology without further postprocessing treatment. The implications for the chemical design for next-generation materials might be to incorporate moderately flexible structures into the backbone with sufficient driving force toward planarization.

■ ASSOCIATED CONTENT

Supporting Information

The Supporting Information is available free of charge at <https://pubs.acs.org/doi/10.1021/acs.jpcllett.0c02778>.

Experimental details, determination of the critical temperature for aggregation at high concentrations, absorption of CT during spin coating without baseline, absorption and emission of CT for measurement times up to 95 s, suppression of the aliasing effect for absorption during spin coating, and determination of the fraction of aggregates (PDF)

■ AUTHOR INFORMATION

Corresponding Author

Anna Köhler – Soft Matter Optoelectronics, Experimentalphysik II and Bayreuth Institute of Macromolecular Research (BIMF) and Bavarian Polymer Institute (BPI), University of Bayreuth, Bayreuth 95440, Germany; orcid.org/0000-0001-5029-4420; Email: Anna.Koehler@uni-bayreuth.de

Authors

Stefan Wedler – Soft Matter Optoelectronics, Experimentalphysik II, University of Bayreuth, Bayreuth 95440, Germany

Cheng Zhou – Departments of Chemistry and Chemical Engineering, National University of Singapore, Singapore 119077 Singapore

Guillermo C. Bazan – Departments of Chemistry and Chemical Engineering, National University of Singapore, Singapore 119077 Singapore; orcid.org/0000-0002-2537-0310

Fabian Panzer – Soft Matter Optoelectronics, Experimentalphysik II, University of Bayreuth, Bayreuth 95440, Germany; orcid.org/0000-0002-2191-9011

Complete contact information is available at:

<https://pubs.acs.org/doi/10.1021/acs.jpcllett.0c02778>

Notes

The authors declare no competing financial interest.

■ ACKNOWLEDGMENTS

We acknowledge financial support by the Bavarian State Ministry of Science, Research, and the Arts (StMWK) through the Collaborative Research Network “Solar Technologies go Hybrid”. S.W. was supported by the Elite Network Bavaria (ENB) in the framework of the Elite Study Program “Macromolecular Science” and “MINT Lehramt plus”. Work at NUS was supported by a startup grant to GCB (R-143-000-A97-133).

■ REFERENCES

- (1) Liu, Q.; Jiang, Y.; Jin, K.; Qin, J.; Xu, J.; Li, W.; Xiong, J.; Liu, J.; Xiao, Z.; Sun, K.; et al. 18% Efficiency Organic Solar Cells. *Science Bulletin* **2020**, *65*, 272–275.
- (2) Karki, A.; Vollbrecht, J.; Dixon, A. L.; Schopp, N.; Schrock, M.; Reddy, G. N. M.; Nguyen, T.-Q. Understanding the High Performance of over 15% Efficiency in Single-Junction Bulk Heterojunction Organic Solar Cells. *Adv. Mater.* **2019**, *31*, 1903868.
- (3) Zhao, H.; Naveed, H. B.; Lin, B.; Zhou, X.; Yuan, J.; Zhou, K.; Wu, H.; Guo, R.; Scheel, M. A.; Chumakov, A.; et al. Hot Hydrocarbon-Solvent Slot-Die Coating Enables High-Efficiency Organic Solar Cells with Temperature-Dependent Aggregation Behavior. *Adv. Mater.* **2020**, *32*, 2002302.
- (4) Ma, W.; Yang, C.; Gong, X.; Lee, K.; Heeger, A. J. Thermally Stable, Efficient Polymer Solar Cells with Nanoscale Control of the Interpenetrating Network Morphology. *Adv. Funct. Mater.* **2005**, *15*, 1617–1622.
- (5) Dang, M. T.; Hirsch, L.; Wantz, G.; Wuest, J. D. Controlling the Morphology and Performance of Bulk Heterojunctions in Solar Cells. Lessons Learned from the Benchmark Poly(3-Hexylthiophene):[6,6]-Phenyl-C61-Butyric Acid Methyl Ester System. *Chem. Rev.* **2013**, *113*, 3734–3765.
- (6) Liu, Y.; Zhao, J.; Li, Z.; Mu, C.; Ma, W.; Hu, H.; Jiang, K.; Lin, H.; Ade, H.; Yan, H. Aggregation and Morphology Control Enables Multiple Cases of High-Efficiency Polymer Solar Cells. *Nat. Commun.* **2014**, *5*, 5293.
- (7) Dou, F.; Buchaca-Domingo, E.; Sakowicz, M.; Rezasoltani, E.; McCarthy-Ward, T.; Heeney, M.; Zhang, X.; Stingelin, N.; Silva, C. The Effect of Phase Morphology on the Nature of Long-Lived Charges in Semiconductor Polymer:Fullerene Systems. *J. Mater. Chem. C* **2015**, *3*, 3722–3729.
- (8) Lu, L.; Zheng, T.; Wu, Q.; Schneider, A. M.; Zhao, D.; Yu, L. Recent Advances in Bulk Heterojunction Polymer Solar Cells. *Chem. Rev.* **2015**, *115*, 12666–12731.
- (9) Mazzi, K. A.; Luscombe, C. K. The Future of Organic Photovoltaics. *Chem. Soc. Rev.* **2015**, *44*, 78–90.
- (10) Scarongella, M.; De Jonghe-Risse, J.; Buchaca-Domingo, E.; Causá, M.; Fei, Z.; Heeney, M.; Moser, J.-E.; Stingelin, N.; Banerji, N. A Close Look at Charge Generation in Polymer:Fullerene Blends with Microstructure Control. *J. Am. Chem. Soc.* **2015**, *137*, 2908–2918.
- (11) Pelzer, K. M.; Darling, S. B. Charge Generation in Organic Photovoltaics: A Review of Theory and Computation. *Molecular Systems Design & Engineering* **2016**, *1*, 10–24.
- (12) Huang, Y.; Kramer, E. J.; Heeger, A. J.; Bazan, G. C. Bulk Heterojunction Solar Cells: Morphology and Performance Relationships. *Chem. Rev.* **2014**, *114*, 7006–7043.
- (13) Moseguí González, D.; Schaffer, C. J.; Pröllner, S.; Schlipf, J.; Song, L.; Bernstorff, S.; Herzig, E. M.; Müller-Buschbaum, P. Codependence between Crystalline and Photovoltage Evolutions in P3ht:Pcbm Solar Cells Probed with in-Operando Giwaxs. *ACS Appl. Mater. Interfaces* **2017**, *9*, 3282–3287.
- (14) Albrecht, S.; Vandewal, K.; Tumbleston, J. R.; Fischer, F. S. U.; Douglas, J. D.; Fréchet, J. M. J.; Ludwigs, S.; Ade, H.; Salleo, A.; Neher, D. On the Efficiency of Charge Transfer State Splitting in Polymer:Fullerene Solar Cells. *Adv. Mater.* **2014**, *26*, 2533–2539.
- (15) Sini, G.; Schubert, M.; Risko, C.; Roland, S.; Lee, O. P.; Chen, Z.; Richter, T. V.; Dolfen, D.; Coropceanu, V.; Ludwigs, S.; et al. On the Molecular Origin of Charge Separation at the Donor-Acceptor Interface. *Adv. Energy Mater.* **2018**, *8*, 1702232.
- (16) Chang, J.-F.; Sun, B.; Breiby, D. W.; Nielsen, M. M.; Sölling, T. I.; Giles, M.; McCulloch, I.; Sirringhaus, H. Enhanced Mobility of Poly(3-Hexylthiophene) Transistors by Spin-Coating from High-Boiling-Point Solvents. *Chem. Mater.* **2004**, *16*, 4772–4776.
- (17) Khan, A. L. T.; Sreearunothai, P.; Herz, L. M.; Banach, M. J.; Köhler, A. Morphology-Dependent Energy Transfer within Polyfluorene Thin Films. *Phys. Rev. B: Condens. Matter Mater. Phys.* **2004**, *69*, 085201.
- (18) Clark, J.; Chang, J.-F.; Spano, F. C.; Friend, R. H.; Silva, C. Determining Exciton Bandwidth and Film Microstructure in

Polythiophene Films Using Linear Absorption Spectroscopy. *Appl. Phys. Lett.* **2009**, *94*, 163306.

- (19) Park, Y. D.; Lee, H. S.; Choi, Y. J.; Kwak, D.; Cho, J. H.; Lee, S.; Cho, K. Solubility-Induced Ordered Polythiophene Precursors for High-Performance Organic Thin-Film Transistors. *Adv. Funct. Mater.* **2009**, *19*, 1200–1206.
- (20) Perez, L. A.; Chou, K. W.; Love, J. A.; van der Poll, T. S.; Smilgies, D.-M.; Nguyen, T.-Q.; Kramer, E. J.; Amassian, A.; Bazan, G. C. Solvent Additive Effects on Small Molecule Crystallization in Bulk Heterojunction Solar Cells Probed During Spin Casting. *Adv. Mater.* **2013**, *25*, 6380–6384.
- (21) McDowell, C.; Abdelsamie, M.; Zhao, K.; Smilgies, D.-M.; Bazan, G. C.; Amassian, A. Synergistic Impact of Solvent and Polymer Additives on the Film Formation of Small Molecule Blend Films for Bulk Heterojunction Solar Cells. *Adv. Energy Mater.* **2015**, *5*, 1501121.
- (22) Reichenberger, M.; Baderschneider, S.; Kroh, D.; Grauf, S.; Köhler, J.; Hildner, R.; Köhler, A. Watching Paint Dry: The Impact of Diiodooctane on the Kinetics of Aggregate Formation in Thin Films of Poly(3-Hexylthiophene). *Macromolecules* **2016**, *49*, 6420–6430.
- (23) Buchhorn, M.; Wedler, S.; Panzer, F. Setup to Study the In Situ Evolution of Both Photoluminescence and Absorption During the Processing of Organic or Hybrid Semiconductors. *J. Phys. Chem. A* **2018**, *122*, 9115–9122.
- (24) Reichenberger, M.; Kroh, D.; Matrone, G. M. M.; Schötz, K.; Pröller, S.; Filonik, O.; Thordardottir, M. E.; Herzig, E. M.; Bäessler, H.; Stingelin, N.; et al. Controlling Aggregate Formation in Conjugated Polymers by Spin-Coating Below the Critical Temperature of the Disorder-Order Transition. *J. Polym. Sci., Part B: Polym. Phys.* **2018**, *56*, 532–542.
- (25) Kim, D. H.; Park, Y. D.; Jang, Y.; Kim, S.; Cho, K. Solvent Vapor-Induced Nanowire Formation in Poly(3-Hexylthiophene) Thin Films. *Macromol. Rapid Commun.* **2005**, *26*, 834–839.
- (26) Pröller, S.; Moseguí González, D.; Zhu, C.; Schaible, E.; Wang, C.; Müller-Buschbaum, P.; Hexemer, A.; Herzig, E. M. Note: Setup for Chemical Atmospheric Control During in Situ Grazing Incidence X-Ray Scattering of Printed Thin Films. *Rev. Sci. Instrum.* **2017**, *88*, 066101.
- (27) Na, J. Y.; Kang, B.; Sin, D. H.; Cho, K.; Park, Y. D. Understanding Solidification of Polythiophene Thin Films During Spin-Coating: Effects of Spin-Coating Time and Processing Additives. *Sci. Rep.* **2015**, *5*, 13288.
- (28) Köhler, A.; Hoffmann, S. T.; Bäessler, H. An Order–Disorder Transition in the Conjugated Polymer MeH-Ppv. *J. Am. Chem. Soc.* **2012**, *134*, 11594–11601.
- (29) Panzer, F.; Sommer, M.; Bäessler, H.; Thelakkat, M.; Köhler, A. Spectroscopic Signature of Two Distinct H-Aggregate Species in Poly(3-Hexylthiophene). *Macromolecules* **2015**, *48*, 1543–1553.
- (30) Scharsich, C.; Fischer, F. S. U.; Wilma, K.; Hildner, R.; Ludwigs, S.; Köhler, A. Revealing Structure Formation in Pcpdtbt by Optical Spectroscopy. *J. Polym. Sci., Part B: Polym. Phys.* **2015**, *53*, 1416–1430.
- (31) Reichenberger, M.; Love, J. A.; Rudnick, A.; Bagnich, S.; Panzer, F.; Stradomska, A.; Bazan, G. C.; Nguyen, T.-Q.; Köhler, A. The Effect of Intermolecular Interaction on Excited States in P-Dts(Fbth2)2. *J. Chem. Phys.* **2016**, *144*, 074904.
- (32) Panzer, F.; Bäessler, H.; Köhler, A. Temperature Induced Order–Disorder Transition in Solutions of Conjugated Polymers Probed by Optical Spectroscopy. *J. Phys. Chem. Lett.* **2017**, *8*, 114–125.
- (33) Hu, H.; Chow, P. C. Y.; Zhang, G.; Ma, T.; Liu, J.; Yang, G.; Yan, H. Design of Donor Polymers with Strong Temperature-Dependent Aggregation Property for Efficient Organic Photovoltaics. *Acc. Chem. Res.* **2017**, *50*, 2519–2528.
- (34) Jackson, N. E.; Savoie, B. M.; Kohlstedt, K. L.; Olvera de la Cruz, M.; Schatz, G. C.; Chen, L. X.; Ratner, M. A. Controlling Conformations of Conjugated Polymers and Small Molecules: The Role of Nonbonding Interactions. *J. Am. Chem. Soc.* **2013**, *135*, 10475–10483.
- (35) Huang, H.; Yang, L.; Facchetti, A.; Marks, T. J. Organic and Polymeric Semiconductors Enhanced by Noncovalent Conformational Locks. *Chem. Rev.* **2017**, *117*, 10291–10318.
- (36) Seifrid, M. T.; Oosterhout, S. D.; Toney, M. F.; Bazan, G. C. Kinetic Versus Thermodynamic Orientational Preferences for a Series of Isomorphous Molecular Semiconductors. *ACS Omega* **2018**, *3*, 10198–10204.
- (37) Thorley, K. J.; McCulloch, I. Why Are S–F and S–O Non-Covalent Interactions Stabilising? *J. Mater. Chem. C* **2018**, *6*, 12413–12421.
- (38) McDearmon, B.; Page, Z. A.; Chabiny, M. L.; Hawker, C. J. Organic Electronics by Design: The Power of Minor Atomic and Structural Changes. *J. Mater. Chem. C* **2018**, *6*, 3564–3572.
- (39) McDowell, C.; Narayanaswamy, K.; Yadagiri, B.; Gayathri, T.; Seifrid, M.; Datt, R.; Ryno, S. M.; Heifner, M. C.; Gupta, V.; Risko, C.; et al. Impact of Rotamer Diversity on the Self-Assembly of Nearly Isostructural Molecular Semiconductors. *J. Mater. Chem. A* **2018**, *6*, 383–394.
- (40) Abdelsamie, M.; Zhao, K.; Niazi, M. R.; Chou, K. W.; Amassian, A. In Situ Uv-Visible Absorption During Spin-Coating of Organic Semiconductors: A New Probe for Organic Electronics and Photovoltaics. *J. Mater. Chem. C* **2014**, *2*, 3373–3381.
- (41) Güldal, N. S.; Kassar, T.; Berlinghof, M.; Ameri, T.; Osvet, A.; Pacios, R.; Destri, G. L.; Unruh, T.; Brabec, C. J. Real-Time Evaluation of Thin Film Drying Kinetics Using an Advanced, Multi-Probe Optical Setup. *J. Mater. Chem. C* **2016**, *4*, 2178–2186.
- (42) Richter, L. J.; DeLongchamp, D. M.; Amassian, A. Morphology Development in Solution-Processed Functional Organic Blend Films: An In Situ Viewpoint. *Chem. Rev.* **2017**, *117*, 6332–6366.
- (43) Manley, E. F.; Strzalka, J.; Fauvel, T. J.; Marks, T. J.; Chen, L. X. In Situ Analysis of Solvent and Additive Effects on Film Morphology Evolution in Spin-Cast Small-Molecule and Polymer Photovoltaic Materials. *Adv. Energy Mater.* **2018**, *8*, 1800611.
- (44) Lin, B.; Zhou, X.; Zhao, H.; Yuan, J.; Zhou, K.; Chen, K.; Wu, H.; Guo, R.; Scheel, M. A.; Chumakov, A.; et al. Balancing the Pre-Aggregation and Crystallization Kinetics Enables High Efficiency Slot-Die Coated Organic Solar Cells with Reduced Non-Radiative Recombination Losses. *Energy Environ. Sci.* **2020**, *13*, 2467–2479.
- (45) Gierschner, J.; Park, S. Y. Luminescent Distyrylbenzenes: Tailoring Molecular Structure and Crystalline Morphology. *J. Mater. Chem. C* **2013**, *1*, 5818.
- (46) Chauhan, M.; Zhong, Y.; Schötz, K.; Tripathi, B.; Köhler, A.; Huettnner, S.; Panzer, F. Investigating Two-Step Mapbi3 Thin Film Formation During Spin Coating by Simultaneous in Situ Absorption and Photoluminescence Spectroscopy. *J. Mater. Chem. A* **2020**, *8*, 5086–5094.
- (47) Zhou, C.; Cui, Q.; McDowell, C.; Seifrid, M.; Chen, X.; Brédas, J.-L.; Wang, M.; Huang, F.; Bazan, G. C. Topological Transformation of Π -Conjugated Molecules Reduces Resistance to Crystallization. *Angew. Chem.* **2017**, *129*, 9446–9449.
- (48) Wedler, S.; Bourdick, A.; Athanasopoulos, S.; Gekle, S.; Panzer, F.; McDowell, C.; Nguyen, T.-Q.; Bazan, G. C.; Köhler, A. What Is the Role of Planarity and Torsional Freedom for Aggregation in a Π -Conjugated Donor–Acceptor Model Oligomer? *J. Mater. Chem. C* **2020**, *8*, 4944–4955.
- (49) De Leener, C.; Hennebicq, E.; Sancho-Garcia, J.-C.; Beljonne, D. Modeling the Dynamics of Chromophores in Conjugated Polymers: The Case of Poly(2-Methoxy-5-(2'-Ethylhexyl)Oxy 1,4-Phenylene Vinylene) (Meh-Ppv). *J. Phys. Chem. B* **2009**, *113*, 1311–1322.
- (50) Haedler, A. T.; Misslitz, H.; Buehlmeier, C.; Albuquerque, R. Q.; Köhler, A.; Schmidt, H.-W. Controlling the Π -Stacking Behavior of Pyrene Derivatives: Influence of H-Bonding and Steric Effects in Different States of Aggregation. *ChemPhysChem* **2013**, *14*, 1818–1829.
- (51) Yan, M.; Rothberg, L. J.; Kwock, E. W.; Miller, T. M. Interchain Excitations in Conjugated Polymers. *Phys. Rev. Lett.* **1995**, *75*, 1992–1995.

(52) Huang, Y.-s.; Westenhoff, S.; Avilov, I.; Sreearunothai, P.; Hodgkiss, J. M.; Deleener, C.; Friend, R. H.; Beljonne, D. Electronic Structures of Interfacial States Formed at Polymeric Semiconductor Heterojunctions. *Nat. Mater.* **2008**, *7*, 483–489.

(53) Sharma, A.; Athanasopoulos, S.; Tapping, P. C.; Sabatini, R. P.; McRae, O. F.; Müllner, M.; Kee, T. W.; Lakhwani, G. Emission Decay Pathways Sensitive to Circular Polarization of Excitation. *J. Phys. Chem. C* **2018**, *122*, 23910–23916.

(54) Seifrid, M. T.; Reddy, G. N. M.; Zhou, C.; Chmelka, B. F.; Bazan, G. C. Direct Observation of the Relationship between Molecular Topology and Bulk Morphology for a Π -Conjugated Material. *J. Am. Chem. Soc.* **2019**, *141*, 5078–5082.

Supporting Information

On the Role of Torsional Flexibility in the Film Formation Process in Two π -Conjugated Model Oligomers

STEFAN WEDLER¹, CHENG ZHOU², GUILLERMO C. BAZAN², FABIAN PANZER¹, AND ANNA KÖHLER^{*1,3}

¹*Soft Matter Optoelectronics, Experimentalphysik II, University of Bayreuth, Bayreuth 95440, Germany*

²*Departments of Chemistry and Chemical Engineering, National University of Singapore, Singapore, 119077*

³*Bayreuth Institute of Macromolecular Research (BIMF) and Bavarian Polymer Institute (BPI), University of Bayreuth, 95440 Bayreuth, Germany*

*mail: Anna.Koehler@uni-bayreuth.de

1 Experimental Methods

1.1 Sample preparation

The molecules 7,7'-(3,3'-dihexyl-[2,2'-bithiophene]-5,5'-diyl)bis(6-fluoro-4-(5-hexylthiophen-2-yl)benzo[c][1,2,5]thiadiazole) (TT) and 7,7'-(4,4-dihexyl-4H-cyclopenta[2,1-b:3,4-b']dithiophene-2,6-diyl)bis(6-fluoro-4-(5-hexylthiophen-2-yl)benzo[c][1,2,5]thiadiazole) (CT) were synthesized as reported previously,¹ their structures are shown in Figure 1 in the main manuscript. Solutions for spin coating were prepared by dissolving each molecule in hexane to a final concentration of 5 mg ml⁻¹ for CT and 4 mg ml⁻¹ for TT. The solutions were stirred at 150 rpm and heated to 50 °C for 30 min to ensure solvation prior to spin coating. For spin coating, 20 µl of the prepared solution was dropped onto a round Spectrosil B substrate (diameter: 13 mm) and the spin coater was set to 500 rpm for the complete measurement time. It needs 1.0 s to reach the final rotation speed. The substrate temperature was set to room temperature for CT and to 51 °C for TT, which is above the critical temperature for aggregation in both cases as detailed in section 2. For spectroscopic measurements in hexane solution, we used a final concentration of 0.05 mg ml⁻¹ for CT and put the solution in a quartz cuvette with 1.00 mm path length.

1.2 In-situ spectroscopy

Transmission measurements during film formation were performed using a white LED which is placed under the rotating chuck of the spin coater with a bore along the rotation axis. For emission measurements, a 520 nm diode laser was used as excitation source. Both, emission from the sample and transmitted white light, was collected via an optical fiber and guided to the home-built detection system. Absorption and emission measurements were performed alternately after each detection frame. The detection system consists of a chopper wheel with mirrored blades, which creates two independent beam paths for transmission and emission measurements. An optical longpass filter (550 nm cut-off wavelength) was placed in the beam path for emission measurements to remove residual laser light. Both transmission and emission spectra were recorded with the same spectrograph consisting of a CCD camera (Andor iDus) coupled to a monochromator (Oriel). Full technical details can be found in reference². The temporal origin is defined as the start of the rotation of the spin coater. Minor oscillations in the absorption spectra originate from an aliasing effect between the rotation of the spin coater and the sampling frequency for acquisition. This aliasing effect was suppressed by smoothing the discrete Fourier transform in the vicinity of the aliasing frequency (see section 5). All emission spectra are corrected for the transmission of all optical elements as well as changes in absorption at the laser wavelength. The relative photoluminescence quantum yield (PLQY) was determined by integrating the corrected emission intensity for each time step. Comparing the relative PLQY at $t = 0$ s with the PLQY value of a dilute solution yields the absolute PLQY during processing, as all material on the substrate is in solution at that stage. The fraction of aggregates (FoA) was calculated from the absorption spectra by decomposing each spectrum into amorphous and aggregated contributions and comparing their spectral areas after correcting for changes in oscillator strength, as detailed in section 6. Color codes developed by Fabio Cramer³ were used in 2D heat maps to prevent visual distortion of the data.

2 Critical temperature for aggregation at high concentrations

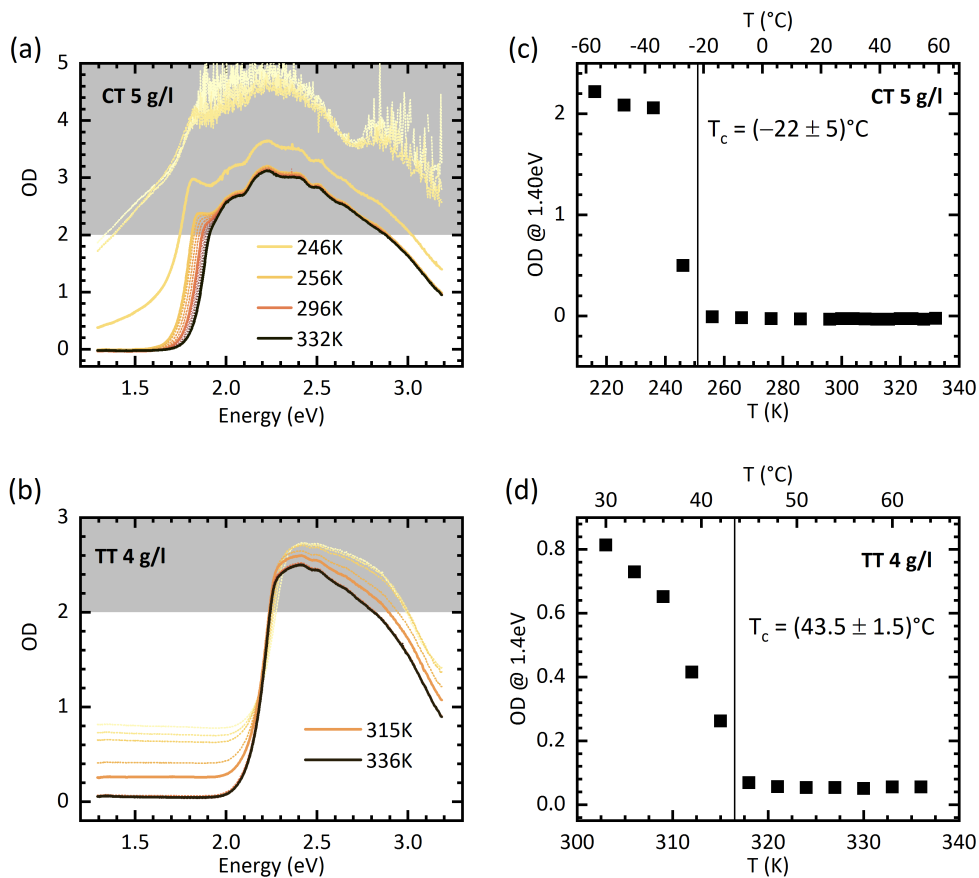


Figure S1: Absorbance spectra for (a) CT and (b) TT in hexane at high concentrations. The spectra were recorded using a quartz glass cuvette with a path length of 1.00 mm and a homebuilt setup.⁴ For CT, the spectra were recorded in steps of 4 K (10 K) above (below) 296 K, for TT the spectra were measured in steps of 3 K. The gray region corresponds to optical density values, where the detector saturates. The evolution of the optical density at the energy of 1.40 eV as a function of temperature is shown in (c) for CT and (d) for TT. It is a measure for scattering and is used for determining the critical temperature for the disorder-order-transition.

3 Absorption of CT during spin casting without baseline

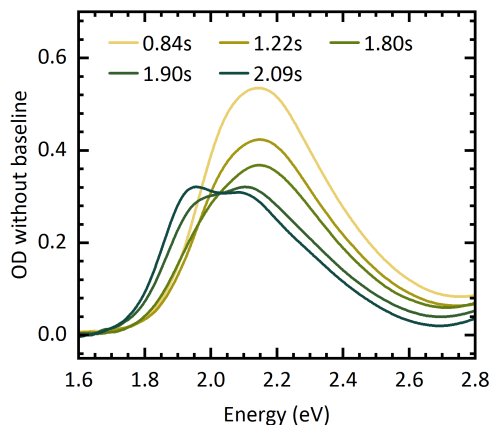


Figure S2: Absorption spectra of CT film during processing (Figure 2b from main manuscript) after subtracting a constant baseline. The isosbestic point is still present, but shifted to 2.03 eV.

4 Full absorption and emission of CT during spin casting

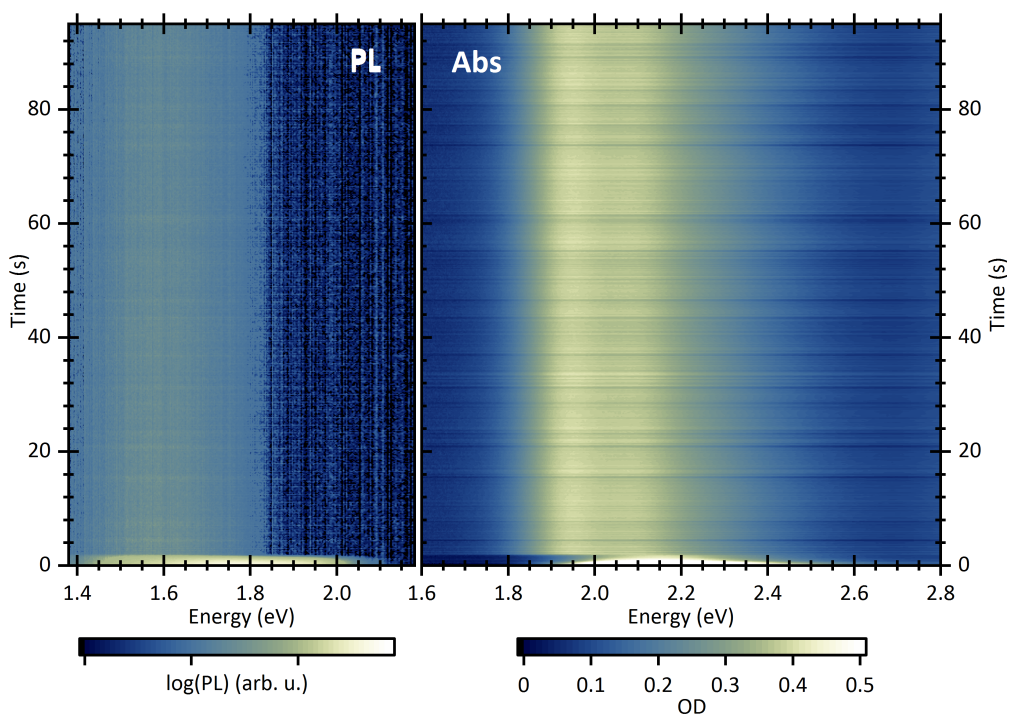


Figure S3: Absorption and emission of the CT film during spin casting for processing times up to 96 s.

5 Suppression of the aliasing effect for absorption during spin casting

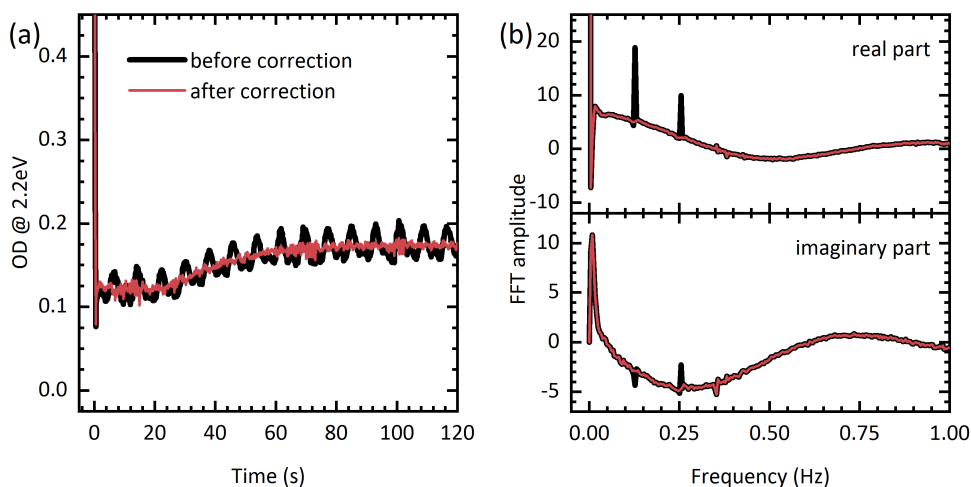


Figure S4: (a) Optical density at 2.2 eV of the TT film from Figure 3 in the main text before and after FFT correction. (b) Corresponding FFT amplitude (top: real part, bottom: imaginary part) before and after correction.

6 Determination of the fraction of aggregates during processing

We calculate the fraction of aggregates (FoA) following the approach of Clark et al.⁵, which has been successfully applied to many organic semiconductor materials.^{6–12} The basic idea is that the absorption spectrum consists of two separate contributions from amorphous chromophores and aggregated chromophores. It is further assumed that there is a direct transformation from one phase into the other phase. This is indicated by an isosbestic point, which corresponds to the photon energy where the extinction coefficient for both phases is equal.

The fraction of aggregates can be calculated by the fraction of the absorption, which is made up from the aggregated phase after correcting for relative changes in oscillator strength F . It can be calculated by the change of aggregate absorption ΔA_{agg} divided by the change of amorphous absorption ΔA_{am} , which is proportional to the ratio of extinction coefficients:

$$F = -\frac{\Delta A_{\text{agg}}}{\Delta A_{\text{am}}} = \frac{\epsilon_{\text{agg}}}{\epsilon_{\text{am}}} \quad (1)$$

The spectrum of the amorphous film for each spin casting experiment was taken as the first spectrum within the temporal range with an isosbestic point. To suppress noise we averaged the first 10 spectra (about 1.0 s), as dynamics are slow. The spectrum of the aggregated species was determined by the scaling method. We averaged the last 20 spectra where film formation was finished and the spectra remained constant. The spectra of the amorphous phase were then multiplied by a factor that they match the high energy side of the final film spectra. The difference between the final film and the scaled amorphous spectrum then yields the spectrum of the aggregated phase. Figure S5 shows this decomposition for TT processed from hexane solution, along with a visualisation of the spectral areas

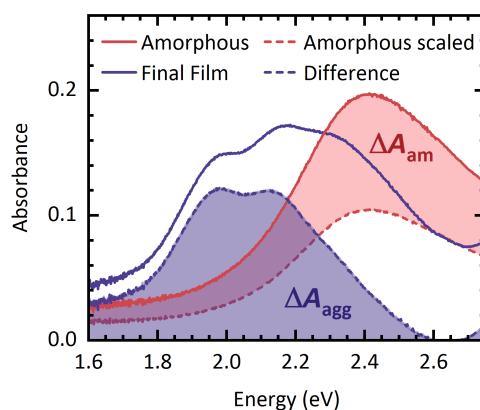


Figure S5: Decomposition of final film absorption into amorphous and aggregated contributions for TT. The spectral areas used for the relative change of oscillator strength are highlighted as well.

needed for the calculation of F . This procedure is impossible for the in situ measurement for the CT film. The evolution of the absorption spectra is too fast to allow for reliable calculation of F .

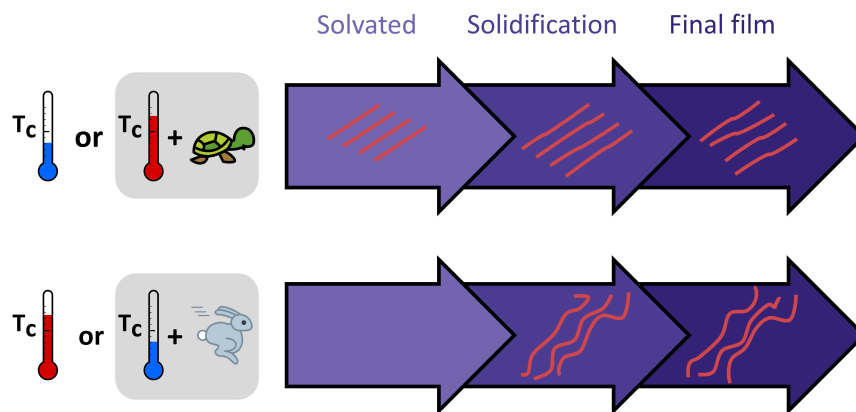
The absorption spectra for each single time step were subsequently separated into amorphous and aggregated contributions using a least-square fit for the linear superposition of both spectral components. This allows to calculate an average F -value from the corresponding integrals of each time step, yielding $F = 0.9 \pm 0.1$. The fraction of aggregates can then be calculated to

$$\text{FoA}(t) = \frac{A_{\text{agg}}(t)}{A_{\text{agg}}(t) + F \cdot A_{\text{am}}(t)} \quad (2)$$

References

- [1] Zhou, C.; Cui, Q.; McDowell, C.; Seifrid, M.; Chen, X.; Brédas, J.-L.; Wang, M.; Huang, F.; Bazan, G. C. Topological Transformation of π -Conjugated Molecules Reduces Resistance to Crystallization. *Angew. Chem.* **2017**, *129*, 9446–9449.
- [2] Buchhorn, M.; Wedler, S.; Panzer, F. Setup to Study the in Situ Evolution of Both Photoluminescence and Absorption during the Processing of Organic or Hybrid Semiconductors. *J. Phys. Chem. A* **2018**, *122*, 9115–9122.
- [3] Cramer, F. Geodynamic Diagnostics, Scientific Visualisation and StagLab 3.0. *Geosci. Model Dev.* **2018**, *11*, 2541–2562.
- [4] Wedler, S.; Bourdick, A.; Athanasopoulos, S.; Gekle, S.; Panzer, F.; McDowell, C.; Nguyen, T.-Q.; Bazan, G. C.; Köhler, A. What Is the Role of Planarity and Torsional Freedom for Aggregation in a π -Conjugated Donor–Acceptor Model Oligomer? *J. Mater. Chem. C* **2020**, *8*, 4944–4955.
- [5] Clark, J.; Chang, J.-F.; Spano, F. C.; Friend, R. H.; Silva, C. Determining Exciton Bandwidth and Film Microstructure in Polythiophene Films Using Linear Absorption Spectroscopy. *Appl. Phys. Lett.* **2009**, *94*, 163306.
- [6] Panzer, F.; Bässler, H.; Köhler, A. Temperature Induced Order–Disorder Transition in Solutions of Conjugated Polymers Probed by Optical Spectroscopy. *J. Phys. Chem. Lett.* **2017**, *8*, 114–125.
- [7] Perevedentsev, A.; Chander, N.; Kim, J.-S.; Bradley, D. D. C. Spectroscopic Properties of Poly(9,9-Dioctylfluorene) Thin Films Possessing Varied Fractions of β -Phase Chain Segments: Enhanced Photoluminescence Efficiency via Conformation Structuring. *J. Polym. Sci. Pol. Phys.* **2016**, *54*, 1995–2006.
- [8] Reichenberger, M.; Love, J. A.; Rudnick, A.; Bagnich, S.; Panzer, F.; Stradomska, A.; Bazan, G. C.; Nguyen, T.-Q.; Köhler, A. The Effect of Intermolecular Interaction on Excited States in p - DTS(FBTTH2)2. *J. Chem. Phys.* **2016**, *144*, 074904.
- [9] Reichenberger, M.; Baderschneider, S.; Kroh, D.; Grauf, S.; Köhler, J.; Hildner, R.; Köhler, A. Watching Paint Dry: The Impact of Diiodooctane on the Kinetics of Aggregate Formation in Thin Films of Poly(3-Hexylthiophene). *Macromolecules* **2016**, *49*, 6420–6430.
- [10] Scharsich, C.; Lohwasser, R. H.; Sommer, M.; Asawapirom, U.; Scherf, U.; Thelakkat, M.; Neher, D.; Köhler, A. Control of Aggregate Formation in Poly(3-Hexylthiophene) by Solvent, Molecular Weight, and Synthetic Method. *J. Polym. Sci. Pol. Phys.* **2012**, *50*, 442–453.
- [11] Scharsich, C.; Fischer, F. S. U.; Wilma, K.; Hildner, R.; Ludwigs, S.; Köhler, A. Revealing Structure Formation in PCPDTBT by Optical Spectroscopy. *J. Polym. Sci. Pol. Phys.* **2015**, *53*, 1416–1430.
- [12] Unger, T.; Panzer, F.; Consani, C.; Koch, F.; Brixner, T.; Bässler, H.; Köhler, A. Ultrafast Energy Transfer between Disordered and Highly Planarized Chains of Poly[2-Methoxy-5-(2-Ethylhexyloxy)-1,4-Phenylenevinylene] (MEH-PPV). *ACS Macro Lett.* **2015**, *4*, 412–416.

10 Processing condition dependent aggregation pathways in conjugated polymers



Matthew J Dyson, Hazem Bakr, Stefan Wedler, Konstantin Schötz, Mihirsinh Chauhan, Paul N Stavrinou, Natalie Stingelin, Anna Köhler, and Fabian Panzer

In preparation.

Processing condition dependent aggregation pathways in conjugated polymers

*Matthew J Dyson, Hazem Bakr, Stefan Wedler, Konstantin Schötz, Mihirsinh Chauhan, Paul N Stavrinou, Natalie Stingelin, Anna Köhler, Fabian Panzer**

Matthew J Dyson

Molecular Materials and Nanosystems and Institute for Complex Molecular Systems, Eindhoven University of Technology, 5600 MB Eindhoven (The Netherlands)

Stefan Wedler, Hazem Bakr, Mihirsinh Chauhan, Konstantin Schötz, Anna Köhler, Fabian Panzer
Soft Matter Optoelectronics, University of Bayreuth, Bayreuth 95440 (Germany)

Paul N Stavrinou

Department of Engineering Science, University of Oxford, Oxford, OX1 3PJ (UK)

Natalie Stingelin

School of Materials Science & Engineering and School of Chemical & Biomolecular Engineering, Georgia Institute of Technology, Atlanta, Georgia 30332 (USA)

Abstract

Achieving reproducible optoelectronic devices using solution processed conjugated polymers can be extremely challenging, with small or even imperceptible processing condition variations causing changes in absorption and emission spectra as well as charge mobility. Here, we demonstrate the role of both polymer solubility and solvent evaporation rate in determining the conjugated polymer aggregate formation mechanism and hence the optoelectronic property determining local chain arrangement. This is achieved by using concurrent in situ absorption and photoluminescence (PL) spectroscopy during film formation of prototypical poly(3-hexylthiophene-2,5-diyl) (P3HT) films to establish the temporal evolution of inter/intra-molecular coupling and energetic site disorder over time. Reduced solubility and slower solvent evaporation promote aggregate formation within the solution, providing greater steric freedom and hence reduced energetic and torsional disorder. In contrast, high solubility and rapid evaporation promote concentration induced aggregation, associated with more disordered chain arrangements. This conceptual framework explains many previously disparate processing-structure-property observations, and can be employed to guide processing parameter selection to increase the robustness of conjugated polymer film properties to variation in deposition conditions.

1. Introduction

The sensitivity of conjugated polymer local chain arrangement to solution processing conditions¹⁻⁴ can be a mixed blessing. This is because the desirable ability to fine tune properties such as charge mobility^{5,6} and emission/absorption⁷⁻¹⁰ is often offset by time-consuming microstructural optimisation, yet it is decisive to achieve efficient organic optoelectronic devices.¹¹ The morphology of conjugated polymer thin films typically consists of amorphous domains with disordered chain alignment, as well as aggregated domains with better chain ordering.^{1,12} The latter play a crucial role for e.g. charge separation or charge transport,^{9,13} and are thus important for efficient organic devices. Solution processing of conjugated polymers allows to tune the overall film morphology in versatile ways by adjusting processing parameters, which however, also complicates transitioning from film deposition via spin-coating to large-area compatible methods.^{14,15} Fundamentally understanding structure-property relationships during processing is thus a central challenge in scaling up conjugated polymer devices for printable applications such as organic photovoltaics,¹⁶ light emitting diodes,¹⁷ field effect transistors¹⁸ and photodetectors.¹⁹ In this respect the impact of single processing parameters such as substrate temperature,²⁰ solvent polarity²¹ and solvent evaporation rate²² on the aggregate formation mechanism was investigated individually,

while considering them together (as they are indeed coupled) to better understand film formation dynamics has received surprisingly little attention so far. In contrast, the steady state properties of aggregates, e.g. of final thin films, or in solution using a bad solvent, were investigated in detail in the past. Here, powerful models were derived, allowing to gain insight into the local chain arrangement of aggregates based on their absorption and emission properties.^{8,10,23–27} Even though the evolution of aggregates during processing was repeatedly investigated using different in situ methods,^{3,28–34} these powerful models were not yet applied to optical data measured in situ during aggregate formation. Furthermore, a generalisable framework that explains the influence of multiple processing conditions on the aggregate properties remains unestablished.

Here, we in detail investigate the aggregate formation mechanism of the model conjugated polymer poly(3-hexylthiophene-2,5-diyl) (P3HT) during blade coating by simultaneous in situ absorbance and photoluminescence (PL) spectroscopy, thoroughly analysed by modified Franck Condon models. Systematically varying both substrate temperature and solvent allows to clarify the impact of different processing conditions (i.e., solvent evaporation rate, solvent atmosphere and polymer solubility) on formation dynamics and optical properties of the aggregates. With that we can identify different aggregate species and aggregate formation pathways, which can be influenced by changing processing parameters. From our results it becomes clear that not only solubility determines the film formation process, but that timing in the sub second time range can tip the scales regarding which aggregate formation pathway is taken.

2. Results

2.1. Extracting Microstructural Insight from Optical Spectra

We begin by briefly reviewing typical optical signatures of measured absorption and PL spectra of conjugated polymers such as P3HT (Figure 1). As mentioned above, aggregated and amorphous domains often coexist,^{1,12,35} so that also the optical spectra are a superposition of the individual contributions. Aggregates have short-range order, which may extend over a few chains,³⁵ with constituent chains electronically coupled via π - π stacking.³⁶ This coupling alters the shape and reduces the energetic position of the aggregate spectra.³⁷ To extract the spectral contribution of the neat aggregated phase from the total measured spectra in both absorbance and PL, a non-aggregated (e.g., solution) spectrum is rescaled to match the high energy edge of the measured spectrum, and then subtracted (Figure 1).⁹

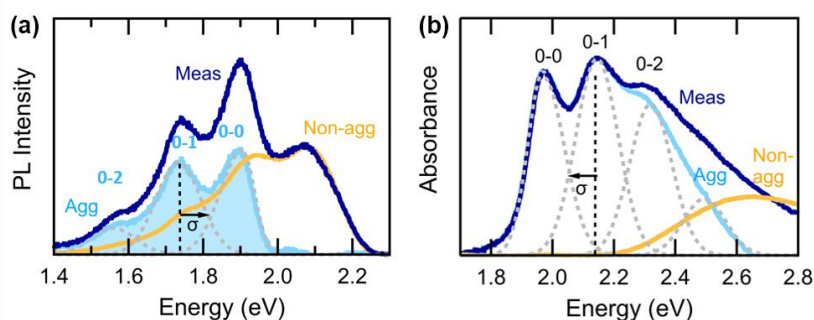


Figure 1: Decoupling spectral contributions. Measured spectra (dark blue) of PL (a) and absorption (b) containing contributions from aggregated and disordered phase. Subtracting the non-aggregated spectral contribution (orange) leaves just the aggregate spectrum (light blue). Fitting the vibronic peaks (dashed grey) allows to determine the 0-0/0-1 peak ratio and peak width σ .

In both absorption and PL, the resulting aggregate-only spectra exhibit a clear vibronic progression of the electronic $S_1 - S_0$ transition, with a peak spacing of ~ 0.175 eV due to coupling with an effective vibrational mode that is dominated by the C=C symmetric stretch.^{25,27} From the resulting neat aggregate spectra it is further possible to extract valuable insights about the electronic structure: Energetic site disorder σ from peak width, the effective bandgap of the participating species from the 0-0 peak location, and the balance between intra and interchain excitonic coupling from the 0-0/0-1 vibronic peak ratio as derived by the so called HJ aggregate model developed by Spano *et al.*^{8,10,23–27} which has been applied especially to P3HT in the past.^{9,10,24,25,27}

2.2. Final Film Processing Condition Dependence – Solubility not the only factor determining aggregation process

Having reiterated how analysing the measured PL and absorption spectra yields information about the local chain arrangement, our next step is to consider how the aggregate formation is influenced by the timings and the solubility of the solvents used. The latter generally determines whether the conjugated polymer in solution adopts a random coil conformation, or, when the solvent quality decreases, the polymer chains undergoes an order-disorder transition and finally aggregates. For our studies we use the solvents chloroform (CF) and tetrahydrofuran (THF), which both have similar boiling points (61.2 °C chloroform, 66 °C THF) and therefore exhibit similar evaporation rates at the same temperature. To determine the differences in solubility, we measure the optical properties of solutions (concentration of 10 mg ml^{-1}) of regioregular P3HT (weight-averaged molecular weight $M_w \approx 100 \text{ kg mol}^{-1}$) dissolved in both

CF and THF over a range of temperatures (Figure S1). Cooling lowers the solubility, and below a certain critical solution temperature $T_{c,solution}$ aggregation occurs, which changes the shape of the optical spectra substantially, with an emerging absorbance peak at ~ 2.0 eV. Tracking the temperature dependence of the (normalized) absorbance intensity at this photon energy exhibits a strong sigmoidal shape, allowing to quantify $T_{c,solution}$ from the point of inflection (Figure 2a). By doing so we obtain $T_{c,solution} = 40$ °C for the more polar THF (see Hansen solubility parameters^{38,39} in Table S1) and $T_{c,solution} = 10$ °C for CF, indicating unequivocally that P3HT is more soluble in CF than in THF.

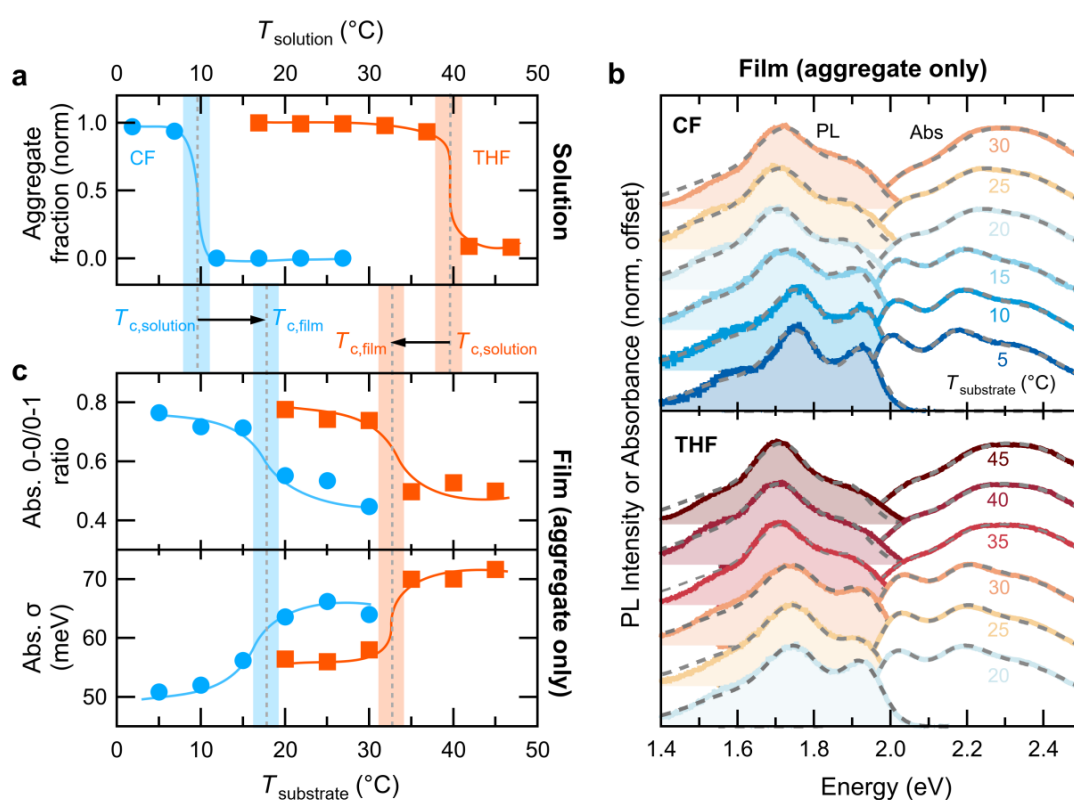


Figure 2: (a) The critical temperature $T_{c,solution}$ at which aggregates form in CF (blue) and THF (orange) solution is determined from UV-vis absorption spectroscopy (Figure S1). (b) Aggregate-only thin film PL (solid) and absorbance (lines) spectra of P3HT films spin-coated from CF (top) and THF (bottom) solution over a range of substrate temperatures (fits dashed, PL excitation energy $E_{ex} = 2.38$ eV). (c) 0-0/0-1 absorbance peak ratios and widths extracted from spectral fits show a critical temperature transition $T_{c,film}$ that does not equal $T_{c,solution}$.

As a next step we blade coated P3HT thin films from CF and THF solutions at different substrate temperatures using the same 10 mg ml⁻¹ solutions than for the solution measurements described above (see Experimental Section in the SI for further information regarding the blade coater setup and processing parameters). Figure 2b shows the PL and absorption spectra of the aggregated phase of P3HT thin films, where the non-aggregated component has been subtracted as outlined in Figure 1. Crucially, relative humidity was kept below 20 % to prevent atmospheric moisture condensation at $T_{\text{substrate}} < 15$ °C. The substrate temperatures were chosen to ensure temperatures below and also above the individual $T_{c,\text{solution}}$ of both solvents (5 to 30 °C for CF and 20 to 45 °C for THF). While all absorbance and PL aggregate spectra show the characteristic Franck-Condon vibronic progression for P3HT,^{9,25,27} there is a clear dependence of spectral lineshape on $T_{\text{substrate}}$ for both solvents. Considering the films coated from CF, there is little variation in spectral shape between films with $T_{\text{substrate}} \geq 20$ °C. However, at $T_{\text{substrate}} \leq 15$ °C, the 0-0/0-1 vibronic peak ratio increases, and the spectra become more structured. A similar trend in spectral properties can be seen for films coated from THF solution, although here the transition in spectral shape occurs between 30 and 35 °C.

To quantify these trends, we fit the aggregate-only PL spectra using a previously established modified Franck-Condon progression with a variable 0-0 peak (coefficient α),²⁵ specifically

$$PL(E) \propto E^3 \left[\alpha \exp\left(\frac{(E - E_0)^2}{2\sigma^2}\right) + \sum_{m=1}^{m=3} \frac{S_{\text{eff}}^m}{m!} \exp\left(-\frac{(E - (E_0 - mE_{\text{vib}}))^2}{2(\sigma + m \cdot \Delta\sigma)^2}\right) \right]. \quad (1)$$

Here E is energy, E_0 the energetic location of the vibrationless 0-0 peak, m peak number, σ peak width, and E_{vib} the effective mode energy with a fixed Huang-Rhys factor $S_{\text{eff}} = 1$.²⁰ In contrast, aggregate-only absorbance spectra are fitted with peaks of equal width and spacing but independent amplitudes A_m , specifically

$$Abs(E) = E \sum_{m=0}^{m=3} A_m \exp\left(-\frac{(E - (E_0 + mE_{\text{vib}}))^2}{2(\sigma + m \cdot \Delta\sigma)^2}\right). \quad (2)$$

The refractive index that usually appears with the same power as the energy in the prefactors is neglected for simplicity.⁴⁰ This comparatively simple model was preferred to a modified and more complicated Franck-Condon progression used in the past,^{27,41} since imperfect subtraction of the non-aggregated component, the presence of multiple types of aggregated species,⁴² and scattering losses may cause deviation from a more tightly defined function. Nonetheless, our approach still ensures extraction of all

relevant parameters, such as σ and the 0-0/0-1 ratio, and is sufficient for subsequent qualitative interpretation. Furthermore, and unlike previous studies,^{25,42} we also introduce a peak broadening term $m \cdot \Delta\sigma$ in equation 1 and 2. This term takes into account an obvious broadening of the peaks with higher vibronic transitions m , which is due to the overlap of vibronic modes with similar energies.⁴³ For most π -conjugated materials this effect plays a role, as it typically affects the most intense vibronic modes in the range between 1300 and 1600 cm^{-1} , associated with C-C, C=C stretching modes and ring breathing modes.⁴⁴⁻⁴⁹ Our comparably simple modification of the effective-mode Franck-Condon approach leads to considerable improvements of the fitting quality and allows for more reliable extraction of the fitting parameters. A more detailed discussion about our approach can be found in the Supporting Information (Figure S2).

Figure 2c shows the extracted 0-0/0-1 peak ratio and energetic site disorder σ (both from absorption) for the different $T_{\text{substrate}}$, where we observe a decrease of the 0-0/0-1 ratio from ~ 0.75 to around 0.5 with increasing $T_{\text{substrate}}$ for both solvents. Concomitantly the peak width σ increases from ~ 50 meV to ~ 65 meV for CF and from ~ 55 meV to ~ 70 meV for THF. Interestingly, the temperature dependence of the 0-0/0-1 ratio and σ clearly show a sigmoidal shape. Similar to the quantification of $T_{\text{c,solution}}$, we assign the inflexion point as a critical transition temperature $T_{\text{c,film}}$, where we obtain $T_{\text{c,film}} = \sim 17.5$ °C for CF and $T_{\text{c,film}} = \sim 32.5$ °C for THF. Thus it is possible to identify a critical temperature for both solutions and for films cast from each solvent. When processing above $T_{\text{c,film}}$, the aggregate spectra of the finished films have a lower 0-0/0-1 ratio and higher σ compared to processing below $T_{\text{c,film}}$. This result is in line with our previous work, where we found that $T_{\text{substrate}}$ during spin coating clearly impacts the optical properties of the final films of various conjugated polymers.²⁰

Similar with the considerations in the case of solution aggregation, also in the case of thin film properties $T_{\text{c,film}}$ of CF is lower than $T_{\text{c,film}}$ of THF. However, the direct comparison between the results in case of the steady state solution aggregation (Figure 2a) and the aggregates formed in the thin films (Figure 2c) shows that $T_{\text{c,solution}}$ deviates from the critical temperatures $T_{\text{c,film}}$ by about 10 °C. Interestingly the deviations appear towards both, higher, and lower temperatures specifically, $T_{\text{c,film}} > T_{\text{c,solution}}$ for CF but $T_{\text{c,film}} < T_{\text{c,solution}}$ for THF. This suggests that solubility is not the only relevant parameter which impacts on the precise properties of the aggregates formed from solution processed P3HT thin films. To understand the deviations in the critical temperatures it is thus necessary to, apart from the steady state optical properties of the final films, also consider and investigate the evolution of optical properties during film formation.

2.3. In situ Spectroscopy well Above and well Below $T_{c, solution}$ –identification of solution aggregation and concentration quenched aggregation pathways

We thus measured concurrent in situ absorbance and PL spectroscopy⁵⁰ (see Experimental Section in SI) and track how spectra evolve during film formation. Figure 3 shows example sets of in situ spectra for P3HT blade-coated from CF solution at $T_{substrate} = 5$ and 25 °C, i.e. at $T_{substrate}$ well below $T_{c, film}$ and $T_{substrate}$ well above $T_{c, film}$, respectively. The top left panel shows measured individual absorbance spectra, while the top right panel shows corresponding PL. For both absorbance and PL the initial spectrum is shaded pale orange, due to the presence of solvated, non-aggregated random coils (see Figure 1),⁹ while subsequent spectra are progressively darker blue. Rescaling and subtracting the spectral component from non-aggregated chains leaves just the aggregated component, shown in the bottom panels. Especially in the case of PL, decomposing the in situ measured spectra in contributions of aggregated and disordered phase is crucial. This is because the contribution from aggregated chains is almost entirely obscured by emission from non-aggregated chains, as the latter have a much higher photoluminescence quantum efficiency (PLQE) due to the lack of aggregation induced PL quenching.⁵¹ Furthermore, we corrected the aggregate-only PL spectra by dividing each spectra by the absorption (equal to $1 - 10^{-Absorbance}$, reflection is neglected) at the PL excitation energy $E_{ex} = 2.38$ eV (520 nm), meaning that the the PL spectral integral approximates the relative PLQE.

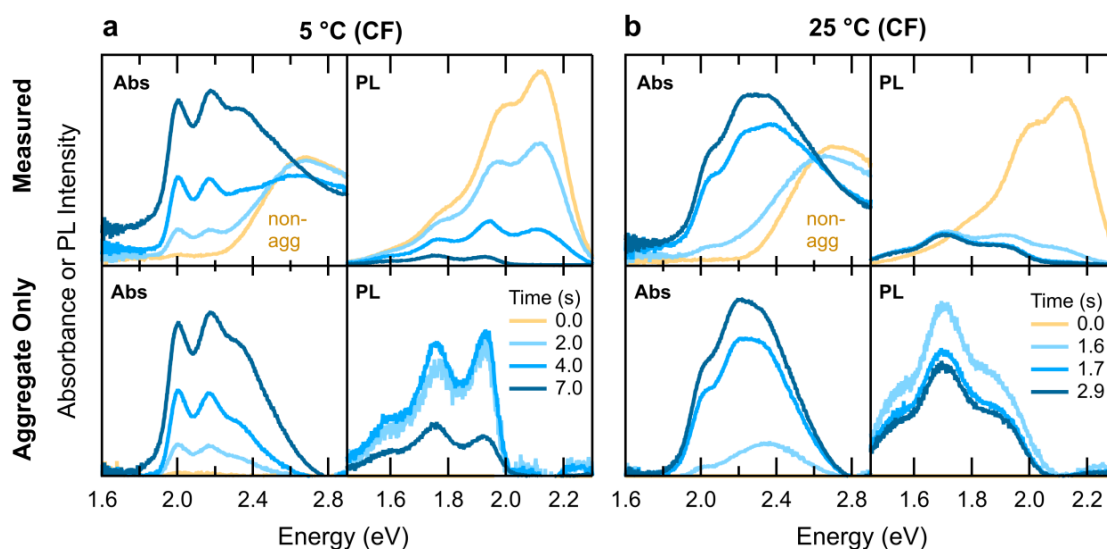


Figure 3: In situ spectroscopy. Measured (top) and aggregate-only (bottom) spectra for $T_{substrate} \approx 5$ °C (a) and 25 °C (b) deposited from CF solution, thus lying below and above $T_{c, film}$. Darker blues indicate longer times. The initial non-aggregated spectrum (pale orange) is first normalised to overlap the measured spectra, then subtracted to leave the aggregate spectra (see Figure 1).

For both substrate temperatures in Figure 3 we observe a clear transition from initial spectra associated with non-aggregated chains (maxima at ~ 2.7 and ~ 2.1 eV in absorbance and PL, respectively) at early times of the processing, to the final spectra that are dominated by aggregated chains with signatures at lower energies (0-0 peaks at ~ 2.0 and ~ 1.9 eV in absorbance and PL, respectively) for the final times. However, the vibronic structure (0-0 and 0-1 peaks at ~ 1.95 and ~ 2.1 eV in absorbance, ~ 1.9 and ~ 1.75 eV in PL) is clearly more pronounced at $T_{\text{substrate}} = 5$ °C, and has a higher 0-0/0-1 peak ratio. Also, the total film formation time t_{final} , that is the time until no significant changes in the optical spectra are observed anymore, decreases from 6.4 s at $T_{\text{substrate}} = 5$ °C to 1.9 s at $T_{\text{substrate}} = 25$ °C. Interestingly we also observe that the intensity of the aggregate PL first increases to a certain maximum intensity before it eventually decreases in the course of processing, where this effect is more pronounced at lower substrate temperatures. To investigate the differences in the aggregate formation process in more detail we fitted each PL and absorbance spectrum using Equation 1 and 2, respectively (see Figures S3 and S4 for details).

Figure 4 shows the same in situ aggregate-only PL and absorbance spectra as in Figure 3, plotted as 2D heat maps, together with the evolution of relevant fit parameters. We extract the evolution of the amount of aggregates from the absorption integral and the relative PL intensity, the 0-0/0-1 vibronic peak ratios and the peak widths σ from both absorption and PL. For $T_{\text{substrate}} = 5$ °C (Figure 4a), aggregate formation begins almost immediately after starting blade coating, which becomes clear from the evolution of aggregate intensity. The amount of aggregates increases continuously within the first 6.4 s, with a clearly steeper slope after 5.2 s. Concomitantly to the presence of aggregate absorption, a clear aggregate PL signal is observed, which exhibits a maximum after about 3.0 s, followed by a decrease to 35 % of the maximum value, with a more pronounced drop of intensity during 5.3 – 6.4 s. Turning to the evolution of the 0-0/0-1 ratio, we observe a value of ~ 0.8 in absorption at the beginning of blade coating, which decreases to 0.74 until 5.3 s, followed by a slight increase to ~ 0.77 after 6.4 s. Similar to absorption but at lower values, the 0-0/0-1 PL ratio decreases gradually from 0.64 to 0.53 within the first 5.4 s. However, opposite to the behavior in absorption, the 0-0/0-1 PL ratio exhibits a clear steepening of the reduction in 0-0/0-1 ratio starting from 5.4 s until 6.4 s, where a final value of 0.40 is reached. The linewidth σ from absorption is constant within the first 5.4 s with a value of 45 meV, while σ from PL continuously decreases from 53 at ~ 1 s to 45 meV at 5.4 s. Thereafter, σ of both absorption and PL increases until 6.4 s, reaching 51 meV in absorption and 47 meV in PL.

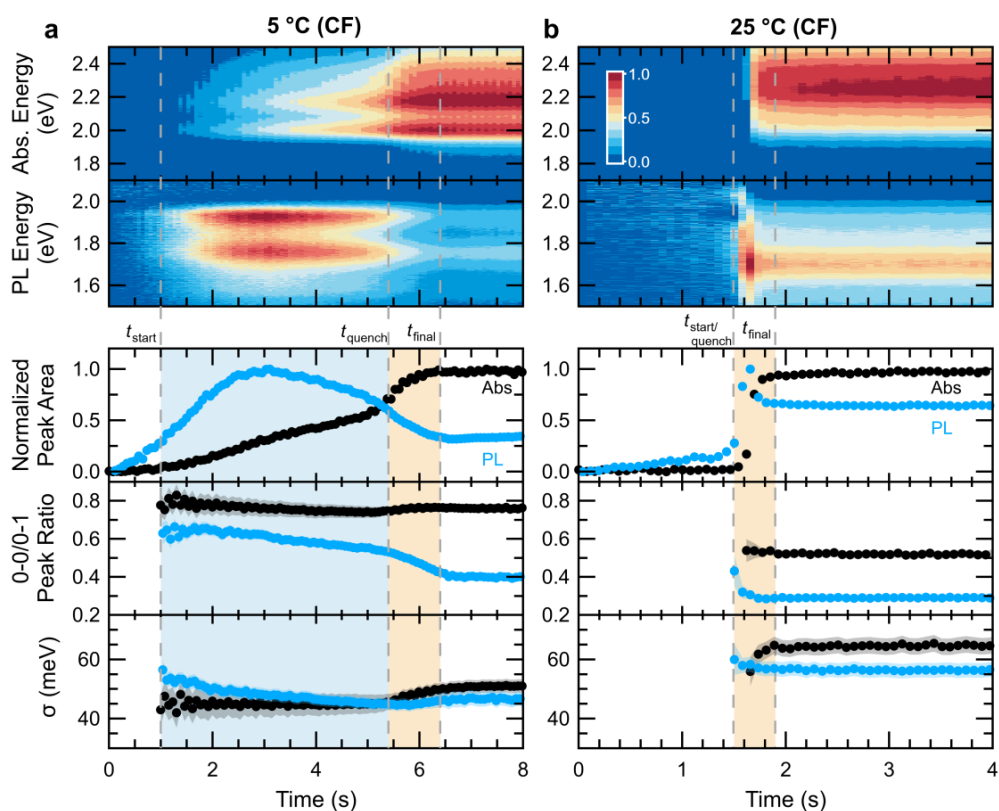


Figure 4: Tracking spectral evolution at $T_{\text{substrate}} = 5\text{ °C}$ (a) and 25 °C (b) for films deposited from CF solution. Top panels show 2D aggregate-only absorbance and PL spectra. Bottom panels show the aggregate fraction or normalised PL intensity, 0-0/0-1 peak ratio and peak width for absorbance (black) and PL (blue) spectra. For the assignment of characteristic times t_{start} , t_{quench} and t_{final} see text. Colored shading indicates the periods between these characteristic times.

For $T_{\text{substrate}} = 25\text{ °C}$ (Figure 4b) aggregate absorption intensity can only be observed after $\sim 1.5\text{ s}$ with a relatively sharp single step increase that is completed after 1.9 s . Only shortly before this increase in absorption, aggregate PL can be observed, which first increases in intensity and then after 1.7 s drops again to a final level of 63 % of the maximum intensity, i.e. clearly less significant than in the case of $T_{\text{substrate}} = 5\text{ °C}$. The 0-0/0-1 peak ratio in absorbance is broadly constant at a level of ~ 0.5 within the entire investigated time range, while the 0-0/0-1 PL peak ratio of the first analysed aggregate spectrum at 1.5 s is 0.43 , immediately decreasing fast to a value of ~ 0.3 at 1.9 s . The peak width σ of the aggregate absorption exhibits a value of 56 meV after 1.6 s of blade coating, increasing quickly to 64 meV after 1.9 s . In PL we observe σ to be mainly constant at 56 meV , with tendentially increased values for the first few data points between $1.5 - 1.9\text{ s}$.

From Figure 4 it becomes clear that for $T_{\text{substrate}} = 5\text{ }^{\circ}\text{C}$, i.e. well below $T_{\text{c, film}}$, the evolution of all extracted optical properties exhibit a kink after about 5.4 s. It is possible to determine the corresponding time t_{quench} of the kink, by considering the intersection of linear fits to the curves before and after the change in parameter dynamics. We also define t_{start} as the time at which the normalized aggregate area in absorption exceeds a value of 3% for the first time (from there onwards, the intensity of the aggregate spectra is generally high enough to allow reasonable analysis). Accordingly, in Figure 4a we can divide the aggregate formation process into a time range from t_{start} to t_{quench} (highlighted in light blue) and a time range from t_{quench} to t_{final} (highlighted in orange). In contrast, at $T_{\text{substrate}} = 25\text{ }^{\circ}\text{C}$ (Figure 4b) a kink in the parameter evolution before reaching t_{final} does not appear. Rather, at this temperature, the extracted parameters show their strongest temporal change directly for the earliest aggregate spectra, quickly reaching constant final values, or the parameters show constant values throughout the time range where aggregates are present. In particular, the 0-0/0-1 ratios are smaller and the σ values are higher than at $T_{\text{substrate}} = 5\text{ }^{\circ}\text{C}$ throughout the investigated time range.

Coming back to the aggregate formation at $T_{\text{substrate}} = 5\text{ }^{\circ}\text{C}$, it becomes clear that aggregates are present during t_{start} to t_{quench} , whose optical spectra exhibit relatively high 0-0/0-1 ratios and small σ values, very similar to the corresponding values of the temperature induced aggregates in solution (Figure S1). Together with the findings from our previous study, where we observed increased 0-0/0-1 ratios in P3HT thin film absorption spectra processed at temperatures well below $T_{\text{c, solution}}$, we associate the optical signatures between t_{start} and t_{quench} with aggregates formation while solvent is still present (here termed 'solution aggregate'). Due to the greater proportion of solvent still present, aggregated chains experience less steric hindrance and thus have greater freedom to adopt more thermodynamically favorable arrangements. This leads to relatively low torsional disorder (i.e. greater planarity and hence intramolecular excitonic coupling), reflected in a comparatively low peak width σ i.e., energetic site disorder $< 55\text{ meV}$ and in high 0-0/0-1 peak ratios > 0.6 in both absorbance and PL.^{52,53} The fact that σ and 0-0/0-1 of the aggregate PL decrease more steeply within the first 5.4 s of processing compared to the corresponding values extracted from absorption (Figure 4a), can be explained by the fact, that excited states undergo spectral diffusion within the density of states of the aggregated phase prior to their radiative recombination. This is in contrast to absorption that probes the entire density of states. A hindered spectral diffusion⁵⁴ due to insufficient proximity between aggregates within the first 4 seconds of blade coating might explain the high values of σ in PL, even exceeding the corresponding absorption values initially.

The changes in optical parameters that happen from t_{quench} onwards (increase in the slope of both absorbance integral and σ , while the slope of PL intensity and 0-0/0-1 peak ratio start to decrease) suggest that the aggregates exhibit an increased torsional and energetic site disorder and thus enhanced inter-chain but decreased intra-chain excitonic coupling.^{9,10,20} This appears plausible when considering that during the solution processing the solvent evaporates progressively with a certain rate, determined by the solvent properties and the processing temperature. As a result, the local chain concentration increases with time, which means that there are continuously fewer solvent molecules surrounding each aggregate. Once most of the solvent has evaporated, the steric hindrance of the chains increases due to the immediate environment with other polymer chains and the underlying carrier substrate. As a consequence, the energetic disorder increases and the planarity of already formed aggregated polymer segments decreases, also leading to a decrease of the conjugation length. This results in an increased inter-chain coupling of less conjugated aggregated chain segments, which is reflected in the reduction of the 0-0/0-1 ratio in the aggregate spectra.^{10,21} Thus, the experimentally observed changes of the optical aggregate parameters in the time range between t_{quench} to t_{final} in Figure 4a indicate the formation of less ordered aggregates. It is imaginable that already existing solution aggregates become more disordered, or that in the course of the solidification process new P3HT aggregates form that exhibit a higher degree of disorder a priori. We assume both processes to happen in parallel. However, at t_{quench} , approximately 70 % of aggregates have already formed (top panel in Figure 4), so that we expect the formation of new less-ordered aggregates to play a minor role.

From the considerations and discussion above, it also becomes clear that for blade coating at $T_{\text{substrate}} = 25 \text{ }^\circ\text{C}$ in CF (Figure 4b), no solution aggregates form. This is not surprising, as one would not expect thermodynamic driving force for solution aggregate formation because of $T_{\text{substrate}} > T_c$.^{9,20,55} Here the largest proportion of aggregates is induced by increasing condensation of the chains in the course of the final solidification process. This is consistent with the work by Abdelsamie et al. who monitored in situ the evolution of aggregate absorption and film thickness during spin coating of well dissolved P3HT in toluene.⁴¹ They observed that the aggregate formation step coincides with the time span of most rapid reduction of solution drop thickness, directly before the final film state is reached.

The rapid changes of 0-0/0-1 and σ at the moment where the first aggregates are observed between 1.5 and 1.9 s indicate that they already form under the influence of steric hindrance, which then increases in the course of the solidification process leading to the final film state. These fundamentally different aggregate formation pathways occur for blade coating from CF, also for other $T_{\text{substrate}}$ (Figure S5), where still well below $T_{c,\text{film}}$, at $T_{\text{substrate}} = 10 \text{ }^\circ\text{C}$ the trends are very similar to $T_{\text{substrate}} = 5 \text{ }^\circ\text{C}$, with significant

solution aggregation. In contrast, films deposited at $T_{\text{substrate}} = 20$ and 30 °C (i.e. well above $T_{c,\text{film}}$) show a single aggregate formation step, i.e. concentration driven aggregation. The same observations are apparent for THF but shifted to higher temperatures, with clear formation of solution aggregates when processing at 20 , 25 and 30 °C, and concentration driven single step aggregation being present at 40 and 45 °C (see SI for all data and further details).

2.4 Understanding the aggregate formation of the odd ones - the importance of timing

Based on the above gained knowledge regarding the evolution of the optical properties of the aggregates for processing well above and well below $T_{c,\text{solution}}$, we now focus on the discrepancies of critical temperatures for film processing and solution from Figure 2, specifically that $T_{c,\text{film}} > T_{c,\text{solution}}$ for CF but $T_{c,\text{film}} < T_{c,\text{solution}}$ for THF. Blade coating at 15 °C from CF led to films with final aggregate properties which one would expect for processing below $T_{c,\text{solution}}$ (i.e., high 0-0/0-1 ratio, low σ) as $T_{c,\text{solution}}$ is ~ 10 °C (Figure 2). Figure 5a shows the in situ aggregate PL and absorption spectra during blade coating at 15 °C, together with the evolution of the 0-0/0-1 ratio and σ , extracted and presented similar to Figure 4. After 1 s (corresponding to t_{start}) the aggregate spectra were sufficiently intense to allow fitting, and similar to the data at 10 °C and 5 °C, the aggregates initially show high 0-0/0-1 ratios in PL and absorption. Even though at 15 °C σ exhibits slightly higher values that increase, which is different from the corresponding dynamics between t_{start} and t_{quench} at 5 °C, a clear discontinuity in the evolution of 0-0/0-1 ratio and σ at ~ 1.2 s (corresponding to t_{quench}) is apparent (Figure 5a).

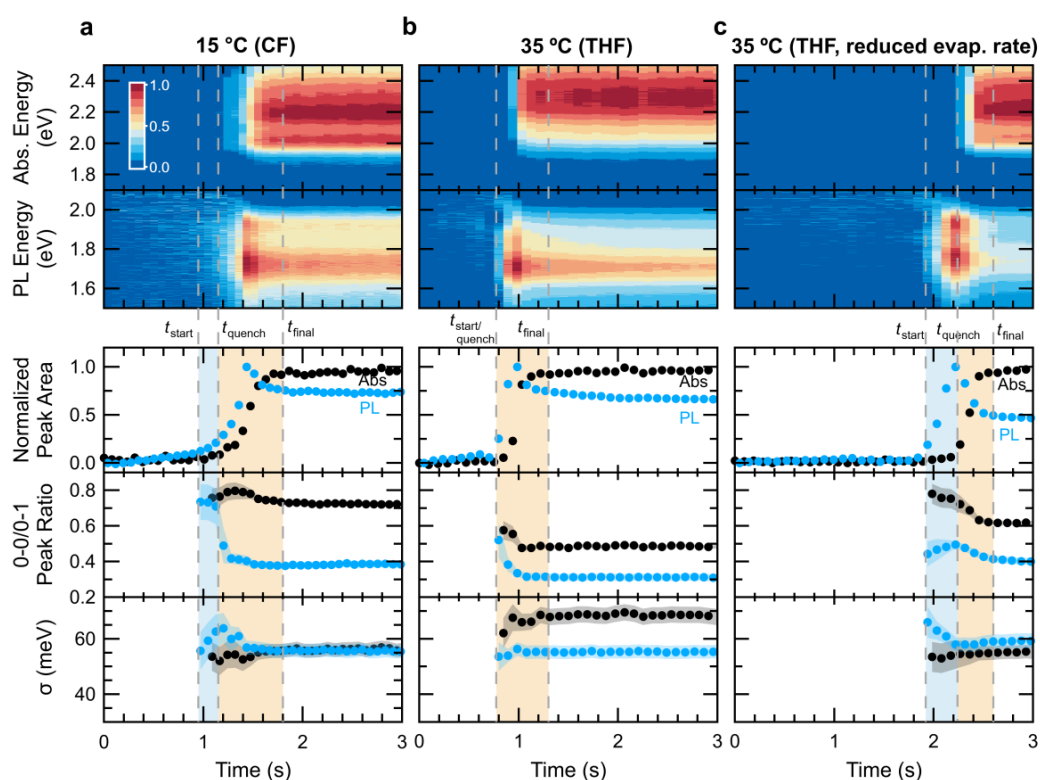


Figure 5: Tracking spectral evolution of ‘anomalous’ data points with an offset between $T_{c,substrate}$ and $T_{c,film}$, specifically $T_{substrate} \approx 15$ °C in CF (a) and $T_{substrate} \approx 35$ °C in THF (b). For $T_{substrate} \approx 35$ °C in THF a further blade coating was performed in solvent rich atmosphere, reducing the evaporation rate (c).

Thus we conclude that solution aggregates form between 1.0 and 1.2 s, even though processing happens 5° C above $T_{c,solution}$. This might appear surprising at first, but can be understood when taking into account that $T_{c,solution}$ also depends on the polymer solution concentration, with T_c increasing with concentration (see Figure S6).⁵⁶ Due to continuous solvent evaporation, shortly before the actual solidification, the local chain concentration apparently becomes high enough for $T_{c,solution}$ to increase above 15 °C. Remarkable here is the short time span in which the neat solution aggregates are present. While at $T_{substrate} = 5$ °C solution aggregation took place over a period of 4.4 s, this decreases to a mere 0.2 s at $T_{substrate} = 15$ °C. After 1.2 s, the amount of aggregates formed is only 15 % of the final amount, i.e. the largest fraction of 85 % forms during the subsequent time span t_{quench} to t_{final} (1.2 s and 1.8 s). This is in sharp contrast to the high fraction (> 70%) of solution aggregates already present at t_{quench} for processing at 5 °C (Figure 4a). Nevertheless, the final optical parameters at 15 °C exhibit relatively high 0-0/0-1 ratios of ~0.7 in absorption and ~0.4 in PL, as well as relatively low σ , especially for absorption, in the range of

55 meV, all comparable to the optical properties of the thin films for blade coating well below $T_{c,solution}$. This suggests that the fraction of solution aggregates does not need to be high, nor do they need to be present (and presumably grow) over a longer time span, to obtain thin films with better ordered aggregates. It rather appears that the decisive factor regarding which aggregate formation pathway is followed is, whether the initial aggregates form under the influence of steric restrictions or not. The properties of the aggregate seeds regarding energetic disorder and electronic coupling then maintain during further aggregate growth or formation, regardless of whether the growth is driven by solubility or concentration. This is even valid when the growth takes place on a sub second time scale as evident from the dynamics at 15 °C in Figure 5a.

With this understanding, also the ‘anomalous’ dataset of THF can be understood and interpreted. Here $T_{substrate}$ was 35 °C, and the final film aggregate spectra exhibit relatively high σ and low 0-0/0-1 values, even though processing happened 5 °C below $T_{c,solution}$ (Figure 2). Thus one would expect the film formation to be clearly influenced by solution aggregates. However, from the evolution of the optical parameters shown in Figure 5b, it can be seen that the film formation process happens exclusively following a concentration induced aggregate formation process (orange shaded time range). The THF evaporation rate at 35°C is so high that the time until the solvent has evaporated to such an extent so that aggregate formation under steric hinderance occurs, is already reached after approx. 0.7 s. This seems to dominate aggregation process, even though a certain driving force for solution-aggregate formation would be expected at 35 °C. A suitable decrease of the evaporation rate would be necessary to allow the formation of aggregate seeds with solution aggregate-like properties so that solution-aggregate-like aggregate properties also persist in the final film.

To test this hypothesis, we repeated the blade coating at 35°C from THF and positioned THF-soaked cotton swabs next to the sample, resulting in a reduced evaporation rate due to solvent-rich atmosphere above the sample. As can be seen from the extracted evolution of optical parameters (Figure 5c), the first aggregates form only after 2 s. At this point, solution aggregates are present, which becomes clear from the typical high 0-0/0-1 ratios and smaller (especially in absorption) σ values. In addition, a kink in the evolution of the optical parameters is now visible at $t_{quench} = 2.2$ s, which marks the onset of the concentration-induced solidification process, being completed after $t_{final}=2.6$ s. Similar to the observations for the blade coating from CF at 15 °C in Figure 5a, the coating from THF at 35 °C with reduced evaporation rate, shows that the time span in which purely solution aggregates exist is only ~ 0.2 s and the fraction of aggregates at t_{quench} is in the range of only 10%. As expected, the existence of solution aggregates in the time range before t_{quench} leads to the aggregate spectra of the final films also exhibiting

solution-aggregate-like properties (Figure S7).

While a shift from t_{quench} to longer times with reduced evaporation rate is consistent with our expectations, observing the first aggregates only after 2.0 s suggests that in Figure 5c the prolonged film formation time is the crucial aspect to facilitate solution aggregate formation. In contrast, the influence of poor solubility (relative to $T_{c,\text{solution}}$) at 35 °C seems to be less important. If the influence of solubility was dominant here, we would have expected the formation of the first aggregates at earlier times, similar to e.g. the results in Figure 4a. The results from Figure 5c thus underline the crucial importance of timing on the formation of solution aggregates, and thus on the overall film formation dynamics as well as final film properties.

Conclusion

In summary, we have outlined an aggregate formation mechanism that rationalizes the dependence of conjugated polymer aggregate spectra on both solubility and solvent evaporation rate. Specifically, we propose that the dominant factor is the proportion of aggregates that form while solution is still present, which requires both low solubility and time for chain diffusion. These aggregates form under conditions chains with significantly reduced steric hindrance, leading to greater intra-molecular coupling and reduced energetic site disorder relative to aggregates induced by increasing concentration. This generalizable framework should inform further work to rationalise processing-structure-property relations across many conjugated polymers, thus reducing the need for optimization to achieve desired properties.

Acknowledgements

MD, HB, MC, NS and AK thank the Marie Skłodowska-Curie Actions Innovative Training Network “H2020-MSCA-ITN-2014 INFORM—675867” for funding. While experimental work presented here was performed at Bayreuth University (Germany), preliminary studies were undertaken at Imperial College London (UK) (for which MD, PS and NS thank the UK Engineering and Physical Sciences Research Council (EPSRC) for funding via the Centre for Doctoral Training in Plastic Electronics Materials (EP/G037515/1)) and at the National Institute of Standards and Technology (NIST) (USA), for which MD thanks the Royal Society of Chemistry (RSC) for a Researcher Mobility Grant along with Sebastian Engmann and Lee Richter for instructive scientific discussion.

Table of Contents

Spectral properties of conjugated polymers are predominantly determined by the proportion of aggregates that form via diffusion in solution rather than induced by increasing concentration. Solution aggregates have reduced torsional and electronic site disorder, and are favoured by lower solubility and slower solvent evaporation. This mechanism provides generalisable guidelines for processing parameter selection.

References

- (1) Treat, N. D.; Westacott, P.; Stingelin, N. The Power of Materials Science Tools for Gaining Insights into Organic Semiconductors. *Annu. Rev. Mater. Res.* **2015**, *45*, 459–490.
- (2) Richter, L. J.; DeLongchamp, D. M.; Bokel, F. A.; Engmann, S.; Chou, K. W.; Amassian, A.; Schaible, E.; Hexemer, A. In Situ Morphology Studies of the Mechanism for Solution Additive Effects on the Formation of Bulk Heterojunction Films. *Adv. Energy Mater.* **2015**, *5*, 1400975.
- (3) Richter, L. J.; DeLongchamp, D. M.; Amassian, A. Morphology Development in Solution-Processed Functional Organic Blend Films: An in Situ Viewpoint. *Chem. Rev.* **2017**, *117*, 6332–6366.
- (4) Hildner, R.; Köhler, A.; Müller-Buschbaum, P.; Panzer, F.; Thelakkat, M. π -Conjugated Donor Polymers: Structure Formation and Morphology in Solution, Bulk and Photovoltaic Blends. *Adv. Energy Mater.* **2017**, *7*, 1700314.
- (5) Han, S.; Yu, X.; Shi, W.; Zhuang, X.; Yu, J. Solvent-Dependent Electrical Properties Improvement of Organic Field-Effect Transistor Based on Disordered Conjugated Polymer/Insulator Blends. *Org. Electron.* **2015**, *27*, 160–166.
- (6) Kumar, A.; Baklar, M. A.; Scott, K.; Kreouzis, T.; Stingelin-Stutzmann, N. Efficient, Stable Bulk Charge Transport in Crystalline/Crystalline Semiconductor-Insulator Blends. *Adv. Mater.* **2009**, *21*, 4447–4451.
- (7) Botiz, I.; Astilean, S.; Stingelin, N. Altering the Emission Properties of Conjugated Polymers. *Polym. Int.* **2016**, *65*, 157–163.
- (8) Hestand, N. J.; Spano, F. C. Expanded Theory of H- and J-Molecular Aggregates: The Effects of Vibronic Coupling and Intermolecular Charge Transfer. *Chem. Rev.* **2018**, *118*, 7069–7163.
- (9) Panzer, F.; Bäessler, H.; Köhler, A. Temperature Induced Order-Disorder Transition in Solutions of Conjugated Polymers Probed by Optical Spectroscopy. *J. Phys. Chem. Lett.* **2017**, *8*, 114–125.
- (10) Spano, F. C.; Silva, C. H- and J-Aggregate Behavior in Polymeric Semiconductors. *Annu. Rev. Phys. Chem.* **2014**, *65*, 477–500.
- (11) Boudouris, B. W.; Ho, V.; Jimison, L. H.; Toney, M. F.; Salleo, A.; Segalman, R. A. Real-Time Observation of Poly(3-Alkylthiophene) Crystallization and Correlation with Transient Optoelectronic Properties. *Macromolecules* **2011**, *44*, 6653–6658.
- (12) Koch, F. P. V.; Rivnay, J.; Foster, S.; Müller, C.; Downing, J. M.; Buchaca-Domingo, E.; Westacott, P.; Yu, L.; Yuan, M.; Baklar, M.; et al. The Impact of Molecular Weight on Microstructure and Charge Transport in Semicrystalline Polymer Semiconductors—Poly(3-Hexylthiophene), a Model Study. *Prog. Polym. Sci.* **2013**, *38*, 1978–1989.
- (13) Bäessler, H.; Köhler, A. *Electronic Properties of Organic Semiconductors*; Wiley-VCH, 2018.
- (14) Teichler, A.; Perelaer, J.; Schubert, U. S. Inkjet Printing of Organic Electronics – Comparison of Deposition Techniques and State-of-the-Art Developments. *J. Mater. Chem. C* **2013**, *1*, 1910–1925.
- (15) Berny, S.; Blouin, N.; Distler, A.; Egelhaaf, H.-J.; Krompiec, M.; Lohr, A.; Lozman, O. R.; Morse, G. E.; Nanson, L.; Pron, A.; et al. Solar Trees: First Large-Scale Demonstration of Fully Solution Coated, Semitransparent, Flexible Organic Photovoltaic Modules. *Adv. Sci.* **2016**, *3*, 1500342.
- (16) Hou, J.; Inganäs, O.; Friend, R. H.; Gao, F. *Organic Solar Cells Based on Non-Fullerene Acceptors. Nature Materials.* 2018, pp 119–128.
- (17) Wang, Y.; Zhu, Y.; Xie, G.; Zhan, H.; Yang, C.; Cheng, Y. Bright White Electroluminescence from a Single Polymer Containing a Thermally Activated Delayed Fluorescence Unit and a Solution-Processed Orange OLED Approaching 20% External Quantum Efficiency. *J. Mater. Chem. C* **2017**, *5*, 10715–10720.
- (18) Sirringhaus, H. 25th Anniversary Article: Organic Field-Effect Transistors: The Path beyond Amorphous Silicon. *Adv. Mater.* **2014**, *26*, 1319–1335.
- (19) Simone, G.; Dyson, M. J.; Meskers, S. C. J.; Janssen, R. A. J.; Gelinck, G. H. Organic Photodetectors and Their Application in Large Area and Flexible Image Sensors. *Adv. Funct. Mater.* **2019**, 1904205.
- (20) Reichenberger, M.; Kroh, D.; Matrone, G. M. M.; Schotz, K.; Proller, S.; Filonik, O.; Thordardottir, M. E.; Herzog, E. M.; Bäessler, H.; Stingelin, N.; et al. Controlling Aggregate Formation in Conjugated Polymers by Spin-Coating Below the Critical Temperature of the Disorder–Order Transition. *J. Polym. Sci. Part B Polym. Phys.* **2018**, *56*, 532–542.

- (21) Scharsich, C.; Lohwasser, R. H.; Sommer, M.; Asawapirom, U.; Scherf, U.; Thelakkat, M.; Neher, D.; Köhler, A. Control of Aggregate Formation in Poly(3-Hexylthiophene) by Solvent, Molecular Weight, and Synthetic Method. *J. Polym. Sci. Part B Polym. Phys.* **2012**, *50*, 442–453.
- (22) Zhao, K.; Yu, X.; Li, R.; Amassian, A.; Han, Y. Solvent-Dependent Self-Assembly and Ordering in Slow-Drying Drop-Cast Conjugated Polymer Films. *J. Mater. Chem. C* **2015**, *3*, 9842–9848.
- (23) Yamagata, H.; Spano, F. C. Interplay between Intrachain and Interchain Interactions in Semiconducting Polymer Assemblies: The HJ-Aggregate Model. *J. Chem. Phys.* **2012**, *136*, 184901.
- (24) Spano, F. C.; Clark, J.; Silva, C.; Friend, R. H. Determining Exciton Coherence from the Photoluminescence Spectral Line Shape in Poly(3-Hexylthiophene) Thin Films. *J. Chem. Phys.* **2009**, *130*, 074904.
- (25) Clark, J.; Silva, C.; Friend, R. H.; Spano, F. C. Role of Intermolecular Coupling in the Photophysics of Disordered Organic Semiconductors: Aggregate Emission in Regioregular Polythiophene. *Phys. Rev. Lett.* **2007**, *98*, 206406.
- (26) Spano, F. C. Modeling Disorder in Polymer Aggregates: The Optical Spectroscopy of Regioregular Poly(3-Hexylthiophene) Thin Films. *J. Chem. Phys.* **2005**, *122*, 234701.
- (27) Clark, J.; Chang, J.-F. F.; Spano, F. C.; Friend, R. H.; Silva, C. Determining Exciton Bandwidth and Film Microstructure in Polythiophene Films Using Linear Absorption Spectroscopy. *Appl. Phys. Lett.* **2009**, *94*, 163306.
- (28) Güldal, N. S.; Kassar, T.; Berlinghof, M.; Unruh, T.; Brabec, C. J.; Sena, N. In Situ Characterization Methods for Evaluating Microstructure Formation and Drying Kinetics of Solution-Processed Organic Bulk-Heterojunction Films. *J. Mater. Res.* **2017**, *32*, 1855–1879.
- (29) Moseguí González, D.; Schaffer, C. J.; Pröllner, S.; Schlipf, J.; Song, L.; Bernstorff, S.; Herzig, E. M.; Müller-Buschbaum, P. Codependence between Crystalline and Photovoltage Evolutions in P3HT:PCBM Solar Cells Probed with in-Operando GIWAXS. *ACS Appl. Mater. Interfaces* **2017**, *9*, 3282–3287.
- (30) Manley, E. F.; Strzalka, J.; Fauvell, T. J.; Marks, T. J.; Chen, L. X. In Situ Analysis of Solvent and Additive Effects on Film Morphology Evolution in Spin-Cast Small-Molecule and Polymer Photovoltaic Materials. *Adv. Energy Mater.* **2018**, *8*, 1800611.
- (31) Güldal, N. S.; Kassar, T.; Berlinghof, M.; Ameri, T.; Osvet, A.; Pacios, R.; Destri, G. L.; Unruh, T.; Brabec, C. J. Real-Time Evaluation of Thin Film Drying Kinetics Using an Advanced, Multi-Probe Optical Setup. *J. Mater. Chem. C* **2016**, *4*, 2178–2186.
- (32) Kim, Y.-J.; Lee, S.; Niazi, M. R.; Hwang, K.; Tang, M.-C.; Lim, D.-H.; Kang, J.-S.; Smilgies, D.-M.; Amassian, A.; Kim, D.-Y. Systematic Study on the Morphological Development of Blade-Coated Conjugated Polymer Thin Films via In Situ Measurements. *ACS Appl. Mater. Interfaces* **2020**, *12*, 36417–36427.
- (33) Engmann, S.; Bokel, F. A.; Ro, H. W.; DeLongchamp, D. M.; Richter, L. J. Real-Time Photoluminescence Studies of Structure Evolution in Organic Solar Cells. *Adv. Energy Mater.* **2016**, *6*, 1–12.
- (34) Pröllner, S.; Liu, F.; Zhu, C.; Wang, C.; Russell, T. P.; Hexemer, A.; Müller-Buschbaum, P.; Herzig, E. M. Following the Morphology Formation In Situ in Printed Active Layers for Organic Solar Cells. *Adv. Energy Mater.* **2016**, *6*, 1501580.
- (35) Noriega, R.; Rivnay, J.; Vandewal, K.; Koch, F. P. V.; Stingelin, N.; Smith, P.; Toney, M. F.; Salleo, A. A General Relationship between Disorder, Aggregation and Charge Transport in Conjugated Polymers. *Nat. Mater.* **2013**, *12*, 1038–1044.
- (36) Grégoire, P.; Vella, E.; Dyson, M.; Bazán, C. M.; Leonelli, R.; Stingelin, N.; Stavrinou, P. N.; Bittner, E. R.; Silva, C. Excitonic Coupling Dominates the Homogeneous Photoluminescence Excitation Linewidth in Semicrystalline Polymeric Semiconductors. *Phys. Rev. B* **2017**, *95*, 180201(R).
- (37) Korovyanko, O.; Österbacka, R.; Jiang, X.; Vardeny, Z.; Janssen, R. Photoexcitation Dynamics in Regioregular and Regiorandom Polythiophene Films. *Phys. Rev. B* **2001**, *64*, 235122.
- (38) Hansen, C. M. *Hansen Solubility Parameters: A User's Handbook*, 2nd ed.; CRC Press: Boca Raton, FL, USA, 2007.
- (39) Duong, D. T.; Walker, B.; Lin, J.; Kim, C.; Love, J.; Purushothaman, B.; Anthony, J. E.; Nguyen, T. Q. Molecular Solubility and Hansen Solubility Parameters for the Analysis of Phase Separation in Bulk Heterojunctions. *J. Polym. Sci. Part B Polym. Phys.* **2012**, *50*, 1405–1413.
- (40) Dyson, M. J.; Pol, T. P. A. van der; Meskers, S. C. Extrinsic Influences on Photoluminescence Spectral Lineshape in Thin Films. *Adv. Opt. Mater.* **2020**, *Under Revi.*
- (41) Abdelsamie, M.; Zhao, K.; Niazi, M. R.; Chou, K. W.; Amassian, A. In Situ UV-Visible Absorption during Spin-

- Coating of Organic Semiconductors: A New Probe for Organic Electronics and Photovoltaics. *J. Mater. Chem. C* **2014**, *2*, 3373–3381.
- (42) Panzer, F.; Sommer, M.; Bäessler, H.; Thelakkat, M.; Köhler, A. Spectroscopic Signature of Two Distinct H-Aggregate Species in Poly(3-Hexylthiophene). *Macromolecules* **2015**, *48*, 1543–1553.
- (43) Yamagata, H.; Maxwell, D. S.; Fan, J.; Kittilstved, K. R.; Briseno, A. L.; Barnes, M. D.; Spano, F. C. HJ-Aggregate Behaviour of Crystalline 7,8,15,16-Tetraazaterrylene: Introducing a New Design Paradigm for Organic Materials. *J. Phys. Chem. C* **2014**, *118*, 28842–28854.
- (44) Garreau, S.; Leclerc, M.; Errien, N.; Louarn, G. Planar-to-Nonplanar Conformational Transition in Thermochromic Polythiophenes: A Spectroscopic Study. *Macromolecules* **2003**, *36*, 692–697.
- (45) Farouil, L.; Alary, F.; Bedel-Pereira, E.; Heully, J.-L. Revisiting the Vibrational and Optical Properties of P3HT: A Combined Experimental and Theoretical Study. *J. Phys. Chem. A* **2018**, *122*, 6532–6545.
- (46) Ariu, M.; Lidzey, D. G.; Lavrentiev, M.; Bradley, D. D. C.; Jandke, M.; Strohriegl, P. Study of the Different Structural Phases of the Polymer Poly(9,9'-Dioctyl Fluorene) Using Raman Spectroscopy. *Synth. Met.* **2001**, *116*, 217–221.
- (47) Sutton, J. J.; Nguyen, T. L.; Woo, H. Y.; Gordon, K. C. Variable-Temperature Resonance Raman Studies to Probe Interchain Ordering for Semiconducting Conjugated Polymers with Different Chain Curvature. *Chem. – An Asian J.* **2019**, *14*, 1175–1183.
- (48) Gao, J.; Wang, J.; An, Q.; Ma, X.; Hu, Z.; Xu, C.; Zhang, X.; Zhang, F. Over 16.7% Efficiency of Ternary Organic Photovoltaics by Employing Extra PC71BM as Morphology Regulator. *Sci. China Chem.* **2020**, *63*, 83–91.
- (49) Scharsich, C.; Fischer, F. S. U.; Wilma, K.; Hildner, R.; Ludwigs, S.; Köhler, A. Revealing Structure Formation in PCPDTBT by Optical Spectroscopy. *J. Polym. Sci. Part B Polym. Phys.* **2015**, *53*, 1416–1430.
- (50) Buchhorn, M.; Wedler, S.; Panzer, F. Setup to Study the in Situ Evolution of Both Photoluminescence and Absorption during the Processing of Organic or Hybrid Semiconductors. *J. Phys. Chem. A* **2018**, *122*, 9115–9122.
- (51) Schwartz, B. J. Conjugated Polymers as Molecular Materials: How Chain Conformation and Film Morphology Influence Energy Transfer and Interchain Interactions. *Annu. Rev. Phys. Chem.* **2003**, *54*, 141–172.
- (52) Niles, E. T.; Roehling, J. D.; Yamagata, H.; Wise, A. J.; Spano, F. C.; Moulé, A. J.; Grey, J. K. J-Aggregate Behavior in Poly-3-Hexylthiophene Nanofibers. *J. Phys. Chem. Lett.* **2012**, *3*, 259–263.
- (53) Raithel, D.; Simine, L.; Pickel, S.; Schötz, K.; Panzer, F.; Baderschneider, S.; Schiefer, D.; Lohwasser, R.; Köhler, J.; Thelakkat, M.; et al. Direct Observation of Backbone Planarization via Side-Chain Alignment in Single Bulky-Substituted Polythiophenes. *Proc. Natl. Acad. Sci.* **2018**, *115*, 2699–2704.
- (54) Hoffmann, S. T.; Bäessler, H.; Koenen, J. M.; Forster, M.; Scherf, U.; Scheler, E.; Strohriegl, P.; Köhler, A. Spectral Diffusion in Poly(Para-Phenylene)-Type Polymers with Different Energetic Disorder. *Phys. Rev. B* **2010**, *81*, 115103.
- (55) Du, B.; Yi, J.; Yan, H.; Wang, T. Temperature Induced Aggregation of Organic Semiconductors. *Chem. - A Eur. J.* **2020**, chem.202002559.
- (56) Wedler, S.; Bourdick, A.; Athanasopoulos, S.; Gekle, S.; Panzer, F.; McDowell, C.; Nguyen, T. Q.; Bazan, G. C.; Köhler, A. What Is the Role of Planarity and Torsional Freedom for Aggregation in a π -Conjugated Donor-Acceptor Model Oligomer? *J. Mater. Chem. C* **2020**, *8*, 4944–4955.
- (57) Tessler, N.; Preezant, Y.; Rappaport, N.; Roichman, Y. Charge Transport in Disordered Organic Materials and Its Relevance to Thin-Film Devices: A Tutorial Review. *Adv. Mater.* **2009**, *21*, 2741–2761.

Processing condition dependent aggregation pathways in conjugated polymers

Supporting Information

*Matthew J Dyson, Hazem Bakr, Stefan Wedler, Konstantin Schötz, Mihirsinh Chauhan, Paul N Stavrinou, Natalie Stingelin, Anna Köhler, Fabian Panzer**

Matthew J Dyson

Molecular Materials and Nanosystems and Institute for Complex Molecular Systems, Eindhoven University of Technology, 5600 MB Eindhoven (The Netherlands)

Stefan Wedler, Hazem Bakr, Mihir Chauhan, Konstantin Schötz, Anna Köhler, Fabian Panzer

Soft Matter Optoelectronics, University of Bayreuth, Bayreuth 95440 (Germany)

Paul N Stavrinou

Department of Engineering Science, University of Oxford, Oxford, OX1 3PJ (UK)

Natalie Stingelin

School of Materials Science & Engineering and School of Chemical & Biomolecular Engineering, Georgia Institute of Technology, Atlanta, Georgia 30332 (USA)

Page	Section/Figure
S2	Experimental details and data evaluation
S4	Figure S1: Temperature dependent solution absorption spectra
S5	Figure S2: Explanation of the additional broadening term used for fitting
S6	Figure S3: Example fitting of in-situ aggregate-only absorbance spectra (5 °C, CF)
S7	Figure S4: Example fitting of in-situ aggregate-only emission spectra (5 °C, CF)
S8	Figure S5: Spectral evolution and extracted parameters for all measurement sets
S15	Figure S6: Concentration dependence of $T_{c,solution}$
S16	Figure S7: Final film spectra for blade coating with and without restricted evaporation (35°C, THF)
S17	Table S1: Hansen solubility parameters for P3HT and solvents used.
S17	Table S2: Aggregate formation onset, regime transition and completion times.
S18	References

Experimental Details

Materials

Regio-regular poly(3-hexylthiophene) (P3HT), obtained from James Bannock and John de Mello at Imperial College London and synthesised using a flow-synthesis method that reduces inter-batch variation, with weight-averaged molecular weight (M_w) of 100 kg mol^{-1} , dispersity of 1.5, and 99% regioregularity.¹ Solvents were obtained from Sigma-Aldrich and use as received.

Sample Preparation

Polymers were dissolved at a concentration of 10 mg ml^{-1} . Solutions were magnetically stirred at $50 \text{ }^\circ\text{C}$ for 3 hours to ensure complete dissolution and homogeneity, before coating onto glass substrates cleared in an ultrasonic bath with soap water, neat DI water, acetone and finally IPA (15 mins in each).

Steady State Solution Spectra

Solutions were prepared as above and transferred to a 1 mm path length fused silica cuvette. Temperature was controlled with an Optistat cryostat (Oxford Instruments), with PL and absorbance spectra recorded after 15 minutes of temperature stabilisation. Further details about experimental setup can be found in Reference ².

In situ Spectra

Concurrent PL and absorption spectra were recorded using the detection system outlined by Buchhorn *et al.*,³ although the spin coater was replaced with a blade coater. This comprised a glass substrate angled at $\sim 15^\circ$ as the blade, attached to a motorised translation stage. A micrometre stage enabled the blade height to be adjusted to $\sim 300 \text{ }\mu\text{m}$ above the substrate. Hot solution was then deposited into the space between blade and substrate using a pipette, remaining in place due to capillary forces prior to coating at 2 cm s^{-1} . Substrate temperature was controlled using a Peltier plate, although below $15 \text{ }^\circ\text{C}$ cooling was supplemented using dry ice. Condensation, and hence the influence of water on film formation was avoided by coating within an enclosed environment, with Argon-gas inflow and the presence of dry ice reducing the relative humidity to below 20 % and hence the dewpoint to below $0 \text{ }^\circ\text{C}$.

Data Processing

Spectral measurements were recorded throughout this process (i.e., from before blade coating to steady state spectra), with time zero set to the first detection frame in absorption after the blade passed the optical path of white light.

Spectral processing steps for both absorbance and PL are as follows:

1. Convert PL spectra to be plotted against energy (rather than wavelength)⁴ by dividing by E^2 and correct for the efficiency of all optical elements using a calibrated standard.
2. Calculate time axis from total duration of measurement and number of acquired spectra, considering time zero as detailed above.
3. Subtract a constant baseline in absorption, using the average absorbance between 1.65 and 1.70 eV for each frame.
4. Plot final spectra.
5. Divide the PL spectra by the absorption, $1 - 10^{-(\text{absorbance})}$ (reflection is neglected) at the excitation wavelength (520 nm, 2.38 eV), thereby extracting an approximate PLQY.
6. Select a spectrum just after time zero only comprising contributions from non-aggregated chains.

7. Vertically scale (PL: also laterally shift) this non-aggregated spectrum to match the high energy side of the measured spectra in overlap region (2.05 to 2.25 eV for PL, 2.75 to 2.95 eV for absorbance with individual adjustments, e.g. see Figure 1 in the main text), then subtract to leave aggregated contribution.
8. Integrate aggregate PL and absorbance peaks.
9. Fit aggregate PL and absorbance spectra in a specific region (1.55-2.0 eV for PL, 1.92-2.6 eV for absorbance with individual adjustments) with Equations 1 and 2, respectively, using the LMFIT python library⁵ with a standard Levenberg-Marquardt minimisation algorithm. Fitting was performed backward in time and fitting results were used as start parameters for the subsequent fit. For absorbance, additional weights $w(E)$ were introduced according to $w(E) = 0.5 \cdot \left(1 + \operatorname{erf}\left(\frac{E - (E_0 + 1.5 \cdot E_{\text{vib}})}{60 \text{ meV}}\right)\right) + 0.2$ to give more attention to 0-0 and 0-1 peaks.
10. Plot extracted parameters and aggregate absorption integral vs time.

Rationalizing the fitting approach

The fitting equations for the aggregate only spectra are described in the manuscript. In emission, we use a modified Franck-Condon approach, modifying the 0-0 peak with a factor α ,⁶ while in absorption we choose a simplified progression of equally spaced Gaussian peaks. For convenience, the equations are reprinted here:

$$PL(E) \propto E^3 \left[\alpha \exp\left(\frac{(E - E_0)^2}{2\sigma^2}\right) + \sum_{m=1}^{m=3} \frac{S_{\text{eff}}^m}{m!} \exp\left(-\frac{(E - (E_0 - mE_{\text{vib}}))^2}{2(\sigma + m \cdot \Delta\sigma)^2}\right) \right] \quad (1)$$

$$Abs(E) = E \sum_{m=0}^{m=3} A_m \exp\left(-\frac{(E - (E_0 + mE_{\text{vib}}))^2}{2(\sigma + m \cdot \Delta\sigma)^2}\right) \quad (2)$$

Here, E is the photon energy, E_0 the energetic location of the 0-0 peak, m peak number, σ peak width, and E_{vib} the effective vibrational mode energy. Following Yamagata et al.,⁷ we include an additional broadening term of $m \cdot \Delta\sigma$, which mimics the presence of several closely spaced vibronic modes in our effective-mode approach. This results in drastically improved fitting quality and allows to extract relevant parameters more reliably, see Figure S2. For simplicity, we assume a fixed Huang-Rhys parameter of 1 in emission.⁶ E_{vib} and $\Delta\sigma$ depend on the relative intensity of the overlapping vibronic modes. In principle they need to be extracted from the fit. To reduce fitting complexity we set them to the constant values of $E_{\text{vib}} = 178$ meV, $\Delta\sigma = 23.4$ meV in emission and $E_{\text{vib}} = 156.2$ meV, $\Delta\sigma = 25.9$ meV in absorption, determined by a global average over all data sets.

The presence of the broadening term further needs to be considered for the calculation of the 0-0/0-1 peak ratio. The intensity of a vibronic line is defined via the spectral integral over the peak. It is proportional to the respective amplitude for Gaussian line shapes with equal peak widths, where intensity ratios can directly be calculated by the ratio of the peak amplitudes. Considering the broadening term results in a correction of the peak ratio according to

$$\frac{I_{0-0}}{I_{0-1}}(PL) = \alpha \frac{\sigma_0}{\sigma_1} = \alpha \frac{\sigma}{\sigma + \Delta\sigma} \qquad \frac{I_{0-0}}{I_{0-1}}(Abs) = \frac{A_0 \cdot \sigma_0}{A_1 \cdot \sigma_1} = \frac{A_0 \cdot \sigma}{A_1 \cdot (\sigma + \Delta\sigma)}$$

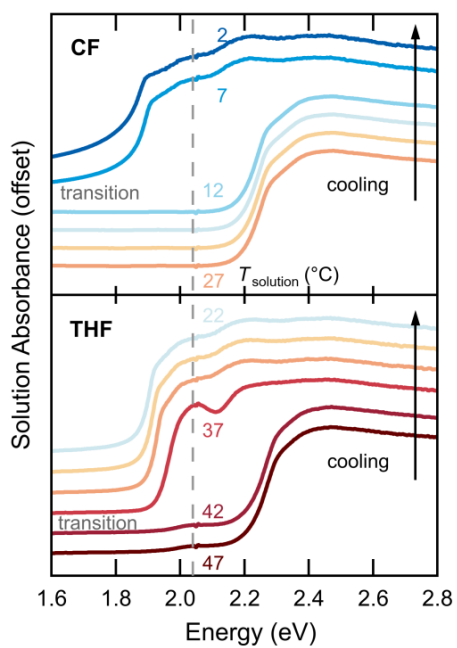


Figure S1: Temperature dependent Absorption of P3HT in CF and THF for a concentration of 10 mg ml^{-1} . Due to the high concentration, the detector saturates at higher energies.

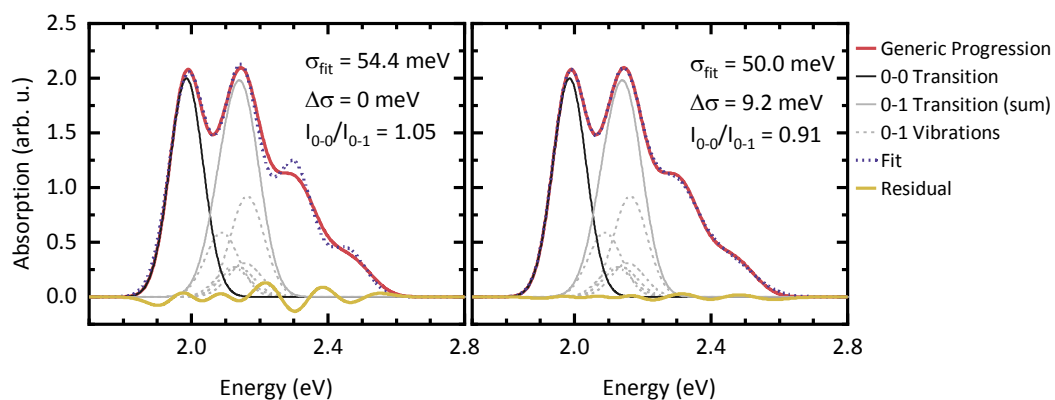


Figure S2: Rationalizing the additional broadening term for a generic multi-mode Franck-Condon progression⁸ calculated with $E_0 = 1.984$ eV, $\sigma = 49.1$ meV and Huang-Rhys parameters of $S(178 \text{ meV}) = 0.425$, $S(170.7 \text{ meV}) = 0.143$, $S(149.2 \text{ meV}) = 0.129$, $S(134.8 \text{ meV}) = 0.128$ and $S(103.9 \text{ meV}) = 0.281$. This results in a theoretical 0-0/0-1 ratio of 0.90. The vibrational energies resemble typical vibrational modes in P3HT.⁹ The standard single-mode approach gives systematically too large results for line width and 0-0/0-1 ratio. The additional broadening term reasonably recovers the parameters used for calculating the generic Franck-Condon progression and reduces the residual significantly.

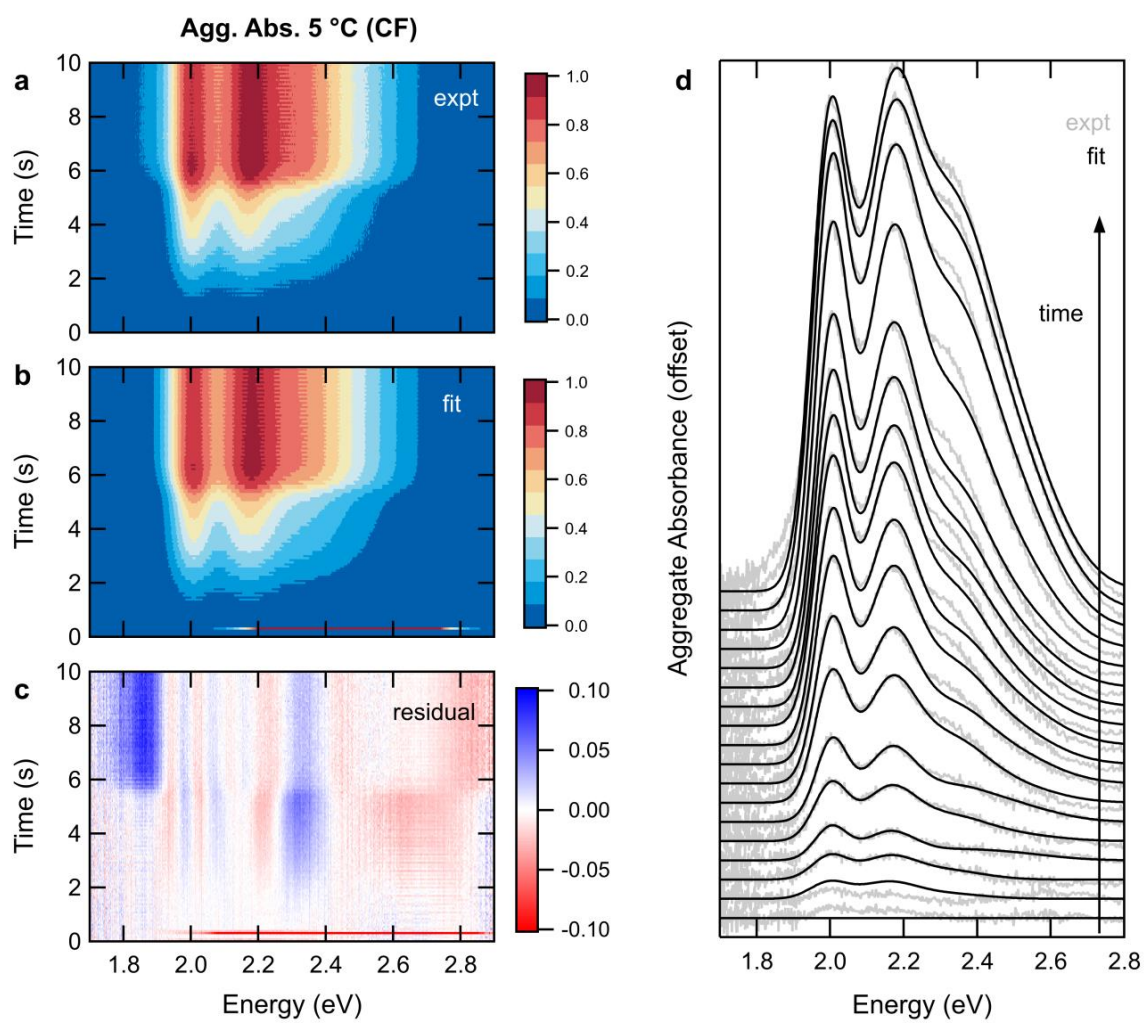


Figure S3: Example aggregate absorbance fits.

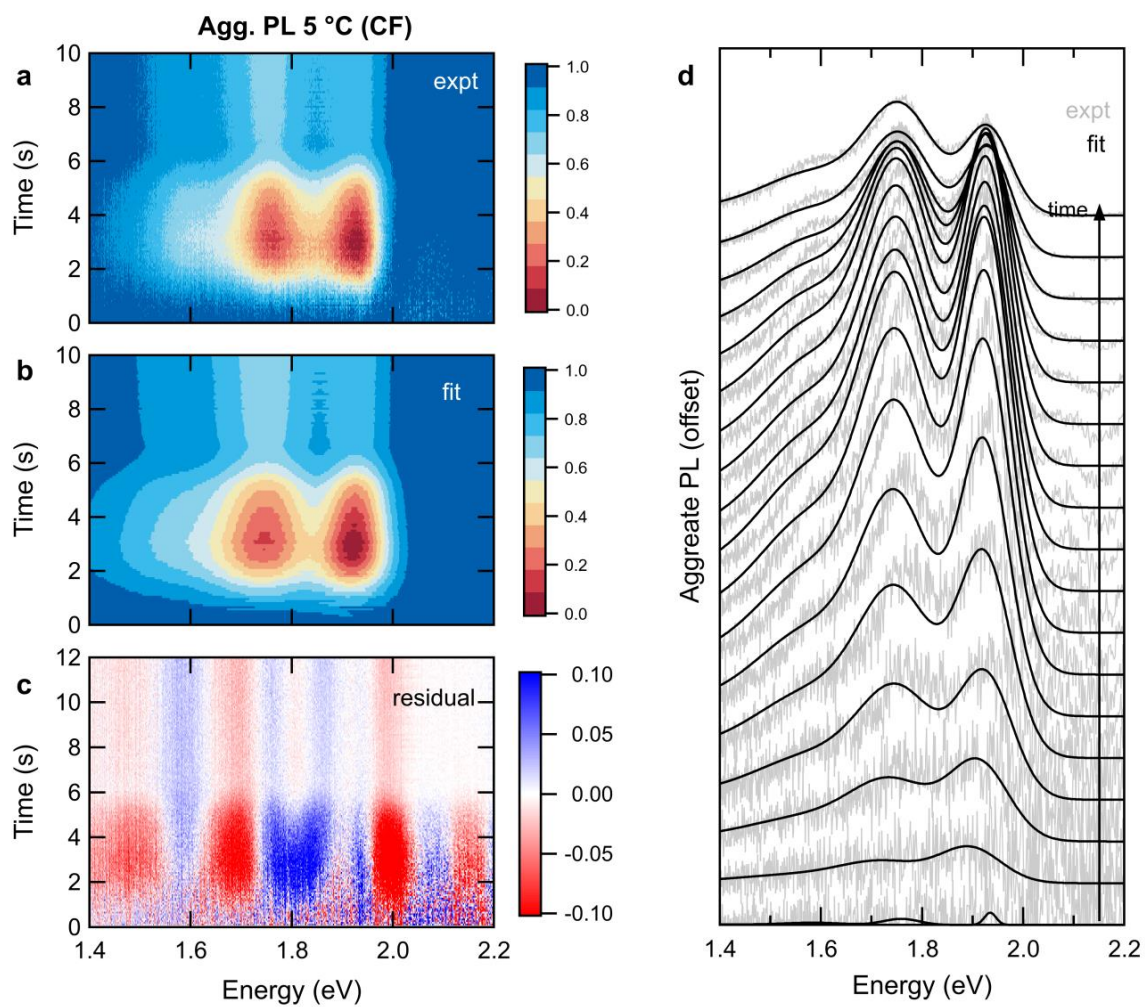


Figure S4: Example aggregate emission fits.

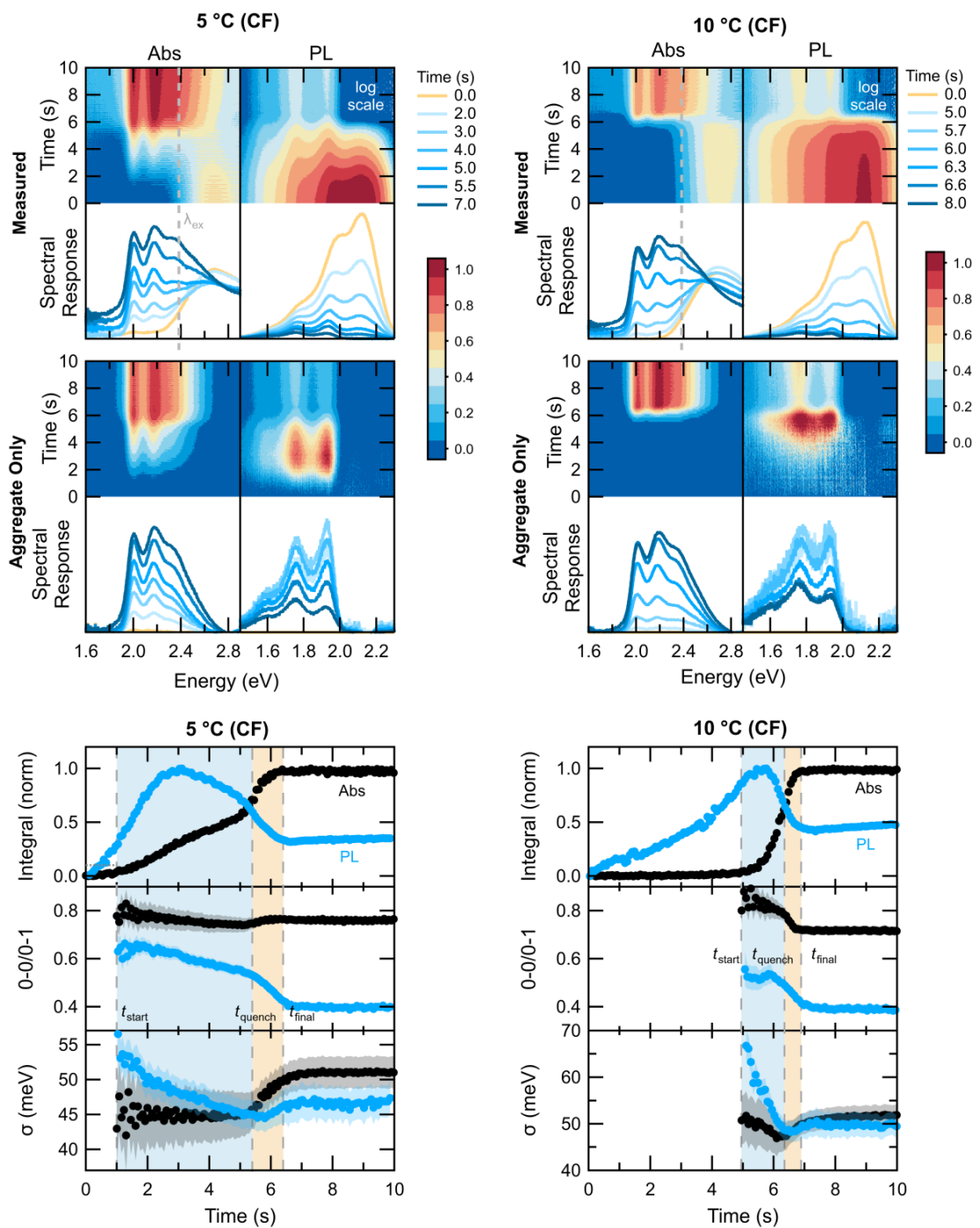


Figure S5: In situ spectra and evolution of optical parameters for all data sets.

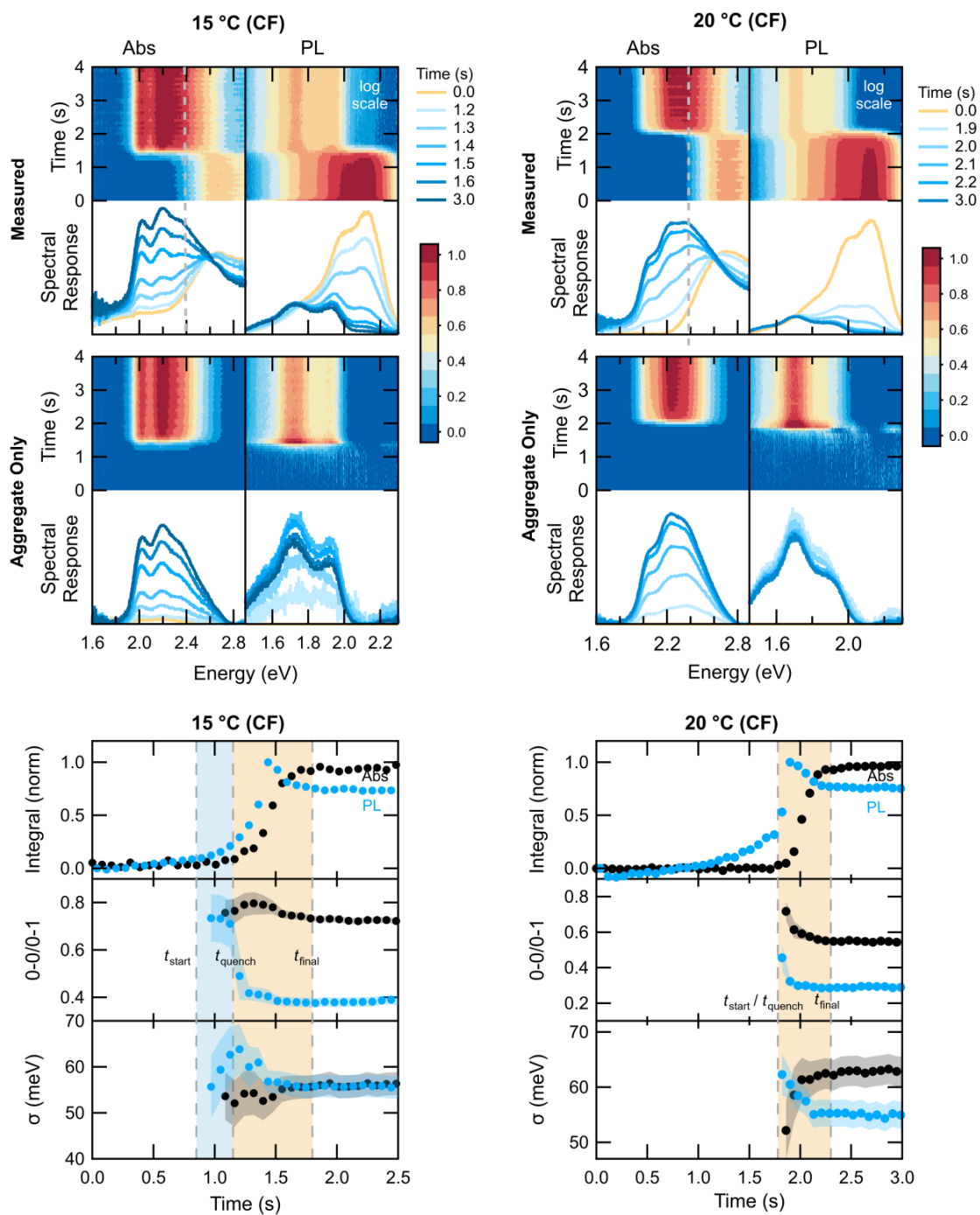


Figure S5 (continued): In situ spectra and evolution of optical parameters for all data sets.

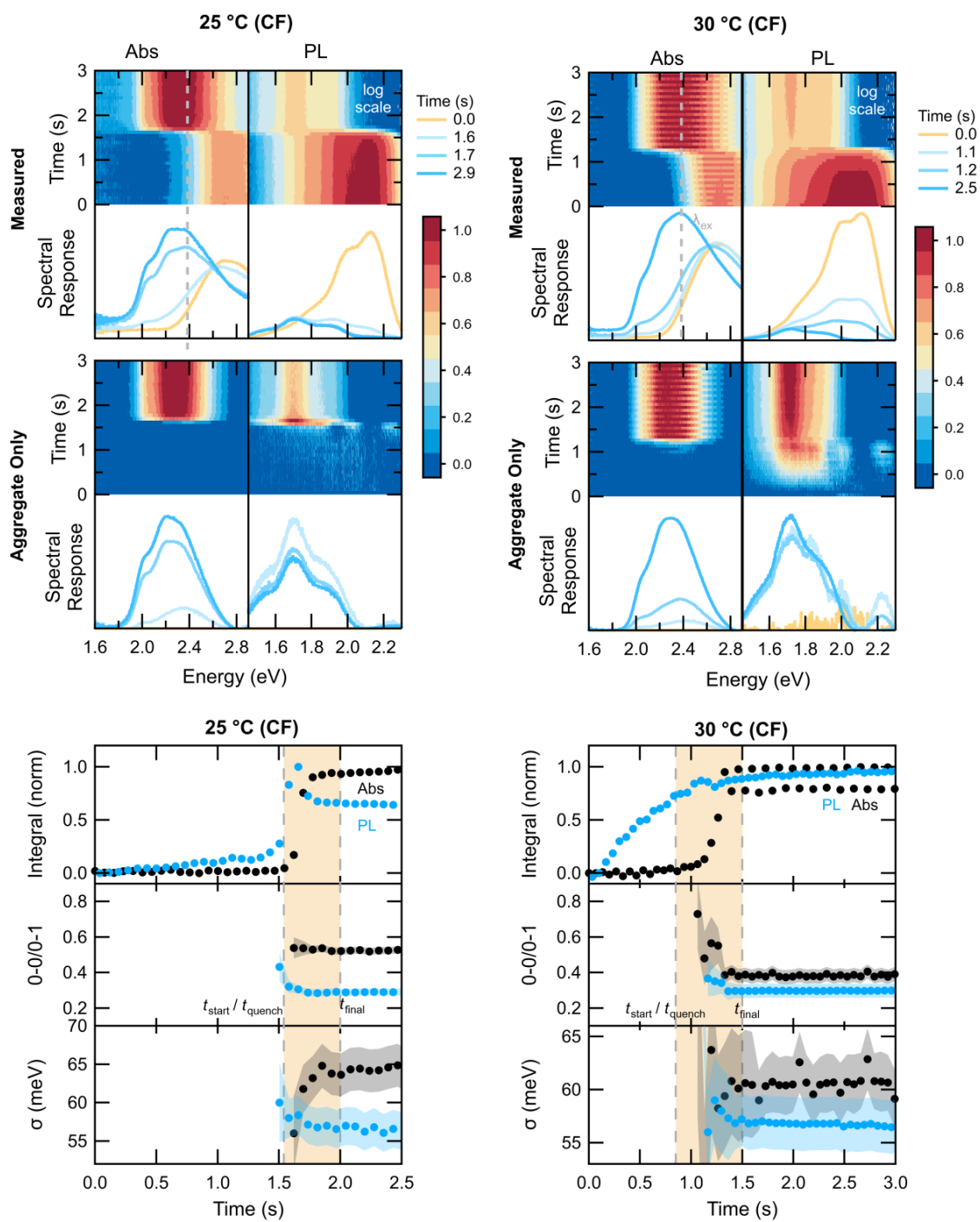


Figure S5 (continued): In situ spectra and evolution of optical parameters for all data sets.

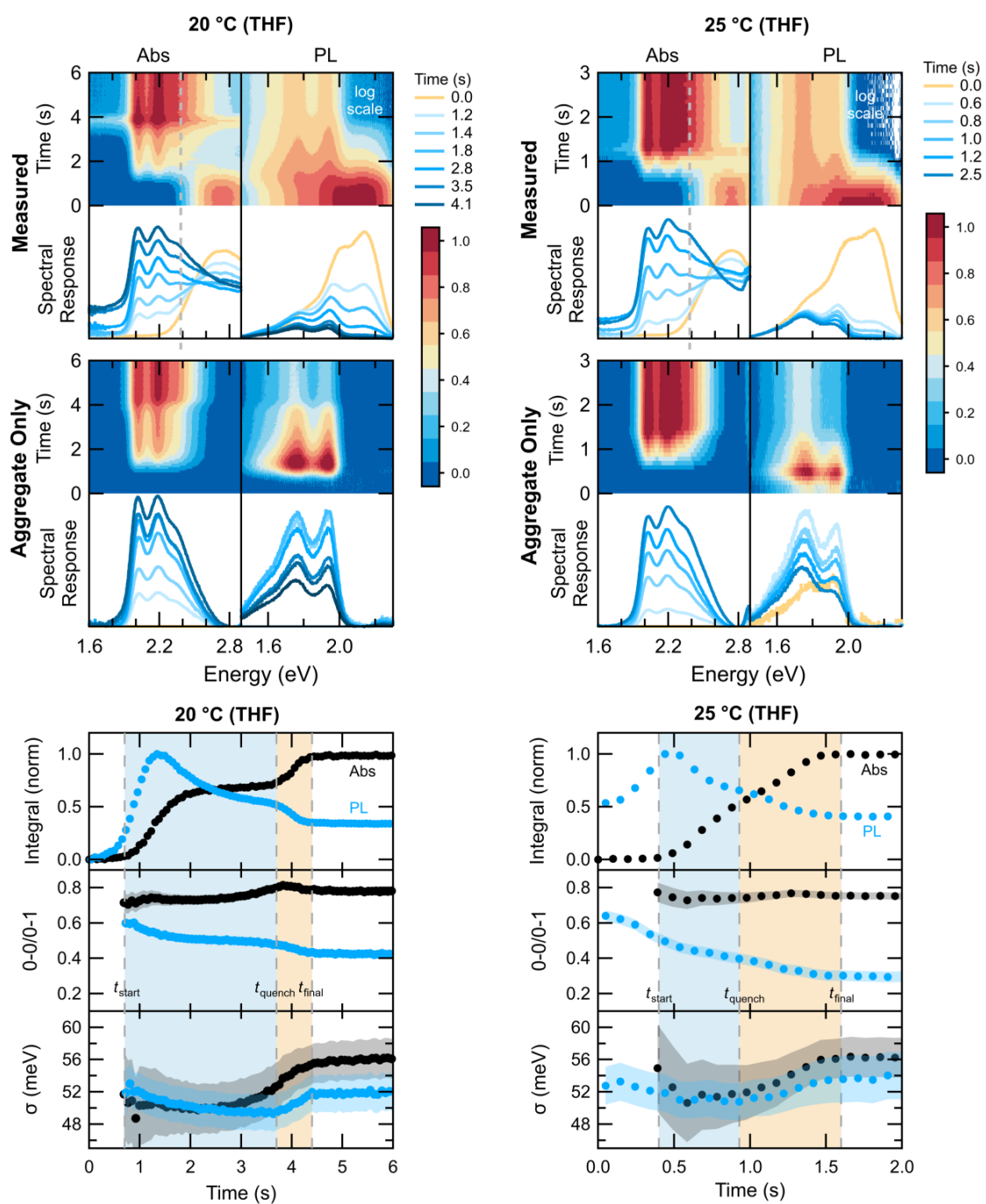


Figure S5 (continued): In situ spectra and evolution of optical parameters for all data sets.

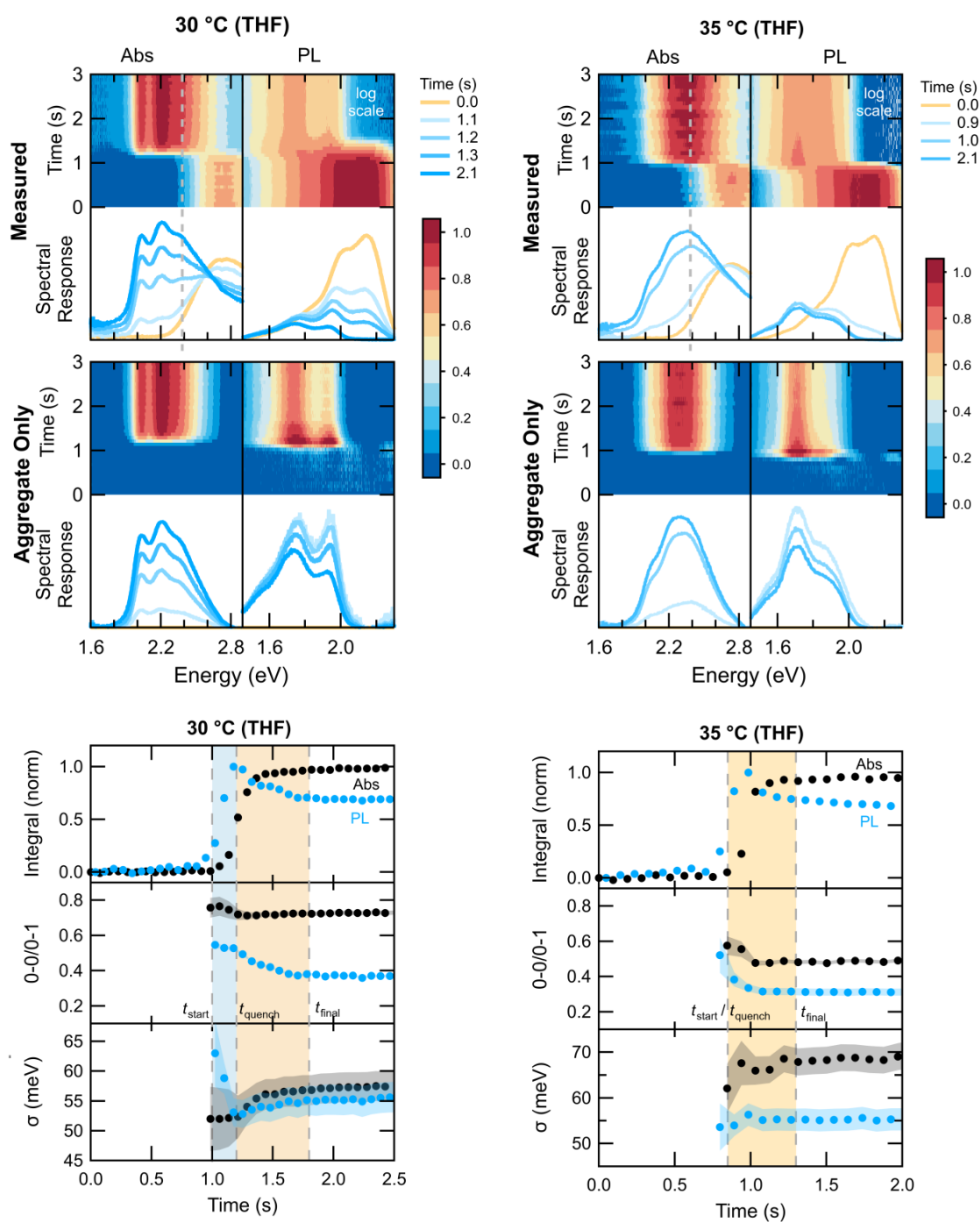


Figure S5 (continued): In situ spectra and evolution of optical parameters for all data sets.

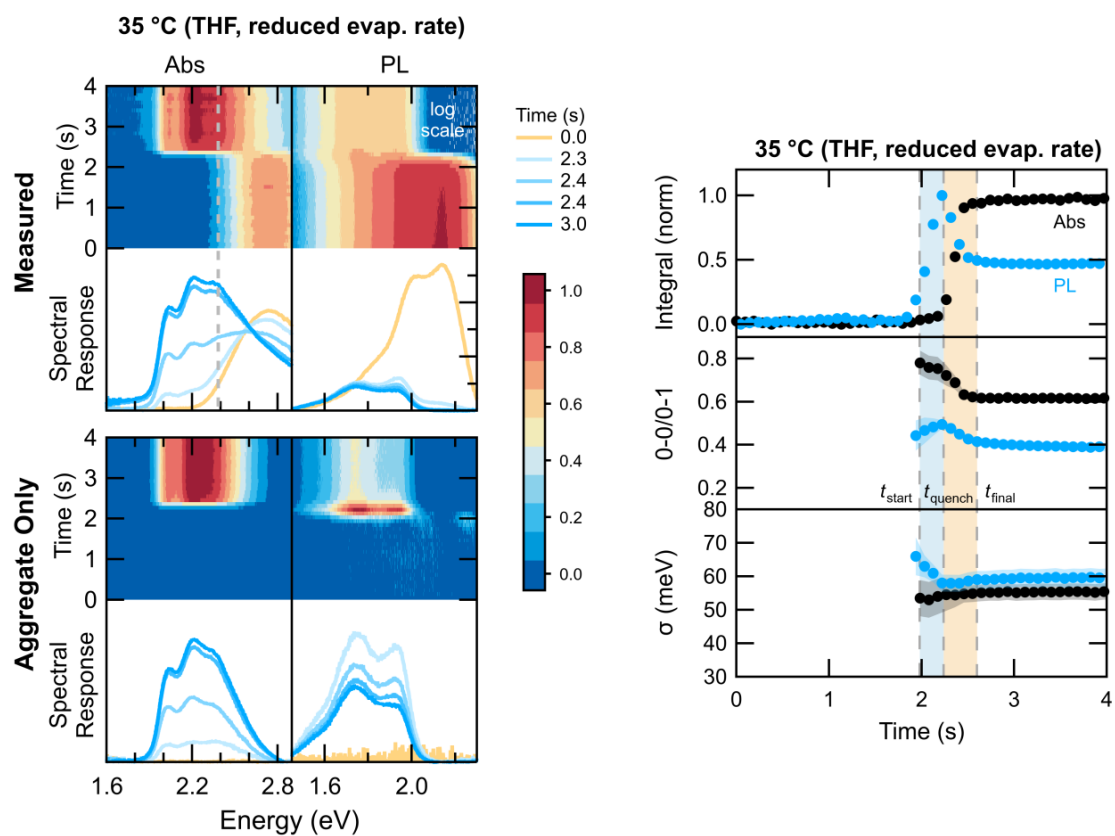


Figure S5 (continued): In situ spectra and evolution of optical parameters for all data sets.

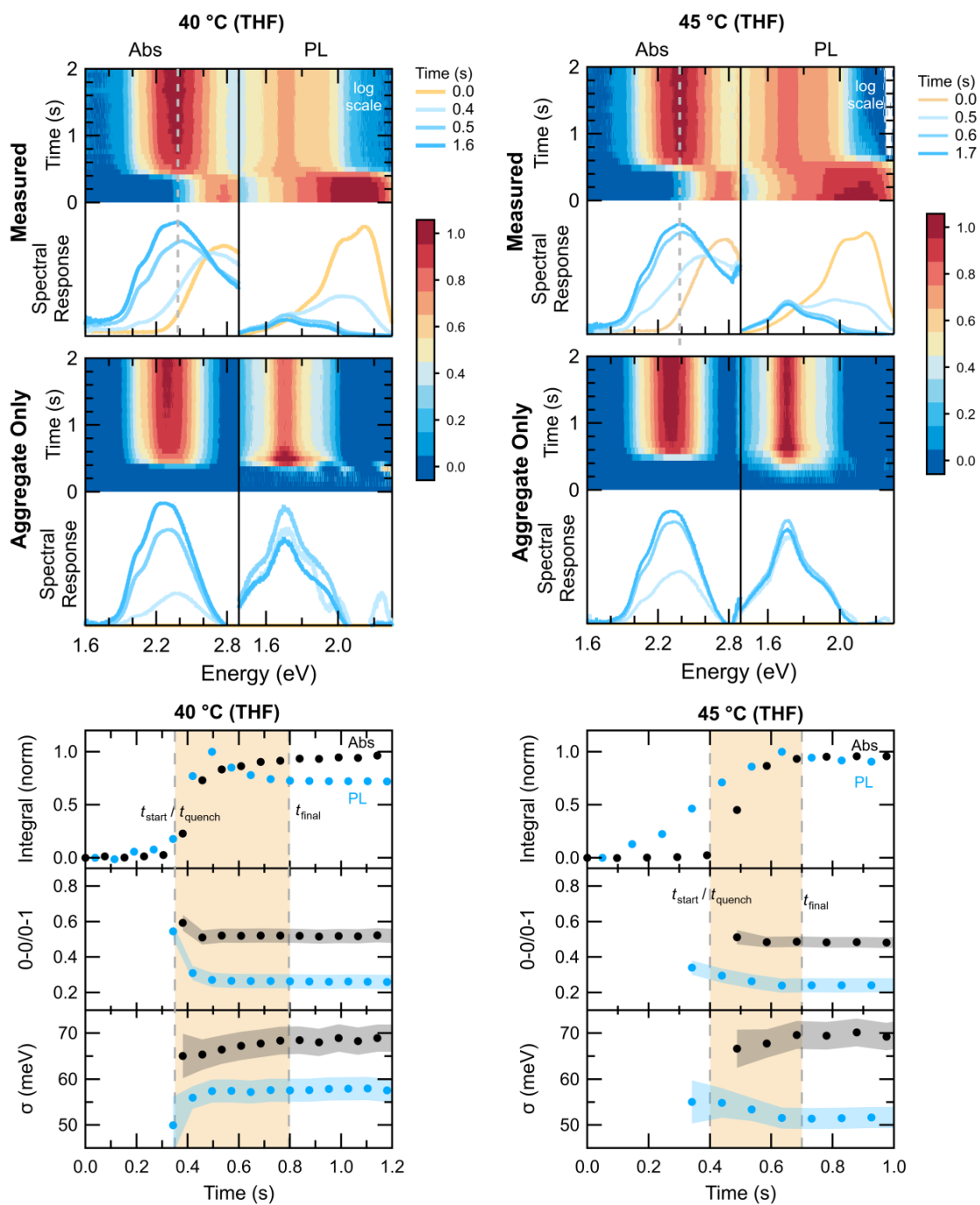


Figure S5 (continued): In situ spectra and evolution of optical parameters for all data sets.

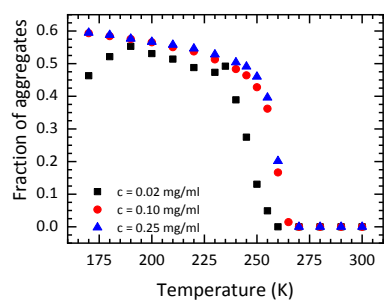


Figure S6: Temperature dependent fraction of aggregate of a different batch of P3HT in THF solution for different concentrations, showing change in T_c with concentration.

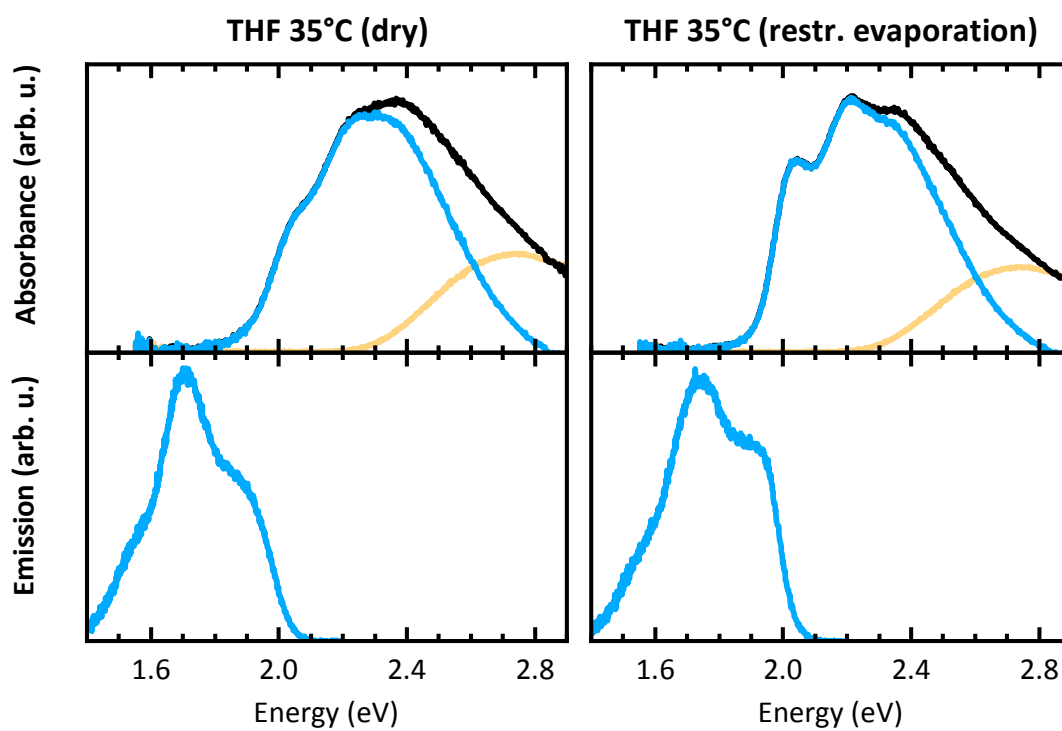


Figure S7: Comparison of steady state PL and absorption spectra of films coated from THF at 35°C without and with reduced evaporation rate. For absorption, the separation of the measured spectra (black) into disordered (orange) and aggregated (blue) contribution is also shown. In emission, only contributions of the aggregated phase are visible.

Table S1: Hansen solubility parameters for P3HT, chloroform (CF) and tetrahydrofuran (THF).¹⁰⁻¹³ δ_d , δ_p and δ_h indicate the dispersion, polar and hydrogen-bonding components, respectively.

Polymer/Solvent	δ_d (MPa ^{0.5})	δ_p (MPa ^{0.5})	δ_h (MPa ^{0.5}) ()
P3HT	18.6	2.9	3.2
CF	17.8	3.1	5.7
THF	16.8	5.7	8.0

Table S2: Approximate aggregate formation onset and completion times from in-situ spectra, corresponding to vertical lines in fitting parameter transients.

T_{sub} (°C)	t_{start} (s)		t_{quench} (s)		t_{final} (s)	
	CF	THF	CF	THF	CF	THF
5	1.00	-	5.40	-	6.4	-
10	4.95	-	6.35	-	6.9	-
15	0.85	-	1.15	-	1.8	-
20	1.78	0.70	1.78	3.70	2.3	4.4
25	1.54	0.40	1.54	0.93	2.0	4.6
30	0.85	1.00	0.85	1.20	1.5	4.8
35	-	0.85	-	0.85	-	1.3
40	-	0.35	-	0.35	-	0.8
45	-	0.4	-	0.4	-	0.7

References

- (1) Bannock, J. H.; Krishnadasan, S. H.; Nightingale, A. M.; Yau, C. P.; Khaw, K.; Burkitt, D.; Halls, J. J. M.; Heeney, M.; de Mello, J. C. Continuous Synthesis of Device-Grade Semiconducting Polymers in Droplet-Based Microreactors. *Adv. Funct. Mater.* **2013**, *23*, 2123–2129.
- (2) Wedler, S.; Bourdick, A.; Athanasopoulos, S.; Gekle, S.; Panzer, F.; McDowell, C.; Nguyen, T. Q.; Bazan, G. C.; Köhler, A. What Is the Role of Planarity and Torsional Freedom for Aggregation in a π -Conjugated Donor-Acceptor Model Oligomer? *J. Mater. Chem. C* **2020**, *8*, 4944–4955.
- (3) Buchhorn, M.; Wedler, S.; Panzer, F. Setup to Study the in Situ Evolution of Both Photoluminescence and Absorption during the Processing of Organic or Hybrid Semiconductors. *J. Phys. Chem. A* **2018**, *122*, 9115–9122.
- (4) Mooney, J.; Kambhampati, P. Get the Basics Right: Jacobian Conversion of Wavelength and Energy Scales for Quantitative Analysis of Emission Spectra. *J. Phys. Chem. Lett.* **2013**, *3318*, 3316–3318.
- (5) Newville, M.; Stensitzki, T.; Allen, D. B.; Ingargiola, A.; Nelson, A. *LMFIT: Non-Linear Least-Square Minimization and Curve-Fitting for Python. Astrophysics Source Code Library*. September 21, 2016, p .
- (6) Clark, J.; Silva, C.; Friend, R. H.; Spano, F. C. Role of Intermolecular Coupling in the Photophysics of Disordered Organic Semiconductors: Aggregate Emission in Regioregular Polythiophene. *Phys. Rev. Lett.* **2007**, *98*, 206406.
- (7) Yamagata, H.; Maxwell, D. S.; Fan, J.; Kittilstved, K. R.; Briseno, A. L.; Barnes, M. D.; Spano, F. C. HJ-Aggregate Behaviour of Crystalline 7,8,15,16-Tetraazaterrylene: Introducing a New Design Paradigm for Organic Materials. *J. Phys. Chem. C* **2014**, *118*, 28842–28854.
- (8) Ho, P. K. H.; Kim, J.-S.; Tessler, N.; Friend, R. H. Photoluminescence of Poly(p-Phenylenevinylene)–Silica Nanocomposites: Evidence for Dual Emission by Franck–Condon Analysis. *J. Chem. Phys.* **2001**, *115*, 2709.
- (9) Farouil, L.; Alary, F.; Bedel-Pereira, E.; Heully, J.-L. Revisiting the Vibrational and Optical Properties of P3HT: A Combined Experimental and Theoretical Study. *J. Phys. Chem. A* **2018**, *122*, 6532–6545.
- (10) Hansen, C. M. *Hansen Solubility Parameters: A User's Handbook*, 2nd ed.; CRC Press: Boca Raton, FL, USA, 2007.
- (11) Machui, F.; Langner, S.; Zhu, X.; Abbott, S.; Brabec, C. J. Determination of the P3HT:PCBM Solubility Parameters via a Binary Solvent Gradient Method: Impact of Solubility on the Photovoltaic Performance. *Sol. Energy Mater. Sol. Cells* **2012**, *100*, 138–146.
- (12) Duong, D. T.; Walker, B.; Lin, J.; Kim, C.; Love, J.; Purushothaman, B.; Anthony, J. E.; Nguyen, T. Q. Molecular Solubility and Hansen Solubility Parameters for the Analysis of Phase Separation in Bulk Heterojunctions. *J. Polym. Sci. Part B Polym. Phys.* **2012**, *50*, 1405–1413.
- (13) Barton, A. F. M. Solubility Parameters. *Chem. Rev.* **1975**, *75*, 731–753.

Appendix

A Graphical user interface for Franck-Condon analysis

I developed a graphical user interface to make the work flow for Franck-Condon fitting easier. It allows to process several spectra from the same file and fitting as many progressions as desired. Further, it automatically calculates the normalization to the photon density of states. Results can be saved to data files along with a plot of the fit. Further processing and plotting, for example in Origin, is easily possible. Figure A.1 shows a screenshot with data and fits from the publication in Chapter 7 (emission of TT in hexane at a concentration of 5.0×10^{-6} M at 220 K, fitted with two multimode Franck-Condon progressions). The source code of the graphical user interface is rather lengthy and can be obtained upon request, the code for the relevant calculations is printed on the following pages.

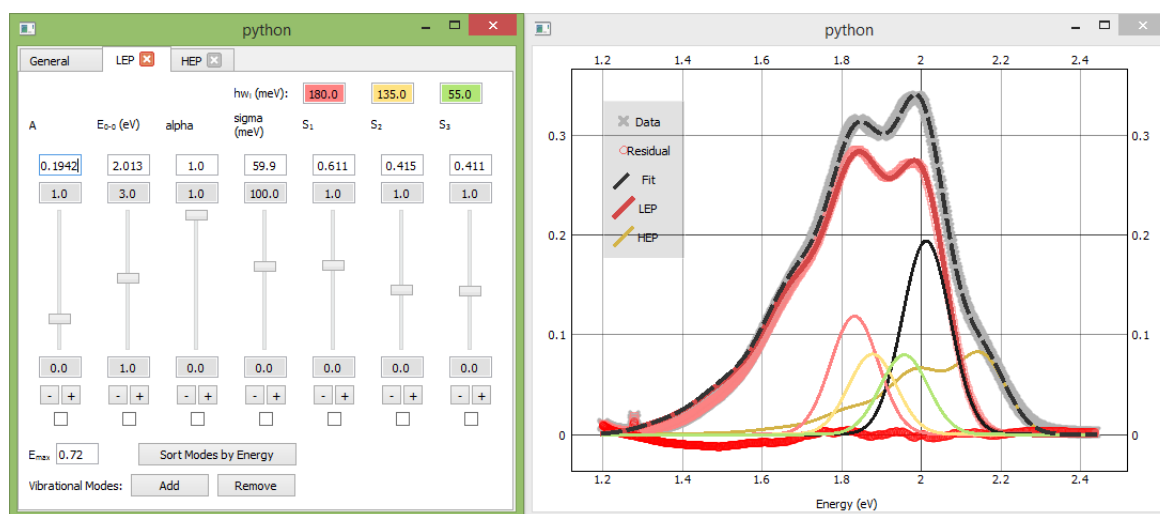


Figure A.1: Screenshot of both windows of the fitting program. The left window contains all adjustable parameters and general settings, the right window shows a plot with the correctly normalized data, all individual progressions, the 0–0 and all 0–1 peaks of the active progression, and the residuals. In case of more than one Franck-Condon progressions, the plot contains also a line, which corresponds to the difference of data and the sum of all inactive progressions.

Source code for calculating Franck-Condon progressions

```
"""
Created on Tue May 23 17:43:16 2017

@author: Stefan Wedler
5 Class which calculates a multimode Franck-Condon progression, which is able
to consider as many vibrational modes as wanted.

Formula for fitting is described in
Ho et al, J. Chem. Phys., 115, 2709 (2001); doi: 10.1063/1.1372508
10 """

import scipy as sc
from scipy.special import factorial
import os
15 from time import strftime

# String constants, which define the identifiers for the parameter dict.
# 1. Constants necessary for every FC progression
_PARAM_E00 = 'E00'
20 _PARAM_EVIB = 'E_vib'
_PARAM_S = 'S'
_PARAM_SIGMA = 'sigma'
_PARAM_AMPL = 'A'

# 2. Constant for aggregation effects:
25 # suppression/enhancement of 0-0 peak, as described in
# Clark 2007; doi: 10.1103/PhysRevLett.98.206406
_PARAM_ALPHA = 'alpha'

# String constants, which define the identifiers for the options dict
30 _OPTION_NORM = 'normalize'
_OPTION_EMAX = 'E_max'
_OPTION_MODE = 'mode'

#%% Helper functions for array conversion, saving and loading parameters
35 def to_array(inp, str_func, var):
    #Helper-function, which takes an input and converts into numpy array.
    if type(inp) is int: inp = float(inp)
    if type(inp) is float:
        inp = [inp]
40 if type(inp) is list:
        inp = sc.array(inp)
    elif type(inp) is not sc.ndarray:
        print(str_func + ': Input error')
        print(' cannot convert ' + var + ' to array-like structure')
45 return []
    return inp

def read_dict(file_in):
    """
50 Reads a dictionary from a file and automatically converts
values of parameter/option keys to the correct dtype.
The keys must be located in the first column and the values
```

```

in the second column. The columns must be separated by single tabs.

55  Input
    -----
    file_in: string
        The name of the file, which will be imported.

60  Returns
    -----
    Dictionary with correct dtypes for parameters and options.
    """
    # read keys from col 1 and values from col 2
65  try:
        keys = sc.genfromtxt(file_in, dtype=str, delimiter='\t', usecols=(0))
        vals = sc.genfromtxt(file_in, dtype=str, delimiter='\t', usecols=(1))
        res = dict(zip(keys, vals))
    except:
70     res = {}

    # make correct type conversions for each value
    # for the array-types: add ',' to prevent conversion problems
    #             with single values
    if _PARAM_E00 in res: res[_PARAM_E00] = float(res[_PARAM_E00])
75  if _PARAM_EVIB in res: res[_PARAM_EVIB] = sc.array(eval(res[_PARAM_EVIB]+' ',''))
    if _PARAM_S in res: res[_PARAM_S] = sc.array(eval(res[_PARAM_S]+' ',''))
    if _PARAM_SIGMA in res: res[_PARAM_SIGMA] = float(res[_PARAM_SIGMA])
    if _PARAM_AMPL in res: res[_PARAM_AMPL] = float(res[_PARAM_AMPL])
    if _PARAM_ALPHA in res: res[_PARAM_ALPHA] = float(res[_PARAM_ALPHA])
80  if _OPTION_EMAX in res: res[_OPTION_EMAX] = float(res[_OPTION_EMAX])
    if _OPTION_NORM in res: res[_OPTION_NORM] = bool(eval(res[_OPTION_NORM]))
    return res

def write_dict(file_out, dict_out, comment = ''):
85     """
        A dictionary is written to a file in human readable format.
        An optional comment can be written on top of the dictionary.

        Input
        -----
        file_out: string
            Contains the file name of the output file.

        dict_out: dict
95         The dictionary, which is written into the output file.

        comment: string (optional)
            optional comment
        """
100    with open(file_out, 'w') as f:
        # handle comment
        if comment != '':
            comment = '# ' + comment.replace('\n', '\n# ') + '\n'
            f.write(comment)
105    # export dict
    for key in dict_out:

```

```

        f.write(str(key) + '\t')
        if isinstance(dict_out[key],sc.ndarray):
            # write numpy arrays elementwise, separated by comma
110         str_tmp = ['{: .4}'.format(s) for s in dict_out[key]]
            f.write(', '.join(str_tmp) + '\n')
        else:
            f.write(str(dict_out[key]) + '\n')

115  """ Helpers for actual FC calculation
def get_vib_numbers(E_vib, E_max):
    """
    Calculates all possible combinations of vibrational quanta recursively,
    whose combined energy is smaller than E_max. The vibrational energies
120     E_vib must be given as list-like object

    Example output
    -----
    One mode:

125     >>> get_vib_numbers(0.15, 0.5)
    [array([0]), array([1]), array([2]), array([3])]
    """
    # E_vib must be converted from list/float to array
130     E_vib = to_array(E_vib, 'get_vib_numbers', 'E_vib')
    # set up result list
    res = []
    # number of vibronic modes
    N = len(E_vib)
    # number of maximum vibronic quanta. Set to one for all non-positives
135     if E_vib[-1] > 0:
        N_max = E_max/E_vib[-1] + 0.001
    else:
        N_max = 1
140     if N==1:
        # one mode: vibronic quanta up to E_max
        for i in sc.arange(N_max, dtype = int):
            res += [(i,)]
    elif N > 1:
145         # more modes: vary the last mode ...
        for m in sc.arange(N_max, dtype = int):
            # ... and make list of other modes recursively
            E_max2 = E_max - m*E_vib[-1]
            res_tmp = [tuple(r) for r in get_vib_numbers(E_vib[:-1], E_max2)]
150             for l in res_tmp:
                res += [l+(m,)]
    return [sc.array(r) for r in res]

155 def calculate_lineshape(x, E0, sigma):
    # Calculates the line shape function (currently only Gaussian).
    gaussian = sc.exp(-0.5 * ((x - E0)/sigma)**2)
    return gaussian

160 # Container class to wrap up all the house keeping

```

```

class FCprogressionMulti():
    # set up all variables and options
    def __init__(self,energy=None,parameters={},**options):
        self.vibrNumbers = None
165     self.FCfactors = None
        self.vibrLines = None
        self.progression = None
        self.energy = energy
        self.mainLines = []
170     # set up parameters, read from filename if not empty
        if isinstance(parameters,str) and os.path.isfile(parameters):
            parameters = read_dict(parameters)
        self.set_parameters(parameters)
        # now the same for all of the options. Take options from parameters
175     # in case there are option keys inside them, but override
        # by explicit options from **options
        options = {**parameters,**options}
        self.set_options(**options)
        # and calculate the progression
180     self.calculate_vibr_numbers()

    # sets all parameters. Use defaults for missing parameters. Should only be
    # used for complete new sets of parameters
    def set_parameters(self,parameters):
185     self.parameters = {}
        # E00
        if _PARAM_E00 in parameters: p = parameters[_PARAM_E00]
        else: p = 0
        self.parameters[_PARAM_E00] = p
190     # amplitude
        if _PARAM_AMPL in parameters: p = parameters[_PARAM_AMPL]
        else: p = 1.0
        self.parameters[_PARAM_AMPL] = p
        # 0-0 suppression
195     if _PARAM_ALPHA in parameters: p = parameters[_PARAM_ALPHA]
        else: p = 1.0
        self.parameters[_PARAM_ALPHA] = p
        # sigma
        if _PARAM_SIGMA in parameters: p = parameters[_PARAM_SIGMA]
200     else: p = 0.05
        self.parameters[_PARAM_SIGMA] = p
        # huang rhys
        if _PARAM_S in parameters: p = parameters[_PARAM_S]
        else: p = sc.array([1.0])
205     self.parameters[_PARAM_S] = p
        # vibrational energies
        if _PARAM_EVIB in parameters: p = parameters[_PARAM_EVIB]
        else: p = sc.array([0.18])
        self.parameters[_PARAM_EVIB] = p
210

    # Set all options given as dictionary. Use defaults for missing options.
    def set_options(self,**options):
        self.options = {}
        # Normalize to 0-0

```

```

215     if _OPTION_NORM in options: o = options[_OPTION_NORM]
        else: o = True
        self.options[_OPTION_NORM] = o
        # E_max
220     if _OPTION_EMAX in options: o = options[_OPTION_EMAX]
        else: o = 4 * self.parameters[_PARAM_EVIB][0]
        self.options[_OPTION_EMAX] = o
        # Absorption or PL
        if _OPTION_MODE in options: o = options[_OPTION_MODE]
        else: o = 'abs'
225     self.options[_OPTION_MODE] = o

    # set the energy axis, where the calculations are performed
    def set_energy(self,energy):
        if isinstance(energy,sc.ndarray):
230             self.energy = energy
            self.calculate_vibr_lines()

    def update_progression(self):
        self.calculate_vibr_numbers()
235

    def calculate_vibr_numbers(self):
        # calculate the vibrational numbers
        hw = self.parameters[_PARAM_EVIB]
        eMax = self.options[_OPTION_EMAX]
240         self.vibrNumbers = sc.array(get_vib_numbers(hw,eMax))
        self.mainLines = []
        # make a list of all vibronic transitions with exactly 1 quantum
        for i in range(len(self.vibrNumbers)):
            if self.vibrNumbers[i].sum() == 1:
245                 self.mainLines.append(i)
        self.calculate_FC_factor()

    def calculate_FC_factor(self):
        vib = self.vibrNumbers
250         S = self.parameters[_PARAM_S]
        self.FCfactors = sc.zeros(len(self.vibrNumbers))
        fc = self.FCfactors
        for i in range(fc.size):
            prefactors = S**vib[i]/factorial(vib[i])
255             # for fitting, the exp(-S) term is not calculated, as it affects
            # all single lines simultaneously
            if _OPTION_NORM in self.options and not self.options[_OPTION_NORM]:
                prefactors *= sc.exp(-S)
            fc[i] = sc.product(prefactors)
260         # recalculate vibrational lines
        self.calculate_vibr_lines()

    def calculate_vibr_lines(self):
        e = self.energy
265         # checking neccessary as otherwise some weird errors pops up...
        if isinstance(e,sc.ndarray):
            # prepare arrays for actual calculation
            vibs = self.vibrNumbers

```

```

270     vib_lines = sc.zeros((len(vibs),len(e)))
        self.vibrLines = vib_lines
        # get numeric values for the progression
        A = self.parameters[_PARAM_AMPL]
        E00 = self.parameters[_PARAM_E00]
        alpha = self.parameters[_PARAM_ALPHA]
275     E_vib = self.parameters[_PARAM_EVIB]
        sigma = self.parameters[_PARAM_SIGMA]
        # use this factor to put the vibronic transitions on the
        # correct side of the 0-0 transition
        if self.options[_OPTION_MODE].lower() == 'abs': AbsPL = 1
280     else: AbsPL = -1
        # calculate contributing single lines and store in vib_lines[i]
        for i,vib in enumerate(vibs):
            # calculate position of considered single line. note: AbsPL = +-1
            E_vib_line = E00 + AbsPL * sc.sum(E_vib*vib)
285     vib_lines[i] = calculate_lineshape(e, E_vib_line, sigma)
            vib_lines[i] *= self.FCfactors[i]
        vib_lines *= A
        # modify 0-0 peak. If not explicitly set, then alpha is 1.0
        vib_lines[0] *= alpha
290     # recalculate whole progression
        self.calculate_progression()

def calculate_progression(self):
    self.progression = sc.sum(self.vibrLines,axis=0)
295

# Here are all the helper functions to vary a distinct parameter
# and recalculate the whole progression
def set_A(self,A):
    if self.parameters[_PARAM_AMPL] == 0:
300     self.parameters[_PARAM_AMPL] = A
        self.calculate_vibr_lines()
    elif isinstance(self.energy,sc.ndarray):
        factor = A / self.parameters[_PARAM_AMPL]
        self.parameters[_PARAM_AMPL] = A
305     self.vibrLines *= factor
        self.calculate_progression()
    else: self.parameters[_PARAM_AMPL] = A

def set_alpha(self,alpha):
310     if self.parameters[_PARAM_ALPHA] == 0:
        self.parameters[_PARAM_ALPHA] = alpha
        self.calculate_vibr_lines()
    elif isinstance(self.energy,sc.ndarray):
        factor = alpha / self.parameters[_PARAM_ALPHA]
315     self.parameters[_PARAM_ALPHA] = alpha
        self.vibrLines[0] *= factor
        self.calculate_progression()
    else: self.parameters[_PARAM_ALPHA] = alpha

320     def set_e00(self,e00):
        self.parameters[_PARAM_E00] = e00
        self.calculate_vibr_lines()

```

```

def set_sigma(self, sigma):
325     self.parameters[_PARAM_SIGMA] = sigma
        self.calculate_vibr_lines()

def set_S(self, S, i):
    S_old = self.parameters[_PARAM_S]
330     if len(S_old) > i:
        S_old[i] = S
        self.calculate_FC_factor()

def set_hw(self, hw, i):
335     hw_old = self.parameters[_PARAM_EVIB]
        if len(hw_old) > i:
            hw_old[i] = hw
            self.calculate_vibr_numbers()

def add_vibration(self, hw, S):
340     self.parameters[_PARAM_S] = sc.append(self.parameters[_PARAM_S], S)
        self.parameters[_PARAM_EVIB] = sc.append(self.parameters[_PARAM_EVIB], hw)
        self.calculate_vibr_numbers()

def remove_vibration(self, i):
345     if i >= len(self.parameters[_PARAM_S]): return
        self.parameters[_PARAM_S] = sc.delete(self.parameters[_PARAM_S], i)
        self.parameters[_PARAM_EVIB] = sc.delete(self.parameters[_PARAM_EVIB], i)
        self.calculate_vibr_numbers()

350
def set_E_max(self, emax):
    self.options[_OPTION_EMAX] = emax
    self.calculate_vibr_numbers()

355
def set_normalize(self, norm):
    self.options[_OPTION_NORM] = norm
    self.calculate_FC_factor()

def set_mode(self, mode):
360     self.options[_OPTION_MODE] = mode
        self.calculate_vibr_lines()

# get the main vibronic modes for plotting
def get_main_modes(self):
365     out = [sc.array(self.vibrLines[0])]
        for i in self.mainLines:
            out.append(sc.array(self.vibrLines[i]))
        return out

370
# save parameters in a file that is human readable and can be used to
# create a FCprogressionMulti object
def save_parameters(self, fileOut, **options):
    comment = 'Parameter report Franck-Condon analysis.\n'\
        + 'Runtime: ' + strftime("%Y-%m-%d %H:%M:%S")
375     dict_out = {**self.parameters, **self.options, **options}
        write_dict(fileOut, dict_out, comment)

```

B Analysis of time-resolved data using reconvolution fitting

Every experimental setup for time resolved measurements has a finite temporal resolution. This resolution is usually characterized by the instrument response function (IRF), which distorts the actual response of a sample $R(t)$. It is a superposition of several contributions, for example the finite pulse width of a pulsed excitation laser, the characteristic response times of detection units, or the bandwidth of electronic measurement devices. The undistorted response of the sample can in principle be recovered, if the IRF is known precisely. The reason is that the measured signal $S(t)$ can be written as a convolution (denoted as star operator) of the response of the sample with the IRF:

$$S(t) = (R * \text{IRF})(t) = \int_{-\infty}^{\infty} R(t') \cdot \text{IRF}(t - t') dt' \quad (\text{B.1})$$

The convolution theorem states that the convolution of two functions in the time domain reduces to a simple multiplication in the Fourier domain according to

$$S(\omega) = R(\omega) \cdot \text{IRF}(\omega) \quad (\text{B.2})$$

where the Fourier transform is indicated by the ω -dependence. In principle, this relation allows to deconvolute the undistorted response $R(t)$ of the sample by dividing the Fourier transform of the measurement $S(\omega)$ by the Fourier transform of the IRF and performing an inverse Fourier transform. However, this approach does not work for actual measurements, as all measured signals are subject to noise. A more practical approach is reconvolution. The response of the sample is modelled by appropriate decay laws. For example, the photoluminescence decay of a single emitter will follow an exponential decay law according to $R(t) = A \cdot \exp(-kt)$ in the most simple case. This a priori information can be used to analyse the decay curve $S(t)$ in a reconvolution fit

$$S(t) = \int_{-\infty}^{\infty} A \cdot \exp(-kt') \cdot \text{IRF}(t - t') dt' \quad (\text{B.3})$$

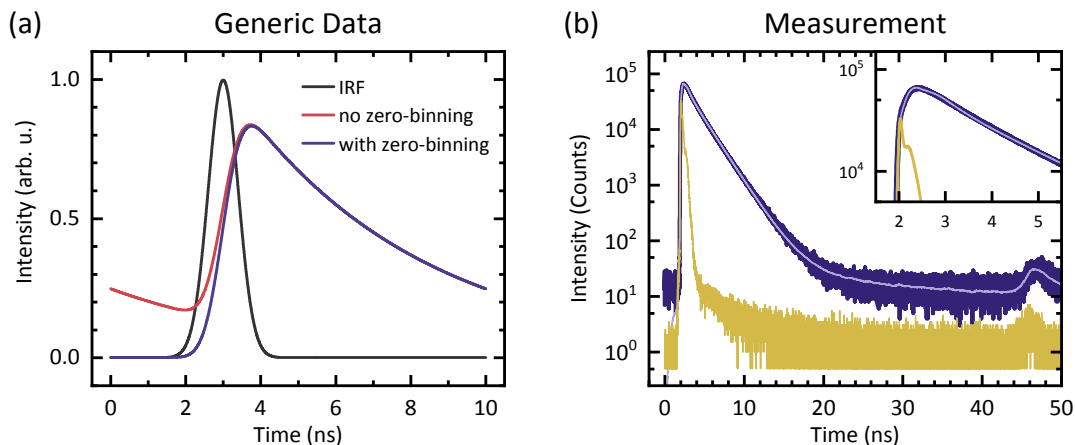


Figure B.1: Examples for convolution calculations. (a) A generic monoexponential decay with rate constant $k = 0.2 \text{ ns}^{-1}$ is convoluted with a Gaussian IRF centered at 3 ns and $\sigma = 0.4 \text{ ns}$ with and without zero-binning. (b) Biexponential reconvolution fit (light blue) of TT in chlorobenzene at a concentration of $5 \times 10^{-5} \text{ M}$, excited at 485 nm and detected at 640 nm (dark blue). The inset shows a magnification of the first 5 ns.

Nonlinear least-square algorithms can calculate the most probable values for the fitting parameters A and k . For this it is important to keep numerical efficiency in mind. The convolution operation is computational expensive, and for typical time correlated single photon counting (TCSPC) measurements this can become a bottleneck, as time traces consist of $2^{16} = 65536$ individual data points. The reconvolution theorem in Equation B.2 provides an easy solution, as the numerical expensive integration is replaced by Fourier transformations, which are numerically cheap when using a fast Fourier transform (FFT) algorithm. However, some practical pitfalls can arise due to the cyclic nature of the FFT for discrete datasets. If the FFT is directly applied to the measured $S(t)$ and $\text{IRF}(t)$, the algorithm assumes that the data is continued periodically. This can be circumvented by so-called zero-binning, that means for a time series consisting of N distinct data points, a further number of N zeros is attached at the end of that data series. Figure B.1 a shows the difference for a generic exponential decay with a rate constant of $k = 0.2 \text{ ns}^{-1}$. It is convoluted with a Gaussian IRF, centered at 3 ns and a width of $\sigma = 0.4 \text{ ns}$. If zero-binning is not performed, the temporal evolution of the exponential decay is assumed to be periodic. This results in a finite residual decay at the beginning. Including zero-binning eliminates this mathematical violation of causality.

I implemented a Python script to perform reconvolution fittings to time resolved measurements, for example the decay of photoluminescence from TCSPC measurements. Figure B.1 b shows an example of a biexponential fit to the decay of TT emission in chlorobenzene ($5 \times 10^{-5} \text{ M}$) detected at 640 nm after pulsed excitation at 485 nm. The IRF is also shown in

yellow and was acquired by measuring the time trace at a detection wavelength of 485 nm, which corresponds to the laser wavelength. The reconvolution fit can recover two decaying contributions of (1.94 ± 0.07) ns (85% intensity) and (0.38 ± 0.07) ns (15% intensity). Furthermore, the measurement artefact near 50 ns is fully recovered by the reconvolution fit. This example further shows that an apparent slower build-up of the signal right after the excitation can be due to the finite width of the IRF, as can be seen in the inset of Figure B.1. Therefore, care needs to be taken to distinguish whether signal build-ups are real and hint to actual physical processes in the material, or whether this is an effect of the IRF shape.

Source code of the analysis script

```
"""
Created on Thu Aug 31 13:48:30 2017

@author: Stefan Wedler
5
little script to do some reconvolution fitting for tcspc measurements.
currently there are three model decays implemented with only the monoexponential
explicitly shown here; more models should be self-explanatory when looking
at the implemented ones.
10
(re)convolution is done by an fft-algorithm, exploiting the convolution
theorem to speed up calculations.
"""

15 import numpy as np
import matplotlib.pyplot as plt
import lmfit

# here comes the convolution stuff which takes care of that nasty
20 # indexing you have when fiddling with ffts (zero binning to avoid
# that the convolution is assumed to be periodic)
def convolve(arr1, arr2):
    n = len(arr1)
    arr1_fft = np.fft.rfft(arr1,n=2*n)
    25 arr2_fft = np.fft.rfft(arr2,n=2*n)
    # residual imaginary parts due to rounding errors are discarded
    return np.real(np.fft.irfft(arr1_fft*arr2_fft)[:n])

# Model function for fitting. It returns either the model for data==None, the
30 # residual for data!=None and the weighted residual for eps!=None.
# For missing IRF, only the model is calculated without convolution
def convolutionMonoExponential(params,t,data=None,irf=None,eps=None):
    # get the parameters and set defaults for missing optional parameters
    parvals = params.valuesdict()
    35 amp = parvals['amplitude']
    tau = parvals['tau']
    # t_irf is a temporal offset between data and irf
    if 't_irf' in parvals:
```

```

        t_irf = parvals['t_irf']
40     else:
        t_irf = 0
        # c is a constant offset. sometimes you have to fiddle with that as well
        if 'c' in parvals:
            c = parvals['c']
45     else:
        c=0
        # calculate the model decay
        model = amp * np.exp(-t/tau)
        # do the convolution of model and irf
50     if irf is not None:
        irf = np.interp(t-t_irf,t,irf,0,0)
        dt = np.diff(t)[0]
        # dt is necessary because the convolution is usually an integral
        model = convolve(model,irf)*dt
55     # add optional offset. I guess it could also be added before the convolution...
        model += c
        # return either model ...
        if data is None:
            return model
60     # ... or residual ...
        if eps is None:
            return model-data
        # ... or the scaled residual when uncertainties are given
        eps = np.where(eps>0,eps,1)
65     return (model-data)/eps

#%% here comes all the real fitting stuff (and setting up inputs)
# choose the fitting function
fitfunction = convolutionMonoExponential
70 # set up the input and output filenames
file_in_data = 'CT in Hex 0.25g-1/180K_800nm.dat'
file_in_irf = 'CT in Hex 0.25g-1/180K_IRF.dat'
file_out = 'CT in Hex 0.25g-1/180K_800nm_FitBiExp.dat'
# if you have short decays and don't want to have all that zeros
75 # dangling at the end of your data, using disk space unnecessarily,
# everything beyond tmax is cropped
tmax = 100
# Data import. maybe you need to adjust skip_header and skip_footer, as they
# now skip that long header if you export it
80 t, irf = np.genfromtxt(file_in_irf,skip_header=133,skip_footer=1,unpack=True)
t,data = np.genfromtxt(file_in_data,skip_header=133,skip_footer=1,unpack=True)
# cropping data
i_tmax = np.argmin(abs(t-tmax))
t=t[:i_tmax]
85 irf = irf[:i_tmax]
data = data[:i_tmax]
# normalizing the irf to its area; gives less large amplitudes
irf = irf / np.trapz(irf,t)
# set up Parameters for fitting. unfortunately you need to adjust that
90 # manually if you want a different fit function to be used
params = lmfit.Parameters()
params.add('amplitude',1e4)

```

```

params.add('tau',2.2,min=.2)
params.add('c',6,vary=True)#,min=0)
95 params.add('t_irf',-0.01,vary=True)
# fitting is done here. as the tcspc count data should be poisson distributed,
# the variance can be calculated according to sigma^2 = counts. the error is then
# estimated as np.sqrt(data)
fit = lmfit.minimize(fitfunction,params=params,args=(t,data,irf,np.sqrt(data)))
100 # print the result and write out all that stuff into output files
print(lmfit.fit_report(fit))
header = 'Reconvolution Fit using ' + fitfunction.__name__ + '\n'
header = header + lmfit.fit_report(fit)
header = header + '\n\nTime (ns)\tData (Counts)\tIRF (normalized)\tFit\tResidual'
105 irf_shifted = np.interp(t-fit.params['t_irf'].value,t,irf,0,0)
data_out = np.concatenate((t,data,irf_shifted,fitfunction(fit.params,t,irf=irf),
                        data - fitfunction(fit.params,t,irf=irf))).reshape((5,len(t))).transpose()
np.savetxt(file_out,data_out,fmt='%.5e',delimiter='\t',header=header)

110 # plot the results always in the same figure, which is ensured by num=1,clear=True
fig,ax = plt.subplots(figsize = (8,6),num=1,clear=True)
#ax.plot(t,abs(fit.residual*100))
ax.semilogy(t,data)
ax.plot(t,irf*1e3)
115 ax.plot(t,fitfunction(fit.params,t,irf=irf))

```


C Improvements of the ultrafast transient absorption setup

During the driving force work it turned out that there are some limitations of the setup as it existed. The main reason is that detection was carried out using a photodiode in combination with a lock-in amplifier. Therefore, data acquisition in the two-dimensional space wavelength vs. time delay could only be performed point by point. Scanning within this two-dimensional space had to be carried out in a highly selective way, as each individual measurement point took 10s or more, depending on the signal quality. One possibility to speed up data acquisition is to replace the monochromatic detection scheme by a polychromatic detection. The combination (slow) chopper–photodiode–lock-in amplifier can be replaced by a line scan camera. To further increase acquisition speed and the signal/noise ratio, it is desirable to implement a detection scheme, which relies on true shot-to-shot measurements. For this, every second pump pulse needs to be blocked by a mechanical chopper. The repetition rate of the RegA 9000 laser system is at 100 kHz, which is large compared to high power amplifiers with repetition rates between 1 kHz and 10 kHz. This creates certain challenges for shot-to-shot measurements. Every second pump pulse needs to be reliably blocked. In principle, acousto-optic modulators can be used as pulse pickers, but they introduce too much loss of laser power, which is critical for this setup. Thus, a mechanical chopper is needed, which can modulate with half the laser repetition rate (here: 50 kHz). It is possible to synchronize the rotation of a chopper wheel to modulation frequencies up to around 10 kHz, which is too low here. It is however possible to synchronize the laser to the rotation of the chopper. Kanal et al. [215] have the same laser system and found a home-built technical solution. I adopted their solution to the transient absorption setup in the Köhler lab.

For this, I instructed the electronics workshop of the university to construct a synchronization unit as well as a high speed mechanical chopper based on the published solution (commercial systems were found to be unreliable).²¹⁵ At first, I used a chopper blade from Scitec Instruments with 445 slits. However, the slit width was too narrow to ensure the generation of reliable synchronization signals. As a result I used a chopper blade with 300 slits fabricated from the mechanical workshop, which reduces the maximum laser repetition frequency to 85 kHz. Incorporating the chopper device into the setup required some redesign of the experimental layout, which is shown in Figure C.1. The basic working principle

is explained and well documented in the PhD thesis of Thomas Unger and my Master thesis,^{216,217} which also both contain the original layout. In short for the new layout, the Vitesse Duo pumps and seeds the regenerative amplifier RegA 9000, which produces 200 fs pulses at 800 nm with a pulse energy of 6 μ J. An autocorrelator uses a small part to monitor pulse shape and width. About 15 % of the RegA output is separated by a beam splitter to generate white-light in a YAG crystal as the probe beam. It is focussed onto the sample and subsequently coupled into a Shamrock SR193 spectrograph for detection. The remaining part of the RegA output is directed to an optical parametric amplifier (OPA 9400), which is used to generate tunable pump pulses. The output of the OPA is directed over a translational stage (Thorlabs DDS300) to control the temporal delay between pump and probe pulse. Subsequently, the pump beam is guided through the fast chopper by two off-axis parabolic mirrors. As the synchronization signal from the chopper is used to trigger the RegA, every second laser pulse is blocked by the chopper blade. Finally, the pump beam is focussed by a spherical mirror onto the white-light spot on the sample, and is dumped afterwards.

For detection, I replaced the photodiode with a fast line scan camera (AViVA EM1), which is synchronized with the laser repetition rate. Two subsequent frames can then be used for calculation of a full transient absorption spectrum at a fixed temporal delay between pump and probe pulses. For data acquisition, the delay stage is set to a certain temporal delay and up to 10000 laser shots are averaged. Thus, one full spectrum at a fixed pump-probe delay can be measured within less than one second, which is faster by orders of magnitude compared to the former lock-in detection scheme. Then the translational stage moves to the next point and the next temporal delay can be measured. In principle, the fast chopper still allows using the lock-in detection scheme. This can be necessary in the NIR spectral range, where the camera is insensitive. For this, the lock-in amplifier locks to the repetition frequency of the laser, which can be viewed as a quasi-shot-to-shot detection and still speeds up data acquisition.

To improve the signal/noise ratio, the full measurement range can be scanned several times. A common approach is that the temporal measurement range is scanned randomly to minimize noise from laser fluctuations. The original translational stage is moved by a stepper motor, which drives a lead screw. Albeit allowing for precise positioning, this operational principle is inherently slow with translational speeds of less than 1 cm/s. Therefore I replaced it with a direct drive translational stage, which is driven by a DC motor. It can reach translational speeds up to 40 cm/s and speeds up measurement significantly. A further advantage is that it can be moved manually once power is off, which greatly simplifies optical alignment.

I measured the transient absorption of PDOPT in THF at a concentration of 0.2 g/l to verify the functionality after all changes. The sample was excited at 500 nm, the scan was performed for 300 positions of the translational stage, 8000 single-shot spectra were averaged per point. The whole scan was repeated 20 times, which lead to a total measurement time

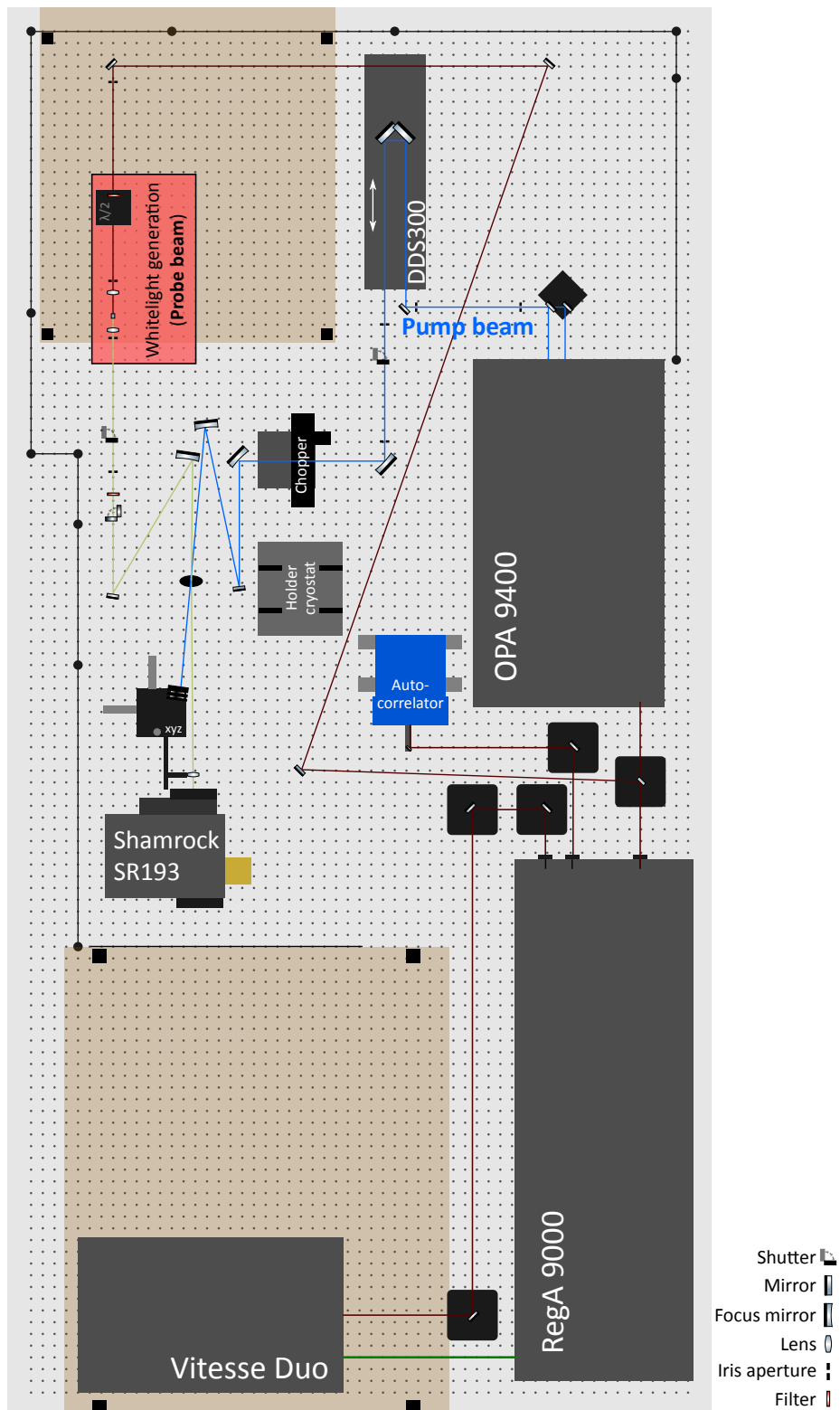


Figure C.1: Layout of the setup after implementing fast chopper and line scan camera. The transparent brown boxes correspond to desks for controller devices, black lines indicate laser safety walls. For a description of the remaining parts see text.

of 105 min. Figure C.2 a and b show 2D heat maps of the photoinduced absorption signal up to 5 ps and over the complete measurement range, respectively. The heat map of the initial evolution shows a characteristic property of the white-light. At negative time delays, a curved pattern with a width of 1.5 ps is obviously visible. This is due to the dispersion of the white-light. Contributions in the red spectral range of the white-light reach the sample earlier than parts in the blue range of its spectrum. Therefore, spectra acquired for one distinct position of the translational stage correspond to different time delays according to the dispersion curve. The influence of dispersion can be corrected and results in this curvature. Figure C.2 c contains transient absorption spectra averaged over specified delay intervals. For early times, the spectra are a superposition of the ground state bleach between 500 nm and 560 nm and structured stimulated emission at 540 nm and above. The stimulated emission shifts to longer wavelengths with increasing time delay and decays with a life time of 0.66 ns, as extracted with a monoexponential fit on the temporal evolution in Figure C.2 d. This result is consistent with emission decay times measured by Konstantin Schötz using the streak camera in the framework of his master thesis.²¹⁸ However, the transient absorption spectra at the longest time delays still have significant contributions of the ground state bleach, indicating quenching of the singlet emission by generation of longer-lived dark states, which absorb outside of the measured spectral region. Possible candidates could be charges generated by autoionization or an unusual strong intersystem crossing to triplet states. However, further investigation is beyond the scope of this test measurement and could be followed up separately.

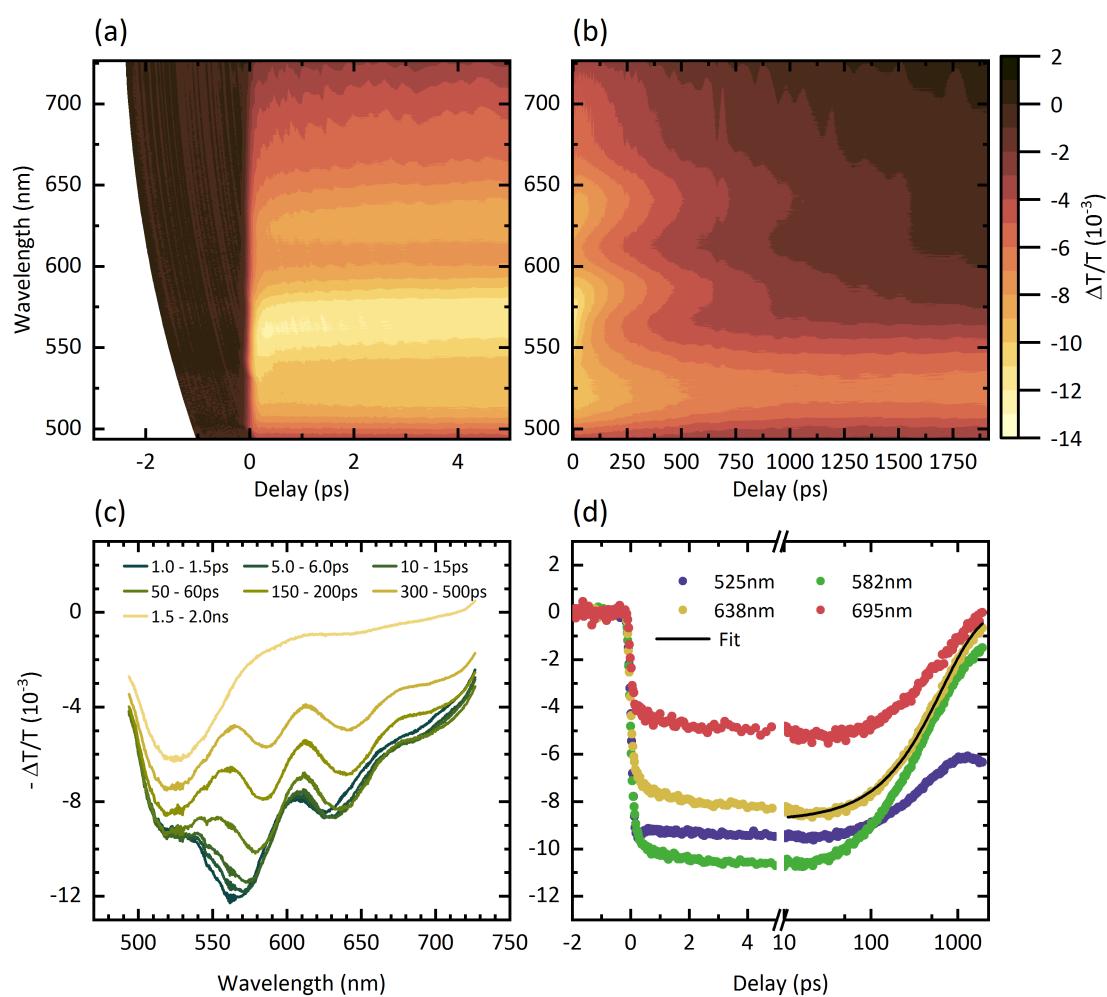


Figure C.2: Test measurements of PDOPT in THF at a concentration of 0.2 g/l. Heat maps of the transient absorption signal (a) near zero time delay and (b) over the full measurement range. (c) Spectra averaged over the time ranges as indicated. (d) Transients at four different wavelengths and a monoexponential fit with a decay time of 0.66 ns.

D Analysis of in situ data

Large data sets are created during in situ film formation experiments. I programmed a graphical user interface in Python to simplify standard calculations on the raw data sets and provide a possibility to get an overview about the different spectral evolutions. Figure D.1 shows a screenshot of the program with data loaded from Chapter 9.

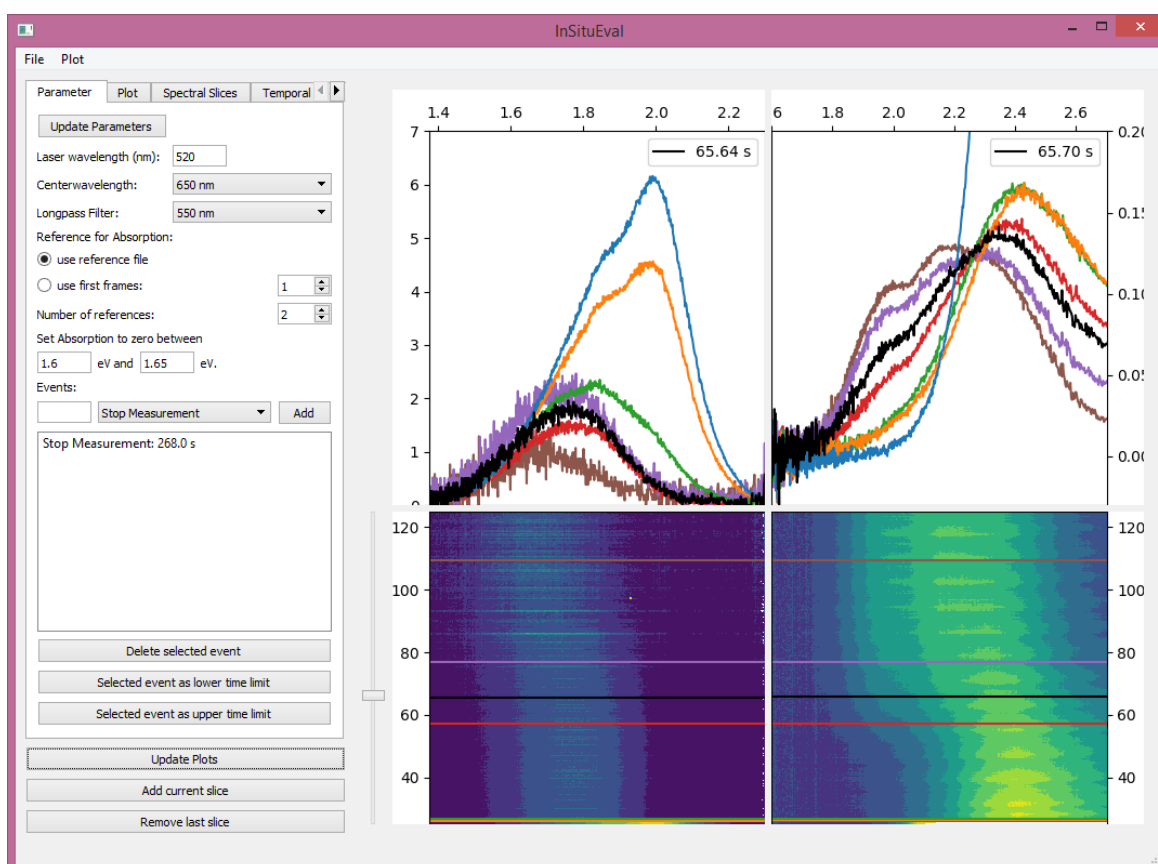


Figure D.1: Screenshot of the GUI with measurement data for TT during spin coating (final graph: see Figure 5.11 or Chapter 9). The black line in the 2D maps is interactively controlled by the slider on the left, spectra at distinct times are shown on top and indicated by coloured lines. The left panel controls basic calculations like choosing the laser wavelength, settings for spectral correction, or creating reference spectra for OD calculation from the first frames. The plot is controlled in a separate tab, further tabs for better control over spectral slices or time traces are included, though not yet implemented. Emission spectra in the left column are normalized to 1.6 eV.

Implemented standard calculations are:

- Assign time axes for absorption and emission
- Background subtraction
- Calculate optical density (OD)
- Create reference spectrum from first frames if necessary
- Simple baseline subtraction in absorption for each frame
- Correcting emission for efficiency of the setup
- Transform x-axis from wavelength (nm) to energy (eV), using Jacobian transformation in emission^{219,220}
- Normalize emission to absorption at laser wavelength
- Normalization calculations for plotting (maximum, spectral area, fixed energy)

The processed 2D maps can be exported (with and without normalization), as well as the spectra at distinct time steps shown in the graphs in the top row. Further, the total emission intensity can be exported into a separate file. The source code for these standard calculations is printed on page 231, the code for the remainder of the program is rather lengthy and can be obtained upon request.

The exported data from the program can then be used for further processing. For spin coating experiments, oscillations can occur due to an aliasing effect between the rotation frequency of the spin coater and the acquisition rate of the CCD camera, as noted by Thilo Kumrey in his Bachelor thesis.²²¹ I suppressed these beat oscillations by applying an interpolation algorithm in the Fourier domain, the code is printed on page 236.

The work in Chapter 10 required more sophisticated analysis, as every single spectrum was separated into amorphous and aggregated contributions. The spectra of the aggregates were further analysed by fitting spectral models using the following work flow:

1. Extract full 2D maps with the graphical interface.
2. Set individual time zero and crop unused data (`crop_data.py`).
3. Separate spectral contributions of aggregated species (`Separating_aggregates.py`).
4. Perform fit of spectral models (`Fitting_Absorption.py`, `Fitting_Emission.py`).

The corresponding Python scripts are distributed over several files and printed on page 237.

Source code for spectral calculations in GUI

```
"""
Created on Mon Nov 13 14:13:27 2017

@author: Stefan Wedler
5 """
import scipy as sc
from scipy.integrate import.simps
import os, glob
# values for displaying correct options in GUI
10 normalize = ['none', 'max', 'fixed', 'area']
dirCorrectionFunctions = 'Korrekturfunktionen'
filters = {'undefined': 0, '440 nm': 440, '515 nm': 515, '550 nm': 550}
centerwavelengths = {'undefined': 0, '650 nm': 650,
                      '700 nm': 700, '750 nm': 750}
15 # little helper function
def get_index_from_array(arr, values=[]):
    indices = []
    try:
        for val in values:
20             pass
    except:
        values = [values]
    for val in values:
        minDiff = abs(val-arr[0])
        i = 0
25         for j, ar in enumerate(arr):
            if abs(ar-val) < minDiff:
                minDiff = abs(ar-val)
                i = j
30         indices.append(i)
    return indices
# all calculations are performed in this class
class Spectrum:
    # initialize all fields
35     def __init__(self):
        self.dirname = ''
        # set up all arrays
        self.rawAbs = sc.zeros((1,1))
        self.rawPL = sc.zeros((1,1))
40         self.background = sc.zeros((1))
        self.reference = None
        self.wavelength = sc.zeros((1,))
        self.energy = sc.zeros((1,))
        self.Abs = sc.zeros((1,1))
45         self.PL = sc.zeros((1,1))
        # the norm-variables are plotted in the GUI
        self.AbsNorm = self.Abs
        self.PLNorm = self.PL
        self.timeTotal = sc.zeros((1,))
50         self.timeAbs = sc.zeros((1,))
        self.timePL = sc.zeros((1,))
        # set up options
```

```

self.options = {'restrict PL': (0,-1),
                'restrict Abs': (0,-1),
55             'BG corrected': False,
                'PL correction': None}

# data import and preliminary calculations
def import_data(self,dirname,ref='',wl=None,tMax = 0):
    self.dirname = dirname
60     fileAbs = os.path.join(dirname,'Absorption.dat')
    filePL = os.path.join(dirname,'PL.dat')
    if ref: fileRef = ref
    else: fileRef = os.path.join(dirname,'Reference.dat')
    fileBg = os.path.join(dirname,'Background.dat')
65     self.rawAbs = sc.genfromtxt(fileAbs,delimiter=' ')#[:,1:]
    self.rawPL = sc.genfromtxt(filePL,delimiter=' ')#[:,1:]
    if os.path.isfile(fileRef):
        self.reference = sc.genfromtxt(fileRef,delimiter=' ')
    self.background = sc.genfromtxt(fileBg,delimiter=' ')
70     # get proper wavelength axis and convert to eV
    if wl == None:
        self.wavelength = sc.linspace(450,900,len(self.background))
        print('Warning: Dummy wavelength axis created')
    elif isinstance(wl,sc.ndarray):
75         self.wavelength = wl
    elif isinstance(wl,str):
        if not '\\\ ' in wl:
            wl = os.path.join(dirname,wl)
            self.wavelength = sc.genfromtxt(wl, usecols=0)
80     self.energy = 1240. / self.wavelength
    self.set_time(tMax)
    # preliminary corrections and calculations
    self.options['BG corrected'] = False # BG correction only once!
    self.subtract_BG()
85     self.correct_setup_efficiency()
    self.convert_PL_to_energy()
    self.calc_OD(0)
    self.options['restrict Abs'] = (0,len(self.energy))
    self.options['restrict PL'] = (0,len(self.energy))
90     # subtract provided background spectrum
    def subtract_BG(self):
        if self.options['BG corrected']: return #BG correction only once!
        if self.reference is not None: self.reference -= self.background
        for d in self.rawAbs:
95             d -= self.background
        for d in self.rawPL:
            d -= self.background
        self.options['BG corrected'] = True
    # search for location of correction function
100    def get_correction_function(self, cwl, lpFilter):
        strSearch = os.path.join(dirCorrectionFunctions, 'KorrFunk_in-Situ_neu_')
        strSearch = strSearch + 'CW' + str(int(cwl))
        strSearch = strSearch + '_Filter' + str(int(lpFilter)) + '.dat'
        files = glob.glob(strSearch)
105    if len(files) == 1:
        self.options['PL correction'] = files[0]

```

```

else:
    self.options['PL correction'] = None
# correct PL for setup efficiency
110 def correct_setup_efficiency(self):
    self.PL = sc.zeros_like(self.rawPL)
    if self.options['PL correction']:
        correction = sc.loadtxt(self.options['PL correction'][:,1])
        correction = correction/correction[511] #normalize
115 else:
        correction = sc.ones_like(self.PL[0])
    for i in range(len(self.rawPL)):
        self.PL[i] = self.rawPL[i] * correction
    self.PLNorm = self.PL
120 # returns the integrated PL intensity. Does not affect state of Spectrum
def calculate_integrated_PL(self):
    pl_local = sc.zeros_like(self.rawPL)
    # Korrekturfunktion laden
    if self.options['PL correction']:
125         correction = sc.loadtxt(self.options['PL correction'][:,1])
        correction = correction/correction[511] #normalize
    else:
        correction = sc.ones_like(self.PL[0])
    # Apply correction function and divide by eV ^= multiply with nm
130 # only -photon counts in pl_local
    for i in range(len(pl_local)):
        pl_local[i] = self.rawPL[i] * correction * self.wavelength
    bounds = self.options['restrict PL']
    print(bounds)
135 integral = sc.zeros(len(pl_local))
    # integral reduces to sum, as wavelength bins are about equidistant
    for i in range(len(integral)):
        integral[i] = pl_local[i,bounds[0]:bounds[1]].sum()
    return integral
140 # Jacobian transformation
def convert_PL_to_energy(self):
    for pl in self.PL:
        pl /= self.energy**2
# Calculate OD; Reference can be constructed from the first frames
145 def calc_OD(self, refframes=0,numRefs=2):
    self.Abs = sc.zeros_like(self.rawAbs)
    if self.reference is None and refframes < 1: refframes = 1
    # take the saved reference frame as reference
    if refframes < 1:
150         data = sc.where(self.rawAbs>1, self.rawAbs, 1)
        ref = sc.where(self.reference>0, self.reference, 0.01)
        for i in range(len(data)):
            self.Abs[i] = sc.log10(ref/data[i])
    # or take the mean first refframes frames as reference
155 else:
        for i in range(numRefs):
            n = numRefs
            dataPart = sc.where(self.rawAbs[i::n]>1, self.rawAbs[i::n], 1)
            refPart = sc.mean(dataPart[:refframes],axis=0)
160             refPart = sc.where(refPart>0,refPart,0.01)

```

```

        ODPart = sc.zeros_like(dataPart)
        for j in range(len(ODPart)):
            ODPart[j] = -sc.log10(dataPart[j]/refPart)
        self.Abs[i:n] = ODPart
165     self.AbsNorm = self.Abs
    # simplest correction for oscillations/offsets
    def level_OD(self,Emin,Emax):
        i = sorted(get_index_from_array(self.energy,[Emin,Emax]))
        for a in self.Abs:
170             a -= sc.mean(a[i[0]:i[1]])
    # calculate time axis
    def set_time(self,tMax):
        n = len(self.rawAbs) + len(self.rawPL)
        if tMax <= 0: tMax = n-1
175         self.timeTotal = sc.linspace(0,tMax,n)
        self.timePL = self.timeTotal[::2]
        self.timeAbs = self.timeTotal[1::2]
    # divide emission by OD at laser
    def correct_PL_laser_wavelength(self,wavelength):
180         # check if there was already a correction for laser wavelength
        if 'Laser' in self.options:
            if self.options['Laser'] == wavelength: return
            self.correct_setup_efficiency()
            self.convert_PL_to_energy()
185         # feature: if wavelength <= 0, don't make any correction
        if wavelength > 0:
            print('correcting for wavelength ' + str(wavelength))
            iLaser = get_index_from_array(self.wavelength,wavelength)[0]
            a = sc.zeros(len(self.timeAbs)+1)
190             a[0] = self.Abs[0,iLaser]
            a[1:] = self.Abs[0:,iLaser]
            a = 0.5 * (a[0:-1]+a[1:])
            for aa,p in zip(a,self.PL):
                p /= 1 - 10**(-aa)
195             self.options['Laser'] = wavelength
    # determine array indices for restricted plotting
    def restrict_Abs(self,eLow=None,eHigh=None):
        if eLow == None:
            iLow = 1023
200         else:
            iLow = sc.absolute(self.energy-eLow).argmin()
        if eHigh == None:
            iHigh = 0
        else:
205             iHigh = sc.absolute(self.energy-eHigh).argmin()
        self.options['restrict Abs'] = (iHigh,iLow)
    def restrict_PL(self,eLow=None,eHigh=None):
        if eLow == None:
            iLow = 1024
210         else:
            iLow = sc.absolute(self.energy-eLow).argmin()
        if eHigh == None:
            iHigh = 0
        else:

```

```

215         iHigh = sc.absolute(self.energy-eHigh).argmin()
        self.options['restrict PL'] = (iHigh,iLow)
# different ways of normalizing
def normalize(self,PL = True, mode=normalize[0], energy = None):
    if PL:
220         self.PLNorm = self.PL * 1
        res = self.PLNorm
        i = self.options['restrict PL']
    else:
        self.AbsNorm = self.Abs * 1
225         res = self.AbsNorm
        i = self.options['restrict Abs']
# case: max
if mode.lower() == normalize[1]:
    for a in res:
230         a /= a[i[0]:i[1]].max()
# case: fixed energy
if mode.lower() == normalize[2] and energy != None:
    i = get_index_from_array(self.energy, [energy])
    for a in res:
235         a /= a[i]
# case: area
if mode.lower() == normalize[3]:
    ints = sc.zeros(len(res))
    for j in range(len(ints)):
240         ints[j] = abs(simps(res[j,i[0]:i[1]],self.energy[i[0]:i[1]]))
        tmp = sc.divide(res.transpose(),ints).transpose()
        for j in range(len(res)):
            res[j] = tmp[j]
# export full 2dMaps in their normalized state
245 def saveData(self, fileOut):
    fileOutAbs = fileOut + '_Abs.dat'
    time = self.timeAbs
    data = self.AbsNorm
    with open(fileOutAbs,'w') as f:
250         for t in time: f.write('\t{:.4f}'.format(t))
            f.write('\n')
        for wl,da in zip(self.energy,sc.transpose(data)):
            out = f'{wl:.4f}\t' + '\t'.join([f'{dd:.5f}' for dd in da]) + '\n'
            f.write(out)
255         fileOutPL = fileOut + '_PL.dat'
        time = self.timePL
        data = self.PLNorm
        with open(fileOutPL,'w') as f:
            for t in time: f.write('\t{:.4f}'.format(t))
260             f.write('\n')
            for wl,da in zip(self.energy,sc.transpose(data)):
                out = f'{wl:.4f}\t' + '\t'.join([f'{dd:.5f}' for dd in da]) + '\n'
                f.write(out)
# export calculated integrated PL
265 def saveIntegratedPL(self, fileOut):
    fileOut = fileOut + '_PL_integrated.dat'
    dataOut = sc.concatenate([self.timePL],[self.calculate_integrated_PL()])
    sc.savetxt(fileOut,dataOut.transpose())

```

Source code for FFT correction of aliasing effect

```
"""
Created on Fri Apr 10 10:05:59 2020

@author: Stefan Wedler
5     This little script performs a correction of disturbing aliasing
      oscillations in the Fourier domain. The frequency spectra are smoothed
      by local polynomial interpolation without the alias-peak.
      An example of the successful correction can be found in the supporting
      information of Chapter 9 (Figure S4)
10    """

import numpy as np

#%% data import
15    file_in_abs = 'cropped_Abs.dat'
    data_in_abs = np.loadtxt(file_in_abs, skiprows=1)
    with open(file_in_abs, 'r') as f:
        time_abs = np.array(f.readline().split(), dtype=float)
    energy_abs = data_in_abs[:, 0]
20    data_in_abs = data_in_abs[:, 1:]
    #%% Actual fft algorithm here
    # setup
    i_interpol = 31, 62    # array indices of disturbing frequency
    order = 3             # order of interpolation polynomial
25    n = 5                # number of points considered for interpolation
    n_out = 1            # additional points affected by correction
    # create necessary data for the polynomial interpolation routine, which is
    # performed by "manual" linear least squares
    t_i = np.zeros(2*n)
30    t_i[:n] = np.arange(-n, 0)
    t_i[n:] = 1+np.arange(n)
    t_i_l = np.array([t_i**l for l in range(order+1)])[:, :-1]
    ls = np.matmul(t_i_l, t_i_l.T)
    # transform to the fourier space
35    data_fft = np.fft.rfft(data_in_abs, axis=1)
    freq = np.fft.rfftfreq(time_abs.size, np.mean(np.diff(time_abs)))
    # set up array for results
    data_fft_corrected = data_fft * 1.0
    # loop over all frequencies to correct
40    for ii in i_interpol:
        # loop over all time traces
        for j in range(data_fft.shape[0]):
            # take relevant part of fft and separate real and imaginary part
            f_i_r, f_i_i = np.zeros(2*n), np.zeros(2*n)
45            f_i_r[:n] = np.real(data_fft[j, ii-n:ii])
            f_i_r[n:] = np.real(data_fft[j, ii+1:ii+n+1])
            f_i_i[:n] = np.imag(data_fft[j, ii-n:ii])
            f_i_i[n:] = np.imag(data_fft[j, ii+1:ii+n+1])
            # linear least squares separately for real and imaginary part
50            rs = np.matmul(t_i_l, f_i_r)
            solr = np.linalg.solve(ls, rs)
            rs = np.matmul(t_i_l, f_i_i)
```

```

    soli = np.linalg.solve(ls,rs)
    # calculate new values from the interpolated polynomial
55    corrected = np.polyval(solr,np.arange(-n_out,n_out+1.0)) + \
        np.polyval(soli,np.arange(-n_out,n_out+1.0))*1j
    data_fft_corrected[j,ii-n_out:ii+1+n_out] = corrected * 1.0
# transform back to the time domain
data_corrected = np.fft.irfft(data_fft_corrected,n=data_in_abs.shape[1],axis=1)
60 # data export is excluded for brevity

```

Source code for separation and fitting of aggregated contributions

File: crop_data.py

```

"""
Created on Thu Apr  9 09:02:08 2020

@author: Stefan Wedler
5 """
t0 = 25.8771

options = {'Cropped': {'start': 312, 'stop': 530,'delta':1}}
energy = {'abs': (1.55,3.71), 'pl': (1.0,2.45) }
10 files = ['Full_Maps_Abs.dat','Full_Maps_PL.dat']

for f_in in files:
    with open(f_in,'r') as f:
        data_in = f.readlines()
15     if 'Abs' in f_in:
        eMin,eMax = energy['abs']
    else:
        eMin,eMax = energy['pl']
20     for opts in options.keys():
        file_out = f_in.replace('Full',opts)
        limits = options[opts]
        with open(file_out,'w') as f:
            for d in data_in:
25                 line_in = d.split('\t')
                 line_out = [line_in[0]]
                 line_out += [d for d in line_in[1+limits['start']:limits['stop']+1:limits['delta']]]
                 if line_out[0] == '':
                     print('File "+f_in+f"' cropped from {line_out[1]} to {line_out[-1]}')
30                 if t0 != 0 :
                     line_out = [''] + [f'{float(d)-t0:.3f}' for d in line_out[1:]]
                     print(f' Time adjusted, new range from {line_out[1]} to {line_out[-1]}')
                 if line_out[0] == '' or eMin <= float(line_out[0]) <= eMax:
                     f.write('\t'.join(line_out)+'\n').replace('\n'*2,'\n')

```

File: HelpersFitting.py

```
"""
Created on Sun Oct 25 18:28:39 2020

@author: Stefan Wedler
5 This file contains several helper functions and variables, which are used
  by all fitting scripts.
"""

import numpy as np
from pandas import DataFrame
10 from os.path import join
from distutils.util import strtobool
from glob import glob
# location of all measurement sets
base_dir = r'C:\Daten\Projekte\P3HT Bladecoating Matt\InSitu Messungen\Data Currently Used V14'
15 all_dirs = [
    'CF/5C',
    'CF/10C',
    'CF/15C',
    'CF/20C',
20    'CF/25C', # redo with new settings
    'CF/30C Hazem', # redo with new settings.
    'THF/20C', # redo with new settings
    'THF/25C', # redo with new settings
    'THF/30C', # redo with new settings
25    'THF/35C Replacement', # redo with new settings.
    'THF/35C Saturated', # redo with new settings.
    'THF/40C', # redo with new settings.
    'THF/45C Hazem',
    ]
30 #%% File input/output
# helpers for loading and saving 2d maps
def load_2d_map(file):
    data = np.loadtxt(file,skiprows=1)
    energy = data[:,0] * 1.0
35    data = data[:,1:] * 1.0
    with open(file, 'r') as f:
        time = np.array(f.readline().split(),dtype=float)
    return data,energy,time
def save_2d_map(file,data,energy,time):
40    with open(file,'w') as f:
        for t in time: f.write('\t{:.4f}'.format(t))
        f.write('\n')
        for e,d in zip(energy,data):
            f.write(f'{e:.4f}\t' + '\t'.join([f'{dd:.5f}' for dd in d])+'\n')
45 # helper for loading a dictionary from options file
def read_dict(file):
    # read dict and do the correct conversions
    try:
        keys = np.genfromtxt(file,dtype=str,delimiter='\t',usecols=(0))
50        vals = np.genfromtxt(file,dtype=str,delimiter='\t',usecols=(1))
        res = dict(zip(keys,vals))
    except:
```

```

    res = {}
    # here comes the conversion stuff
55 tuples = ['offset_range_abs', 'scaling_abs', 'scaling_pl',
            'fit_range_abs', 'fit_range_pl']
    for t in tuples:
        if t in res: res[t] = tuple(eval(res[t]))
    bools = ['pl_redshift', 'hw_vary_pl', 'S_eff_vary_pl', 'sigma_add_vary_abs',
60           'hw_vary_abs']
    for b in bools:
        if b in res: res[b] = bool(strtobool(res[b]))
    floats = ['nonaggregated_abs', 'e00_abs', 'sigma_abs', 'sigma_add_abs', 'hw_abs',
              'nonaggregated_pl', 'e00_pl', 'sigma_pl',
65           'sigma_high_pl', 'alpha_pl', 'hw_pl', 'S_eff_pl']
    for f in floats:
        if f in res:
            try: res[f] = float(res[f])
            except: res[f] = np.nan
70    return res

# helper for making an excel sheet of the fitting parameters
def create_parameters_xls(dirs, fout):
    settings_all = {d.replace('\\Processed_new', ''):
75         read_dict(join(base_dir, d, 'varying_settings.dat')) for d in dirs}
    files_default = glob('defaults*.dat')
    settings_default = {f[:-4]:read_dict(f) for f in files_default}
    frame = DataFrame(**settings_default, **settings_all)
    frame.to_excel(fout)

%% convenience functions
80 # helper for getting indices of array elements
def get_indices(ar, *values):
    indices = [np.argmin(np.abs(ar - ii)) for ii in values]
    if len(indices)>1: indices = np.sort(indices)
    else: indices = indices[0]
85    return indices

%% actual fitting functions
# The fitting functions return either the model, the residual or a scaled
# residual depending on whether data and uncertainties are provided
# Gaussian lineshape
90 def gauss(x, x0, sigma):
    return np.exp(-0.5 * (x-x0)**2 / sigma**2)
# doing a scaling fit including energy shifts
def fit_scaling(pars, x, amorph, data=None):
    parval = pars.valuesdict()
95    dE = parval['dE']
    amp = parval['amp']
    descending = np.mean(np.diff(x))<0
    if descending:
        x = x[::-1]
100    amorph = amorph[::-1]
    # additional shift by 0.01 introduced due to numerical stability
    amorph_interpol = np.interp(x-(dE-0.01), x, amorph) * amp
    if descending: amorph_interpol = amorph_interpol[::-1]
    if data is None: out = amorph_interpol
105    else: out = data - amorph_interpol
    return out

```

```

# emission clark model
def fit_emission_clark_var_sig(pars,energy,data=None,eps=None):
    parvals = pars.valuesdict()
    e00 = parvals['e00']
    sigma = parvals['sigma']
    sigma_high = parvals['sigma_add']
    alpha = parvals['alpha']
    amp = parvals['amp']
    hw = parvals['hw']
    S_eff = parvals['S_eff']
    model = alpha * gauss(energy,e00,sigma)
    factorial = 1.0
    for i in np.arange(1,4):
        factorial *= i
        model += S_eff**i / factorial * gauss(energy,e00 - i*hw,sigma+i*sigma_high)
    model = amp * model * energy**3
    if data is None: return model
    if eps is None: return model - data
    return (model - data) / eps

# absorption gaussians with constant spacing
def fit_absorption_varying_amplitudes(pars,energy,data=None,weights=None):
    parvals = pars.valuesdict()
    e00 = parvals['e00']
    sigma = parvals['sigma']
    hw = parvals['hw']
    sigma_add = parvals['sigma_add']
    amplitudes = np.array([parvals['a0'],parvals['a1'],
                           parvals['a2'],parvals['a3']])
    out = np.zeros_like(energy)
    for i,a in enumerate(amplitudes):
        out += a * gauss(energy,e00 + i*hw, sigma + i*sigma_add)
    out *= energy
    if data is not None: out -= data
    if weights is not None: out /= weights
    return out

```

File: Separating_aggregates.py

```

"""
Created on Sun Oct 25 18:28:39 2020

filename: Separating_Aggregates.py
5 @author: Stefan Wedler

Separation should now be fine for the whole series of P3HT bladecoating
measurements.

10 This script does all the separation stuff to get the aggregate only
spectra. In addition, the emission is corrected for changes in absorption
at the laser wavelength and conversion to photons per energy interval also
takes place.
"""

```

```

15 import numpy as np
import lmfit
from os.path import join
from HelpersFitting import (load_2d_map,get_indices,fit_scaling,read_dict,
20 base_dir,all_dirs)

for i in range(len(all_dirs)):
    all_dirs[i] = join(all_dirs[i],'Processed_new')
defaults = read_dict('defaults_separation.dat')
25 ### loop over all measurement sets
for current_dir in all_dirs:
    working_dir = join(base_dir,current_dir)
    # read default options and replace by optional individual options
    options = read_dict(join(working_dir,'varying_settings.dat'))
30 options = {**defaults,**options}
    offset_range = options['offset_range_abs']
    scaling_abs = options['scaling_abs']
    scaling_pl = options['scaling_pl']
    pl_redshift = options['pl_redshift']
35 # load absorption spectra
    maps_abs, energy_abs, time_abs = load_2d_map(join(working_dir,'Cropped_Maps_Abs.dat'))
    # subtract offset from absorption spectra
    offset_abs = np.mean(maps_abs[np.arange(*get_indices(energy_abs,*offset_range))],axis=0)
    maps_abs = maps_abs - offset_abs
40 # load emission spectra
    maps_pl, energy_pl, time_pl = load_2d_map(join(working_dir,'Cropped_Maps_PL.dat'))
    # calculate absorption at laser wavelength for emission correction
    index_laser = np.argmin(np.abs(energy_abs-1240/520.0))
    absorption_laser = 1.0 - 10**(-maps_abs[index_laser])
45 # do emission intensity correction
    maps_pl = maps_pl / np.interp(time_pl,time_abs,absorption_laser)
    # do conversion of emission from spectral power distribution to photon
    # distribution per interval by dividing through photon energy
    # THIS IS NOT DUE TO JACOBIAN TRANSFORMATION,
50 # BUT RESULTS FROM THE CORRECTION FUNCTION
    maps_pl = maps_pl / energy_pl[:,np.newaxis]
    # create aggregate spectra for absorption and emission. this can either
    # be a spectrum from the loaded 2d maps, or externally loaded
    if np.isnan(options['nonaggregated_abs']):
55 nonaggregated_abs = np.loadtxt(join(working_dir,'External_Nonaggregated_Abs.dat'),usecols=1)
    else:
        nonaggregated_abs = maps_abs.T[get_indices(time_abs,
                                                    options['nonaggregated_abs'])] * 1.0
        out = np.concatenate((energy_abs[:,np.newaxis],
60 nonaggregated_abs[:,np.newaxis]),axis=1)
        np.savetxt(join(working_dir,'Internal_Nonaggregated_Abs.dat'),out,
                    fmt='%.5e',delimiter='\t')
    if np.isnan(options['nonaggregated_pl']):
        nonaggregated_pl = np.loadtxt(join(working_dir,'External_Nonaggregated_PL.dat'),usecols=1)
65 else:
        nonaggregated_pl = maps_pl.T[get_indices(time_pl,
                                                    options['nonaggregated_pl'])] * 1.0
        out = np.concatenate((energy_pl[:,np.newaxis],

```

```

                                nonaggregated_pl[:,np.newaxis]),axis=1)
70     np.savetxt(join(working_dir,'Internal_Nonaggregated_PL.dat'),out,
                fmt='%.5e',delimiter='\t')
    # separate spectra for absorption - standard scaling w/o redshift
    i_scale = np.arange(*get_indices(energy_abs,*scaling_abs))
    # scaling done by "manual" leastsquare approach
75     factor_scaling_abs = np.mean((nonaggregated_abs[:,np.newaxis]*maps_abs)[i_scale],axis=0)
    factor_scaling_abs = factor_scaling_abs / np.mean(nonaggregated_abs[i_scale]**2)
    # scaled amorphous spectrum
    nonaggregated_abs_scaled = nonaggregated_abs[:,np.newaxis] * factor_scaling_abs
    # aggregates is amorphous minus scaled one
80     aggregated_abs = maps_abs - nonaggregated_abs_scaled
    # separate spectra for emission - standard scaling with option of redshift
    print('separate emission spectra')
    i_scale = np.arange(*get_indices(energy_pl,*scaling_pl))
    params = lmfit.Parameters()
85     # additional offset of 0.01 introduced due to numerical stability
    params.add_many(('dE',0.01,pl_redshift,-0.07,0.05), ('amp',1.0,True))
    # prepare arrays for results
    factor_scaling_pl = np.zeros_like(time_pl)
    energy_shift_pl = np.zeros_like(time_pl)
90     nonaggregated_pl_scaled = np.zeros_like(maps_pl)
    aggregated_pl = np.zeros_like(maps_pl)
    # do fit for every time step
    for i in range(time_pl.size):
        fit = lmfit.minimize(fit_scaling,params,args=(energy_pl[i_scale],
95                                nonaggregated_pl[i_scale],
                                    maps_pl[i_scale,i]))

        factor_scaling_pl[i] = fit.params['amp'].value
        energy_shift_pl[i] = fit.params['dE'].value - 0.01
        nonaggregated_pl_scaled[:,i] = fit_scaling(fit.params,energy_pl,
100                                nonaggregated_pl)
    aggregated_pl = maps_pl - nonaggregated_pl_scaled

    # saving results is omitted for brevity

```

File: Fitting_Absorption.py

```

"""
Created on Sun Oct 25 18:28:39 2020

filename: Fitting_Absorption.py
5 @author: Stefan Wedler
"""

import numpy as np
from scipy.integrate import simps
10 import lmfit
from os.path import join
from HelpersFitting import (load_2d_map, read_dict,get_indices,
                            fit_absorption_varying_amplitudes,
                            base_dir,all_dirs)

```

```

15
for i in range(len(all_dirs)):
    all_dirs[i] = join(all_dirs[i], 'Processed_new')

defaults = read_dict('defaults_fitting_abs.dat')
20 include_manual = True
    # prepare lists for getting average values - needed for testing
    hw_means = []
    sigma_add_means = []

25 fit_model = fit_absorption_varying_amplitudes
    %% Looping through all measurement sets
for current_dir in all_dirs:
    working_dir = join(base_dir, current_dir)
    # read options
30 options = read_dict(join(working_dir, 'varying_settings.dat'))
    options = {**defaults, **options}
    # fitting range
    fit_range_abs = options['fit_range_abs']
    # starting parameters
35 params = lmfit.Parameters()
    params.add_many(('e00', options['e00_abs'], True, 1.85, 2.2),
                    ('sigma', options['sigma_abs'], True, 0.03, 0.1),
                    ('sigma_add', options['sigma_add_abs'],
                     options['sigma_add_vary_abs'], 0.0, 0.05),
40                    ('hw', options['hw_abs'], options['hw_vary_abs'], 0.14, 0.2))
    params.add_many(('a0', 0.5, True, 0.0, 2.0),
                    ('a1', 0.5, True, 0.0, 2.0),
                    ('a2', 0.5, True, 0.0, 2.0),
                    ('a3', 0.5, True, 0.0, 2.0))
45    # now load the aggregate only spectra
    # aggregate spectra are already corrected for offset (abs)
    aggregated_abs, energy_abs, time_abs = load_2d_map(join(working_dir, 'Aggregates_Abs.dat'))
    # preparing array for storing fitting results. Calculation for (corrected)
    # peak ratio alpha is also stored there, but preformed after fitting
50 fits_abs = np.zeros_like(aggregated_abs)
    fit_values_abs = np.zeros((time_abs.size, len(params)+3))
    fit_stderr_abs = np.zeros((time_abs.size, len(params)+2))
    # get indices for fitting
    i_fit = np.arange(*get_indices(energy_abs, *fit_range_abs))
55    # the area of the aggregate can be calculated without fitting
    fit_values_abs[:, 0] = -simps(aggregated_abs, energy_abs, axis=0)
    # load manual parameters if present
    try:
        params_manual_abs = np.loadtxt(join(working_dir, 'Fit_Aggregates_Parameters_Manual_Abs.dat')).T
60        if params_manual_abs.ndim == 1:
            params_manual_abs = params_manual_abs[:, np.newaxis]
    except:
        params_manual_abs = np.array([[[]]])
    # loop over all aggregate spectra for actual fitting
65    for j in range(len(time_abs)):
        # do fitting in reverse. better for reusing parameters as start
        i = -1-j
        # in case of negative times do not fit. the algorithm is unstable

```

```

# and takes useless time
70 if time_abs[i] <= 0: continue
# the actual fit
if include_manual and time_abs[i] in params_manual_abs[0]:
    keys = {key:kk+2 for kk,key in enumerate(params.keys())}
    i_time = get_indices(params_manual_abs[0],time_abs[i])
75 for key in keys:
    params[key].value = params_manual_abs[keys[key],i_time]
result = params
else:
    weights = 0.5*(1+np.erf((energy_abs-params['e00'].value-\
80 1.5*params['hw'].value)/0.060))+0.2
    fit = lmfit.minimize(fit_model,params,
                        args=(energy_abs[i_fit],
                              aggregated_abs[i_fit,i],
                              weights[i_fit]))
85     result = fit.params
# save fits and parameters
fits_abs[:,i] = fit_model(result,energy_abs)
for i_p,p in enumerate(result):
    # +1 needed as area is stored as well
90     fit_values_abs[i,i_p+1] = 1.0 * result[p].value
    fit_stderr_abs[i,i_p] = result[p].stderr
# reuse result as next starting parameter
params = result.copy()
# calculate the residual, which is used for plotting afterwards
95 residual_abs = aggregated_abs - fits_abs
# here the 0-0/0-1 ratio is calculated as well as the sigma-corrected value
# first calculate some needed values
area_scaled = fit_values_abs[:,0] / fit_values_abs[-20:,0].mean()
error_scaling = 1.0 - np.where(area_scaled<1,area_scaled,1)
100 keys = {key:i+1 for i,key in enumerate(params.keys())}
# and do more realistic estimation for sigma error
fit_stderr_abs[:,keys['sigma']-1] = np.sqrt((1e-3 + error_scaling * 4.0e-3)**2\
      + 0.04**2*fit_values_abs[:,keys['sigma']]**2)
# actual calculation of alpha from a0/a1
105 alpha_abs = fit_values_abs[:,keys['a0']] / fit_values_abs[:,keys['a1']]
fit_values_abs[:, -2] = alpha_abs
# error is assumed to scale somehow with the relative area of aggregates
alpha_stderr_abs = 0.01 + error_scaling * 0.065
fit_stderr_abs[:, -2] = alpha_stderr_abs
110 # now correct alpha for different linewidths
sig = fit_values_abs[:,keys['sigma']]
sig_add = fit_values_abs[:,keys['sigma_add']]
alpha_cor_abs = alpha_abs * sig / (sig + sig_add)
fit_values_abs[:, -1] = alpha_cor_abs
115 # error by standard error propagation
alpha_cor_stderr_abs = (fit_stderr_abs[:,keys['sigma']-1]/sig * sig_add/(sig + sig_add))**2
alpha_cor_stderr_abs += (alpha_stderr_abs/alpha_abs)**2
alpha_cor_stderr_abs = np.sqrt(alpha_cor_stderr_abs) * alpha_cor_abs
fit_stderr_abs[:, -1] = alpha_cor_stderr_abs
120
# now comes all the saving stuff - omitted for brevity

```

File: Fitting_Emission.py

```
"""
Created on Sun Oct 25 18:28:39 2020

filename: Fitting_Emission.py
5 @author: Stefan Wedler
"""

import numpy as np
from scipy.integrate import simps
import lmfit
10 from os.path import join
from HelpersFitting import (load_2d_map,read_dict,get_indices,
                            fit_emission_clark_var_sig,
                            base_dir,all_dirs)

for i in range(len(all_dirs)):
15     all_dirs[i] = join(all_dirs[i], 'Processed_new')
defaults = read_dict('defaults_fitting_pl.dat')
include_manual = True
fit_model = fit_emission_clark_var_sig
# prepare lists for getting average values - needed for testing
20 hw_means = []
sigma_add_means = []
%% Looping through all measurement sets
for current_dir in all_dirs:
    working_dir = join(base_dir,current_dir)
25     # read options
    options = read_dict(join(working_dir, 'varying_settings.dat'))
    options = {**defaults,**options}
    # fitting range
    fit_range_pl = options['fit_range_pl']
30     # starting parameters
    params = lmfit.Parameters()
    params.add_many(('e00',options['e00_pl'],True,1.7,1.96),
                    ('sigma',options['sigma_pl'],True,0.0,0.09),
                    ('sigma_high',options['sigma_high_pl'],False,0.0,0.1),
35     ('alpha',options['alpha_pl'],True,0.3,1.5),
                    ('amp',50.0,True),
                    ('hw',options['hw_pl'],options['hw_vary_pl'],0.14,0.2),
                    ('S_eff',options['S_eff_pl'],options['S_eff_vary_pl']))

    # now load the aggregate only spectra
40     # aggregate spectra are already corrected for laser absorption (pl) and
    # efficiency of optical elements (pl)
    aggregated_pl,energy_pl,time_pl = load_2d_map(join(working_dir, 'Aggregates_PL.dat'))
    # preparing array for storing fitting results.
    fits_pl = np.zeros_like(aggregated_pl)
45     fit_values_pl = np.zeros((time_pl.size,len(params)+2))
    fit_stderr_pl = np.zeros((time_pl.size,len(params)+1))
    # the area of the aggregate can be calculated without fitting
    i_fit = np.arange(*get_indices(energy_pl,1.4,2.0))
    fit_values_pl[:,0] = -simps(aggregated_pl[i_fit],energy_pl[i_fit],axis=0)
50     # get indices for fitting
    i_fit = np.arange(*get_indices(energy_pl,*fit_range_pl))
    # load manual parameters if present
```

```

try:
    params_manual_pl = np.loadtxt(join(working_dir, 'Fit_Aggregates_Parameters_Manual_PL.dat')).T
55     if params_manual_pl.ndim == 1:
        params_manual_pl = params_manual_pl[:,np.newaxis]
except:
    params_manual_pl = np.array([[ ]])
# loop over all aggregate spectra for actual fitting
60 for j in range(len(time_pl)):
    # do fitting in reverse. better for reusing parameters as start
    i = -1-j
    # in case of negative times do not fit.
    if time_pl[i] <= 0: continue
65     # the actual fit
    if include_manual and time_pl[i] in params_manual_pl[0]:
        keys = {key:kk+2 for kk,key in enumerate(params.keys())}
        i_time = get_indices(params_manual_pl[0],time_pl[i])
        for key in keys:
70             params[key].value = params_manual_pl[keys[key],i_time]
        result = params
    else:
        fit = lmfit.minimize(fit_model,params,
                            args=(energy_pl[i_fit],aggregated_pl[i_fit,i]))
75     result = fit.params
    # save fits and parameters
    fits_pl[:,i] = fit_model(result,energy_pl)
    for i_p,p in enumerate(result):
        fit_values_pl[i,i_p+1] = 1.0 * result[p].value
80     fit_stderr_pl[i,i_p] = result[p].stderr
    # reuse result as next starting parameter
    params = result.copy()
# calculate the residual, which is used for plotting afterwards
residual_pl = aggregated_pl - fits_pl
85 # here the 0-0/0-1 ratio is calculated as well as the sigma-corrected value
# first calculate some needed values
area_scaled = fit_values_pl[:,0] / fit_values_pl[-20:,0].mean()
error_scaling = 1.0 - np.where(area_scaled<1,area_scaled,1)
keys = {key:i+1 for i,key in enumerate(params.keys())}
90 # and do more realistic estimation for sigma error
fit_stderr_pl[:,keys['sigma']-1] = np.sqrt((1e-3 + error_scaling * 6.5e-3)**2 \
        + 0.04**2*fit_values_pl[:,keys['sigma']]**2)
# fit_stderr_pl[:,keys['alpha']-1] = 0.01 + error_scaling * 0.065
# now correct alpha for different linewidths
95 sig = fit_values_pl[:,keys['sigma']]
sig_add = fit_values_pl[:,keys['sigma_high']]
alpha_cor_pl = fit_values_pl[:,keys['alpha']] * sig / (sig + sig_add)
fit_values_pl[:, -1] = alpha_cor_pl
# error by standard error propagation
100 alpha_cor_stderr_pl = (fit_stderr_pl[:,keys['sigma']-1]/sig * sig_add/(sig + sig_add))**2
alpha_cor_stderr_pl += (fit_stderr_pl[:,keys['alpha']-1]/fit_values_pl[:,keys['alpha']]**2
alpha_cor_stderr_pl = np.sqrt(alpha_cor_stderr_pl) * alpha_cor_pl
fit_stderr_pl[:, -1] = alpha_cor_stderr_pl
# now comes all the saving stuff - omitted for brevity

```

Acknowledgements

I worked on this thesis now for the last four years. There are some people who also significantly contributed to the success of this work, and here I want to acknowledge them for their support.

First of all I want to thank my supervisor Anna Köhler. She gave me the opportunity to work in this interesting field of organic semiconductors. She further provided me opportunities to visit quite some inspiring and interesting conferences and seminars, which I am very grateful for. Anna, your steady support and trust in me kept me motivated, also in frustrating times when certain things grew larger and larger and took much longer than anticipated. A warm thank you also to Heinz Bässler in this respect for his ongoing interest and all the discussions we had.

Thank you to Fabian Panzer. Fabi, your input to this solution paper were one key driving factor for finishing it. I am also very grateful for our collaborations regarding all the in situ stuff, especially that you let me contribute to the P3HT processing paper. From time to time you gave me the push I needed to come further. Thank you for this and for sharing some musical experiences as well.

Special thanks to my plus colleague office mate Julian Kahle in the *Abteilung für Flachwitze und linguistische Verrenkungen*. You were always helpful and open-minded in every possible situation, let it be building and doing stuff in the lab, discussing scientific things, and more important discussing all the non-scientific things of importance.

I want to thank the close collaborators of the solution paper, which took its time to mature. Thank you to Axel Bourdick for teaching me how to get people organised. A warm thank you to Stavros Athanasopoulos. You readily shared your experience with all the quantum chemical calculations and gave this project the DFT expertise it needed at the right time. Also thank you very much for your DFT workshop.

Thank you to my bachelor student Max Dörr for giving me the opportunity to gain some supervision skills. I am grateful for this experience and happy that your thesis turned out well.

All the scientific work would not be possible without all the people who work in the background of our working group and keep it running. Thank you Frank Schirmer for your simple and pragmatic solutions to all possible and impossible technical problems. Thank you Irene Bauer for all the little and large miracles in the chemistry lab. Thank you Michaela Fischer and Laura Schwarze for keeping everyone and everything organised, and thank you

Thomas Dabisch for your genuinely good mood and overwhelming friendliness. At this point also many thanks to Michael Gaag from the electronics workshop for his great engagement and endurance during the construction of the fast chopper device.

So far for the scientific acknowledgement. One driving factor that motivated me to keep going was of course also the open and friendly atmosphere in our working group. I am grateful for the present and the former kicker crew Julian Kahle, Simon Biberger, Tobias Meier, Daniel Kroh and Steffen Tscheuschner. Do the Bibster! Thank you to the Schafkopf-Stammtisch crew Julian, Simon, Andy, and the former members Alex and Thomas. Thank you to all the present and former colleagues I had the pleasure to share some time during the last four years and did not mention so far. Including Konstantin Schötz for his guitarristic contributions, Thomas Unger as my former master thesis supervisor and fellow ultrafast sufferer, Steffen Tscheuschner, Alex Rudnick and Markus Reichenberger for all the Feierabendbiere and the Lärmbrüder for all the highly professional attempts of making some Lärm.

Finally and most important, thank you to my beloved girlfriend Lisa Eberhard. We went together through this adventure for the last three years with all the work-related highs and lows, everyone fighting their own scientific demons. Thank you for your unconditional support during the hard times, thank you for caring about me, thank you for all the joyful hours, weeks and years we are allowed to spend together.

Erklärung und eidesstattliche Versicherung

Hiermit versichere ich an Eides statt, dass ich die vorliegende Arbeit selbstständig verfasst und keine anderen als die von mir angegebenen Quellen und Hilfsmittel verwendet habe.

Weiterhin erkläre ich, dass ich die Hilfe von gewerblichen Promotionsberatern bzw. -vermittlern oder ähnlichen Dienstleistern weder bisher in Anspruch genommen habe, noch künftig in Anspruch nehmen werde.

Zusätzlich erkläre ich hiermit, dass ich keinerlei frühere Promotionsversuche unternommen habe.

Bayreuth, den

Stefan Wedler